

**DESIGN AND EXPLORATION OF METAL-  
ORGANIC FRAMEWORK, METAL OXIDE,  
AND SULFIDE COMPOSITES FOR  
SUPERCAPACITOR APPLICATIONS**

**Ph.D. Thesis**

*by*

**MAYANK KUMAR SINGH**

Under the supervision of

**Dr. DHIRENDRA KUMAR RAI**

**&**

**Dr. SRIMANTA PAKHIRA**



**DEPARTMENT OF METALLURGICAL ENGINEERING AND  
MATERIALS SCIENCE  
INDIAN INSTITUTE OF TECHNOLOGY INDORE**

**APRIL 2023**

**DESIGN AND EXPLORATION OF METAL-  
ORGANIC FRAMEWORK, METAL OXIDE,  
AND SULFIDE COMPOSITES FOR  
SUPERCAPACITOR APPLICATIONS**

**Ph.D. Thesis**

*by*

**MAYANK KUMAR SINGH**

Under the supervision of

**Dr. DHIRENDRA KUMAR RAI**

**&**

**Dr. SRIMANTA PAKHIRA**



**DEPARTMENT OF METALLURGICAL ENGINEERING AND  
MATERIALS SCIENCE  
INDIAN INSTITUTE OF TECHNOLOGY INDORE**

**APRIL 2023**



# INDIAN INSTITUTE OF TECHNOLOGY INDORE

I hereby certify that the work which is being presented in the thesis entitled “**Design and Exploration of Metal-Organic Framework, Metal Oxide, and Sulfide Composites for Supercapacitor Applications**”, in the partial fulfillment of the requirements for the award of the degree of **Doctor of Philosophy** and submitted in the **Department of Metallurgical Engineering and Materials Science, Indian Institute of Technology Indore**, is an authentic record of my own work carried out during the time period from **July 2019** to **April 2024** under the supervision of **Dr. Dharendra Kumar Rai**, Associate Professor, Department of Metallurgical Engineering and Materials Science, and **Dr. Srimanta Pakhira**, Department of Physics, Indian Institute of Technology Indore.

The matter presented in this thesis has not been submitted by me for the award of any other degree of this or any other institute.

Signature of the student with date  
(MAYANK KUMAR SINGH)

This is to certify that the above statement made by the candidate is correct to the best of my/our knowledge.

Signature of Thesis Supervisor with date  
(Dr. DHIRENDRA KUMAR RAI)

13/11/2024

Signature of Thesis Supervisor with date  
(Dr. SRIMANT PAKHIRA)

**Dr. Srimanta Pakhira, Ph.D.**  
Associate Professor  
Department of Physics and  
Centre for Advanced Electronics  
Indian Institute of Technology Indore, M.P., India

**MAYANK KUMAR SINGH** has successfully given his/her Ph.D. Oral Examination held on 20/08/2024

Signature of Thesis Supervisor with date  
(Dr. DHIRENDRA KUMAR RAI)

13/11/2024

Signature of Thesis Supervisor with date  
(Dr. SRIMANTA PAKHIRA)

13.11.2024

**Dr. Srimanta Pakhira, Ph.D.**  
Associate Professor  
Department of Physics and  
Centre for Advanced Electronics  
Indian Institute of Technology Indore, M.P., India





## ACKNOWLEDGEMENTS

I attribute my gratitude to "**Lord Shiva**" for the immense generosity I feel, as it is He and only He who has bestowed it upon me.

The journey of pursuing my **Ph.D.** at **IIT Indore** has been incredibly meaningful in my life. I am deeply grateful to all the remarkable individuals I have encountered along the way, who have enriched my experiences and broadened my knowledge.

First and foremost, I extend my heartfelt thanks to my Ph.D. supervisors, **Dr. Dharendra Kumar Rai**, and **Dr. Srimanta Pakhira** for their exceptional guidance and unwavering support throughout my graduate studies. Working under Dr. Rai's guidance has been a privilege, and I will always treasure the invaluable experiences and insights gained during this time.

Special thanks go to my PSPC committee members, **Dr. Ajay Kumar Kushwaha** and **Dr Sumanta Samal** for their excellent advice, suggestions, and support in my research endeavors.

I acknowledge with gratitude the support from all members of the Department of Metallurgical Engineering and Materials Science (MEMS) and the Sophisticated Instrumentation Center (SIC) for their contributions to both technical and non-technical discussions. I am grateful to the Indian Institute of Technology Indore for the Teaching Assistantship fellowship which supported my academic journey.

A heartfelt thank you goes out to my lab colleagues at IIT Indore, including Dr. Sarathkumar Krishnan, Ms. Sheetal Gupta, Mr. Kushwanth, Ms. Neha, Ms. Suporna, and Mr. Govind. I would like to extend special appreciation to **Sarathkumar Krishnan** for his unwavering support and friendship throughout this journey. His consistent support has been invaluable, and I am truly grateful for his friendship during this significant chapter of my life.

I also extend thanks to my lab seniors and graduate students who have moved on, including, Dr. Senthilkumaran M, Dr. Anoop Kumar Gupta, Mr. Ankit Solanki, Ms. Chhavi Shivare, Mr. Saiyam Jaim, Mr. Rajat Kushwaha, Mr. Nikhil Gupta, Mr. Sahil Rapartiwar and Mr. Prakhar Gautam. Gratitude also extends to my friends Dr. Jayachandran, Dr. Anshu, Mr. Piyush Kumar, Mr. Vikesh, Mr. Shrish, Mr. Abhishek Ojha, Mr. Arpit, Mr. Dilip, Mr Rahul, Mr. Kaushal, Ms. Hema Priya.

I deeply appreciate Mrs. Priya Rai, Ms. Kinjal Rai, and Ms. Ipsita Rai for creating a familiar atmosphere and providing unwavering support.

I also extend my thanks to friends and well-wishers Mr. Sonu, Mr. Dipu, Ms. Harita, Mr. Abhigyan, Mr. Vivek Vaibhav, Mr. Gaurav, Mr. Saurav Arya, Mr. Pushkar Mishra, and Mr. Anirban Ghosh, for their consistent support throughout this journey.

Finally, I extend profound gratitude to my family, whose unwavering support has been instrumental in my achievements. I am especially thankful to my mother, Mrs. Ranjana Singh, my father, Mr. Arun Kumar Singh, my brother, Mr. Abhishek Singh, my sisters, Mrs. Priyambu, Mrs. Priya, and Ms. Runu, as well as my sister-in-law, Mrs. Priti, and niece, Ira, for their unconditional love and encouragement.

A special thanks goes to Ms. Aradhana Rai for her patience in tolerating me and her unwavering support throughout my Ph.D. journey.

In conclusion, I am immensely grateful to everyone who directly or indirectly supported and helped me during my Ph.D. journey. Your contributions have made this experience truly unforgettable.

**Dedicated to my father.**  
**“Mr. Om Prakash Singh”**

# LIST OF PUBLICATIONS

## First author publications

- [1] **Mayank K. Singh**, Anoop K. Gupta, Sarathkumar Krishnan, Nikita Guha, and Dharendra K. Rai\*(2021). “A new hierarchically porous Cu-MOF composited with rGO as an efficient hybrid supercapacitor electrode material”. **Journal of Energy Storage** **43**, 103301 (I.F-9.6)
- [2] **Mayank K. Singh**, Sarathkumar Krishnan, and Dharendra K. Rai\*(2022). Rational design of  $Ti_3C_2T_x$  MXenes coupled with hierarchical CoS as a flexible symmetric supercapacitor. **Electrochimica Acta**, **2023**, **441**, 141825 (I.F-6.6)
- [3] **Mayank K. Singh**, Sarathkumar Krishnan, Khushwant Singh, and Dharendra K. Rai\*(2024). Effective assembling of nickel oxide-reduced graphene oxide heterostructures for ultrahigh capacity supercapattery. **Journal of Power Sources**, **2024**,**595**, 234060 (I.F-9.2)
- [4] **Mayank K. Singh**, Sarathkumar Krishnan, Khushwant Singh and Dharendra K. Rai\*(2024). CNT Interwoven Cu-MOF: A Synergistic Electrochemical Approach for Solid-State Supercapacitor and Hydrogen Evolution Reaction ACS Energy& Fuels (**Revision Submitted**)
- [5] **Mayank K. Singh**, Neha, Khushwant Singh, Suporna Bhowmik, Sheetal Gupta and Dharendra K. Rai\*(2024). An experimental and theoretical investigation of NiO-rGO composites for hydrogen evolution reactions, Materials Letters (**Revision Submitted** )
- [6] **Mayank K. Singh**, Sarathkumar Krishnan, and Dharendra K. Rai\*(2024). High energy sodium-ion storage through high entropy metal-organic framework. (**Manuscript Under Preparation**)

### Co-author publications.

- [1] Sarathkumar Krishnan, Sobhan Chatterjee, Ankit Solanki, Nikita Guha, **Mayank K. Singh**, Anoop K. Gupta, and Dharendra K. Rai (2020). Aminotetrazole-Functionalized SiO<sub>2</sub> Coated MgO Nanoparticle Composites for Removal of Acid Fuchsin Dye and Detection of Heavy Metal Ions: **ACS Appl. Nano Mater.** **2020, 3, 11203–11216. (I.F-5.2)**
- [2] Krishnan, S.; AK Gupta, **Mayank K. Singh**, N.; Guha, D K Rai (2022). Nitrogen-rich Cu-MOF decorated on reduced graphene oxide nanosheets for hybrid supercapacitor applications with enhanced cycling stability. **Chemical Engineering Journal** **435, 135042. (I.F 15.4)**
- [3] N. Guha, A. Gupta, S. Chatterjee, S. Krishnan, **Mayank K. Singh**, D. K. Rai. Environmentally benign melamine functionalized silica-coated iron oxide for selective CO<sub>2</sub> capture and fixation into cyclic carbonate. **Journal of CO<sub>2</sub> Utilization**, **49 (2021) 101575. (I.F-8.2)**
- [4] Sarathkumar Krishnan, Senthilkumaran, **Mayank K. Singh**, and Dharendra K. Rai (2023) Two-dimensional Ti<sub>3</sub>C<sub>2</sub>T<sub>x</sub> MXene nanosheets for CO<sub>2</sub> electroreduction in aqueous electrolytes. **Energy Advances.** **2023,2, 1166-1175.**
- [5] Girish Khanna, Sarathkumar Krishnan, **Mayank K. Singh**, Dharendra Kumar Rai, Sumanta Samal. A detailed investigation regarding the corrosion and electrocatalytic performance of Fe-Co-Ni-Cr-V high entropy alloy. **Electrochimica Acta**, **2023 460, 142582. (I.F-6.6)**
- [6] Shivendu Mishra, **Mayank K. Singh**, Dilip Pandey, Dharendra K. Rai \* and Abhinav Raghuvanshi. A two-dimensional semiconducting Cu(I)-MOF for binder and conductive additive-free supercapattery. **Journal of Materials Chemistry A**, **2024**, <https://doi.org/10.1039/D3TA04708C>. **(I.F-11.9)**
- [7] Rajat Kushwaha, **Mayank K. Singh**, Sarathkumar Krishnan, Dharendra K Rai. Machine learning enabled property prediction

- of carbon-based electrodes for supercapacitors **Journal of Materials Science, 2023 58 (39), 15448-15458. (I.F-4.5)**
- [8] VGSPSKS Geethapriyan Thangamani, Palani I. A., **Mayank K. Singh**, Dharendra K. Rai. Post-processing of Wire Arc Additive Manufactured Stainless Steel 308L to Enhance Compression and Corrosion Behavior using Laser Shock Peening Process. **Journal of Materials Engineering and Performance, 2023 <https://doi.org/10.1007/s11665-023-08592-z>. (I.F-2.3)**
- [9] Girish Khanna, **Mayank K. Singh**, Dharendra Kumar Rai, Sumanta Samal (2024). Lightweight single-phase Al-Cr-Ti-V multi-principal element alloy as fast and efficient electrocatalyst. **Materials Letters, 136404 (I.F 3.0)**
- [10] Khushwant Singh, **Mayank K. Singh**, Sarathkumar Krishnan, Suporna Bhowmik, Sheetal Gupta, Dharendra K. Rai. Highly selective ion transport by freestanding Zn-Imidazole complex intercalated graphene oxide membrane for enhanced blue energy harvesting. **Chemical Engineering Journal, 150683 (I.F 15.4)**

## LIST OF CONFERENCES

1. *2<sup>nd</sup> International Meeting on Energy Storage Devices (Indian Institute of Technology Roorkee, India-2023)*

**Poster:** High energy sodium-ion storage through high entropy metal-organic framework.

2. *24th Annual Conference on Materials Science (YUCOMAT-2023), Herceg Novi, Montenegro Serbia*

**Oral:** Rational design of  $Ti_3C_2T_x$  MXene coupled with hierarchical CoS for a flexible supercapattery

3. *International Seminar on Recent Advances in Chemistry & Materials Sciences (Indian Chemical Society, Kolkata, India - 2022)*

**Oral:** Cu-MOF/rGO as a Hybrid Supercapacitor

4. *World Nano Congress on Advanced Science & Technology (Vellore Institute of Technology, India - 2021)*

**Oral:** Cu-MOF/rGO as a Hybrid Supercapacitor

5. *36th M.P Young Scientists Congress (M.P. Council of Science and Technology, Indore, India - 2021)*

**Oral:**  $Ti_3C_2T_x$  MXene coupled with hierarchical CoS as Supercapacitor.

6. *THE INTERNATIONAL CONFERENCE ON BEYOND FOSSIL FUELS: The Future of Alternative Energy Technologies organized by IIT BHU at BHU, 2022*

**Poster:** Rational design of  $Ti_3C_2T_x$  MXene coupled with hierarchical CoS for a flexible supercapattery.

7. *SUPERCAPS & BATTERIES-INDIA” organized by Indian Institute of Technology Kharagpur, 2022*

**Oral:** Cu-MOF Interwoven CNT as a High-Performance Solid-State Supercapacitor

## AWARDS AND ACHIEVEMENTS

- 1) Awarded Science and Engineering Research Board-International Travel Grant (**SERB-ITG**) to attend the YUCOMAT-2023 conference in Montenegro by the Department of Science and Technology, Government of India.
- 2) Selected to attend the **International Winter School organized by JNCSAR**, Bangalore India in Dec 2022.
- 3) **Young scientist award** at 36<sup>th</sup> M.P. Young Scientist Congress, by M.P. Council of Science and Technology, Government of India, March. 2021, Bhopal, India.
- 4) ACS Nano-Letters Award for **Best Oral Presentation** at World Congress for Science and Technology Conference organized by Vellore Institute of Technology, March. 2021, Vellore, India.
- 5) **Best Poster Presentation** Award at “SUPERCAPS & BATTERIES-INDIA” organized by Indian Institute of Technology Kharagpur, 2022, India.
- 6) Conferred Young Scientist Award by GRABS Educational Trust, India.

# TABLE OF CONTENTS

Title page.....	i
Declaration Page.....	iii
Acknowledgment.....	iv
Dedication.....	vi
List of publications.....	vii
List of conferences and awards.....	x
Table of contents.....	xii
List of figures.....	xvi
List of tables.....	xxiv
Nomenclature.....	xxv
Acronyms.....	xxvi
Abstract.....	xxvii

## Contents

<b>Chapter 1 .....</b>	<b>30</b>
<b>Introduction.....</b>	<b>30</b>
1.1 Electrochemical Energy Storage .....	30
1.2 Supercapacitors .....	33
1.2.1 Historical Perspective of Supercapacitors .....	33
1.2.2 Types of Supercapacitors Based on Energy Storage Mechanism.....	35
1.2.3 Supercapacitor Components .....	45
1.2.4 Evaluation Metrics for Supercapacitor Performance.....	57
1.3 Objectives and Scope of the Thesis.....	63
<b>Chapter 2 .....</b>	<b>82</b>
2.1 Introduction .....	83
2.2 Experimental Section .....	85
2.2.1 Chemicals .....	85

2.2.2 Synthesis of Graphene Oxide and Reduced Graphene Oxide (R).....	86
2.2.3 Synthesis of Cu-MOF (M).....	86
2.2.4 Synthesis of Cu-MOF-rGO Composite (MR) .....	86
2.2.5 Synthesis of Cu-MOF-CNT Composite (MC) .....	87
2.2.6 Single-crystal X-ray diffraction study .....	87
2.2.7 Characterization.....	88
2.2.8 Electrochemical Measurements .....	88
2.2.9 Preparation of Electrodes and Electrochemical Testing .....	89
2.2.10 Fabrication of Symmetrical Supercapacitor Device (SSC).....	89
2.3 Results and Discussion.....	90
2.3.1 Synthesis.....	90
2.3.2 Structural, Morphological, and Physical Characterizations .....	91
2.3.3 Electrochemical Properties .....	100
Summary.....	116
<b>Chapter 2 - Section 2.....</b>	<b>128</b>
2.4 Results and Discussion.....	128
2.4.1 Physical and Morphological Characterization.....	129
2.4.2 Electrochemical performance .....	136
<b>Chapter 3 .....</b>	<b>157</b>
3.1 Introduction .....	157
3.2 Experimental Section .....	159
3.2.1 Chemicals .....	159
3.2.2 Synthesis of reduced graphene oxide (rGO).....	160
3.2.3 Synthesis of nickel oxide (NiO) .....	160
3.2.4 Synthesis of nickel oxide-reduced graphene oxide (NiO-rGO) Composite.....	161
3.2.5 Preparation of Electrodes for Electrochemical Testing .....	161

3.3 Characterization .....	162
3.3.1 Physiochemical Characterization .....	162
3.3.2 Electrochemical Characterization.....	162
3.3.3 Computational Study .....	163
3.4 Results and discussion.....	163
3.4.1 Synthesis.....	163
3.4.2 Structural, Physical and Morphological Characterization .	165
3.4.3 Electrochemical Properties .....	170
<b>Chapter 4 .....</b>	<b>199</b>
4.1 Introduction .....	199
4.2 Experimental Section .....	202
4.2.1 Chemicals .....	202
4.2.2 Preparation of carbon cloth (CC) substrate .....	202
4.2.3 Synthesis of MXene ( $Ti_3C_2T_x$ ) .....	202
4.2.4 Synthesis of carbon cloth coated cobalt sulfide (CoS@CC) .....	203
4.2.5 Synthesis of carbon cloth-coated cobalt sulfide (CoS) and $Ti_3C_2T_x$ (MXene) ( $Ti_3C_2T_x/CoS@CC$ ).....	203
4.2.6 Material characterizations.....	204
4.2.7 Electrochemical measurements .....	204
4.2.8 Fabrication of flexible symmetric supercapacitor (SSC) device.....	204
4.3 Results and Discussion.....	205
4.3.1 Synthesis and Characterization.....	205
4.3.2 Electrochemical studies .....	211
<b>Chapter 5 .....</b>	<b>234</b>
5.1 Introduction .....	234
5.2 Experimental Section .....	237

5.2.1 Chemicals .....	237
5.2.2 Synthesis .....	237
5.2.3 Preparation of Electrodes.....	238
5.3 Characterization .....	238
5.3.1 Physiochemical Characterization .....	238
5.3.2 Electrochemical Measurements.....	239
<b>Chapter 6 .....</b>	<b>259</b>
6.1 Conclusion.....	259
6.2 Future Research Directions .....	261

## LIST OF FIGURES

<b>Figure 1.1</b> Ragone plot of the different electrochemical energy storage devices. [14].....	32
<b>Figure 1.2</b> Historic timeline for the development of supercapacitor[20] .....	34
<b>Figure 1.3</b> Electrical double layer mechanism: a) Helmholtz model, b) Gouy- Chapman model and c) Gouy-Chapman-Stern model ( $\psi_s$ -Surface electric potential and $d$ is the effective diameter). [26].....	37
<b>Figure 1.4</b> Representation of the structure of double layer showing different adsorption regions of hydrated cations and less hydrated anions, according to Grahame's model. [26].....	38
<b>Figure 1.5</b> The schematic illustration of the energy storage mechanisms through surface redox capacitance. [39] .....	41
<b>Figure 1.6</b> The schematic illustration of the energy storage mechanisms through Intercalation Pseudocapacitor. [39] .....	43
<b>Figure 1.7</b> The schematic illustration of the energy storage mechanisms through Battery-type Faradaic Reaction[39] .....	43
<b>Figure 1.8</b> Hybrid supercapacitor electrode components.....	45
<b>Figure 1.9</b> Components of Supercapacitors .....	46
<b>Figure 1.10</b> Schematic diagram of electrochemical cells (a) three-electrode configuration, and (b) two electrode system configurations (RE and CE are shorted). .....	58
<b>Figure 1.11</b> Electrochemical signatures of EDLC, Pseudocapacitor and Battery: CV and GCD curves.[99].....	59
<b>Figure 1.12</b> EIS- detailed Nyquist plot interpretation[104] .....	62
<b>Figure 2.1</b> (a) Angle between both the isophthalate unit of 5,5'-MDIP linker (b) Dimension of the larger cage (c) dimension of the smaller cages.....	93
<b>Figure 2.2</b> (a) Asymmetric unit of Cu-MOF ( <b>M</b> ); (b) showing two types of microporous cages; (c) overall framework.....	94

<b>Figure 2.3</b> PXRD pattern of (a) experimental and simulated <b>M</b> (b) <b>M</b> , <b>R</b> , and <b>MR</b> .....	95
<b>Figure 2.4</b> TGA profile of <b>M</b> , <b>R</b> , and <b>MR</b> .....	96
<b>Figure 2.5</b> FT-IR spectra of <b>M</b> , <b>R</b> and <b>MR</b> .....	97
<b>Figure 2.6</b> FE-SEM images of (a) <b>M</b> , (b) <b>R</b> , (c) <b>M/R</b> ; TEM images of <b>M</b> (d), <b>R</b> (e), and <b>M/R</b> (f) .....	99
<b>Figure 2.7</b> (a) EDX spectra of <b>MR</b> . Apart from constituent elements (C, O, and Cu), the spectrum also shows trace amounts of Ca, Mg, Au, Na, and Si due to the glass slide substrate and gold coating.(b) Mapping of C, O, and Cu elements in <b>MR</b> composite .....	99
<b>Figure 2.8 (a,b,c)</b> . HRTEM and corresponding SAED pattern (inset) of <b>R</b> , <b>M</b> and <b>MR</b> . .....	100
<b>Figure 2.9</b> . Digital photographs of three <b>MR</b> composites with different proportions of <b>R</b> and <b>M</b> . .....	101
<b>Figure 2.10</b> . CV profiles of <b>MR</b> at different ratios. ....	101
<b>Figure 2.11</b> . N <sub>2</sub> adsorption/desorption isotherms and specific surface area of (a) 3:1 of <b>RM</b> (b) 1:1 of <b>RM</b> (c) 1:3 of <b>RM</b> .....	102
<b>Figure 2.12</b> . (a) Comparison of CVs of <b>M-GCE</b> , <b>R-GCE</b> , and <b>MR-GCE</b> at a scan rate of 100 mV.s <sup>-1</sup> in 1M Na <sub>2</sub> SO <sub>4</sub> ; (b-c-d) CV profiles of the <b>M-GCE</b> , <b>R-GCE</b> , and <b>MR-GCE</b> at different scan rates (10—500 mV.s <sup>-1</sup> ); (e) percentage EDLC and pseudocapacitive contributions to the overall capacitance of <b>MR</b> at different scan rates (50-250 mV.s <sup>-1</sup> ) ...	104
<b>Figure 2.13</b> Linear fitting of <i>i</i> vs. <i>v</i> (a-c) and <i>i</i> vs. <i>v</i> <sup>1/2</sup> (d-e) for <b>M-GCE</b> , <b>R-GCE</b> , and <b>M-/R-GCE</b> , respectively.....	105
Figure 2.14. Charge storage kinetics <i>ln i</i> (μA) vs <i>ln v</i> (mV/s): estimation of values of <i>b</i> for <b>M</b> (a), <b>R</b> (b), and <b>M/R</b> (c) .....	106
<b>Figure 2.15</b> (a-c) Percentage EDLC and pseudocapacitive contributions to the overall capacitance of <b>M,R</b> and <b>MR</b> at different scan rates (10-250 mV.s <sup>-1</sup> ).....	107
<b>Figure 2.16 (a)</b> Comparison of GCD of <b>M-GCE</b> , <b>R-GCE</b> , and <b>MR-GCE</b> at a current density of 1 A.g <sup>-1</sup> in 1M Na <sub>2</sub> SO <sub>4</sub> ; (b) GCD profiles of the <b>M-GCE</b> at different scan rate (1-10A.g <sup>-1</sup> ); (c) comparison of specific capacitance of <b>M-GCE</b> , <b>R-GCE</b> , and <b>MR</b> at 1 A.g <sup>-1</sup> ; (d) comparison of	

the change in specific capacitance of <b>M</b> -GCE, <b>R</b> -GCE, and <b>MR</b> at varying current density.....	109
<b>Figure 2.17.</b> Nyquist plot (a) and bode phase angle plot (b) for <b>M</b> , <b>R</b> , and <b>MR</b> , (c) Cycling stability of <b>MR</b> at 10 A.g <sup>-1</sup> for 4000 cycles (insets show first and last 25 GCD cycles).....	110
<b>Figure 2.18.</b> Comparison of CVs of fresh <b>MR</b> and the one retrieved after 4000 GCD cycles. ....	112
<b>Figure 2.19</b> Comparison of EIS of fresh <b>MR</b> and the one retrieved after 4000 GCD cycles. ....	112
<b>Figure 2.20</b> a) CV profile of <b>MR//MR</b> at different scan rate (10—500 mV.s <sup>-1</sup> ) ; (b) GCD profiles of the <b>MR//M/R</b> at different scan rate (1-10Ag <sup>-1</sup> ), (c) specific capacitance of <b>MR//MR</b> at varying current density, (d) Ragone plot (energy density versus power density) of <b>MR//MR</b> (Photograph of the fabricated device in the inset of <b>Figure 20 d</b> ). ...	113
<b>Figure 2.1</b> PXRD patterns of <b>M</b> , <b>C</b> , and <b>MC</b> . ....	129
<b>Figure 2.2</b> TGA curve of <b>M</b> , <b>C</b> , and <b>MC</b> nanocomposite.....	130
<b>Figure 2.3</b> FTIR spectra of <b>M</b> , <b>C</b> , and <b>MC</b> nanocomposite.....	132
<b>Figure 2.4</b> XPS spectra of <b>MC</b> (a) Full survey spectrum, high-resolution spectra of (b) Cu 2p, (c) C 1s, and (d) O 1s. ....	133
<b>Figure 2.5</b> FE-SEM of (a) <b>M</b> (b) <b>C</b> and (c) <b>MC</b> composite. TEM of (d) <b>M</b> and (f) <b>C</b> (h) <b>MC</b> (e,g,h) SAED pattern (inset) of <b>M</b> , <b>C</b> and <b>MC</b> .134	134
<b>Figure 2.6.</b> (a) EDX and (b) Mapping of <b>MC</b> composite. ....	135
<b>Figure 2.7</b> BET curve of <b>M</b> , <b>C</b> , and <b>MC</b> nanocomposite. ....	136
<b>Figure 2.8</b> (a) CV and (b,c) GCD profiles of <b>MC</b> in Positive and Negative Potential range at 50 mVs <sup>-1</sup> and 1 Ag <sup>-1</sup> .....	137
<b>Figure 2.9</b> Digital photographs of three <b>MC</b> composites with different proportions of <b>M</b> and <b>C</b> . ....	137
<b>Figure 2.10</b> Cyclic Voltammetry of <b>MC</b> in different ratio of <b>M</b> and <b>C</b> .....	138
<b>Figure 2.11</b> (a) Comparison of CVs of <b>M</b> , <b>C</b> , and <b>MC</b> at 10 mV.s <sup>-1</sup> scan rate in 1M KOH; (b, c,d) CV profiles of the <b>M</b> , <b>C</b> , and <b>MC</b> at different scan rates (10-500 mV.s <sup>-1</sup> ).....	139
<b>Figure 2.12</b> Charge storage kinetics ln i (μA) vs ln v (mV/s): estimation of values of b for <b>M</b> (a), <b>C</b> (b), and <b>MC</b> (c) .....	140

<b>Figure 2.13</b> (a) Percentage EDLC and pseudocapacitive contributions to the overall capacitance of <b>MC</b> at different scan rates (10-50 mVs <sup>-1</sup> ) (b, c) comparison of calculated CV profile of <b>MC</b> for surface only capacitance and overall experimental at 10 and 50 mVs <sup>-1</sup> .....	141
<b>Figure 2.14</b> (a) Comparison of GCD of <b>M</b> , <b>C</b> , and <b>MC</b> at a current density of 1 Ag <sup>-1</sup> in 1M KOH; (b) Specific capacitance value at 1 Ag <sup>-1</sup> <b>M</b> , <b>C</b> , and <b>MC</b> (c) GCD of <b>MC</b> at different current density(1-10Ag <sup>-1</sup> ) and (d) Specific capacitance value of <b>M</b> , <b>C</b> , and <b>MC</b> at different current density (1-10Ag <sup>-1</sup> ).....	142
<b>Figure 2.15</b> (a) Nyquist plots for <b>M</b> , <b>C</b> and <b>MC</b> with magnification (inset) and (b) Bode plots for <b>M</b> , <b>C</b> and <b>MC</b> .....	145
<b>Figure 2.16</b> (a) Cycling performance of <b>MC</b> at 10 A.g <sup>-1</sup> for 5000 cycles (insets show first and last five cycles), (b & c) Nyquist and (inset) Bode plots of fresh <b>MC</b> after 5000. ....	146
<b>Figure 2.17</b> CV profiles of <b>MC</b> before and after 5000 cycles at 100 mVs <sup>-1</sup> .....	147
<b>Figure 2.18</b> (a) FE-SEM of <b>MC</b> after 5000 cycles (b,c) EDX and elemental mapping of <b>MC</b> after 5000 cycles.....	147
<b>Figure 2.19</b> (a) CV performance at different scan rates (b) GCD profiles at different current densities (1-10 Ag <sup>-1</sup> ) (c) Specific capacitance variations with changing current densities. (d) Cycling stability of the device for 10000 consecutive cycles (insets show first and last cycle of the device), (e) Ragone plot (energy density vs. power density) of the fabricated device [36–41](f) Glowing LED and running FAN using the fabricated device. ....	149
<b>Figure 3.1</b> Comparison of PXRD patterns of NiCO <sub>3</sub> at different aging temperatures.....	164
<b>Figure 3.2</b> Comparison of PXRD patterns of NiO at different calcination temperatures.....	165
<b>Figure 3.3</b> (a) PXRD patterns of NiO, rGO, and NiO-rGO (b) Raman Spectra of NiO, rGO, and NiO-rGO (c,d,e) TGA and DSC curve of .....	168
<b>Figure 3.4</b> FE-SEM of (a) NiO (b) rGO and (c) NiO-rGO (d) EDX spectra of NiO-rGO and (e) Mapping of Ni, C, and O elements in NiO-	

rGO composite. TEM of (f) NiO and (g) rGO (h) NiO-rGO (i-k ) HRTEM and corresponding SAED pattern (inset) of NiO, rGO and NiO-rGO.....	169
<b>Figure 3.5</b> CV and GCD profiles of NiO-rGO in Positive and Negative Potential range at 50 mVs <sup>-1</sup> .....	171
<b>Figure 3.6</b> CV profiles of composite with three different ratios of components at 50 mVs <sup>-1</sup> .....	171
<b>Figure 3.7</b> CV profile comparison of Ni-Foam with (a) NiO, (b) rGO, and (c) NiO-rGO at 10 mVs <sup>-1</sup> scan rate. ....	172
<b>Figure 3.8</b> (a) Comparison of CVs of NiO, rGO, and NiO-rGO at 10 mV.s <sup>-1</sup> scan rate in 1M KOH; (b,c,d) CV profiles of the NiO, rGO, and NiO-rGO at different scan rates (5-50 mV.s <sup>-1</sup> ).....	173
<b>Figure 3.9 (a-f)</b> . Charge storage kinetics: ln i vs. ln v plots of (a) NiO, (b) rGO, and (c) NiO-rGO. The slope of each plot represents the value of b and (d) Percentage surface and diffusion-controlled capacity contributions at different scan rates to the overall capacity of NiO-rGO; (e, f) Contributions of surface and diffusion-controlled processes to the overall CV profile of NiO-rGO at 5 mVs <sup>-1</sup> and 20 mVs <sup>-1</sup> .....	174
<b>Figure 3.10</b> (a) Comparison of GCD and Specific capacity of NiO, rGO, and NiO-rGO at a current density of 1 Ag <sup>-1</sup> in 1M KOH. ....	175
<b>Figure 3.11.</b> (a-c) GCD of NiO, rGO, and NiO-rGO at a different current density; (b) Specific (d) Specific capacity value of NiO, rGO, and NiO-rGO at different current density (1-5Ag <sup>-1</sup> ), (e&f) Nyquist and Bode plots for NiO, rGO and NiO-rGO. ....	178
<b>Figure 3.12</b> (a) Cycling performance of NiO-rGO at 10 A.g-1 for 5000 cycles (insets show first and last 10 cycles), (b& c) Nyquist and Bode plots of fresh NiO-rGO after 5000.(d) CV profiles of NiO-rGO before and after 5000 cycles at 50 mVs <sup>-1</sup> .....	181
<b>Figure 3.13</b> FE-SEM of NiO-rGO after 5000 cycles. (b-d) EDX and elemental mapping of NiO/rGO after 5000 cycles. ....	182
<b>Figure 3.14</b> (a) CV profiles at different scan rates (b) GCD profiles at different current densities (1-10 Ag-1) (c) Specific capacitance variations with changing current densities. (d) Cycling performance for 10000 consecutive cycles (insets show first and last cycle of the device),	

(e) Ragone plot (energy density vs. power density) of the fabricated device [51–58] (f) Glowing LED and running FAN using the fabricated device. ....	183
<b>Figure 3.15</b> DFT optimized structure of (a) NiO (b) graphene (c) NiO-graphene; violet, grey and red represent nickel, oxygen, and carbon respectively. ....	186
<b>Figure 3.16</b> Density of States (DOS) for the NiO and graphene, with Partial Density of states (PDOS) for NiO/graphene.....	187
<b>Figure 4.1</b> PXRD pattern of Ti <sub>3</sub> AlC <sub>2</sub> and Ti <sub>3</sub> C <sub>2</sub> T <sub>x</sub> .....	206
<b>Figure 4.2</b> (a) P-XRD pattern of Ti <sub>3</sub> C <sub>2</sub> T <sub>x</sub> @CC, CoS@CC, and Ti <sub>3</sub> C <sub>2</sub> T <sub>x</sub> /CoS@CC; (b) Raman Spectra of Ti <sub>3</sub> C <sub>2</sub> T <sub>x</sub> @CC, CoS@CC, and Ti <sub>3</sub> C <sub>2</sub> T <sub>x</sub> /CoS@CC.....	207
<b>Figure 4.3</b> Raman Spectrum of carbon cloth (CC) .....	208
<b>Figure 4.4</b> (a, b). FESEM of Ti <sub>3</sub> C <sub>2</sub> T <sub>x</sub> and CoS .....	209
<b>Figure 4.5</b> (a, b, c, d). EDX and elemental mapping of Ti <sub>3</sub> C <sub>2</sub> T <sub>x</sub> and CoS .....	209
<b>Figure 4.6</b> FE-SEM images of (a,b) Ti <sub>3</sub> C <sub>2</sub> T <sub>x</sub> @CC, (c,d) CoS@CC, (e,f) Ti <sub>3</sub> C <sub>2</sub> T <sub>x</sub> /CoS@CC at lower and higher magnification; (g) Elemental mapping of Ti <sub>3</sub> C <sub>2</sub> T <sub>x</sub> /CoS@CC (h) EDX spectra of Ti <sub>3</sub> C <sub>2</sub> T <sub>x</sub> /CoS@CC.....	210
<b>Figure 4.7</b> CV curves of Ti <sub>3</sub> C <sub>2</sub> T <sub>x</sub> /CoS@CC in negative and positive potential windows at 100 mVs <sup>-1</sup> .(c) Linear Sweep Voltammetry of Ti <sub>3</sub> C <sub>2</sub> T <sub>x</sub> /CoS@CC positive potential.(d) CV profiles of different ratios of Ti <sub>3</sub> C <sub>2</sub> T <sub>x</sub> /CoS@CC .....	212
<b>Figure 4.8</b> (a) Comparison of CVs of Ti <sub>3</sub> C <sub>2</sub> T <sub>x</sub> @CC, CoS@CC, and Ti <sub>3</sub> C <sub>2</sub> T <sub>x</sub> /CoS@CC at a scan rate of 100 mVs <sup>-1</sup> in 1M KOH; (b,c,d) CV profiles of Ti <sub>3</sub> C <sub>2</sub> T <sub>x</sub> @CC, CoS@CC and Ti <sub>3</sub> C <sub>2</sub> T <sub>x</sub> /CoS@CC at different scan rates (5—100 mVs <sup>-1</sup> ).....	214
<b>Figure 4.9</b> (a) Percentage EDLC and pseudocapacitancy contributions at different scan rates to the overall capacity of Ti <sub>3</sub> C <sub>2</sub> T <sub>x</sub> @CC; (b, c) Comparison of calculated CV profile of Ti <sub>3</sub> C <sub>2</sub> T <sub>x</sub> @CC composite for diffusion only capacity and overall experimental CV at 20 and 100 mVs <sup>-1</sup> scan rates.....	215

**Figure 4.10** (a) Percentage EDLC and pseudocapacity contributions at different scan rates to the overall capacity of **CoS@CC**; (b, c) Comparison of calculated CV profile of **CoS@CC** composite for diffusion only capacity and overall experimental CV at 20 and 100 mVs<sup>-1</sup> scan rates.....216

**Figure 4.11** (a) Percentage EDLC and pseudocapacity contributions at different scan rates to the overall capacity of **Ti<sub>3</sub>C<sub>2</sub>T<sub>x</sub>/CoS@CC**; (b, c) Comparison of calculated CV profile of **Ti<sub>3</sub>C<sub>2</sub>T<sub>x</sub>/CoS@CC** composite for diffusion only capacity and overall experimental CV at 20 and 100 mVs<sup>-1</sup> scan rates. ....217

**Figure 4.12** (a) Comparison of GCD of **Ti<sub>3</sub>C<sub>2</sub>T<sub>x</sub>@CC**, **CoS@CC**, and **Ti<sub>3</sub>C<sub>2</sub>T<sub>x</sub>/CoS@CC** at a current density of 1 Ag<sup>-1</sup> in 1M KOH; (b) Comparison of specific capacity of **Ti<sub>3</sub>C<sub>2</sub>T<sub>x</sub>@CC**, **CoS@CC**, and **Ti<sub>3</sub>C<sub>2</sub>T<sub>x</sub>/CoS@CC** at 1 Ag<sup>-1</sup> in 1M KOH (c) GCD profiles of **Ti<sub>3</sub>C<sub>2</sub>T<sub>x</sub>/CoS@CC** at various current density. ....218

**Figure 4.13** (a-d). GCD profiles of (a) **Ti<sub>3</sub>C<sub>2</sub>T<sub>x</sub>@CC** (b) **CoS@CC** and (c) **Ti<sub>3</sub>C<sub>2</sub>T<sub>x</sub>/CoS@CC** at various current density ranging from 1 to 10 A.g<sup>-1</sup> (d) Comparison of change in specific capacities of **Ti<sub>3</sub>C<sub>2</sub>T<sub>x</sub>@CC**, **CoS@CC**, and **Ti<sub>3</sub>C<sub>2</sub>T<sub>x</sub>/CoS@CC** at various current density.....219

**Figure 4.14** (a) Nyquist plot of **Ti<sub>3</sub>C<sub>2</sub>T<sub>x</sub>@CC**, **CoS@CC**, and **Ti<sub>3</sub>C<sub>2</sub>T<sub>x</sub>/CoS@CC**; (b) Cycling stability of **Ti<sub>3</sub>C<sub>2</sub>T<sub>x</sub>/CoS@CC** at 10 Ag<sup>-1</sup> for 1000 cycles (insets show first and last 25 GCD cycles). .....220

**Figure 4.15** (a,b). Comparison of CVs of **Ti<sub>3</sub>C<sub>2</sub>T<sub>x</sub>/CoS/CC** before after 1000 GCD cycles.....221

**Figure 4.16** (a) FE-SEM images of **Ti<sub>3</sub>C<sub>2</sub>T<sub>x</sub>/CoS/CC** after 1000 charge-discharge cycles. (b,c) EDX spectrum and elemental mapping of **Ti<sub>3</sub>C<sub>2</sub>T<sub>x</sub>/CoS/CC** after 1000 charge-discharge cycles.....221

**Figure 4.17** (a) Schematic of the flexible symmetric device (b) CV profiles of the flexible symmetric device at different scan rates (5-500 mV.s<sup>-1</sup>), (c,d,e ) comparison of CV profiles in stretching, bending, and twisting condition.....222

**Figure 4.18** (a) GCD profiles of the flexible symmetric device at different current densities (1-10 A.g<sup>-1</sup>), (b) Specific capacity variations of the device with changing current densities (1-10 A.g<sup>-1</sup>), (c) Cycling

performance and Coulombic efficiency of the device at 10 A.g <sup>-1</sup> for 10000 consecutive cycles (d) Ragone plot of energy density vs. power density of the device along with some similar electrode materials reported recently.....	223
<b>Figure 5.1</b> PXRD patterns of Binary PBAs. ....	242
<b>Figure 5.2</b> PXRD patterns of Ternary PBAs. ....	242
<b>Figure 5.3</b> PXRD patterns, FTIR, TGA, and XPS patterns of HEPBAs. ....	244
<b>Figure 5.4 (a-j).</b> The fitted XPS spectrum of (a) C (b) Zn (c) Cu (d) Co (e) Fe (f) K (g) Mg (h) N (i) Ni (j) O .....	245
<b>Figure 5.5</b> SEM of binary PBAs .....	246
<b>Figure 5.6</b> SEM of ternary PBAs .....	246
<b>Figure 5.7</b> FESEM,EDX, Elemental Mapping, TEM, HRTEM, and SAED pattern of HEPBA.....	247
<b>Figure 5.8</b> CV and GCD profiles of binary PBAs .....	248
<b>Figure 5.9</b> CV and GCD profiles of ternary PBAs .....	248
<b>Figure 5.10.</b> CV profiles of HEPBAs at different scan rates (10-500 mV.s <sup>-1</sup> ) (b) Power law for charging and discharging (c) GCD of HEPBA at different current density (d) Specific capacity of PBAs (e) Nyquist plot (inset) Bode plot (f) stability analysis of 5000 cycles. ....	250
<b>Figure 5.11 a-c.</b> GCD of a composite at 1 Ag <sup>-1</sup> and associated P-XRD pattern (c) zoomed portion of the change in peak position at 17.2 and 35.2° .....	251
<b>Figure 5.12</b> (a) CV profiles of AC and HEPBA in negative and positive range respectively. (b) CV profiles of HEPBA at different scan rates (c) GCD profiles at different current densities (1-10 Ag <sup>-1</sup> ) (c) Specific capacitance variations with changing current densities. (d) Specific capacity at different current density (e) Ragone plot (energy density vs. power density) of the fabricated device (f) Cycling performance for 10000 consecutive cycles (insets show Glowing LED using the fabricated device).....	252

## LIST OF TABLES

<b>Table 1.</b> Crystallographic parameters of <b>Cu-MOF (M)</b> .	91
<b>Table 2.</b> Comparison of weight loss percentages of <b>M, R, and MR</b>	96
<b>Table 3.</b> Comparison table of different MOFs and their derivatives with MR for supercapacitor performance.	115
<b>Table 4.</b> Comparison table of weight loss percentage of <b>MC</b> with temperature.	131
<b>Table 5.</b> Comparison table of BET curve of <b>M, C, and MC</b> nanocomposite.	135
<b>Table 6.</b> Comparison table for efficiency in devices. [1–5]	150
<b>Table 7.</b> Comparison table of the charge storage performance of the present <b>NiO-rGO</b> with various metal-oxide carbonaceous composites	176
<b>Table 8.</b> Comparison of different Metal Sulfide MXene Composite for supercapacitor performance.	225
<b>Table 9.</b> Comparison of charge storage performance of different electrode materials investigated in the thesis.	261

## NOMENCLATURE

<b>F</b>	Farad
<b>V</b>	Voltage
<b>Wh/kg</b>	Watt-hr/kilogram
<b>W/kg</b>	Watt/kilogram
<b>C<sub>h</sub></b>	Helmholtz capacitance
<b>C<sub>d</sub></b>	Double layer capacitance
<b>Ψ<sub>s</sub></b>	Surface electrode potential
<b>ε<sub>r</sub></b>	Relative permittivity of medium
<b>ε<sub>0</sub></b>	Relative permittivity of vacuum
<b>°C</b>	Degree Celsius
<b>A</b>	Electrolyte accessible area
<b>F/g</b>	Farad/gram
<b>m<sup>2</sup>/g</b>	Meter square/gram
<b>Pt</b>	Platinum
<b>Pd</b>	Palladium
<b>Pb</b>	Lead
<b>Au</b>	Gold
<b>Ox.</b>	Oxidation
<b>Red.</b>	Reduction
<b>n</b>	Number of electrons transferred
<b>m</b>	Mass of the active materials
<b>C<sub>sp</sub></b>	Specific capacitance
<b>ΔV</b>	Potential window
<b>Ag/AgCl</b>	Silver/Silver chloride
<b>v</b>	Scan rate
<b>t<sub>0</sub></b>	Time relaxation constant
<b>f<sub>0</sub></b>	Frequency
<b>ΔG</b>	Gibbs free energy
<b>E<sub>cell</sub></b>	Cell potential
<b>A/g</b>	Ampere/gram

## ACRONYMS

<b>EES</b>	Electrochemical Energy Storage
<b>MXene</b>	Transition Metal Carbides and Nitrides
<b>AAIB</b>	Aqueous Ammonium-ion Battery
<b>EDLC</b>	Electrical Double Layer Capacitor
<b>RuO<sub>2</sub></b>	Ruthenium Oxide
<b>CV</b>	Cyclic Voltammetry
<b>GCD</b>	Galvanostatic Charge-Discharge
<b>ESR</b>	Electrolyte Series Resistance
<b>SCE</b>	Saturated Calomel Electrode
<b>AC</b>	Activated Carbon
<b>AC</b>	Alternating Current
<b>ARB</b>	Aqueous Rechargeable Batteries
<b>PBA</b>	Prussian Blue Analogues
<b>OER</b>	Oxygen Evolution Reactions
<b>HER</b>	Hydrogen Evolution Reactions
<b>P-XRD</b>	Powder X-Ray Diffraction
<b>FT-IR</b>	Fourier Transform Infrared Spectroscopy
<b>FE-SEM</b>	Field Emission Scanning Electron Microscopy
<b>XPS</b>	X-Ray Photoelectron Spectroscopy
<b>CE</b>	Counter Electrode
<b>RE</b>	Reference Electrode
<b>WE</b>	Working Electrode
<b>TMD</b>	Transition Metal Dichalcogenides
<b>SC</b>	Supercapacitor
<b>C<sub>s</sub></b>	Specific capacitance
<b>MOF</b>	Metal-organic Framework
<b>TGA</b>	Thermogravimetric Analysis
<b>EDX</b>	Energy Dispersive X-Ray Spectroscopy
<b>TEM</b>	Transmission Electron Microscopy
<b>SSC</b>	Symmetrical Supercapacitor
<b>EIS</b>	Electrochemical Impedance Spectroscopy



# ABSTRACT

## **Design and Exploration of Metal-Organic Framework, Metal Oxide, and Sulfide Composites for Supercapacitor Applications**

*by*

**Mayank Kumar Singh**

**Sustainable Energy & Environmental Materials (SEEM)**

**Laboratory**

Department of Metallurgical Engineering and Materials Science,

Indian Institute of Technology Indore, India.

Thesis supervisor: **Dr. Dharendra Kumar Rai & Dr. Srimanta**

**Pakhira**

This thesis reports the exploration of diverse charge storage mechanisms (EDLC, pseudo, battery) and their combination employing a range of materials for efficient energy storage devices using various electrode materials based on metal-organic framework (MOF), metal oxide, sulfide composites, and high entropy prussian blue analog (HEPBA) for supercapacitor application. The investigation revolves around the synthesis and characterization of new electrode materials based on metal-organic frameworks (MOFs), metal oxides, sulfide composites, and high entropy prussian blue analog (HEPBA). One key aspect explored in this study is the synergistic effect achieved by combining Cu (II) metal-organic frameworks (Cu-MOF) with carbonaceous materials such as reduced graphene oxide (rGO) and carbon nanotubes (CNTs). This composite electrode demonstrates a unique blend of pseudocapacitive and EDLC behaviors, leading to enhanced capacitive performance and cyclic. Further, the development of binder-free NiO-rGO composite electrodes highlights a remarkable combination of battery-like characteristics and EDLC behavior. These electrodes exhibit ultra-high charge storage capacity and exceptional cyclic stability, paving the way for high-performance supercapattery devices with

superior energy and power densities. Another significant contribution of this research involves the exploration of novel  $\text{Ti}_3\text{C}_2\text{T}_x/\text{CoS}$  composite electrodes deposited on flexible carbon cloth substrates. These electrodes exhibit a combination of pseudocapacitive and battery-type behavior showing high electrochemical stability, making them promising candidates for next-generation flexible supercapacitors. Additionally, another study investigates the use of high-entropy Prussian blue analogs (HEPBAs) as cathode materials, showcasing battery-type behavior with significantly high energy and power densities. This novel approach holds great potential for advancing the development of energy storage devices capable of offering high energy density without compromising power density. Overall, this thesis contributes valuable insights into the design, development, and optimization of composite electrode materials for supercapacitors, with a strong emphasis on understanding and harnessing diverse charge storage mechanisms. The research outcomes have broader implications for advancing sustainable energy technologies and addressing critical challenges in energy storage, ultimately driving progress toward a cleaner and more sustainable energy future.

# Chapter 1

## Introduction

### Background

Nanotechnology holds a pivotal role across various facets of our lives and in cutting-edge scientific domains. It can be described as a "scientific exploration of functional systems at the molecular or atomic scale, typically ranging from 1-100 nm. A fundamental aspect of nanotechnology lies in the significant increase in surface area to volume ratio, which enables novel quantum mechanical phenomena in nanomaterials due to their reduced size and specific shapes.[1] While such effects are not observable in macro or micro dimensions, they become pronounced within the nanometer scale range. Embracing the remarkable advancements of nanotechnology, nanomaterials such as metal-organic frameworks (MOFs), metal oxides, metal sulfides, two-dimensional materials like graphene and MXene, and various composites exhibit remarkable properties.[2] These promising properties, coupled with easy synthesis methods, hold immense potential for their utilization in numerous demanding applications.[3–6] This thesis reports on the utilization of this class of materials to design electrochemical energy storage devices with improved performance. For readers' understanding, the underlying principles of electrochemical energy storage and rationales for choosing suitable materials are discussed in the following sections.

### 1.1 Electrochemical Energy Storage

Addressing the challenges posed by increasing population, pollution, global warming, and geopolitical issues necessitates the exploration of renewable energy sources. However, the intermittent nature of renewable energy sources has led to a mismatch between energy demand and supply, which mandates the need to store surplus

energy at times of low demand and disburse the stored energy during high demand, thus addressing the mismatch of demand and supply associated with renewable energy sources. [7] This approach of making renewable energies as mainstream energy sources over fossil fuels has caused a growing interest in designing and developing efficient and sustainable energy storage solutions.

In this context, electrochemical energy storage systems like batteries and supercapacitors stand out among various energy storage devices due to their distinct advantages. The development of consumer electronics, electric vehicles, and smart grid applications necessitates energy storage devices that exhibit high power and energy density, long cycle life, and fast charging and discharging capabilities.[8–10] Regrettably, no single electrochemical energy storage device encompasses all these attributes. **Figure 1.1** illustrates different energy storage devices based on their power and energy density (presented as a Ragone plot), which arises due to the different charge storage mechanisms in different devices. Battery demonstrates high energy density but suffers from low power density and poor cycle life due to the involvement of Faradaic charge storage. [11,12] On the other hand, supercapacitors show less energy density; however, they possess high power density, long cycle life, and a rapid charging-discharging ability.[13]

Depending on the charge storage mechanisms, supercapacitors are classified into two types: electrochemical double-layer capacitors (EDLCs) and pseudocapacitors. Storage of charge in EDLCs occurs at the electrode-electrolyte interface via reversible ion adsorption. In contrast, in the case of pseudocapacitors, charges are stored through rapid faradaic processes involving redox reactions at or near the electrode surface.

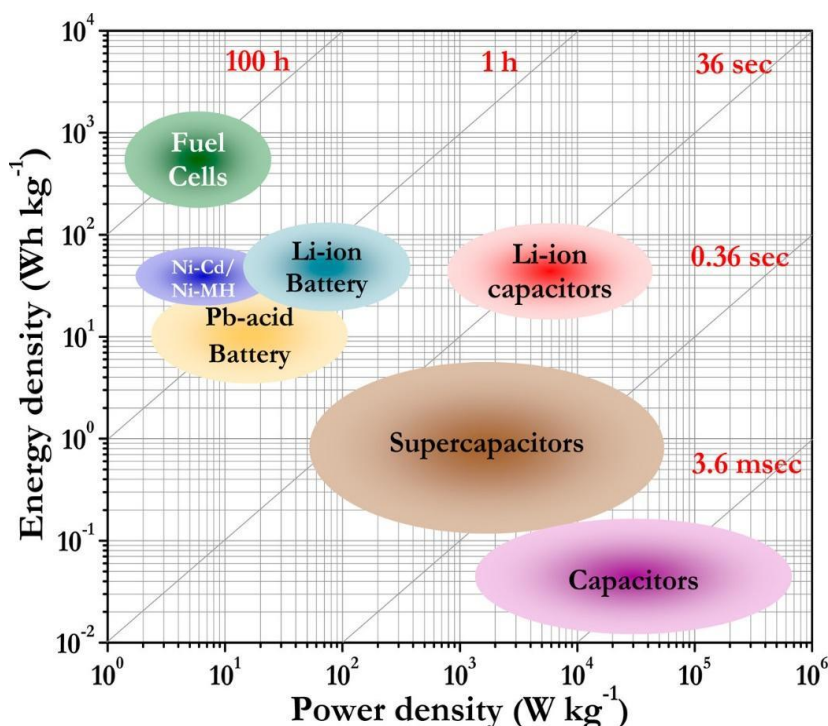


**Figure 1.1** Ragone plot of the different electrochemical energy storage devices. [14]

Currently, researchers are working on the development of a hybrid energy storage device that combines both the features of high energy density and high-power density to meet the current energy requirements. To achieve this, the energy density of supercapacitors or the power densities of batteries must be increased. Increasing the energy densities of supercapacitors has been relatively more straightforward than enhancing the power densities of batteries due to their capacitive mechanism, high-rate capability, materials properties, and simple electrochemical reactions. Conversely, the diffusion-limited nature of electrode reactions and the formation of solid-electrolyte interfaces present challenges for batteries, making high power density realization in batteries more difficult. Given these advantages, it becomes evident that supercapacitors are the optimal choice for future energy storage devices that can store energy with high power density while maintaining a good energy density. To enhance supercapacitors' energy density without significantly compromising power density, it is necessary to judiciously blend some Faradaic characteristics in capacitive materials by combining some redox active materials. In this regard, different

carbonaceous composites of metal oxides ( $\text{Fe}_3\text{O}_4$ ,  $\text{Co}_3\text{O}_4$ ,  $\text{NiO}$ ,  $\text{Ru}_2\text{O}$ ,  $\text{MgO}$ ,  $\text{MoO}_3$ ,  $\text{WO}_3$ , etc.), MXenes, metal-organic frameworks (MOFs), and conducting polymers (polyacetylene, polyaniline, and polypyrrole) have become an appealing choice, owing to their redox-active centers.[15–17] The ongoing research into electrode materials for supercapacitors shows promise for expanding the field of energy storage by enhancing the capabilities of supercapacitor devices through understanding the charge storage mechanism of composite materials that display a combination of EDLC and pseudocapacitive properties, offering a more effective approach to develop enhanced energy storage systems.

## 1.2 Supercapacitors

### 1.2.1 Historical Perspective of Supercapacitors

The history of supercapacitor progression with time is given in **Figure 1.2**. Ewald Georg Von Kleist and Pieter van Musschenbroek designed and demonstrated the first capacitor in 1745–1746, named Leyden Jar, which had two metal parts: a water-filled glass jar and a conductive chain. They discovered that moving the glass jar created static electricity stored at the electrode/electrolyte junction. It wasn't clear how static electricity worked until the 19th century. In 1853, von Helmholtz used colloidal suspensions to study the electrical double-layer (EDL) model in capacitors. In continuation, in the 19<sup>th</sup> and early 20<sup>th</sup> centuries, famous electrochemists, including Gouy, Chapman, Stern, and Grahame, researched the EDL model's theory and mechanism. Further, GE patented the first electrochemical supercapacitor in the mid-19th century. This invention introduced an energy-storage system using porous carbon electrodes in water where energy is stored at the electrical double-layer contact. After this wonderful breakthrough, Robert Rightmare at SOHIO and NEC created the first commercial electrochemical capacitor, the supercapacitor. Further, NEC's pioneering work in growing the electrochemical capacitor business enabled supercapacitors to power clock chips and

CMOS memories in electronic gadgets as the most common uses of supercapacitors, proving its continuous usefulness.[18,19]

An important discovery happened in 1971 in the field of supercapacitors, which employed ruthenium dioxide ( $\text{RuO}_2$ ) as electrode material and stored charge via faradaic processes. It was called pseudocapacitors. This discovery of pseudocapacitance allowed electrochemical capacitors to hold more charges. Based on this finding, the Pinnacle Research Institute (PRI) began a project in the 1980s to produce a high-performance supercapacitor using ruthenium/tantalum oxide pseudocapacitance, thus the name PRI capacitor. PRI capacitors are only available for military use because of the high cost of noble metals Ruthenium and Tantalum. Further, the US Department of Energy and Maxwell Technologies Inc. created high-performance supercapacitors for commercial use in the late 19th century. Today, companies like Nesscap, Elton, Nippon Chemicon, and CAP-XX create and develop supercapacitors for numerous purposes, making supercapacitors an essential part of various industries, including electric vehicles, military applications, medical devices, and robotics.

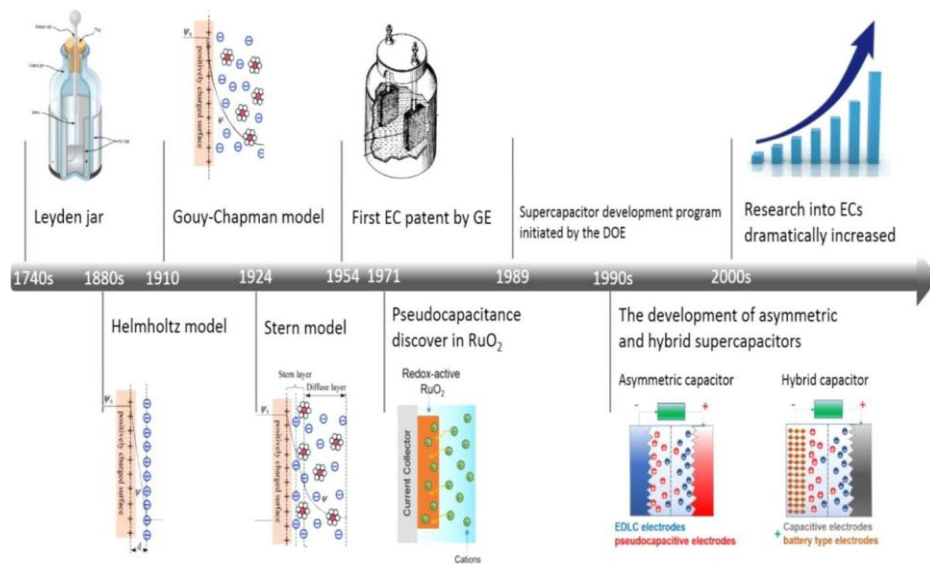


**Figure 1.2** Historic timeline for the development of supercapacitor[20]

The increasing energy demands led to the hybridization of batteries with supercapacitors, offering improved cycle lives, energy density, power density, and output voltage. Continuous advancements in electrode materials, electrolyte solutions, and design aspects have further enhanced the performance of supercapacitors. These advancements continue to drive innovation in power applications, making supercapacitors an integral part of modern energy storage systems. [21]

## **1.2.2 Types of Supercapacitors Based on Energy Storage Mechanism**

### **1.2.2.1 Electrochemical Double-Layer Capacitors**

Electrical double-layer capacitors (EDLCs) store energy like conventional capacitors by accumulating opposite electrostatic charges at the interface between the electrode and electrolyte. However, EDLCs can store larger amounts of energy compared to traditional capacitors due to smaller distances of charge separation and the utilization of high surface area activated materials as electrodes, providing more sites for charge storage.[22] The underlying principle of double-layer capacitance relies on the utilization of high surface area carbon powders or porous materials that undergo physical and/or chemical changes. To delve into this mechanism, it's crucial to understand that an electrochemical capacitor employing the double-layer capacitance mechanism requires two interfaces of electrode/electrolyte, which work in opposition to each other. One interface becomes positively charged while the other becomes negatively charged relative to the electrolyte solutions, typically separated by a separator between the two electrodes. The capacitive behavior of an individual electrode can be studied independently, yet the presence of a second electrode, namely a counter electrode, must be included in the electrical circuit. This configuration is termed a capacitor cell or a two-electrode system. However, it's preferable to include a third reference electrode for better understanding, where potential measurements can be studied and regulated, thereby isolating any external factors that might influence the working

electrode.[23] This setup is known as a three-electrode system. The distinctions between both configurations will be elaborated upon in subsequent sections of this chapter.

The determination of the double-layer capacitance and its dependence on the potential of the electrode is necessary to provide detailed information on the electrode structure and behavior in a supercapacitor device. This is mainly attributed to the fact that the charge,  $Q$ , held on each side of the electrode interface (electron density on the electrode side and ion density on the electrolyte side) is dependent on the potential ( $E$ ) of the electrode, which corresponds to the Fermi level of electron energy states in this electrode. This prevails the differential quantity of capacitance,  $C$ , defined as  $C = \frac{dQ}{dE}$ . Different models have been suggested to describe the capacitive behavior, all starting with the prototype consisting of two parallel plates of opposite charges separated by a small distance. The chronological models proposed are discussed herein, with their correct description of the structure at electrode interfaces. In 1853, Hermann von Helmholtz introduced the concept of double-layer capacitance, initially conceiving it in terms of the distribution of opposite charges.[24] The Helmholtz model for the electrode-electrolyte interface suggests the formation of two separate layers with opposite charges on the electrode surface when an electrode bearing a charge is immersed in an electrolyte. These layers were considered to have a thickness comparable to one atom and were known as the Helmholtz double-layer model, depicted in **Figure 1.3 a**. Later, it was realized that the proposed model by Helmholtz did not consider the thermal fluctuation effect according to the Boltzmann principle, which led to the assumption that the ions in the solution remain stagnant. Further, Gouy and Chapman introduced the thermal fluctuation factor into the modified version of the double-layer capacitance, in which the ions were assumed to be point charges, and a three-dimensional diffusive distribution of the electrolyte ions was envisaged (**Figure 1.3 b**).[25]

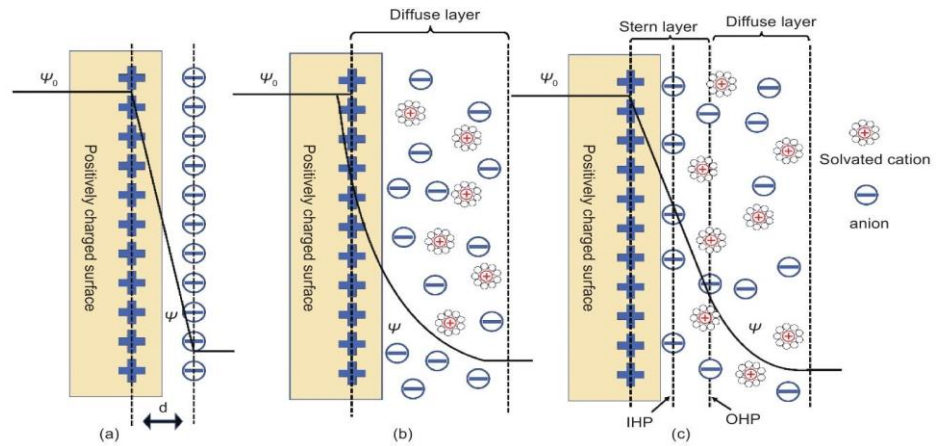


**Figure 1.3** Electrical double layer mechanism: a) Helmholtz model, b) Gouy- Chapman model and c) Gouy-Chapman-Stern model ( $\psi$ s-Surface electric potential and  $d$  is the effective diameter). [26]

This model overestimated the total capacitance, calculated on account of an incorrect potential profile at the local region of the electrode/electrolyte interface. The mathematical treatment suggested by Gouy and Chapman calculates the diffusive double-layer capacitance, and further, the overestimation problem was overcome by the model proposed by Stern in 1924. In his model, the combination of the two regions described by Helmholtz and Gouy-Chapman was recognized. In the inner region, the ions of finite size were distributed according to Langmuir's adsorption isotherm, while the region beyond the inner one and into the electrolyte was treated as a diffusive region of ionic charge distribution, as modeled by Gouy and Chapman (**Figure 1.3 c**). The total size of the ions also included their hydration shells, as depicted by Helmholtz, to account for the geometrical limitations of the compact region of ion adsorption at the electrode surface. [27] The total capacitance in the double layer ( $C_{dl}$ ) can therefore be treated as a combination of two capacitances in series, the Helmholtz compact layer capacitance ( $C_H$ ) and the diffusive capacitance ( $C_{dif}$ ). Hence,  $C_{dl}$  can be expressed as follows:

$$\frac{1}{C_{dl}} = \frac{1}{C_H} + \frac{1}{C_{dif}} \quad \text{Equation 1}$$

The distinction between the Helmholtz compact layer and diffusive layer can be inferred from the distance of the closest approach of counter-ions in the solution to the electrode surface. By introducing this distance, a good basis for the interpretation of electrode/electrolyte interface phenomena can be understood.

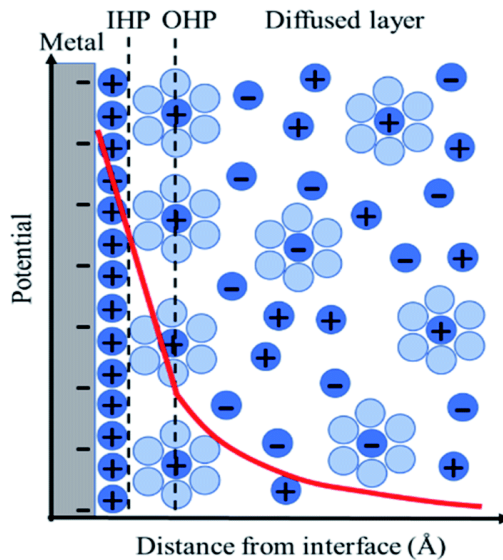


**Figure 1.4** Representation of the structure of double layer showing different adsorption regions of hydrated cations and less hydrated anions, according to Grahame's model. [26]

However, Grahame afterward emphasized the distinction between the inner Helmholtz plane (IHP) and outer Helmholtz plane (OHP), which correspond to the different distances of the closest approach for cations and anions at the interface, as demonstrated in **Figure 1.4**. This categorization arises from the fact that cations are commonly smaller than anions, in which the former also retain solvation shells. This difference leads to the conclusion that anions have smaller approach distances than hydrated cations. Consequently, inner-layer capacitances at positively charged electrodes are usually twice that of corresponding negatively charged electrodes. These aspects are of great significance to evaluate and understand the double-layer capacitance, considering the ions of the electrolyte, solvent and electrodes used. Typically, carbon materials exhibit characteristics suitable for electrical double-layer capacitors (EDLCs). [R] These carbon materials boast maximum surface areas ranging from 500 to 2000 m<sup>2</sup>/g, characterized by well-

defined porous structures.[28,29] Additionally, they demonstrate exceptional conductivity, facilitating efficient electron transfer. Theoretically, they can provide specific capacitance values in the range of 300-500 F/g. However, practical considerations limit their capacitance to 100-250 F/g due to the inability to access the entire surface area, resulting in a relatively low energy density of approximately 3-10 Wh/kg.[30,31] For example, Athika et al. synthesized zero-dimensional carbon quantum dots using a simple one-step hydrothermal method and evaluated them for supercapacitor electrode applications. The electrode exhibited a maximum specific capacitance of 97 F/g at a current density of 0.12 A/g, demonstrating good stability over 1000 cycles. [32]Furthermore, Wang et al. developed one-dimensional carbon nanofibers derived from electrospun polyacrylonitrile membranes through carbonization and utilized them as supercapacitor electrodes. They achieved a maximum specific capacitance of 257 F/g at a current density of 0.25 A/g. [33] Additionally, Fan et al. fabricated two-dimensional pitch-derived pillared carbon nanosheets using MgO templates for supercapacitor applications. The unique pillared structure facilitated efficient ion transport, resulting in an excellent specific capacitance of 289 F/g at a scan rate of 2 mV/s in a 6M KOH electrolyte. Moreover, to enhance supercapacitor performance, three-dimensional hierarchical porous carbon materials with high specific surface areas have also been reported. Liu et al. synthesized hierarchical (micro/meso/macro) porous carbon derived from chitosan using SiO<sub>2</sub> templates and evaluated it in a three-electrode system for supercapacitor applications in a 6M KOH electrolyte. They achieved a high specific capacitance of 250.5 F/g at a current density of 0.5 A/g.[34]Overall, EDLC supercapacitors offer a compelling alternative or complement to traditional energy storage technologies, providing high power density, long cycle life, rapid charging, and other desirable characteristics for a wide range of applications in energy storage devices.

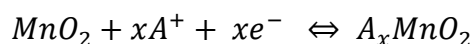
### 1.2.2.2 Pseudocapacitors

Conway introduced the term "pseudocapacitance" to describe materials that demonstrate electrochemical characteristics (such as cyclic voltammetry and charge-discharge curves) resembling those of traditional capacitors (EDLC), despite employing different charge storage mechanisms. Unlike EDLCs, pseudocapacitive reactions are of faradic origin and involve charge storage through rapid and reversible redox processes at the electrode surface. Pseudocapacitive materials undergo battery-like redox reactions and exhibit electrochemical features such as quasi-rectangular cyclic voltammograms and quasi-triangular charge-discharge curves. The charge storage mechanisms in pseudocapacitive materials may involve either surface-redox reactions occurring at or near the electrode surface or intercalation-type reactions, which will be briefly discussed in the subsequent sections.[35–38]

#### 1.2.2.2.1 Surface Redox or Intrinsic Pseudocapacitors

The primary mechanism for charge storage in surface-redox pseudocapacitors is the occurrence of charge transfers, also known as redox reactions, at the electrode's surface. **Figure 1.6** demonstrates that the CV and GCD profiles of surface-redox pseudocapacitors substantially resemble those of carbon-based materials, which shows EDLC behavior. This suggests that the charge storage is linearly dependent on the potential window. The materials that possess inherent electrochemical characteristics are known as intrinsic pseudocapacitive materials. Transition metal oxides and other surface-redox pseudocapacitive materials have been the subject of research since 1971. Trasatti and Buzzanca first documented the pseudocapacitance of RuO<sub>2</sub> in Supercapacitors that exhibit inherent (redox) pseudocapacitive behavior. Similarly, other transition metal oxides like MnO<sub>2</sub> and Fe<sub>3</sub>O<sub>4</sub> also demonstrate inherent (redox) pseudocapacitance. Due to their ability to exist in various valence states, they are capable of initiating rapid and reversible redox processes at the surface of the electrode. This characteristic makes them superior to EDLCs since they can store a much higher amount of energy at a high charge-discharge rate. **Figure**

1.5 illustrates the charge storage method and electrochemical characteristics of redox pseudocapacitors.  $MnO_2$  serves as an example, where charges are stored by surface or bulk redox reactions occurring between the +4 and +3 oxidation states of Mn.



In the above reaction mechanism, the symbol "A" embodies an alkali metal cation ( $Li^+$ ,  $Na^+$ ,  $K^+$ ). The pseudocapacitive properties of Mn-oxides strongly depend on their crystallinity and crystallographic structures. Based on the different arrangements of the  $MnO_6$  octahedra, the Mn-oxides can be classified in the diverse crystalline structures such as  $\alpha$ ,  $\beta$ ,  $\gamma$ ,  $\delta$ , and  $\lambda$  forms where  $\alpha$ ,  $\beta$ , and  $\gamma$  phases have 1D tunnels, whereas  $\delta$  and  $\lambda$  show 2D layered and 3D spinel structures, respectively.[39]

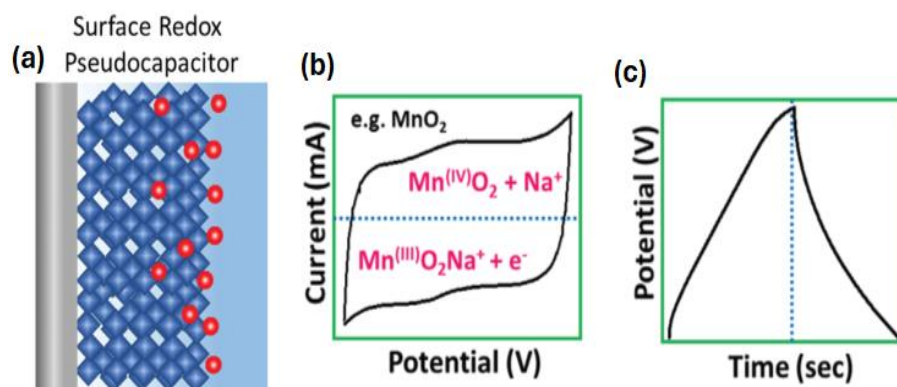


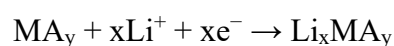
**Figure 1.5** The schematic illustration of the energy storage mechanisms through surface redox capacitance. [39]

The different physical processes and the electrode materials are responsible for these two distinct mechanisms (EDLC and pseudocapacitance). Nevertheless, the similarities can be ascribed to the relationship between potential and the amount of charges developed at the electrode/electrolyte interface or within the inner surface due to adsorption/desorption processes. Thus, without such electrochemical features, the materials cannot be qualified as pseudocapacitive, and it is not appropriate to calculate the capacitance values. Typically, conductive polymers (CPs) and transition metal compounds (TMCs) are

the fundamental materials explored as pseudocapacitive electrode materials.

#### *1.2.2.2 Intercalation Pseudocapacitors*

In addition to surface redox reactions, certain layered materials like TiO<sub>2</sub>, Nb<sub>2</sub>O<sub>5</sub>, and MoO<sub>3</sub> undergo faradaic charge transfer through the intercalation of electrolyte ions into tunnels or layers without undergoing a crystallographic phase change.[40] Remarkably, these materials demonstrate reversible and rapid charge storage rates that approach or even surpass those of traditional surface-redox pseudocapacitive materials. Therefore, they cannot be directly classified as redox pseudocapacitors. Dunn and Simon define this type of charge storage mechanism as "intercalation pseudocapacitors," which is commonly observed in non-aqueous electrolyte systems. The electrochemical characteristics of intercalation pseudocapacitance include a linear relationship between current and scan rate, minimal variation in capacity with charging time, and insignificant shifting of peak potentials with scan rate.[41] A distinguishing feature of intercalation pseudocapacitance is that materials do not undergo phase transformations during intercalation. The general reaction mechanism can be expressed as:



In contrast to EDLCs, the charge storage process for intercalation pseudocapacitance is not restricted to the surface, allowing for the utilization of the bulk of the materials for reversible faradic electrochemical reactions. Nb<sub>2</sub>O<sub>5</sub> serves as a typical example of intercalation pseudocapacitance, as depicted in the corresponding electrochemical profiles shown in **Figure 1.6**.

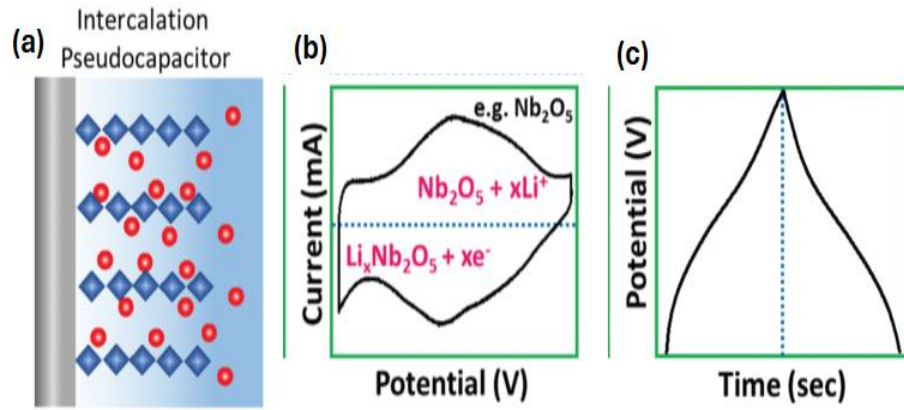


**Figure 1.6** The schematic illustration of the energy storage mechanisms through Intercalation Pseudocapacitor. [39]

#### 1.2.2.2.3 Battery Type Faradic Reactions

The conventional battery-type electrode materials are different from the capacitor-like electrodes in terms of the redox processes, which are responsible for the phase change of the electrode materials during the electrochemical process.[42] Moreover, during the charging-discharging process, the potential of the battery-type electrode remains constant, agreeing to the phase rule and following the Nernst equation, as shown in **Figure 1.7**.

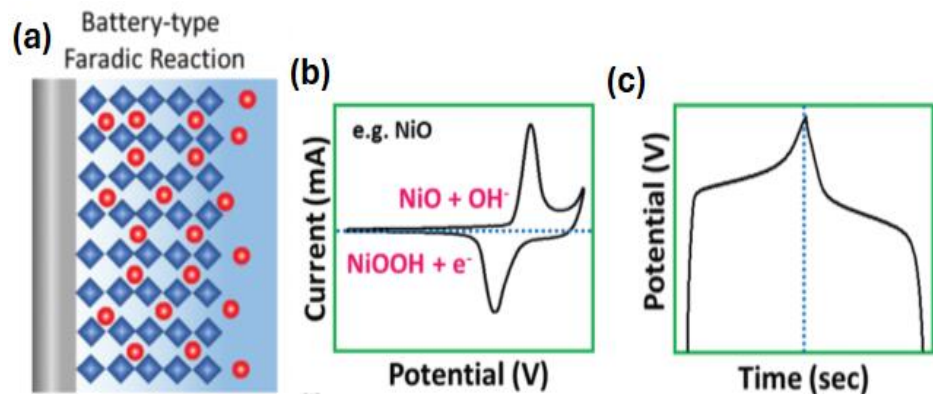


**Figure 1.7** The schematic illustration of the energy storage mechanisms through Battery-type Faradaic Reaction[39]

Therefore, the materials with solid-state diffusion-controlled faradic (battery-type) reactions display a couple of well-defined redox peaks in CV profiles and flat (plateau) charge/discharge profiles similar to a battery. The typical battery materials include Ni, Co, Cu, and Cd-

constructed oxide/ hydroxide, sulfide/selenide, and phosphide that react with hydroxide ions in alkaline media to store a charge.

#### *1.2.2.2.4 Hybrid capacitors*

Hybrid supercapacitors store energy by combining the non-faradic (EDLC) and faradaic (Pseudocapacitor) charge storage principles. The goal of hybrid supercapacitors is to use the benefits of both EDLCs and pseudocapacitors characteristics while mitigating their downsides to obtain superior electrochemical performance and charge storage capabilities. Hybrid supercapacitors have shown greater energy and power densities compared to EDLCs and pseudocapacitors while preserving cycle stability and rate capabilities. [43] Three types of hybrid supercapacitors can be distinguished based on the electrode configuration: i) asymmetric hybrids, ii) battery-type hybrids, and iii) composite hybrids.[44] These categories represent various design methods and offer distinct qualities in terms of performance and applications. In the asymmetric hybrid configuration, the EDLC-type electrode is negative, and the pseudocapacitor-based electrode is used as a positive electrode to achieve high energy density by extending the working voltage window. Similarly, battery-type hybrid capacitors comprise the EDLC-type negative electrode and a battery-type positive electrode to achieve high-performance supercapacitors. Additionally, their performance bridges the gap between the supercapacitors and the battery. In the case of composite hybrid configuration, both EDLC and pseudocapacitor electrode materials are combined to fabricate an electrode whose charge storage mechanism involves both electrostatic ion adsorption and the faradaic process.[45]

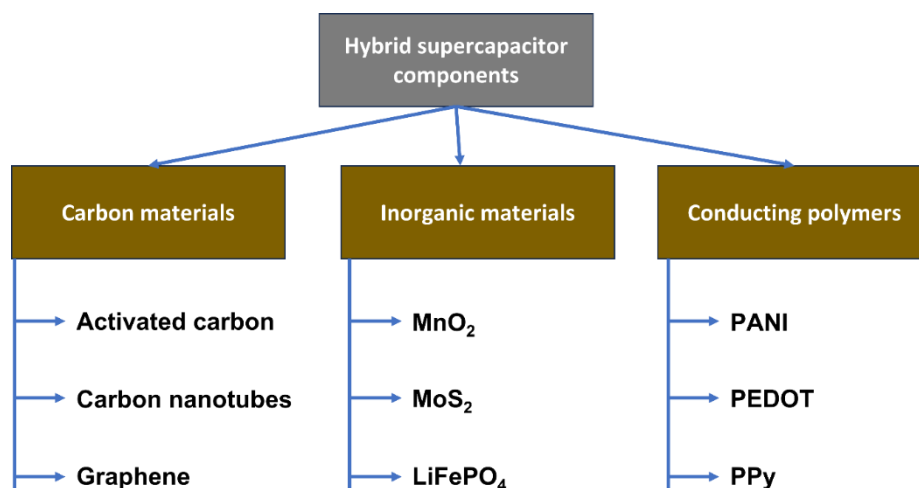


**Figure 1.8** Hybrid supercapacitor electrode components

Owing to the synergistic effect of EDLC and pseudocapacitive behavior, the composite hybrid performs better than EDLC and pseudocapacitor devices. **Figure 1.8** depicts different types of materials used to fabricate hybrid capacitors. Recently, Sarathkumar et al. prepared the hybrid electrode integrated with pseudocapacitor type Cu-MOF and highly conductive EDLC type rGO for symmetrical hybrid supercapacitor applications. The hybrid electrode (CuMOF/rGO) exhibits a maximum energy density of  $30.56 \text{ Wh.kg}^{-1}$  at a power density of  $0.6 \text{ kW.kg}^{-1}$  and a maximum power density of  $12 \text{ kW.kg}^{-1}$  at  $14.59 \text{ Wh.kg}^{-1}$  energy density, with the capacity retention of 90.07% after 10,000 cycles. [R] Overall, hybrid capacitors offer a compelling solution for energy storage applications that require high power density, long cycle life, rapid charging, and safety considerations, making them suitable for a wide range of applications.

### 1.2.3 Supercapacitor Components

The supercapacitor is typically composed of five main components, a positive electrode and a negative electrode, constituting the two parallel plates, each deposited on a current collector and separated by an electrolyte and a separator (**Figure 1.9**).[46] The positive and negative electrodes can be identical or different to fabricate symmetric or asymmetric supercapacitors, respectively. Most commonly, the electrode consists of a porous carbon material with a high surface area

or a pseudo-capacitive element, including metal oxides or conducting polymers. The electrodes are immersed in the same electrolyte solution, which provides the means for either an electrostatic charge storage mechanism or redox reactions, as mentioned in the previous section. Different kinds of electrolytes have been investigated, including aqueous and non-aqueous media, which determine the potential stability window of the supercapacitor cell and, consequently, the maximum energy that can be stored in the device. The electrically insulating but ionically conducting separator is usually placed between the two electrodes to prevent short circuits. Detailed discussion regarding each of these individual components is elaborated in later subsections of this thesis. Also, capacitive performance, energy density, power density, understanding of the reason for different electrochemical behaviors, potential optimization, and stability hugely depend on the choice of materials for each cell component, so detailed assessment of each of the electrode, electrolyte, and separator is crucial.[47]

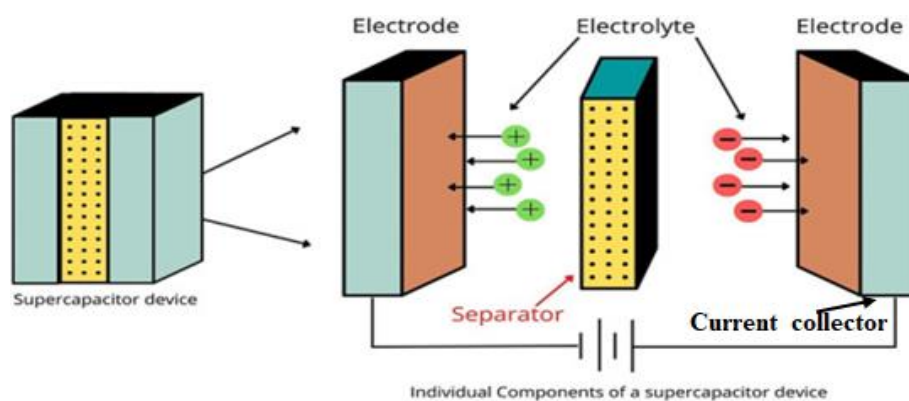


**Figure 1.9** Components of Supercapacitors

*1.2.3.1 Electrodes:* The charge storage capacity of a supercapacitor strongly depends upon the electrode materials used. The electroactive surface area of the electrode greatly influences the performance and participation of electrodes in the electrochemical reaction. Another important feature of the electrode that renders its properties in electrochemical reactions is porosity. The particle size of electrode materials plays a crucial role in determining the performance of supercapacitors. Smaller particles generally have a higher surface area-

to-volume ratio, which provides more active sites for charge storage and enhances the specific capacitance. This increased surface area also facilitates better access of the electrolyte to the electrode surface. Additionally, smaller particles result in shorter ion diffusion paths within the electrode material, reducing internal resistance and improving rate capability, allowing the supercapacitor to charge and discharge more quickly.

However, the benefits of smaller particles must be balanced against potential drawbacks. While they increase surface area, they can also affect conductivity. Extremely small particles might agglomerate, forming clusters that hinder conductivity. Furthermore, smaller particles may suffer from structural instability due to high surface energy, leading to degradation over multiple charge-discharge cycles. This structural instability can negatively impact the long-term stability of the supercapacitor. Additionally, nanoparticles are prone to aggregation and detachment from the electrode surface during cycling, which can diminish cycle life and stability. Thus, while smaller particle sizes can enhance supercapacitor performance, careful consideration must be given to balancing these factors for optimal performance and longevity. The pore size of electrode materials that yield maximum capacitances should be very close to the electrolyte's ion size. The electrode materials of supercapacitor are divided into different types: (1) carbon-based material [48] (2) conducting polymers [49] (3) metal oxides and sulfides, such as manganese oxide ( $\text{MnO}_2$ ) [50], cobalt oxide ( $\text{Co}_3\text{O}_4$ ) [51], nickel oxide ( $\text{NiO}$ ) [52], ruthenium oxide ( $\text{RuO}_2$ ) [53], molybdenum sulfides ( $\text{MoS}_2$ ), [54] (4) MXenes [55] (5) MOF based materials [56].

- **Carbon materials:** Carbon materials have the advantages of high surface area, low cost, easy processing, high chemical stability, good electronic conductivity, non-toxicity, and wider operating range. Carbon-based electrodes show a mechanism very close to EDLC. The electrochemical characterization curve of carbon materials confirms the EDLC mechanism of SC. High

surface area carbon materials generally include activated carbon, carbon aerogels, carbon nanotubes, and template porous carbon. With regard to carbon materials, different dimensions of carbon nanostructure give carbon-based materials different properties as detailed below.[57]

*Zero-dimensional carbon material:* Zero-dimensional (0-D) carbon materials refer to sphere-shaped carbon particles with an aspect ratio~1. 0-D carbon materials mainly include activated carbon (AC), carbon nanosphere, and mesoporous carbon. They possess a very large specific surface area (hundreds to thousands of  $\text{m}^2 \text{g}^{-1}$ ) with tunable pore size and distribution, which are critical factors that govern the performance of supercapacitors. Normally, 0-D carbon materials are produced from carbon-rich precursors by physical (thermal) activation at high temperatures. Yang et al. prepared a carbon nanosphere by using F108 (PEO132–PPO50–PEO132) as the structure-directing agent. After carbonization and KOH activation, it showed the highest specific capacitance of  $147 \text{ F g}^{-1}$  in 6 M KOH electrolyte and 97.5% capacitance retention over 10,000 cycles. [58] Li et al. fabricated carbon nanospheres by hydrothermal method with the highest specific capacitance of  $207 \text{ F g}^{-1}$  at a current density of  $0.5 \text{ A g}^{-1}$  in 1 M  $\text{Na}_2\text{SO}_4$  electrolyte with high-rate capability ( $181 \text{ F g}^{-1}$  at a current density of  $10 \text{ A g}^{-1}$ ).[59]

*One-dimensional carbon material:* Carbon nanotubes (CNTs), the most typical 1-D carbon material, exhibit a much higher conductivity than AC. CNTs can be categorized as single-walled carbon nanotubes (SWCNTs) or multi-walled carbon nanotubes (MWCNTs) and can be produced by arc-discharge method, chemical vapor deposition (CVD), pyrolysis of hydrocarbons, and pulsed laser vaporization. Since its discovery, CNTs have received great attention for their potential applications in energy storage. Previous research reported that pure CNTs possessed specific capacitance in a range of 20–100  $\text{F g}^{-1}$  in aqueous electrolytes.[60,61]

*Two-dimensional carbon material:* Graphene, a typical two-dimensional (2-D) carbon material, is a one-atom-thick 2-D monolayer

consisting of  $sp^2$ -hybrid carbon. Several approaches have been utilized to prepare graphene, including CVD, mechanical stripping, solvent spalling, and reduction of graphene oxide (GO). Excellent electric conductivity ensures that graphene can be used in energy storage devices. Recently, Taniya et al. have prepared a few-layered graphene by carbonizing peanut shells and activating them with KOH. The as-prepared carbon nanosheets featured a high specific surface area of  $2070 \text{ m}^2\text{g}^{-1}$  and a high specific capacitance of  $186 \text{ F g}^{-1}$  in  $1 \text{ M H}_2\text{SO}_4$  electrolyte. [62]

*Three-dimensional carbon material:* As we know, microstructures of electrode materials play an important role in the performance of energy storage systems. With increasing in dimensionality, a greater percentage of active surface is contacted with electrolyte, which will efficiently improve the electrochemical properties of electrode materials. From this point of view, a three-dimensional (3-D) structure with well-interconnected pores not only offers continuous channels to guarantee good contact with electrolytes but also accelerates charge transfer by reducing the diffusion pathways. Usually, 3D carbon materials are grown on a flexible substrate such as metal foam or polymer substrate by CVD, hydrothermal method, or template method. Wang et al. prepared N, O-rich carbon aerogel from polyimide gel after carbonization and activation. As a result, the sample exhibited a high capacitance of  $386 \text{ F g}^{-1}$  at  $1 \text{ A g}^{-1}$  in  $1 \text{ M H}_2\text{SO}_4$  electrolyte.[63] Also, Lei's group prepared a flexible carbon fiber aerogel (CFA) by simply carbonizing and activating natural cotton with KOH. The CFA presented an interleaved network structure with high conductivity and exhibited a specific capacitance of  $283 \text{ F g}^{-1}$  at  $1 \text{ A g}^{-1}$  in a  $6 \text{ M KOH}$  electrolyte. [64]

- **Conducting polymers (CPs):** CPs are suitable for supercapacitors due to their low cost, less environmental impact, high conductivity, high potential window, high porosity, and flexible redox participation through chemical alteration. CPs store charges through the redox mechanism by the insertion–reinsertion mechanism of electrolyte ions. The widely used

conducting polymers for supercapacitor applications are polyaniline (PANI), polypyrrole (PPY), and Poly(3,4-ethylenedioxythiophene) (PEDOT). [R]

- **Transition metal oxides and sulfides (TMOs, TMSs):** Transition metal oxides and sulfides have high specific capacitances and conductivity, making them worthy for electrode material yielding high energy and power-delivering SC. There are many well-known metal oxides, e.g., ruthenium oxide ( $\text{RuO}_2$ ), showing pseudocapacitive behavior having a wide potential window, suitable in acidic mediums also, but it is too expensive, which renders its application in aerospace and military. Another transition metal oxide,  $\text{MnO}_2$ , which is cheaper and less toxic, is considered an alternative to  $\text{RuO}_2$ , but it is also deficient by limited proton exchange in its crystal form with low electronic conductivity that sometimes affects its electrochemical performance of stability. For supercapacitor application, various forms of  $\text{RuO}_2$ -based electrodes have been prepared, such as metal sulfide- $\text{RuO}_2$  electrodes, metal oxide- $\text{RuO}_2$  electrodes, carbon material- $\text{RuO}_2$  electrodes, and multicomponent  $\text{RuO}_2$ -based electrodes. Asim et al. decorated carbon nanotubes (CNTs) grown carbon cloth (CNTS-CC) with  $\text{RuO}_2$  nanorods ( $\text{RuO}_2$ -NRs) via chemical vapor deposition (CVD) and the annealing process. The results showed that the designed material had high specific capacitance ( $176 \text{ F g}^{-1}$ ) and superior cycling stability (97% retention after 10,000 cycles at  $40 \text{ mA cm}^{-2}$ ). [65] Similarly, another metal oxide,  $\text{Co}_3\text{O}_4$ , is a kind of transition metal oxide belonging to the spinel family, which has the advantage of high theoretical specific capacitance ( $3560 \text{ F g}^{-1}$ ), comparatively low cost, environmental friendliness, and good chemical durability, so it is a promising active material. Indira Priyadarshini first prepared  $\text{Co}_3\text{O}_4$  nanoparticles by the sol-gel method by coating the synthesized slurry uniformly on the Ni foam substrate, and it showed the specific capacitance of the electrode at  $11 \text{ mA cm}^{-2}$  is

761.25 F g<sup>-1</sup>. [66] Shanmugavadivel and co-workers prepared a MnCo<sub>2</sub>O<sub>4</sub> electrode by a simple solution combustion method showing the maximum specific capacitance of 270 F g<sup>-1</sup> and only 7.6% capacitance loss after 1000 cycles. [67] Also, a battery-type flexible electrode fabricated by coating mesoporous NiCo<sub>2</sub>O<sub>4</sub> on an ultrafine nickel wire by electrodeposition displays a high specific capacity of 315.4 C g<sup>-1</sup> at 1 A g<sup>-1</sup> and 8.4% area-specific capacity loss after 50,000 cycles. [68]

Transition metal sulfides have the characteristics of high faradaic redox activities, unique physical or chemical properties, and long-cycle performance. The conductivity of metal sulfides is higher than that of corresponding oxides, owing to less electronegative sulfur, which facilitates the electron transfer. [69] [70]. Owing to the good electrical conductivity and specific capacitance of Co<sub>9</sub>S<sub>8</sub> and large specific surface area provided by the hollow nanoneedles structure, remarkable electrochemical properties are displayed (a high specific capacitance of 1966 F g<sup>-1</sup> at 1 A g<sup>-1</sup> and excellent capacitance retention of 92.9% after 5000 cycles). Although promising progress has been obtained in TMOs-TMSs-based electrode materials, low energy density is still an obstacle to the development of supercapacitors.

- **MXenes:** MXenes, a new class of 2D layered materials discovered by Gogotsi and colleagues, have attracted significant research interest in electrochemical energy storage over the past decade. MXenes are transition metal carbides, nitrides, or carbonitrides, with the general formula M<sub>n+1</sub>X<sub>n</sub>T<sub>x</sub>, where M is an early transition metal (Sc, Ti, V, Cr, Zr, Nb, Mo, Hf, or Ta), X is carbon and/or nitrogen, and T is terminal surface groups (-O, -OH, F, etc.). Most commonly, MXenes are derived from their corresponding MAX phases with the formula M<sub>n+1</sub>AX<sub>n</sub>, where A is an element from groups (Cd, Al, Si, P, S, Ga, Ge, As, In, Sn, Tl, Pb, or S). MXenes are obtained by selectively etching the A elements from the MAX phase using strong acids, such as

hydrofluoric acid, followed by exfoliation. Owing to their desirable characteristics, including high electrical and thermal conductivity, good oxidation resistance, high surface area, hydrophilicity, and a layered 2D structure that can host a wide variety of intercalants, they have been used for different applications but have received considerable attention as electrode materials for supercapacitors.[71,72] Recently, Gogotsi et al. made two different  $\text{Ti}_3\text{C}_2\text{T}_x$  architectures: macroporous  $\text{Ti}_3\text{C}_2\text{T}_x$ , and hydrogel  $\text{Ti}_3\text{C}_2\text{T}_x$ . Both were used in SC applications with  $\text{H}_2\text{SO}_4$  electrolytes. The obtained volumetric capacitance of  $1500 \text{ F cm}^{-3}$  at  $2 \text{ mVs}^{-1}$  of the hydrogel  $\text{Ti}_3\text{C}_2\text{T}_x$  film demonstrated exceptional capacitance retention of 90% after 10000 cycles. Notably, the macroporous  $\text{Ti}_3\text{C}_2\text{T}_x$  film outperformed the best-reported carbon material for SCs with a gravimetric capacitance of  $210 \text{ F g}^{-1}$  at  $10 \text{ Vs}^{-1}$  scan rate. [73]In another reported work, the performance of a 2D  $\text{V}_2\text{CT}_x$  MXene electrode for a supercapacitor was investigated in seawater electrolytes. The specific volumetric and gravimetric capacitances of the  $\text{V}_2\text{CT}_x$  MXene electrode were at  $317.8 \text{ F cm}^{-3}$  and  $181.1 \text{ F g}^{-1}$ , respectively, with a capacitance retention of 89.1% after 5000 cycles.[74] Similarly, in another work,  $\text{Ti}_3\text{C}_2\text{T}_x$  MXene/rGO composite demonstrated its suitability as a material for supercapacitor by combining the strong metallic conductivity of  $\text{Ti}_3\text{C}_2\text{T}_x$  with the wide surface area of rGO, showing a volumetric capacitance of  $1040 \text{ F cm}^{-3}$  at  $2 \text{ mV s}^{-1}$ .[75]. Polymers like polyaniline (PANI) or polypyrrole (PPy) have also been added to MXenes to boost their effectiveness. The hydrogen bonding interactions between the NH groups on pyrrole monomers and surface groups on  $\text{Ti}_3\text{C}_2\text{T}_x$  facilitate the direct growth of polypyrrole (PPy) on the MXene surface that generates in between the layer of MXene and, thus, prevents restacking of MXene sheets.[76,77] Wu et al. demonstrated the insertion of PPy chains into the  $\text{Ti}_3\text{C}_2$  MXene layers, rendering improved electrochemical performance. Another composite with

a bimetallic composite of Co-Fe oxide and  $\text{Ti}_3\text{C}_2\text{T}_x$  MXene showed a volumetric capacitance of  $2467.6 \text{ F cm}^3$ . [78] Similarly,  $\text{Co}_3\text{O}_4$  nanoparticles MXene (Co-MXene) composite has been shown to prevent the restacking of MXene layers, affording superior gravimetric capacitance of  $1081 \text{ F g}^{-1}$  at  $0.5 \text{ A g}^{-1}$ . [79] Overall, MXene-based supercapacitors hold great promise for high-performance energy storage applications, offering a combination of high conductivity, large surface area, electrochemical stability, and tunability. [80]

- **Metal-organic Framework:** Metal-organic frameworks (MOFs) are a novel class of porous crystalline materials built by using metal ions/clusters and organic linkers. The merits of high porosity, atomic-level dispersion of metal nodes, and tuneable structures make MOFs highly promising candidates in diverse applications, including gas separation, catalysis, sensing, and energy storage and conversion. [81] However, the straightforward utilization of pristine MOFs is hindered due to their inherent drawbacks of poor electrical conductivity. [82] To resolve this issue, it is rational to combine MOFs with conductive materials, such as carbon materials and conductive polymers (CPs) to form a desired composite, where the synergistic effect achieves enhanced electrochemical performance. [83] For example, Wen et al. synthesized Ni-MOF/CNT composites by adding different amounts of CNTs during the synthesis of Ni-MOFs. Ni-MOF/CNT showed enhanced capacitance and rate performance compared with those of pristine Ni-MOFs due to the improved conductivity. [84] Similarly, composites of Ni-MOFs and GO were also prepared and explored as electrode materials for SCs. The optimized Ni-MOFs@GO electrode could achieve high specific capacitance ( $2192 \text{ F g}^{-1}$ , at  $1 \text{ A g}^{-1}$ ). [85] Similarly, Cu-based MOF and rGO (rGO/HKUST-1) by Srimuk et al., as symmetric SC devices, showed that rGO successfully enhances the electrical

conductivity of HKUST-1 by exhibiting high specific capacitance ( $193 \text{ Fg}^{-1}$ ), improved specific energy ( $42 \text{ W hkg}^{-1}$ ) and specific power ( $3100 \text{ Wkg}^{-1}$ ). [86] In addition to being directly used as electrode materials for SCs, MOFs can also be used as sacrificial templates/precursors to prepare porous electrode materials, including carbon, metal oxide/hydroxide, metal sulfide, and heterostructure composites. Overall, while MOFs offer intriguing properties for supercapacitor applications, further research is needed to address challenges related to electrical conductivity, stability, synthesis, and scalability to realize their full potential in supercapacitor applications. [87]

*1.2.3.2 Electrolytes:* The electrolyte used in the supercapacitor is a combination of salt and solvent. It is another important part of the supercapacitor, which generates ionic conductivity and charge compensation across the electrode in an electrochemical cell. The important parameters for the selection of an electrolyte are (a) the ionic size and type, (b) electrode materials, (c) ion and solvent concentration, (d) ion and solvent interaction, and (e) the potential window of the device, etc.[88]

Majorly there are four types of electrolytes:

- **Organic electrolyte:** Organic electrolytes have been commercially used to a large extent because of their high operating potential range from 2.5-2.8 V. It also works well with cheap current collectors and packaging. Generally, organic electrolytes like conductive salts, e.g., Tetraethylammonium tetrafluoroborate ( $\text{TEABF}_4$ ) dissolved in propylene carbonate, are used for EDLCs, but the practical drawbacks of organic electrolytes are their specific capacitance, high cost, toxicity, and flammability. It also requires tough assembling and lots of complex filtrations to remove the impurities. It is also not

flexible with rising temperatures above 70° C because of the low ignition temperatures.[10,89]

- **Aqueous electrolytes:** Aqueous electrolytes are electrolytes composed primarily of water (H<sub>2</sub>O) and dissolved ions, typically salts. These electrolytes conduct electricity by dissociating into positively charged ions (cations) and negatively charged ions (anions) when dissolved in water and provide high capacitance and conductivity. Aqueous electrolytes are generally safer compared to organic electrolytes, which are commonly used in supercapacitors. Besides all good properties, the aqueous electrolyte is not the correct choice for commercial purposes because it only works in the small potential window due to narrow decomposition voltage. Some of the aqueous electrolytes which are commonly used are Na<sub>2</sub>SO<sub>4</sub>, H<sub>2</sub>SO<sub>4</sub>, KOH, Li<sub>2</sub>SO<sub>4</sub>, K<sub>2</sub>SO<sub>4</sub>, etc.[90]
- **Ionic liquid electrolytes (ILs):** Ionic liquid electrolytes are composed of room-temperature molten salts that remain in a liquid state near or at room temperature. These liquids consist entirely of ions, which are typically organic cations combined with various anions. Both aqueous and organic electrolytes do not work well with high temperatures above 70 ° C and 80 ° C, respectively. IL electrolytes work well even at high temperatures due to their high thermal and chemical stabilities. It has a very high potential window, negligible vapor pressure, and inflammable properties. The commonly used IL electrolytes are 1-ethyl-3-methylimidazolium acetate (EMIMAc), 1-ethyl-3-methylimidazolium bis (trifluoromethyl sulfonyl) imide (EMI-TFSI), etc. [91]
- **Gel and solid polymer electrolytes:** Both gel and solid polymer electrolytes are attractive alternatives to traditional liquid electrolytes in various electrochemical devices due to their improved safety, stability, and potential for customization. In this electrolyte, polymer plays an important role in increasing the

potential window with high stability and it also compensates the presence of electrolyte and separator together to make the device lightweight and less complex. A gel electrolyte incorporates a liquid electrolyte into a microporous polymer matrix that holds in the liquid electrolyte through capillary forces, creating a solid polymer film. The chosen separator must be insoluble in the desired electrolyte and provide adequate ionic conductivity. Non-polar rigid polymers such as PTFE, PVA, PVDF, and cellulose acetate offer good ion conductivity when used as gel electrolytes. This electrolyte supplies less conductivity as compared to liquid electrolytes, but it improves the efficiency of ionic mobility inside the devices. [92]

*1.2.3.3 Separator:* A separator plays a role in preventing physical contact between the two opposite electrodes. It should have a strong mechanical strength to provide sustainability and prevent the migration of carbon particles. The material should also allow ionic conductivity and electronic insulating capability. It is thin, porous, and chemically resistant to corrosion from electrolytes. Supercapacitors use cellulose paper, polymer, and glass wool as separators in the devices to work well in ambient temperatures.[93,94]

*1.2.3.4 Current collector:* It is used in supercapacitor devices to assemble and feed electric charges stored within the active capacitive material. Metal foils of aluminum, copper, and nickel with a thickness between 20 and 80  $\mu\text{m}$  are mainly used as current collectors or electrode substrates due to high conductance properties and low costs. The choice of current collector material depends on factors such as desired performance, mechanical flexibility, and compatibility with electrode materials. Additionally, optimizing the interface between the current collector and electrode materials is important to minimize resistance and maximize the energy storage efficiency of supercapacitors.[95]

## 1.2.4 Evaluation Metrics for Supercapacitor Performance

Electrochemical characterization is the most powerful technique used to investigate the performance of materials for energy storage applications. It helps understand the electrochemical reactions and their mechanisms involved in charge transfer, mass transport, electrode-electrolyte interaction, electron transport, etc. The following electrochemical techniques, like cyclic voltammetry (CV), galvanostatic charge-discharge (GCD), electrochemical impedance spectroscopy (EIS), etc., are useful for exploring several properties of supercapacitors.

In electrochemical measurements, the potential, current, and charge are the primary electrochemical signals that act as analytical signals. Thus, these signals form the core experimental design for all the electrochemical characterizations. The electrochemical characterization is carried out in an electrochemical reaction chamber called an electrochemical cell. There are two kinds of electrode systems present in electrochemical cells, namely, two electrode systems and three electrode systems. A three-electrode system configuration is commonly known as a half-cell configuration (**Figure 1.10a**), and a two-electrode system configuration is known as a full-cell configuration (**Figure 1.10b**). The three-electrode system consists of a working electrode (WE) (made up of test material), a reference electrode (RE) (Ag/AgCl or Hg/Hg<sub>2</sub>Cl<sub>2</sub>), and a counter/auxiliary electrode (CE) (platinum, silver, etc.). The potential of the WE is measured with respect to the RE (whose potential is almost constant in the narrow potential window) by keeping both electrodes as close as possible to minimize the solution resistance. The current is measured between the WE and the CE. The CE prevents the RE from passing any current, thus enabling RE to maintain a constant potential and exhibit an ideal nonpolarizable behavior. In this way, WE electrode potential is accurately measured with respect to RE. Full cell test is carried out using a two-electrode system where the RE is shorted with the CE, so the setup consists of only two electrodes, i.e.,

the WE and CE. The full cell works similarly to that of the practical device composed of positive and negative electrodes. [96]

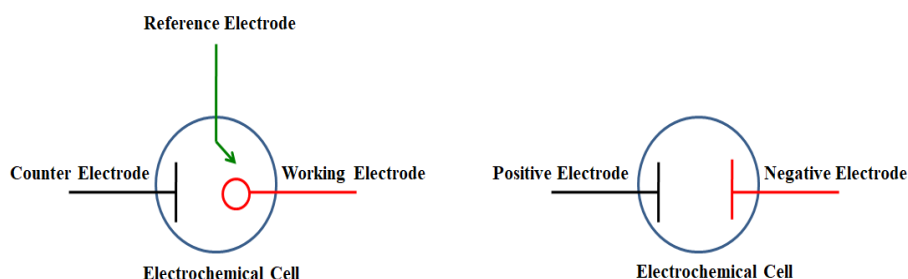


**Figure 1.10** Schematic diagram of electrochemical cells (a) three-electrode configuration, and (b) two electrode system configurations (RE and CE are shorted).

The advantage of using this cell is that it can show the more practical performance of the active electrode materials. In the case of supercapacitors, the full cell can be assembled in a symmetric configuration (both electrodes of the same material) or in an asymmetric configuration (both electrodes are made up of different materials).[97]

#### 1.2.4.1 Cyclic voltammetry

Cyclic voltammetry (CV) is one of the most versatile, important, and elementary potentiodynamic electroanalytical characterization techniques to study the electrode material for supercapacitor application. Here, the voltage is linearly ramped between the working electrode and a reference electrode in a cyclic manner in a three-electrode configuration or between the positive electrode and the negative electrode in a two-electrode configuration. The current in response is measured and plotted against the applied potential, which is known as a cyclic voltammogram. The CV provides both qualitative and quantitative information like:

- Redox behavior.
- Charge storage.
- Charge-transport.
- Mass transport (diffusion and migration).
- Polarization and reversibility associated with the electrochemical response of the material.

The recorded data is used to characterize the various electrochemical properties involved in the system, such as redox behavior, type of charge storage mechanism, operating potential window, and electrochemical reversibility of the electrode material. Cyclic voltammetry (CV) with a three-electrode setup is thought to be the most suitable technique to investigate the charge storage mechanisms in an electrode material. The shape of the resulting CV curves is analyzed as the first stage in the analytical process during CV testing (**Figure 1.11**). EDLC and the majority of pseudocapacitors materials typically have rectangular-shaped CV curves. However, some pseudocapacitors materials may exhibit distinct redox peaks that signify electrochemical reactions that are very likely to be reversible.[98]

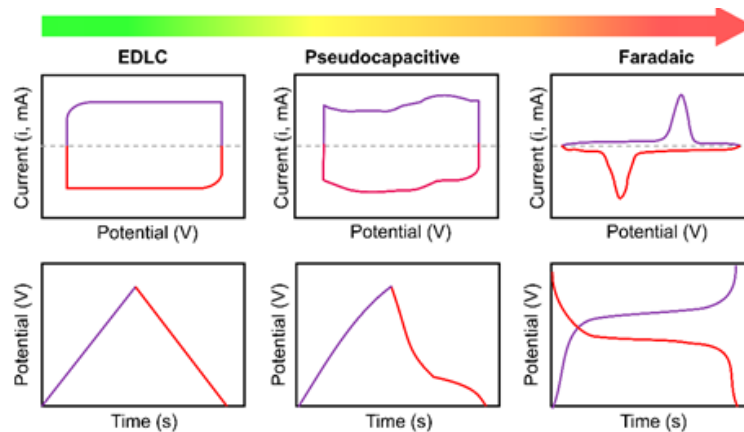


**Figure 1.11** Electrochemical signatures of EDLC, Pseudocapacitor and Battery: CV and GCD curves.[99]

The relationship between peak current ( $i$ ) and the scan rate ( $v$ ) can differentiate the charge storage mechanism. For pure EDLC materials, the observed current ( $i$ ) linearly varies with the scan rate ( $v$ ); however, for materials involving the faradaic process,  $i$  is directly proportional to the square root of  $v$ . Further, charge storage kinetic analysis can be performed to elucidate the surface-controlled (EDLC) and diffusion-controlled (faradaic) behavior of the electrode materials. The overall peak current response at any potential in CV depends on the scan rate with the power-law relationship, given in Equation 2.

$$i = av^b \quad \text{Equation 2}$$

where  $i$  is the peak current value at a given potential,  $v$  is the scan rate, and  $a$  and  $b$  are the variable constants. In the plot of  $\ln i$  vs.  $\ln v$  (from the linearized form of **Equation 2**:  $\ln i = \ln a + b \ln v$ ), the slope of the plot gives the value of  $b$ , which indicates the charge storage mechanism of an electrode. If  $b \approx 0.5$ , capacitive behavior is considered diffusion-controlled, while  $b \approx 1$  represents the surface-controlled capacitive performance. [100]

To quantify the contribution of the surface and the diffusion-controlled capacitance in the overall specific capacitance of the electroactive material, the Dunn method can be helpful. In this method, the cyclic voltammetric current response at any potential as a function of scan rate can be expressed as a combination of surface-controlled and diffusion-controlled processes, given in Equation 3. [101]

$$i(V) = k_1v + k_2v^{1/2} \quad \text{Equation 3}$$

Where,  $i(V)$  is the current at a given potential  $V$ ,  $v$  is the scan rate,  $k_1$  and  $k_2$  are the constant values for the surface and diffusion-controlled processes, respectively.

#### 1.2.4.2 Galvanostatic Charge-Discharge

The galvanostatic charge-discharge (GCD) test, also referred to as chronopotentiometry studies, is used to analyze the charge storage performance of the electrode materials in two and three-electrode configurations. In this, the electrode is subjected to a steady current from an initial potential to the set maximum potential. During the charging process, the electrode or device is charged with a predetermined current density till the set potential value and discharged back to the initial potential with the same current density. The recorded data in between the initial and maximum set potential against time is called a GCD plot. The specific capacitance and capacity, rate capability, charge storage mechanism, and reversibility are evaluated from the GCD curves. From the shape of the GCD curves, the charge storage can be qualitatively elucidated. **Figure 1.11** shows the triangular-type GCD curves

corresponding to the EDLC-type electrode materials, whereas non-triangular shape and typical voltage plateaus signify the faradaic signatures of the electrode materials. The specific capacitance is calculated from the GCD curves (Equation 4), [102,103]

$$C = \frac{I \Delta t}{m \Delta V} \quad \text{Equation 4}$$

where C is specific capacitance (F.g<sup>-1</sup>), I is the current (A), Δt is the discharge time (s), m is the mass of the coated active material (g), and ΔV is the potential window.

If the material shows battery-type behavior, the specific capacity (mAh/g) can be calculated from the following Equation 5,

$$C = \frac{I \Delta t}{m} \quad \text{Equation 5}$$

Specific capacitance, energy density, and power density of the symmetric device can be calculated from the GCD curves using the following equations.

$$C = \frac{2I \Delta t}{m \Delta V} \quad \text{Equation 6}$$

$$E_d (Wh/kg) = \frac{0.5 \times C \Delta V^2}{3.6} \quad \text{Equation 7}$$

$$P_d (W/kg) = \frac{3600 \times E_d}{\Delta t} \quad \text{Equation 8}$$

where E<sub>d</sub> is the energy density (Wh/kg) and P<sub>d</sub> is the power density (W/kg).

### 1.2.4.3 Electrochemical Impedance Spectroscopy

Electrochemical impedance spectroscopy (EIS) is carried out to elucidate the conductive nature and ion transportability of the electrode materials. EIS results are plotted in two ways: Nyquist plot and Bode plot. A Nyquist plot is a graphical representation used to analyze the impedance behavior of a system, particularly in electrochemical

impedance spectroscopy (EIS). It consists of plotting the real part ( $Z'$ ) versus the imaginary part ( $Z''$ ) of the impedance measurements obtained from the sample. [104]

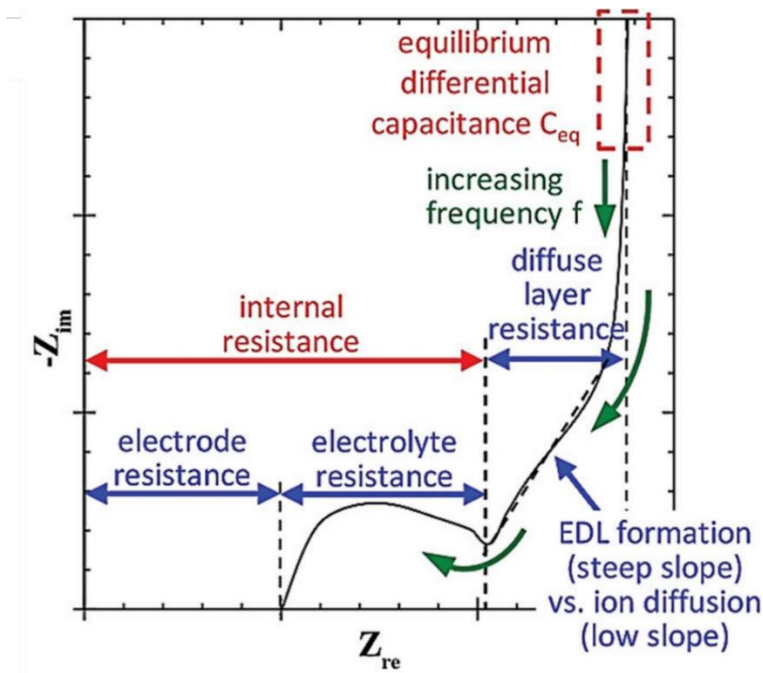


**Figure 1.12** EIS- detailed Nyquist plot interpretation[104]

In the Nyquist plot, the intercept on the real axis by the line tracing the impedance values gives the equivalent series resistance ( $R_s$ ) of electrolyte resistance and contact resistance at the electrode and electrolyte interface. The orientation of the impedance line in the Nyquist plot is also an important consideration for assessing capacitive behavior. The impedance line parallel to the imaginary axis indicates a pure EDLC behavior of a supercapacitor; however, its inclination towards the real axis suggests the involvement of faradaic character in the overall capacitive behavior. The detailed interpretation of the Nyquist plot from low frequency to high frequency is shown in **Figure 1.12** A Bode plot is a graphical representation used to analyze the frequency response of a system, showing both magnitude and phase information as functions of frequency. It consists of phase shift (in degrees) at the y-axis versus frequency at the x-axis. In the bode plot, the phase angle at the lower frequency helps to identify the capacitive nature of the electrode materials. Generally, a  $90^\circ$  phase angle at a lower

frequency refers to an ideal capacitor behavior, and the lowest phase angle is considered to involve the faradaic process in the charge storage process. Additionally, the rates of charging/discharging of the electrode materials can be measured using phase relaxation time constants ( $t_0$ ), which can be calculated from the following equation (**Equation 14**) [105,106]

$$t_0 = \frac{1}{f_0} \quad \text{Equation 14}$$

where  $t_0$  is the phase relaxation constant and  $f_0$  is the AC frequency at which both capacitive and resistive impedances have equal magnitude, which is achieved at 45° phase angle.

### **1.3 Objectives and Scope of the Thesis**

Meeting the escalating energy demand, driven by increased human activity, is crucial for sustainable development. Traditional energy sources are limited in stock and have environmental implications, mandating the exploration of green and renewable sources like wind, solar, and hydro energy. However, these sources are intermittent, necessitating efficient energy storage devices. To address this, there is a pressing need to design and synthesize advanced energy storage devices. In the current era, electrical energy is indispensable, with global demand expected to rise significantly. The scientific community is actively engaged in pioneering research to develop new energy technologies that can effectively meet the growing demand and contribute to a sustainable energy future. Therefore, to maintain the relevance of renewable energy resources, it is imperative to explore efficient energy storage systems. The development of highly efficient electrochemical energy storage devices, like batteries and supercapacitors, holds great promise for transitioning from traditional fossil fuels to cleaner, sustainable energy sources. This has captivated the attention of today's scientific community, leading to the exploration of advanced electroactive materials for advanced energy storage applications.

Supercapacitors have impressive features such as high-power density, rapid charging, long cyclic stability, and user-friendly lightweight designs. Based on their charge storage mechanisms, supercapacitors (SCs) are categorized into two types: i) electrical double-layer capacitors (EDLC) and ii) pseudocapacitors. In EDLC, charge storage occurs through ion accumulation at the electrode-electrolyte interface. [107] In pseudocapacitors, charge storage takes place due to fast-redox reactions at or near the surface of the electrode. Compared to batteries, one of the demerits of supercapacitors is their lower energy density, leading to low specific capacitance. Improving the energy density of supercapacitor electrode materials requires materials with high energy storage capacity and a basic understanding of the charge and ions transport mechanisms inside supercapacitors.

One way to improve the low energy density of SCs involves rational designing of the electrode materials, which includes excellent conductivity, highly porous structures with large surface area, and good chemical stability. Currently, researchers are trying to develop different types of materials, e.g., metal oxides and their composites ( $\text{Fe}_3\text{O}_4$ ,  $\text{Co}_3\text{O}_4$ ,  $\text{NiO}$ ,  $\text{Ru}_2\text{O}$ ,  $\text{MgO}$ ,  $\text{MoO}_3$ ,  $\text{WO}_3$ , etc.), MXenes and their composites and Metal-organic frameworks (MOFs) and their composites with carbon materials. Carbonaceous materials improve overall conductivity as well as the surface area which leads to superior performance in energy storage devices. [47]

This thesis focuses on investigating diverse charge storage mechanisms (EDLC, pseudo, battery) and their combination employing a range of materials for efficient energy storage devices using various electrode materials based on MOF, metal oxide, and sulfide composites for supercapacitor application. Overall, this thesis provides a comprehensive investigation into the design and development of various composite electrodes to understand different charge storage mechanisms for sustainable energy technologies, contributing to the realization of affordable and clean energy solutions. The entire thesis consists of six chapters, as described below:

**Chapter 1** attempts to familiarize the readers with the fundamental aspects of supercapacitors, mainly focusing on types of supercapacitors and related electrode materials and their charge storage mechanisms. The chapter also discusses the components of a supercapacitor along with a brief introduction to electrochemical techniques employed to evaluate its charge storage performance and mechanism. Overall, this chapter is dedicated to inciting the interest in designing and developing electrode materials presented in this thesis.

**Chapter 2** is focused on synthesizing a Cu(II) metal-organic framework (Cu-MOF) and thereafter compositizing with different carbonaceous (rGO and CNT) materials, showing a combination of pseudo and EDLC behavior. To better understand the effect of 2D reduced graphene oxide (rGO) and 1D carbon nanotube (CNT) on Cu-MOF, this chapter has been divided into two parts. The first and second parts discuss the synergetic effects brought out by blending rGO and CNT, respectively, with Cu (II) metal-organic framework (Cu-MOF), serving as a negative electrode material for hybrid supercapacitors. The electrochemical studies revealed that the compositization of both 1D and 2D carbon materials with Cu-MOF composite led to significant improvement in the capacitive as well as cyclic performance of Cu-MOF to different extents.

**Chapter 3** reports a binder-free NiO-rGO composite electrode material showing a combination of battery and EDLC behavior exhibiting an ultra-high charge storage capacity of  $850 \text{ Cg}^{-1}$  at  $1 \text{ Ag}^{-1}$  with excellent capacity retention of 91% after 5000 charge/discharge cycles. The assembled symmetric device using this composite also shows a superior energy density ( $56.6 \text{ W h kg}^{-1}$ ) and power density ( $9.65 \text{ kW kg}^{-1}$ ) with stable performance up to 10000 charge/discharge cycles. The experimental data of charge storage capacity have also been rationalized and supported by the first principle DFT methods through investigation of ion-electrode interaction energetics.

**Chapter 4** reports a novel  $\text{Ti}_3\text{C}_2\text{T}_x/\text{CoS}$  composite with a combination of battery and pseudo material on a carbon cloth (CC) substrate to

fabricate a flexible supercapattery device. The prepared hierarchical material with multiple attributes, such as high conductivity, rapid charge/discharge, improved electrochemical stability, and high surface area, features excellent pseudocapacitive performance. The flexible symmetrical supercapacitor device fabricated using the electrode shows good specific capacity with high stability after 10000 cycles. The results suggest that as-prepared material could be a promising candidate for the next-generation flexible supercapacitor.

**Chapter 5** introduces the adoption of Prussian blue analogs having multiple metal cations, referred to as high-entropy Prussian blue showing battery-type behavior. This alteration enhances entropy stability, induces cocktail effects, and slows diffusion, resulting in improved electrode energy density, charge-discharge efficiency, stability, and cycle performance. The electrochemical investigations showed that using high-entropy Prussian blue analog (HEPBA) as cathode material renders exceptionally high energy density ( $252 \text{ Wh.kg}^{-1}$ ) and high-power density ( $20 \text{ kW kg}^{-1}$ ). The performance yielded by HEPBAs clearly indicates its potential to be used as electrode materials for energy storage devices which can offer high energy density without compromising the power density, which is the ultimate goal of a researcher in the field of energy storage.

**Chapter 6** discusses the overall conclusion of the thesis by comparing the capacitive performance of the different electrode materials chosen based on combination of all possible charge storage mechanisms in supercapacitors. Further, an account of the future prospects of these materials has been given.

## References

- [1] E. Roduner, Size matters: why nanomaterials are different, *Chem. Soc. Rev.* 35 (2006) 583. <https://doi.org/10.1039/b502142c>.
- [2] N. Baig, I. Kammakakam, W. Falath, Nanomaterials: a review of synthesis methods, properties, recent progress, and challenges, *Mater. Adv.* 2 (2021) 1821–1871. <https://doi.org/10.1039/D0MA00807A>.
- [3] N. Shreyash, S. Bajpai, Mohd.A. Khan, Y. Vijay, S.K. Tiwary, M. Sonker, Green Synthesis of Nanoparticles and Their Biomedical Applications: A Review, *ACS Appl. Nano Mater.* 4 (2021) 11428–11457. <https://doi.org/10.1021/acsnm.1c02946>.

- [4] J. Lee, S. Mahendra, P.J.J. Alvarez, Nanomaterials in the Construction Industry: A Review of Their Applications and Environmental Health and Safety Considerations, *ACS Nano* 4 (2010) 3580–3590. <https://doi.org/10.1021/nn100866w>.
- [5] R. Rao, C.L. Pint, A.E. Islam, R.S. Weatherup, S. Hofmann, E.R. Meshot, F. Wu, C. Zhou, N. Dee, P.B. Amama, J. Carpena-Nuñez, W. Shi, D.L. Plata, E.S. Penev, B.I. Yakobson, P.B. Balbuena, C. Bichara, D.N. Futaba, S. Noda, H. Shin, K.S. Kim, B. Simard, F. Mirri, M. Pasquali, F. Fornasiero, E.I. Kauppinen, M. Arnold, B.A. Cola, P. Nikolaev, S. Arepalli, H.-M. Cheng, D.N. Zakharov, E.A. Stach, J. Zhang, F. Wei, M. Terrones, D.B. Geohegan, B. Maruyama, S. Maruyama, Y. Li, W.W. Adams, A.J. Hart, Carbon Nanotubes and Related Nanomaterials: Critical Advances and Challenges for Synthesis toward Mainstream Commercial Applications, *ACS Nano* 12 (2018) 11756–11784. <https://doi.org/10.1021/acsnano.8b06511>.
- [6] P.C. Ray, Size and Shape Dependent Second Order Nonlinear Optical Properties of Nanomaterials and Their Application in Biological and Chemical Sensing, *Chem. Rev.* 110 (2010) 5332–5365. <https://doi.org/10.1021/cr900335q>.
- [7] J. Rugolo, M.J. Aziz, Electricity storage for intermittent renewable sources, *Energy Environ. Sci.* 5 (2012) 7151. <https://doi.org/10.1039/c2ee02542f>.
- [8] A. Afif, S.M. Rahman, A. Tasfiah Azad, J. Zaini, M.A. Islan, A.K. Azad, Advanced materials and technologies for hybrid supercapacitors for energy storage – A review, *Journal of Energy Storage* 25 (2019) 100852. <https://doi.org/10.1016/j.est.2019.100852>.
- [9] M. Yaseen, M.A.K. Khattak, M. Humayun, M. Usman, S.S. Shah, S. Bibi, B.S.U. Hasnain, S.M. Ahmad, A. Khan, N. Shah, A.A. Tahir, H. Ullah, A Review of Supercapacitors: Materials Design, Modification, and Applications, *Energies* 14 (2021) 7779. <https://doi.org/10.3390/en14227779>.

- [10] C. Zhong, Y. Deng, W. Hu, J. Qiao, L. Zhang, J. Zhang, A review of electrolyte materials and compositions for electrochemical supercapacitors, *Chem. Soc. Rev.* 44 (2015) 7484–7539. <https://doi.org/10.1039/C5CS00303B>.
- [11] V. Etacheri, R. Marom, R. Elazari, G. Salitra, D. Aurbach, Challenges in the development of advanced Li-ion batteries: a review, *Energy Environ. Sci.* 4 (2011) 3243. <https://doi.org/10.1039/c1ee01598b>.
- [12] D. Aurbach, B. Markovsky, G. Salitra, E. Markevich, Y. Talyossef, M. Koltypin, L. Nazar, B. Ellis, D. Kovacheva, Review on electrode–electrolyte solution interactions, related to cathode materials for Li-ion batteries, *Journal of Power Sources* 165 (2007) 491–499. <https://doi.org/10.1016/j.jpowsour.2006.10.025>.
- [13] C. Liu, Z. Yu, D. Neff, A. Zhamu, B.Z. Jang, Graphene-Based Supercapacitor with an Ultrahigh Energy Density, *Nano Lett.* 10 (2010) 4863–4868. <https://doi.org/10.1021/nl102661q>.
- [14] V. Aravindan, J. Gnanaraj, Y.-S. Lee, S. Madhavi, Insertion-Type Electrodes for Nonaqueous Li-Ion Capacitors, *Chem. Rev.* 114 (2014) 11619–11635. <https://doi.org/10.1021/cr5000915>.
- [15] M. Wohlfahrt-Mehrens, J. Schenk, P.M. Wilde, E. Abdelmula, P. Axmann, J. Garche, New materials for supercapacitors, *Journal of Power Sources* 105 (2002) 182–188. [https://doi.org/10.1016/S0378-7753\(01\)00937-5](https://doi.org/10.1016/S0378-7753(01)00937-5).
- [16] N.N. Loganathan, V. Perumal, B.R. Pandian, R. Atchudan, T.N.J.I. Edison, M. Ovinis, Recent studies on polymeric materials for supercapacitor development, *Journal of Energy Storage* 49 (2022) 104149. <https://doi.org/10.1016/j.est.2022.104149>.
- [17] P. Lamba, P. Singh, P. Singh, P. Singh, Bharti, A. Kumar, M. Gupta, Y. Kumar, Recent advancements in supercapacitors based on different electrode materials: Classifications, synthesis methods and comparative performance, *Journal of Energy Storage* 48 (2022) 103871. <https://doi.org/10.1016/j.est.2021.103871>.
- [18] M.A. Brown, G.V. Bossa, S. May, Emergence of a Stern Layer from the Incorporation of Hydration Interactions into the Gouy–

- Chapman Model of the Electrical Double Layer, *Langmuir* 31 (2015) 11477–11483. <https://doi.org/10.1021/acs.langmuir.5b02389>.
- [19] K. Brezesinski, J. Wang, J. Haetge, C. Reitz, S.O. Steinmueller, S.H. Tolbert, B.M. Smarsly, B. Dunn, T. Brezesinski, Pseudocapacitive Contributions to Charge Storage in Highly Ordered Mesoporous Group V Transition Metal Oxides with Iso-Oriented Layered Nanocrystalline Domains, *J. Am. Chem. Soc.* 132 (2010) 6982–6990. <https://doi.org/10.1021/ja9106385>.
- [20] Y. Shao, M.F. El-Kady, J. Sun, Y. Li, Q. Zhang, M. Zhu, H. Wang, B. Dunn, R.B. Kaner, Design and Mechanisms of Asymmetric Supercapacitors, *Chem. Rev.* 118 (2018) 9233–9280. <https://doi.org/10.1021/acs.chemrev.8b00252>.
- [21] Y. Wang, Y. Xia, Recent Progress in Supercapacitors: From Materials Design to System Construction, *Advanced Materials* 25 (2013) 5336–5342. <https://doi.org/10.1002/adma.201301932>.
- [22] W. Yang, M. Ni, X. Ren, Y. Tian, N. Li, Y. Su, X. Zhang, Graphene in Supercapacitor Applications, *Current Opinion in Colloid & Interface Science* 20 (2015) 416–428. <https://doi.org/10.1016/j.cocis.2015.10.009>.
- [23] S. Zhang, N. Pan, Supercapacitors Performance Evaluation, *Advanced Energy Materials* 5 (2015) 1401401. <https://doi.org/10.1002/aenm.201401401>.
- [24] A. Eftekhari, The mechanism of ultrafast supercapacitors, *Journal of Materials Chemistry A* (2018).
- [25] K.B. Oldham, A Gouy–Chapman–Stern model of the double layer at a (metal)/(ionic liquid) interface, *Journal of Electroanalytical Chemistry* 613 (2008) 131–138. <https://doi.org/10.1016/j.jelechem.2007.10.017>.
- [26] Y. Wang, L. Zhang, H. Hou, W. Xu, G. Duan, S. He, K. Liu, S. Jiang, Recent progress in carbon-based materials for supercapacitor electrodes: a review, *J Mater Sci* 56 (2021) 173–200. <https://doi.org/10.1007/s10853-020-05157-6>.

- [27] C. Lei, N. Amini, F. Markoulidis, P. Wilson, S. Tennison, C. Lekakou, Activated carbon from phenolic resin with controlled mesoporosity for an electric double-layer capacitor (EDLC), *J. Mater. Chem. A* 1 (2013) 6037. <https://doi.org/10.1039/c3ta01638b>.
- [28] M.M. Sabzehmeidani, S. Mahnaee, M. Ghaedi, H. Heidari, V.A.L. Roy, Carbon based materials: a review of adsorbents for inorganic and organic compounds, *Mater. Adv.* 2 (2021) 598–627. <https://doi.org/10.1039/D0MA00087F>.
- [29] B. Freitas, W.G. Nunes, D.M. Soares, F.C. Rufino, C.M. Moreira, L.M. Da Silva, H. Zanin, Robust, flexible, freestanding and high surface area activated carbon and multi-walled carbon nanotubes composite material with outstanding electrode properties for aqueous-based supercapacitors, *Mater. Adv.* 2 (2021) 4264–4276. <https://doi.org/10.1039/D0MA00783H>.
- [30] H. Yang, S. Kannappan, A.S. Pandian, J.-H. Jang, Y.S. Lee, W. Lu, Graphene supercapacitor with both high power and energy density, *Nanotechnology* 28 (2017) 445401. <https://doi.org/10.1088/1361-6528/aa8948>.
- [31] R. Dubey, V. Guruviah, Review of carbon-based electrode materials for supercapacitor energy storage, *Ionics* 25 (2019) 1419–1445. <https://doi.org/10.1007/s11581-019-02874-0>.
- [32] S. Zhang, L. Sui, H. Dong, W. He, L. Dong, L. Yu, High-Performance Supercapacitor of Graphene Quantum Dots with Uniform Sizes, *ACS Appl. Mater. Interfaces* 10 (2018) 12983–12991. <https://doi.org/10.1021/acsami.8b00323>.
- [33] W. Geng, F. Ma, G. Wu, S. Song, J. Wan, D. Ma, MgO-templated hierarchical porous carbon sheets derived from coal tar pitch for supercapacitors, *Electrochimica Acta* 191 (2016) 854–863. <https://doi.org/10.1016/j.electacta.2016.01.148>.
- [34] H. Li, R. Ma, F. Chen, D. Wang, H. Zhang, C. Lu, Constructing Interconnected Microporous Structures in Carbon by Homogeneous Activation as a Sustainable Electrode Material for

- High-Performance Supercapacitors, *Molecules* 28 (2023) 6851.  
<https://doi.org/10.3390/molecules28196851>.
- [35] S. Fleischmann, J.B. Mitchell, R. Wang, C. Zhan, D. Jiang, V. Presser, V. Augustyn, Pseudocapacitance: From Fundamental Understanding to High Power Energy Storage Materials, *Chem. Rev.* 120 (2020) 6738–6782.  
<https://doi.org/10.1021/acs.chemrev.0c00170>.
- [36] C. Costentin, J.-M. Savéant, Energy storage: pseudocapacitance in prospect, *Chem. Sci.* 10 (2019) 5656–5666.  
<https://doi.org/10.1039/C9SC01662G>.
- [37] X. Yu, S. Yun, J.S. Yeon, P. Bhattacharya, L. Wang, S.W. Lee, X. Hu, H.S. Park, Emergent Pseudocapacitance of 2D Nanomaterials, *Advanced Energy Materials* 8 (2018) 1702930.  
<https://doi.org/10.1002/aenm.201702930>.
- [38] B.E. Conway, V. Birss, J. Wojtowicz, The role and utilization of pseudocapacitance for energy storage by supercapacitors, *Journal of Power Sources* 66 (1997) 1–14. [https://doi.org/10.1016/S0378-7753\(96\)02474-3](https://doi.org/10.1016/S0378-7753(96)02474-3).
- [39] N.R. Chodankar, H.D. Pham, A.K. Nanjundan, J.F.S. Fernando, K. Jayaramulu, D. Golberg, Y. Han, D.P. Dubal, True Meaning of Pseudocapacitors and Their Performance Metrics: Asymmetric versus Hybrid Supercapacitors, *Small* 16 (2020) 2002806.  
<https://doi.org/10.1002/sml.202002806>.
- [40] Y. Liu, S.P. Jiang, Z. Shao, Intercalation pseudocapacitance in electrochemical energy storage: recent advances in fundamental understanding and materials development, *Materials Today Advances* 7 (2020) 100072.  
<https://doi.org/10.1016/j.mtadv.2020.100072>.
- [41] T. Ling, P. Da, X. Zheng, B. Ge, Z. Hu, M. Wu, X.-W. Du, W.-B. Hu, M. Jaroniec, S.-Z. Qiao, Atomic-level structure engineering of metal oxides for high-rate oxygen intercalation pseudocapacitance, *Sci. Adv.* 4 (2018) eaau6261.  
<https://doi.org/10.1126/sciadv.aau6261>.

- [42] S. Sahoo, R. Kumar, E. Joanni, R.K. Singh, J.-J. Shim, Advances in pseudocapacitive and battery-like electrode materials for high performance supercapacitors, *J. Mater. Chem. A* 10 (2022) 13190–13240. <https://doi.org/10.1039/D2TA02357A>.
- [43] D.P. Chatterjee, A.K. Nandi, A review on the recent advances in hybrid supercapacitors, *J. Mater. Chem. A* 9 (2021) 15880–15918. <https://doi.org/10.1039/D1TA02505H>.
- [44] D.P. Dubal, O. Ayyad, V. Ruiz, P. Gómez-Romero, Hybrid energy storage: the merging of battery and supercapacitor chemistries, *Chem. Soc. Rev.* 44 (2015) 1777–1790. <https://doi.org/10.1039/C4CS00266K>.
- [45] D.-G. Wang, Z. Liang, S. Gao, C. Qu, R. Zou, Metal-organic framework-based materials for hybrid supercapacitor application, *Coordination Chemistry Reviews* 404 (2020) 213093. <https://doi.org/10.1016/j.ccr.2019.213093>.
- [46] N.I. Jalal, R.I. Ibrahim, M.K. Oudah, A review on Supercapacitors: types and components, *J. Phys.: Conf. Ser.* 1973 (2021) 012015. <https://doi.org/10.1088/1742-6596/1973/1/012015>.
- [47] Z.S. Iro, C. Subramani, S.S. Dash, A Brief Review on Electrode Materials for Supercapacitor, *International Journal of Electrochemical Science* 11 (2016) 10628–10643. <https://doi.org/10.20964/2016.12.50>.
- [48] A. Borenstein, O. Hanna, R. Attias, S. Luski, T. Brousse, D. Aurbach, Carbon-based composite materials for supercapacitor electrodes: a review, *J. Mater. Chem. A* 5 (2017) 12653–12672. <https://doi.org/10.1039/C7TA00863E>.
- [49] G.A. Snook, P. Kao, A.S. Best, Conducting-polymer-based supercapacitor devices and electrodes, *Journal of Power Sources* 196 (2011) 1–12. <https://doi.org/10.1016/j.jpowsour.2010.06.084>.
- [50] C. Wu, Y. Zhu, M. Ding, C. Jia, K. Zhang, Fabrication of plate-like MnO<sub>2</sub> with excellent cycle stability for supercapacitor electrodes, *Electrochimica Acta* 291 (2018) 249–255. <https://doi.org/10.1016/j.electacta.2018.08.126>.

- [51] J.P. Cheng, X. Chen, J.-S. Wu, F. Liu, X.B. Zhang, V.P. Dravid, Porous cobalt oxides with tunable hierarchical morphologies for supercapacitor electrodes, *CrystEngComm* 14 (2012) 6702. <https://doi.org/10.1039/c2ce26057c>.
- [52] H. Xiao, S. Yao, H. Liu, F. Qu, X. Zhang, X. Wu, NiO nanosheet assembles for supercapacitor electrode materials, *Progress in Natural Science: Materials International* 26 (2016) 271–275. <https://doi.org/10.1016/j.pnsc.2016.05.007>.
- [53] V. Subramanian, Mesoporous anhydrous RuO<sub>2</sub> as a supercapacitor electrode material, *Solid State Ionics* 175 (2004) 511–515. <https://doi.org/10.1016/j.ssi.2004.01.070>.
- [54] K.-J. Huang, J.-Z. Zhang, G.-W. Shi, Y.-M. Liu, Hydrothermal synthesis of molybdenum disulfide nanosheets as supercapacitors electrode material, *Electrochimica Acta* 132 (2014) 397–403. <https://doi.org/10.1016/j.electacta.2014.04.007>.
- [55] Y. Chen, H. Yang, Z. Han, Z. Bo, J. Yan, K. Cen, K.K. Ostrikov, MXene-Based Electrodes for Supercapacitor Energy Storage, *Energy Fuels* 36 (2022) 2390–2406. <https://doi.org/10.1021/acs.energyfuels.1c04104>.
- [56] B. Xu, H. Zhang, H. Mei, D. Sun, Recent progress in metal-organic framework-based supercapacitor electrode materials, *Coordination Chemistry Reviews* 420 (2020) 213438. <https://doi.org/10.1016/j.ccr.2020.213438>.
- [57] R. Kumar, E. Joanni, S. Sahoo, J.-J. Shim, W.K. Tan, A. Matsuda, R.K. Singh, An overview of recent progress in nanostructured carbon-based supercapacitor electrodes: From zero to bi-dimensional materials, *Carbon* 193 (2022) 298–338. <https://doi.org/10.1016/j.carbon.2022.03.023>.
- [58] X. Yang, H. Xia, Z. Liang, H. Li, H. Yu, Monodisperse Carbon Nanospheres with Hierarchical Porous Structure as Electrode Material for Supercapacitor, *Nanoscale Res Lett* 12 (2017) 550. <https://doi.org/10.1186/s11671-017-2318-z>.
- [59] J. Liu, X. Wang, J. Gao, Y. Zhang, Q. Lu, M. Liu, Hollow porous carbon spheres with hierarchical nanoarchitecture for application

- of the high performance supercapacitors, *Electrochimica Acta* 211 (2016) 183–192. <https://doi.org/10.1016/j.electacta.2016.05.217>.
- [60] R.A. Fisher, M.R. Watt, W. Jud Ready, Functionalized Carbon Nanotube Supercapacitor Electrodes: A Review on Pseudocapacitive Materials, *ECS J. Solid State Sci. Technol.* 2 (2013) M3170–M3177. <https://doi.org/10.1149/2.017310jss>.
- [61] H. Pan, J. Li, Y.P. Feng, Carbon Nanotubes for Supercapacitor, *Nanoscale Res Lett* 5 (2010) 654–668. <https://doi.org/10.1007/s11671-009-9508-2>.
- [62] J. Zhang, J. Jiang, H. Li, X.S. Zhao, A high-performance asymmetric supercapacitor fabricated with graphene-based electrodes, *Energy Environ. Sci.* 4 (2011) 4009. <https://doi.org/10.1039/c1ee01354h>.
- [63] D. Wang, W. Fan, S. Yuan, T. Liu, Improving hierarchical porous structure of carbon aerogels for more efficient ion transport for supercapacitors with commercial level mass loading, *Electrochimica Acta* 323 (2019) 134811. <https://doi.org/10.1016/j.electacta.2019.134811>.
- [64] P. Cheng, T. Li, H. Yu, L. Zhi, Z. Liu, Z. Lei, Biomass-Derived Carbon Fiber Aerogel as a Binder-Free Electrode for High-Rate Supercapacitors, *J. Phys. Chem. C* 120 (2016) 2079–2086. <https://doi.org/10.1021/acs.jpcc.5b11280>.
- [65] S. Asim, M.S. Javed, S. Hussain, M. Rana, F. Iram, D. Lv, M. Hashim, M. Saleem, M. Khalid, R. Jawaria, Z. Ullah, N. Gull, RuO<sub>2</sub> nanorods decorated CNTs grown carbon cloth as a free standing electrode for supercapacitor and lithium ion batteries, *Electrochimica Acta* 326 (2019) 135009. <https://doi.org/10.1016/j.electacta.2019.135009>.
- [66] C.I. Priyadharsini, G. Marimuthu, T. Pazhanivel, P.M. Anbarasan, V. Aroulmoji, V. Siva, L. Mohana, Sol–Gel synthesis of Co<sub>3</sub>O<sub>4</sub> nanoparticles as an electrode material for supercapacitor applications, *J Sol-Gel Sci Technol* 96 (2020) 416–422. <https://doi.org/10.1007/s10971-020-05393-x>.

- [67] L. Ren, J. Chen, X. Wang, M. Zhi, J. Wu, X. Zhang, Facile synthesis of flower-like  $\text{CoMn}_2\text{O}_4$  microspheres for electrochemical supercapacitors, *RSC Adv.* 5 (2015) 30963–30969. <https://doi.org/10.1039/C5RA02663F>.
- [68] N. Wang, B. Sun, P. Zhao, M. Yao, W. Hu, S. Komarneni, Electrodeposition preparation of  $\text{NiCo}_2\text{O}_4$  mesoporous film on ultrafine nickel wire for flexible asymmetric supercapacitors, *Chemical Engineering Journal* 345 (2018) 31–38. <https://doi.org/10.1016/j.cej.2018.03.147>.
- [69] J. Rehman, K. Eid, R. Ali, X. Fan, G. Murtaza, M. Faizan, A. Laref, W. Zheng, R.S. Varma, Engineering of Transition Metal Sulfide Nanostructures as Efficient Electrodes for High-Performance Supercapacitors, *ACS Appl. Energy Mater.* 5 (2022) 6481–6498. <https://doi.org/10.1021/acsaem.1c03937>.
- [70] Q. Liu, X. Hong, X. Zhang, W. Wang, W. Guo, X. Liu, M. Ye, Hierarchically structured  $\text{Co}_9\text{S}_8@ \text{NiCo}_2\text{O}_4$  nanobrushes for high-performance flexible asymmetric supercapacitors, *Chemical Engineering Journal* 356 (2019) 985–993. <https://doi.org/10.1016/j.cej.2018.09.095>.
- [71] Y. Gogotsi, B. Anasori, The Rise of MXenes, *ACS Nano* 13 (2019) 8491–8494. <https://doi.org/10.1021/acsnano.9b06394>.
- [72] G. Murali, J.K. Reddy Modigunta, Y.H. Park, J.-H. Lee, J. Rawal, S.-Y. Lee, I. In, S.-J. Park, A Review on MXene Synthesis, Stability, and Photocatalytic Applications, *ACS Nano* 16 (2022) 13370–13429. <https://doi.org/10.1021/acsnano.2c04750>.
- [73] T. Guo, D. Zhou, L. Pang, M.A. Darwish, Z. Shi, Sandwich-type macroporous  $\text{Ti}_3\text{C}_2\text{T}$  MXene frameworks for supercapacitor electrode, *Scripta Materialia* 213 (2022) 114590. <https://doi.org/10.1016/j.scriptamat.2022.114590>.
- [74] H. He, Q. Xia, B. Wang, L. Wang, Q. Hu, A. Zhou, Two-dimensional vanadium carbide ( $\text{V}_2\text{CT}$ ) MXene as supercapacitor electrode in seawater electrolyte, *Chinese Chemical Letters* 31 (2020) 984–987. <https://doi.org/10.1016/j.ccllet.2019.08.025>.

- [75] Q. Yang, Z. Xu, B. Fang, T. Huang, S. Cai, H. Chen, Y. Liu, K. Gopalsamy, W. Gao, C. Gao, MXene/graphene hybrid fibers for high performance flexible supercapacitors, *J. Mater. Chem. A* 5 (2017) 22113–22119. <https://doi.org/10.1039/C7TA07999K>.
- [76] W. Liang, I. Zhitomirsky, MXene-polypyrrole electrodes for asymmetric supercapacitors, *Electrochimica Acta* 406 (2022) 139843. <https://doi.org/10.1016/j.electacta.2022.139843>.
- [77] J. Vigneshwaran, J. Jose, S. Thomas, A. Gagliardi, M. Thelakkat, S.P. Jose, Flexible quasi-solid-state supercapacitors based on Ti<sub>3</sub>C<sub>2</sub>-Polypyrrole nanocomposites, *Electrochimica Acta* 429 (2022) 141051. <https://doi.org/10.1016/j.electacta.2022.141051>.
- [78] W. Xie, Y. Wang, J. Zhou, M. Zhang, J. Yu, C. Zhu, J. Xu, MOF-derived CoFe<sub>2</sub>O<sub>4</sub> nanorods anchored in MXene nanosheets for all pseudocapacitive flexible supercapacitors with superior energy storage, *Applied Surface Science* 534 (2020) 147584. <https://doi.org/10.1016/j.apsusc.2020.147584>.
- [79] Y. Zhang, J. Cao, Z. Yuan, L. Zhao, L. Wang, W. Han, Assembling Co<sub>3</sub>O<sub>4</sub> Nanoparticles into MXene with Enhanced electrochemical performance for advanced asymmetric supercapacitors, *Journal of Colloid and Interface Science* 599 (2021) 109–118. <https://doi.org/10.1016/j.jcis.2021.04.089>.
- [80] P.A. Shinde, A.M. Patil, S. Lee, E. Jung, S. Chan Jun, Two-dimensional MXenes for electrochemical energy storage applications, *J. Mater. Chem. A* 10 (2022) 1105–1149. <https://doi.org/10.1039/D1TA04642J>.
- [81] O. Shekhah, J. Liu, R.A. Fischer, Ch. Wöll, MOF thin films: existing and future applications, *Chem. Soc. Rev.* 40 (2011) 1081. <https://doi.org/10.1039/c0cs00147c>.
- [82] B. Dhara, S.S. Nagarkar, J. Kumar, V. Kumar, P.K. Jha, S.K. Ghosh, S. Nair, N. Ballav, Increase in Electrical Conductivity of MOF to Billion-Fold upon Filling the Nanochannels with Conducting Polymer, *J. Phys. Chem. Lett.* 7 (2016) 2945–2950. <https://doi.org/10.1021/acs.jpcllett.6b01236>.

- [83] S. Li, F. Huo, Metal–organic framework composites: from fundamentals to applications, *Nanoscale* 7 (2015) 7482–7501. <https://doi.org/10.1039/C5NR00518C>.
- [84] S. Sun, Y. Wang, L. Chen, M. Chu, Y. Dong, D. Liu, P. Liu, D. Qu, J. Duan, X. Li, MOF(Ni)/CNT composites with layer structure for high capacitive performance, *Colloids and Surfaces A: Physicochemical and Engineering Aspects* 643 (2022) 128802. <https://doi.org/10.1016/j.colsurfa.2022.128802>.
- [85] R. Sahoo, S. Ghosh, S. Chand, S. Chand Pal, T. Kuila, M.C. Das, Highly scalable and pH stable 2D Ni-MOF-based composites for high performance supercapacitor, *Composites Part B: Engineering* 245 (2022) 110174. <https://doi.org/10.1016/j.compositesb.2022.110174>.
- [86] P. Jagódka, K. Matus, A. Łamacz, On the HKUST-1/GO and HKUST-1/rGO Composites: The Impact of Synthesis Method on Physicochemical Properties, *Molecules* 27 (2022) 7082. <https://doi.org/10.3390/molecules27207082>.
- [87] A. Mohanty, D. Jaihindh, Y.-P. Fu, S.P. Senanayak, L.S. Mende, A. Ramadoss, An extensive review on three dimension architectural Metal-Organic Frameworks towards supercapacitor application, *Journal of Power Sources* 488 (2021) 229444. <https://doi.org/10.1016/j.jpowsour.2020.229444>.
- [88] B. Pal, S. Yang, S. Ramesh, V. Thangadurai, R. Jose, Electrolyte selection for supercapacitive devices: a critical review, *Nanoscale Adv.* 1 (2019) 3807–3835. <https://doi.org/10.1039/C9NA00374F>.
- [89] X. Wang, Y. Li, F. Lou, M.E. Melandsø Buan, E. Sheridan, D. Chen, Enhancing capacitance of supercapacitor with both organic electrolyte and ionic liquid electrolyte on a biomass-derived carbon, *RSC Adv.* 7 (2017) 23859–23865. <https://doi.org/10.1039/C7RA01630A>.
- [90] M.Z. Iqbal, S. Zakar, S.S. Haider, Role of aqueous electrolytes on the performance of electrochemical energy storage device, *Journal of Electroanalytical Chemistry* 858 (2020) 113793. <https://doi.org/10.1016/j.jelechem.2019.113793>.

- [91] G. Kaur, S.C. Sivasubramanian, A. Dalvi, Solid-state supercapacitors using ionic liquid dispersed Li<sup>+</sup>-NASICONs as electrolytes, *Electrochimica Acta* 434 (2022) 141311. <https://doi.org/10.1016/j.electacta.2022.141311>.
- [92] S. Alipoori, S. Mazinani, S.H. Aboutalebi, F. Sharif, Review of PVA-based gel polymer electrolytes in flexible solid-state supercapacitors: Opportunities and challenges, *Journal of Energy Storage* 27 (2020) 101072. <https://doi.org/10.1016/j.est.2019.101072>.
- [93] J. Li, H. Jia, S. Ma, L. Xie, X.-X. Wei, L. Dai, H. Wang, F. Su, C.-M. Chen, Separator Design for High-Performance Supercapacitors: Requirements, Challenges, Strategies, and Prospects, *ACS Energy Lett.* 8 (2023) 56–78. <https://doi.org/10.1021/acsenerylett.2c01853>.
- [94] S. Ahankari, D. Lasrado, R. Subramaniam, Advances in materials and fabrication of separators in supercapacitors, *Mater. Adv.* 3 (2022) 1472–1496. <https://doi.org/10.1039/D1MA00599E>.
- [95] A. Abdisattar, M. Yeleuov, C. Daulbayev, K. Askaruly, A. Tolynbekov, A. Taurbekov, N. Prikhodko, Recent advances and challenges of current collectors for supercapacitors, *Electrochemistry Communications* 142 (2022) 107373. <https://doi.org/10.1016/j.elecom.2022.107373>.
- [96] W. Sun, R. Zheng, X. Chen, Symmetric redox supercapacitor based on micro-fabrication with three-dimensional polypyrrole electrodes, *Journal of Power Sources* 195 (2010) 7120–7125. <https://doi.org/10.1016/j.jpowsour.2010.05.012>.
- [97] N. Salehifar, J.S. Shayeh, S.O. Ranaei Siadat, K. Niknam, A. Ehsani, S. Kazemi Movahhed, Electrochemical study of supercapacitor performance of polypyrrole ternary nanocomposite electrode by fast Fourier transform continuous cyclic voltammetry, *RSC Adv.* 5 (2015) 96130–96137. <https://doi.org/10.1039/C5RA18694C>.
- [98] P. Giannakou, R.C.T. Slade, M. Shkunov, Cyclic Voltammetry Studies of Inkjet-printed NiO supercapacitors: Effect of Substrates,

- Printing and Materials, *Electrochimica Acta* 353 (2020) 136539.  
<https://doi.org/10.1016/j.electacta.2020.136539>.
- [99] A.G. Olabi, Q. Abbas, M.A. Abdelkareem, A.H. Alami, M. Mirzaeian, E.T. Sayed, Carbon-Based Materials for Supercapacitors: Recent Progress, Challenges and Barriers, *Batteries* 9 (2022) 19. <https://doi.org/10.3390/batteries9010019>.
- [100] M. Cui, Z. Wang, Y. Jiang, H. Wang, Engineering the grain boundary: a promising strategy to configure NiCoP4O12/NiCoP nanowire arrays for ultra-stable supercapacitor, *Front. Chem. Sci. Eng.* 16 (2022) 1259–1267. <https://doi.org/10.1007/s11705-021-2132-0>.
- [101] A.M. Afzal, N. Muzaffar, M.W. Iqbal, G. Dastgeer, A. Manzoor, M. Razaq, S.M. Wabaidur, E.A. Al-Ammar, S.M. Eldin, Exploring the charge storage mechanism in high-performance Co@MnO<sub>2</sub>-based hybrid supercapacitors using Randles–Ševčík and Dunn’s models, *J Appl Electrochem* 54 (2024) 65–76. <https://doi.org/10.1007/s10800-023-01939-3>.
- [102] A. Mishra, G. Bera, P. Mal, G. Padmaja, P. Sen, P. Das, B. Chakraborty, G.R. Turpu, Comparative electrochemical analysis of rGO-FeVO<sub>4</sub> nanocomposite and FeVO<sub>4</sub> for supercapacitor application, *Applied Surface Science* 488 (2019) 221–227. <https://doi.org/10.1016/j.apsusc.2019.05.259>.
- [103] R. Devi, V. Kumar, S. Kumar, M. Bulla, S. Sharma, A. Sharma, Electrochemical Analysis of MnO<sub>2</sub> ( $\alpha$ ,  $\beta$ , and  $\gamma$ )-Based Electrode for High-Performance Supercapacitor Application, *Applied Sciences* 13 (2023) 7907. <https://doi.org/10.3390/app13137907>.
- [104] H. Peng, B. Yao, X. Wei, T. Liu, T. Kou, P. Xiao, Y. Zhang, Y. Li, Pore and Heteroatom Engineered Carbon Foams for Supercapacitors, *Adv. Energy Mater.* 9 (2019) 1803665. <https://doi.org/10.1002/aenm.201803665>.
- [105] J. Zhao, A.F. Burke, Electrochemical Capacitors: Performance Metrics and Evaluation by Testing and Analysis, *Advanced Energy Materials* 11 (2021) 2002192. <https://doi.org/10.1002/aenm.202002192>.

- [106] V.K. Mariappan, K. Krishnamoorthy, P. Pazhamalai, S. Sahoo, D. Kesavan, S.-J. Kim, Two-dimensional famatinite sheets decorated on reduced graphene oxide: A novel electrode for high performance supercapacitors, *Journal of Power Sources* 433 (2019) 126648. <https://doi.org/10.1016/j.jpowsour.2019.05.056>.
- [107] V.V.N. Obreja, On the performance of supercapacitors with electrodes based on carbon nanotubes and carbon activated material—A review, *Physica E: Low-Dimensional Systems and Nanostructures* 40 (2008) 2596–2605. <https://doi.org/10.1016/j.physe.2007.09.044>.

## **Chapter 2**

# **Hierarchical Porous Cu-MOF composite with 2D rGO and 1D CNT as Supercapacitor: Understanding Pseudo-and EDLC-Type Charge Storage Mechanism**

## 2.1 Introduction

Energy is one of the primary inputs in the development of any nation, and its demand is continuously increasing [1]. Conventional energy resources cannot fulfill the current energy demand because of their limited stock [2], which has led to the exploration of non-conventional sources like wind energy [3], solar energy [4], hydro energy [5], etc. However, these non-traditional sources are intermittent energy sources and require energy storage devices to maintain the continuous supply of energy [6,7]. To meet the ever-increasing demand for energy sustainably, it is essential to explore non-conventional sources in the most efficient ways, which mandates the design and synthesis of new energy storage devices with superior performance.

Based on the energy and power densities, energy storage devices are classified as capacitors, supercapacitors, batteries, and fuel cells. Supercapacitors are energy storage devices that possess superior features to batteries in terms of high power density [8], good reversibility [9], and longer cyclic life [10]. Depending on the charge storage mechanisms, supercapacitors are classified into two types: electrochemical double-layer capacitors (EDLCs) and pseudocapacitors. Storage of charge in EDLCs occurs at the electrode-electrolyte interface via reversible ion adsorption [11], whereas in the case of pseudocapacitors, charges are stored through faradaic processes involving redox reactions [12]. Although EDLCs display excellent cyclic stability [13], they suffer from low capacitance [14]. Pseudocapacitors show high capacitance, but response time is longer than EDLCs. Compared to batteries, one of the demerits of supercapacitors is their lower energy density, leading to low specific capacitance. Improving the energy density of supercapacitor electrode materials requires materials with high energy storage capacity and a basic understanding of the charge and ions transport mechanisms inside supercapacitor [15,16].

Currently, researchers are trying to improve the energy density without compromising power density and response time of supercapacitors by developing different types of materials, e.g., metal oxides and their composites ( $\text{Fe}_3\text{O}_4$ ,  $\text{Co}_3\text{O}_4$ ,  $\text{NiO}$ ,  $\text{Ru}_2\text{O}$ ,  $\text{MgO}$ ,  $\text{MoO}_3$ ,  $\text{WO}_3$ , etc.) [17–22], hollow materials (spherical, nonspherical, boxes, etc.) [23], MXenes and their composites [24]. Also, efforts have been made to develop different nanostructured porous electrode materials to achieve higher specific surface area and facilitate ion diffusion for the enhanced electrochemical performance of energy storage devices. Among such materials, metal-organic framework (MOF) is an emerging material class, offering varied chemical compositions and porous frameworks tunable at the molecular level, resulting in high specific surface area, defined pore size, and large pore volume [25–28]. Owing to these properties, MOFs show their applicability in various fields, including energy storage [29–32], sensor [33], catalysis [34],  $\text{CO}_2$  capture and fixation [35], etc. However, the low intrinsic conductivity of MOFs suppresses their energy storage performance in supercapacitor applications. Scientific explorations have been done to enhance the supercapacitor performance by assembling MOFs with highly conductive carbonaceous materials (rGO, CNT, etc.). Many reports have recently been published using MOF-rGO composites as supercapacitor electrode materials with high specific capacitance [29,36,37]. In such composites, rGO, because of its high electrical conductivity, ensures fast electron and ionic transport, while MOFs facilitate enhanced ion adsorption due to porous structure with high surface area. Moreover, the presence of redox-active metal centers in the MOF skeleton may also render additional charge storage through pseudocapacitance, leading to higher energy density and specific capacitance [38]. For instance, Yang et al. reported Ni-MOF/CNT composite with a high specific capacitance of  $1765 \text{ Fg}^{-1}$  at  $0.5 \text{ Ag}^{-1}$  current density due to the synergistic effect of redox-active MOF and highly conductive CNT [39]. In another work, Zou et al. synthesized MOF-derived  $\alpha$ -NiS nanorods, which showed a capacitance of  $744 \text{ Fg}^{-1}$  at  $1 \text{ Ag}^{-1}$  with 89% retentivity up to 20000 cycles [40]. Ni-doped MOF/rGO composite was reported by Banerjee et al.,

which showed a specific capacitance of  $758 \text{ Fg}^{-1}$ [41]. The rGO composite of a dual MOF with Ni-Co metals, synthesized by Mousavi et al., showed a specific capacitance of  $860 \text{ F.g}^{-1}$  at  $1 \text{ Ag}^{-1}$  [42]. The high specific capacitances of above-mentioned MOF-rGO composite electrode materials are the manifestation of enhanced electrochemical features arising due to synergy of MOF and rGO while keeping the mechanical and thermal stability uncompromised.

In this chapter a new Cu-MOF using a tetracarboxylic H<sub>4</sub>L (3,3',5,5'-tetracarboxydiphenylmethane) (5,5'-MDIP ligand) linker has been reported. The presence of redox-active  $\text{Cu}^{2+}$  centres in the 3D porous MOF with suitable channel structures to facilitate the ion transport prompted us to explore its applicability as supercapacitor electrode material. Further, the synthesized Cu-MOF (**M**) was composited with 2D rGO (**R**) and 1D CNT (**C**) and are discussed in two distinct sections of this chapter individually.

## 2.2 Experimental Section

### 2.2.1 Chemicals

Graphite flakes-99.5%, sodium nitrate ( $\text{NaNO}_3$ )- 98%, potassium permanganate ( $\text{KMnO}_4$ )-99.0%, hydrogen peroxide ( $\text{H}_2\text{O}_2$ )-35%, and hydrochloric acid ( $\text{HCl}$ )-35% were procured from SRL Chemical and TCI Chemical and were used to synthesize graphene oxide. Copper nitrate trihydrate ( $\text{Cu}(\text{NO}_3)_2 \cdot 3\text{H}_2\text{O}$ )-98%, dimethylformamide (DMF)-99.8% and tetracarboxylic H<sub>4</sub>L ligand (3,3',5,5'-tetracarboxydiphenylmethane)  $\geq 95\%$  were obtained from local commercial sources and used as it is. Ethanol was purchased from Changshu Hongsheng Fine Chemicals. Throughout the experiment, deionized water (DI water,  $18.2 \text{ M}\Omega\text{cm}^{-1}$ ) was used. All the reagents and solvents were dried and purified before use.

### **2.2.2 Synthesis of Graphene Oxide and Reduced Graphene Oxide (R)**

The synthesis of graphene oxide and reduced graphene oxide (**R**) were done using the modified Hummer's method [43]. Graphite with an average flake size of  $\leq 35\mu\text{m}$  was used to synthesize GO using modified Hummer's Method. In this method, 2g of graphite was mixed with 1g of  $\text{NaNO}_3$  and then added to 60 mL of sulfuric acid ( $\text{H}_2\text{SO}_4$ , 98 %) in a 100 mL beaker kept on an ice bath. Subsequently, 6g  $\text{KMnO}_4$  was added slowly with vigorous stirring while maintaining the temperature between 5- 10 °C. After continuously stirring the mixture for 6 h, the mixture turned viscous and brownish. Afterwards, the addition of 100 mL of DI water followed by 10 mL of  $\text{H}_2\text{O}_2$  (30 wt% aqueous solution) was done slowly. The GO thus obtained was filtered and washed using DI water and ethanol. The as-synthesized GO was dried in a vacuum oven for 6 h to get the dry powder.

For reduction of GO to obtain rGO, 100 mg of GO was dispersed in 10mL DI water. To this dispersion, a solution of 1g of  $\text{NaBH}_4$  in 6 mL DI water was added gradually, and the resulting mixture was refluxed for 24 h. Afterward, the product was filtered and washed thoroughly with DI water and ethanol and dried in a vacuum oven.

### **2.2.3 Synthesis of Cu-MOF (M)**

In a typical synthesis, 500 mg of the commercial  $\text{H}_4\text{L}$  linker [(3,3',5,5'-tetracarboxydiphenyl methane)] (5,5'-MDIP), 1.8 g of  $\text{Cu}(\text{NO}_3)_2 \cdot 3\text{H}_2\text{O}$ , 50 ml of 3:1 ratio of DI water and DMF, and 0.5 mL of concentrated HCl were added in a Teflon-lined stainless-steel autoclave. Afterwards, the autoclave was correctly closed and kept in a muffle furnace at 90 °C for 48 h. After the completion, it was cooled to room temperature. The **M** crystals were filtered and washed properly with DI water and ethanol and then adequately dried under the air.

### **2.2.4 Synthesis of Cu-MOF-rGO Composite (MR)**

To synthesize **MR** composites of different ratios, the mixture of **M** and **R** in a particular ratio (1:3, 1:1, and 3:1) was grounded in a mortar

and pestle. Subsequently, the grounded mixture was dispersed in ethanol and subjected to ultrasonication for 5 h to get a proper suspension. The as-obtained suspension was evaporated in an oven to get the desired ratio of composite. Ultrasonication was done using ultrasonic cleaner PCi Analytics.

### **2.2.5 Synthesis of Cu-MOF-CNT Composite (MC)**

The syntheses of Cu-MOF/CNT (**MC**) composites of different ratios were done using a facile ultrasonication technique. Before compositization, the activation of CNTs was done using sonication in 100 ml of 70% HNO<sub>3</sub> for 1h. After that, the activated CNTs were thoroughly washed by repeated centrifugation and dried in the oven at 80 °C overnight. Thereafter, the mixture of **M** and activated **C** was grounded in a mortar and pestle in a particular w/w ratio (10:90, 20:80, 30:70, 40:60, 50:50, and 60:40). Following this, the grounded mixture was dispersed in ethanol and ultrasonicated for 5 hours. The suspension produced was subjected to evaporation in an oven to get the desired ratio of **MC** composite.

### **2.2.6 Single-crystal X-ray diffraction study**

Single-crystal X-ray diffraction was performed on a Rigaku-Oxford Supernova CCD diffractometer (graphite monochromated Mo K $\alpha$  radiation,  $\lambda = 0.71073 \text{ \AA}$ ), having a low-temperature attachment. As obtained data were evaluated using CrysAlisPro CCD software and scaled/reduced using CrysAlisPro RED software. Afterwards, the structure was solved by the direct method using SHELXL 2014/7, followed by full-matrix least-squares refinements against F<sup>2</sup> (all data are HKLF 4 format) using SHELXL 2014/7 [44]. Direct methods were used to obtain the positions of all the atoms. An anisotropic displacement parameter was used to refine non-hydrogen atoms, while an anisotropic parameter was used to locate hydrogen atoms at geometrically calculated positions. The lattice solvent molecules of **M** were highly disordered and could not be modelled as discrete atomic sites; therefore,

the PLATON-SQUEEZE54 refinement program was used to calculate the solvent contributions.

### 2.2.7 Characterization

The crystallinity and phase analyses were done using Powder X-ray diffraction (PXRD) (Bruker's AXA D8 Advance system) in the  $2\theta$  range of 5 to  $60^\circ$  at a scanning rate of  $0.02^\circ \text{ min}^{-1}$  using  $\text{CuK}\alpha$  ( $\lambda = 1.54 \text{ \AA}$ ) as the source. To understand characteristics and stability, thermogravimetric analyses (TGA) were carried out on Mettler Toledo gravimetric analyzer instrument under  $\text{N}_2$  atmosphere from room temperature to  $800^\circ \text{C}$  at a heating rate of  $10^\circ \text{C}$ . FTIR spectra were recorded using Bruker Tensor 27 spectrometer in the wavelength range  $400 \text{ cm}^{-1}$  to  $4000 \text{ cm}^{-1}$ . Morphological and elemental analyses were done using Field Emission Scanning Electron Microscopy (FESEM) (JEOL -7610F Plus) equipped with Energy Dispersive Spectroscopy (EDS). Transmission electron microscopy (TEM) was done using FEI TECNAI 20 at an operating voltage of 200 kV.

### 2.2.8 Electrochemical Measurements

Autolab 204 potentiostat was used to do all the electrochemical measurements using a standard three-electrode cell setup, consisting of 5 mm Glassy Carbon (GC) as a working electrode, Pt as a counter electrode, and Ag/AgCl as a reference electrode. The potential range of -1.0 to -0.1 V was used to perform CV and GCD at different scan rates and current densities. EIS studies were performed at a frequency range of 10 mHz to 100 kHz in 10 mV AC amplitude.

GCD curves were used to calculate the specific capacitance using the following equation:

$$C = \frac{I \Delta t}{m \Delta V} \quad (1)$$

Where  $C$  is specific capacitance ( $\text{F}\cdot\text{g}^{-1}$ ),  $I$  is current (A),  $\Delta t$  is the discharge time (s),  $m$  is mass of the coated active material (g), and  $\Delta V$  is the potential range.

The energy density ( $E$ ) and power density ( $P$ ) were calculated using the following equations:

$$E \left( Wh/kg \right) = \frac{1}{2} C \Delta V^2 \times \frac{1000}{3600} \quad (2)$$

$$P \left( W/kg \right) = \frac{E}{\Delta t} \quad (3)$$

Where  $\Delta V$  is the potential range

### **2.2.9 Preparation of Electrodes and Electrochemical Testing**

The as-synthesized electrode materials were coated on three separate glassy carbon electrodes to make three working electrodes. Before coating, glassy carbon electrodes (GCEs with a diameter of 5mm each) were polished with a 0.3-micron alumina powder slurry and then sonicated in ethanol and DI water. Afterwards, they were dried in a vacuum oven. Later, 20 mg of each synthesized material were dispersed in 2.0 ml of ethanol in different glass vials with the aid of ultrasonic agitation to give 10 mg/mL suspension. Finally, 50  $\mu$ L of each suspension was drop cast on GCE with the help of a micropipette, and the solvent was allowed to evaporate in an oven. All electrochemical measurements were carried out in a 1 M Na<sub>2</sub>SO<sub>4</sub> for Cu-MOF/rGO and 1M KOH for Cu-MOF/CNT electrolyte solution.

### **2.2.10 Fabrication of Symmetrical Supercapacitor Device (SSC)**

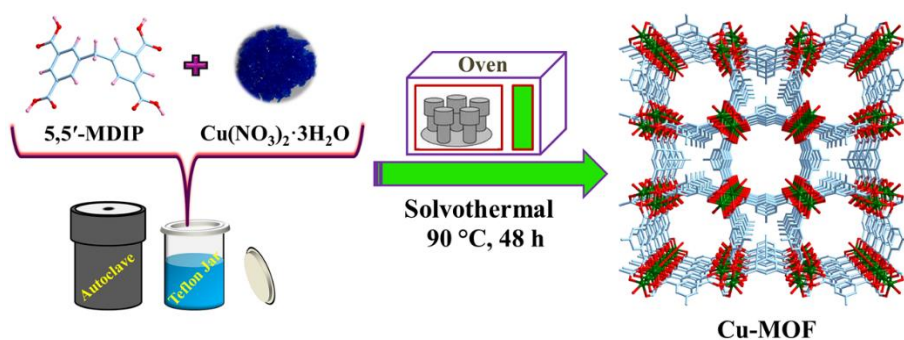
The construction of the solid-state supercapacitor (SSC) involved using a Swagelok cell with a 16 mm diameter. To create the electrode material slurry for device assembly, a mixture was prepared by combining 80% active materials, 10% carbon black, and 10% polyvinylidene difluoride (PVDF) in few drops of N-methyl pyrrolidone (NMP). After that, the as-obtained slurry was coated on a circular Ni-Foam cutting of 1.5 cm diameter and dried in an oven for 8 h at 60°C. The electrolyte solution was prepared by adding 1g of PVA in 10 mL of water; subsequently, the resultant solution was heated at 90°C for 3 h with continuous stirring,

followed by the addition of 10 mL of 1M KOH solution. Afterward, both electrodes were dipped in the polyvinyl alcohol-potassium hydroxide (PVA-KOH) electrolyte and partially dried in an oven. Finally, the device was fabricated by sandwiching the cellulose paper separator with electrode materials coated on Ni-foams in the Swagelok cell assembly.

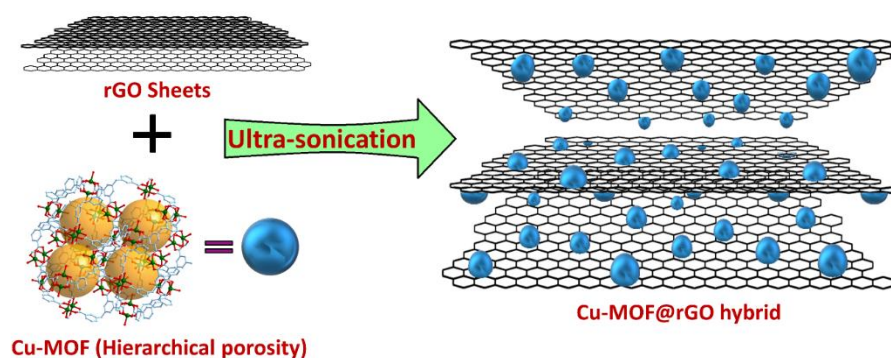
## 2.3 Results and Discussion

### 2.3.1 Synthesis

The blue colour crystals of **M** (Cu-MOF) were grown by a facile solvothermal technique using a tetracarboxylic linker 5,5'-MDIP and  $\text{Cu}(\text{NO}_3)_2 \cdot 3\text{H}_2\text{O}$  in 1:3 equivalent in the solvent mixture of N, N-dimethylformamide (DMF) and water (**Scheme 1**). The obtained **M** crystals were mixed with rGO (**R**) by thorough grinding. Subsequently, the ethanol suspension of the mixture was subjected to ultrasonication, which facilitated the even dispersion of **M** on 2D sheets of **R** and led to the formation of a robust **MR** composite (**Scheme 2**). The structural and morphological characterizations of the as-synthesized **M**, **R**, and their composite **MR** were done using different characterization techniques. Besides providing a suitable channel for rapid ion transport, the uniform dispersion of the **M** onto the surface of the **R** thwarts the restacking of 2D sheets of **R** and thus makes it more accessible for ion adsorption. Synergistically, both components improve the supercapacitor performance of the **MR** composite.



**Scheme 1.** Synthesis of Cu-MOF (**M**)



**Scheme 2.** Synthesis of Cu-MOF/rGO (MR)

### 2.3.2 Structural, Morphological, and Physical Characterizations

The crystallographic data of **M** single crystal has been deposited to Cambridge Crystallographic Data Center with CCDC number 2077792. The single-crystal X-ray diffraction study reveals that Cu-MOF (**M**) with molecular formula  $\{[\text{Cu}_2(5,5\text{'-MDIP})(\text{H}_2\text{O})_2].2(\text{H}_2\text{O}).3(\text{DMF})\}_n$  crystallizes in the tetragonal crystal system with space group  $I4/mmm$  (**Table 1**). In the framework of Cu-MOF, both isophthalate units of the 5,5'-MDIP linker are oriented at an angle of  $112.84^\circ$  with respect to each other (**Figure 2.1a**). Every 5,5'-MDIP linker utilizes its four carboxylate groups to link four di-copper paddle-wheel secondary building units (SBUs), *i.e.*  $[\text{Cu}_2(\text{COO})_4]$  (**Figure 2.2 a**). Each Cu(II) ion in the SBUs are equatorially coordinated with four oxygen atoms from different carboxylate linkers  $[\text{Cu}\cdots\text{O}: 1.922(6)\text{\AA} - 1.945(6)\text{\AA}]$  and axially coordinated with an O atom of the water molecule  $[\text{Cu}\cdots\text{O}: 2.110(10)\text{\AA}]$ , exhibiting a distorted square pyramidal geometry.

**Table 1.** Crystallographic parameters of Cu-MOF (**M**).

Empirical formula	$\text{C}_{17}\text{H}_8\text{Cu}_2\text{O}_{10}$
Formula weight	499.31
Crystal system, Space group	Tetragonal, $I4/mmm$
$a$ , $\text{\AA}$	18.644(2)
$b$ , $\text{\AA}$	18.644(2)

$c$ , Å	19.336(5)
$\alpha$ (deg)	90
$\beta$ (deg)	90
$\gamma$ (deg)	90
$V$ , Å <sup>3</sup>	6721(2)
$Z$	8
$\rho_{\text{calc}}$ g/cm <sup>3</sup>	0.987
$\mu$ , mm <sup>-1</sup>	1.296
Temperature (K)	100
Radiation type	MoK $\alpha$
$\theta$ range (deg)	2.107 to 24.997
$\theta$ max (deg)	24.997
F(000)	1984
$R_1$ , $wR_2$ [ $I > 2s(I)$ ]	$R_1 = 0.0808$ , $wR_2 = 0.2162$
$R_1$ , $wR_2$ (all data)	$R_1 = 0.1560$ , $wR_2 = 0.2648$
Refl. collected	36159
Independent refl.	1689
GOOF	0.965
Index ranges	$-22 \leq h \leq 21$ , $-22 \leq k \leq 19$ , $-12 \leq l \leq 22$
Absorption correction	Semi-empirical from equivalents
Max. and min. transmission	1.00000, 0.32221
Refinement method	Full-matrix least-squares on $F^2$
Data / restraints / parameters	1689 / 0 / 74
Largest diff. peak and hole (e Å <sup>-3</sup> )	0.872 and -0.649
CCDC no.	2077792

$${}^a R_1 = \sum(|F_o| - |F_c|) / \sum |F_o|. \quad {}^b R_2 = [\sum \{w(F_o^2 - F_c^2)^2\} / \sum \{w(F_o^2)^2\}]^{1/2}.$$

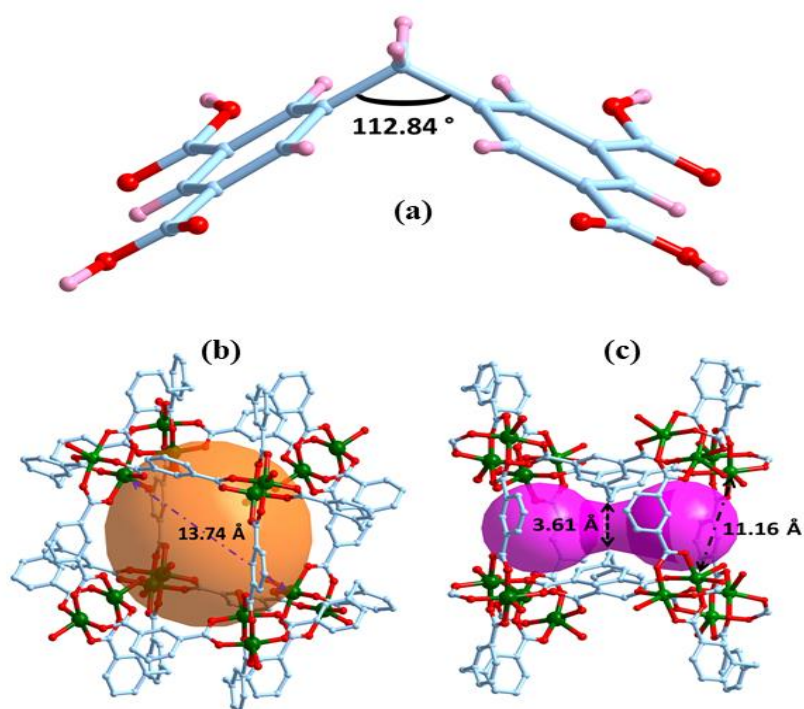


**Figure 2.1** (a) Angle between both the isophthalate unit of 5,5'-MDIP linker (b) Dimension of the larger cage (c) dimension of the smaller cages

Further, these units are extended through Cu(II)-OOC linkage to generate a highly porous framework. A closer view of the framework reveals two types of microporous cages present in the 3D structure of **M** (**Figure 2.2b**). The larger cages are nearly spherical with a dimension of 13.74(1) Å (distance refers to diagonal Cu-to-Cu connection), formed by eight [Cu<sub>2</sub>(COO)<sub>4</sub>] SBUs and sixteen 5,5'-MDIP linkers, leading to a Cu<sub>8</sub>(CO<sub>2</sub>)<sub>16</sub> polyhedron (**Figure 2.1b**). The smaller cages are of Indian pellet drum-shaped with a central dimension of 3.61(6) Å (distance refers to diagonal C(methylene)-to- C(methylene)) and the terminal dimension of 11.16(3) Å (distance refers to diagonal Cu-to-Cu connection), which consist of eight [Cu<sub>2</sub>(COO)<sub>4</sub>] SBUs and ten 5,5'-MDIP linkers (**Figure 2.1c**). The overall framework has both types of cages in a 1:1 ratio, which interestingly running along one direction and forming two types of one-dimensional channels. The larger and smaller channels are comprised of larger and smaller cages, respectively (**Figure 2.2c**). The channels associated with cages are filled by disordered solvent molecules. These disordered lattices and coordinated

solvent/water molecules were treated by SQUEEZE refinement of PLATON to calculate the effective solvent-accessible void volume, which was found to be  $\sim 40\%$  ( $\text{\AA}^3$ ) per unit cell.

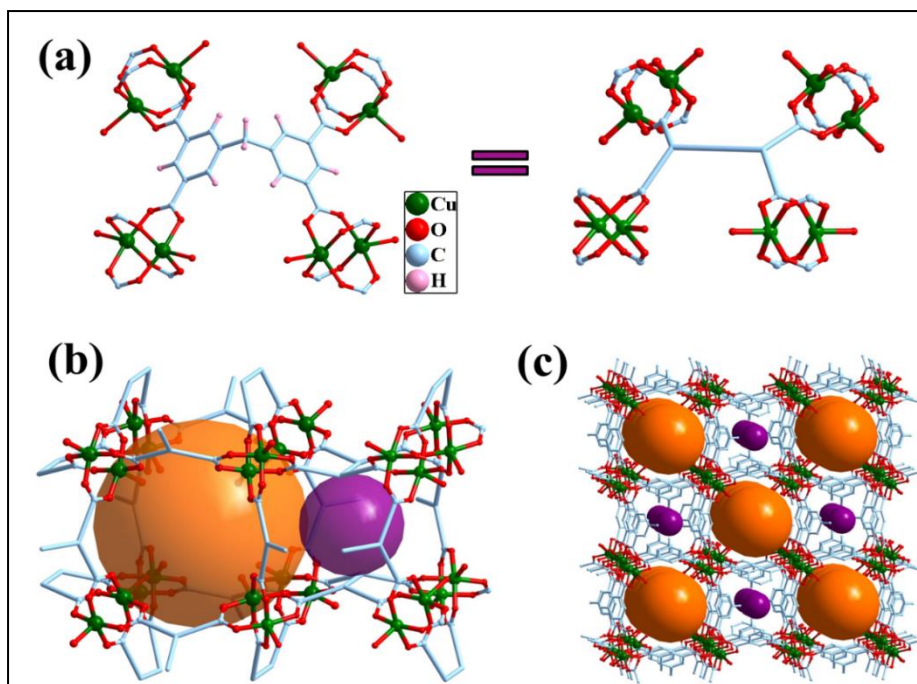


**Figure 2.2** (a) Asymmetric unit of Cu-MOF (**M**); (b) showing two types of microporous cages; (c) overall framework

To assess the phase purity, the experimental PXRD pattern of **M** powder was compared with the simulated one obtained from the single crystal diffraction (**Figure 2.3a**). The figure shows that the two patterns match very well, suggesting a single phase in **M** powder. Overall, from the structural analysis of the highly porous **M**, it is evident that the one-dimensional channels can offer suitable corridors for ion transfer, which is an essential feature for achieving a high electrochemical response. The PXRD patterns of as-synthesized **R**, **M**, and **MR** are shown in **Figure 2.3b**, explaining the crystallinity and phase purity of the as-prepared samples. The PXRD pattern of **R** shows the characteristic peaks of (002) and (100) planes of rGO at  $24^\circ$  and  $43^\circ$ , confirming the formation of rGO[37,38]. As mentioned already, the PXRD pattern of **M** shows several peaks corresponding to a tetragonal system, which matches well with the simulated pattern and, thus, confirms its phase purity. In the composite **MR**, besides **M** peaks, two peaks at  $24^\circ$  and  $43^\circ$  related to rGO can also be seen, confirming the composite formation. Moreover,

it is evident from the PXRD of composite that the blending of **R** with **M** has not affected its framework integrity and phase purity as no alteration in the PXRD pattern of **M** is observed. Overall, PXRD data confirms the formation of **MR** composite consisting of pure phases of **M** and **R**.

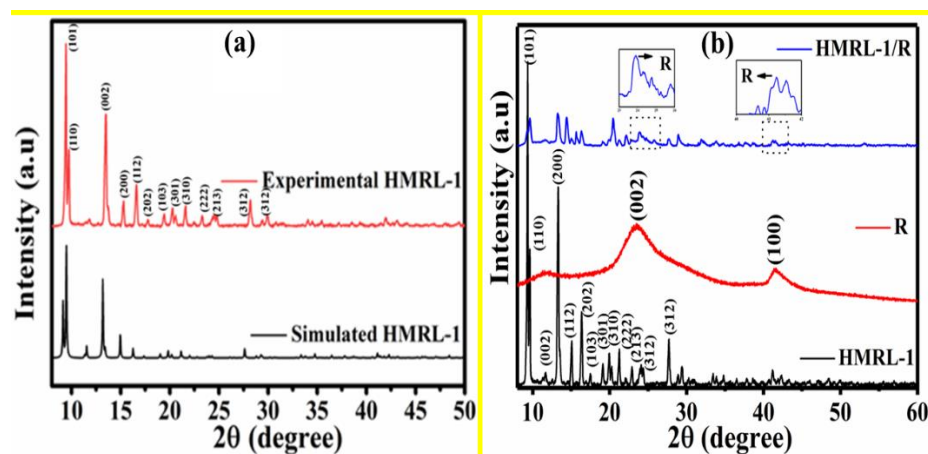


**Figure 2.3** PXRD pattern of (a) experimental and simulated **M** (b) **M**, **R**, and **MR**

The thermal stabilities and decomposition patterns of **M**, **R**, and **MR** were studied using TGA under  $N_2$  atmosphere from 30 to 800°C (**Figure 2.4**). The TGA profile of **R** shows a typical two weight loss steps of rGO, corresponding to the loss of adsorbed water and solvent (4.0% weight loss up to 180 °C) and a rapid weight loss due to the decomposition of the carbon network (89.0% weight loss, 180 - 540°C) [47].

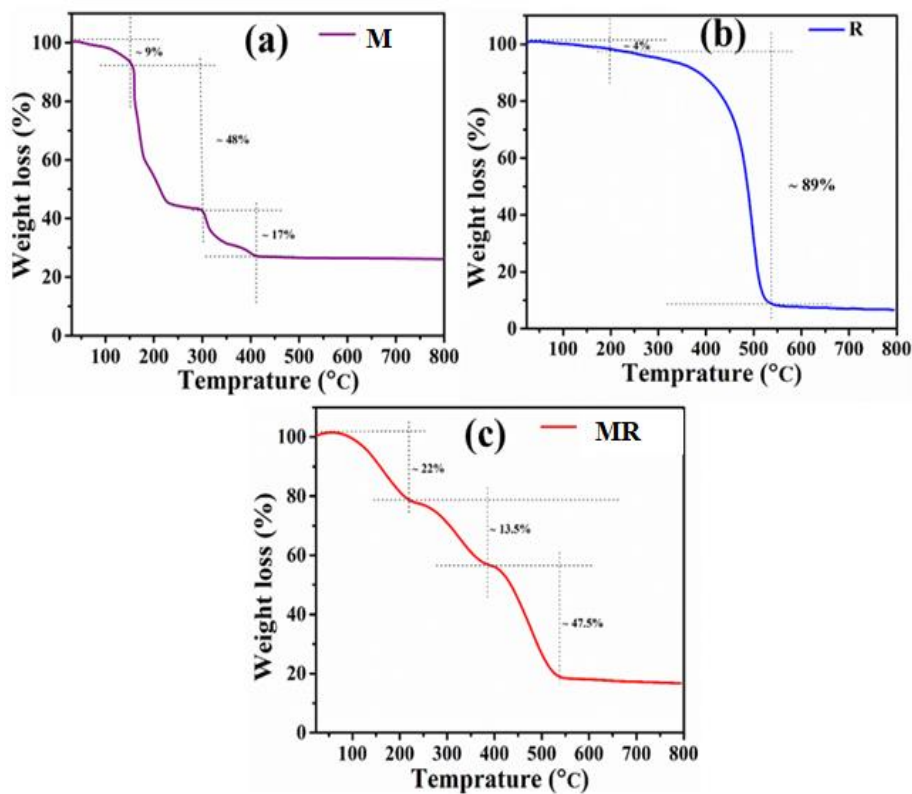


**Figure 2.4** TGA profile of **M**, **R**, and **MR**

**Table 2.** Comparison of weight loss percentages of **M**, **R**, and **MR**

Sample	Weight loss in %		
	1	2	3
<b>M</b>	9 % (30-160°C)	48 % (160-280°C)	17 % (280-410°C)
<b>R</b>	4 % (30-180°C)	89 % (180-540°C)	-
<b>MR</b>	22 % (30-200°C)	13.5 % (200-385°C)	47.5 % (385-540°C)

In the case of **M**, a three-step weight loss is observed, corresponding to (i) desorption of adsorbed and coordinated water

molecules (9.0% weight loss up to 160 °C), (ii) decarboxylation of the carboxylic group of the linkers and loss of other solvents present in the cages (48.0% weight loss, 160 - 300°C), and (iii) decomposition of organic moieties (17% weight loss, 300- 410°C) [48]. The TGA profile of **MR** also shows a three-step decomposition pattern. However, the corresponding weight loss percentages suggest a combined decomposition behaviour of both **M** and **R** components (**Table 2**), indicating the successful formation of the composite.

To investigate the different functional groups, present in the as-synthesized materials, FTIR spectroscopy was done (**Figure 2.5**). In the case of **M**, the low energy peak for the Cu-O bond is observed at 475  $\text{cm}^{-1}$ , while peaks between 600-900  $\text{cm}^{-1}$  correspond to the bending vibration of linker C-H groups. The peaks related to symmetric and asymmetric vibrations of carboxylate groups can be seen at 1590  $\text{cm}^{-1}$  and 1660  $\text{cm}^{-1}$ , respectively [49]. The broad peak around 3300  $\text{cm}^{-1}$  corresponds to the stretching vibration of the hydroxyl group due to the adsorbed water [48]. In the FTIR spectrum of **R**, two characteristic peaks of rGO are observed at 1530 and 2927  $\text{cm}^{-1}$ , corresponding to C=C and C-H bond vibrations, respectively [50]. The IR spectrum of **MR** shows peaks arising from both **M** and **R**.

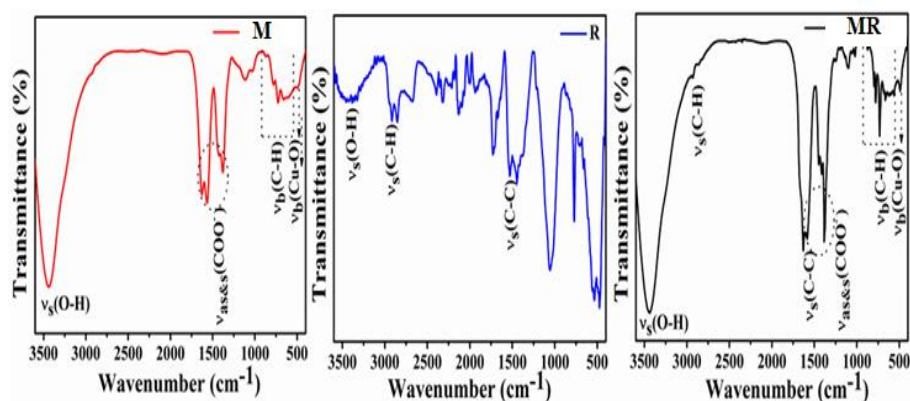


**Figure 2.5** FT-IR spectra of **M**, **R** and **MR**

The morphologies of **R**, **M**, and **MR** were examined by FE-SEM and TEM studies, and the corresponding micrographs are depicted in

**Figure 2.6.** From FE-SEM and TEM images of **M** (**Figure 2.6a&d**), it is evident that the as-synthesized Cu-MOF has an irregular shape of crystals with varying crystallite sizes. FESEM image of **R** (**Figure 2.6b**) displays a layered sheet-like structure, which can also be observed from the TEM image (**Figure 2.6e**), where the transparent sheet is clearly visible. In the case of **MR** FE-SEM image (**Figure 2.6c**), dispersion of **M** crystals on the 2D sheets of **R** can be observed, which is also supported from its TEM images (**Figure 2.6f**), where a central dark portion, representing Cu-MOFs, can be seen on transparent 2D sheets of **R**. The EDX spectra of **MR** confirms the presence of C, O, and Cu elements in equivalent proportion (**Figure 2.7a**). At the same time, elemental mapping of the composite shows a uniform distribution of these elements (**Figure 2.7b**), suggesting an even dispersion of Cu-MOF on rGO sheets during the composite formation. Furthermore, HR-TEM images of **R**, **M**, and **MR** and their corresponding SAED patterns (**Figure 2.8a-c**) were also examined. The observed interplanar spacing ( $d$ ) value of 0.385 nm for **R** corresponds to its 002 planes, while that of **M** at 0.26 nm relates to its 201. In the case of composite, the  $d$  values corresponding to both of its components can be observed. The SAED pattern of **R** exhibits diffused rings, suggesting its disordered structure, while that of **M** reveals multiple diffraction lines denoting its polycrystalline nature. For **MR**, the SAED pattern shows a combined nature of crystalline as well as an amorphous structure.

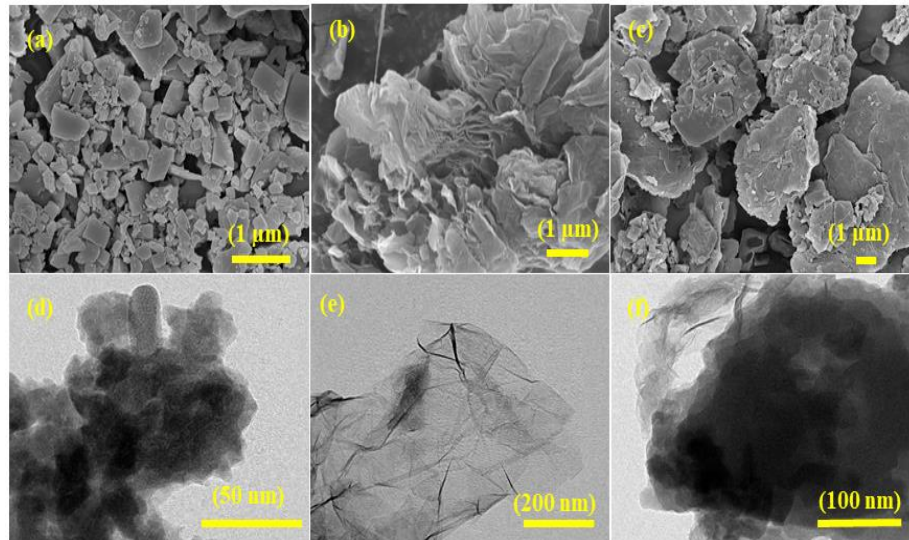


**Figure 2.6** FE-SEM images of (a) **M**, (b) **R**, (c) **M/R**; TEM images of **M** (d), **R** (e), and **M/R** (f)

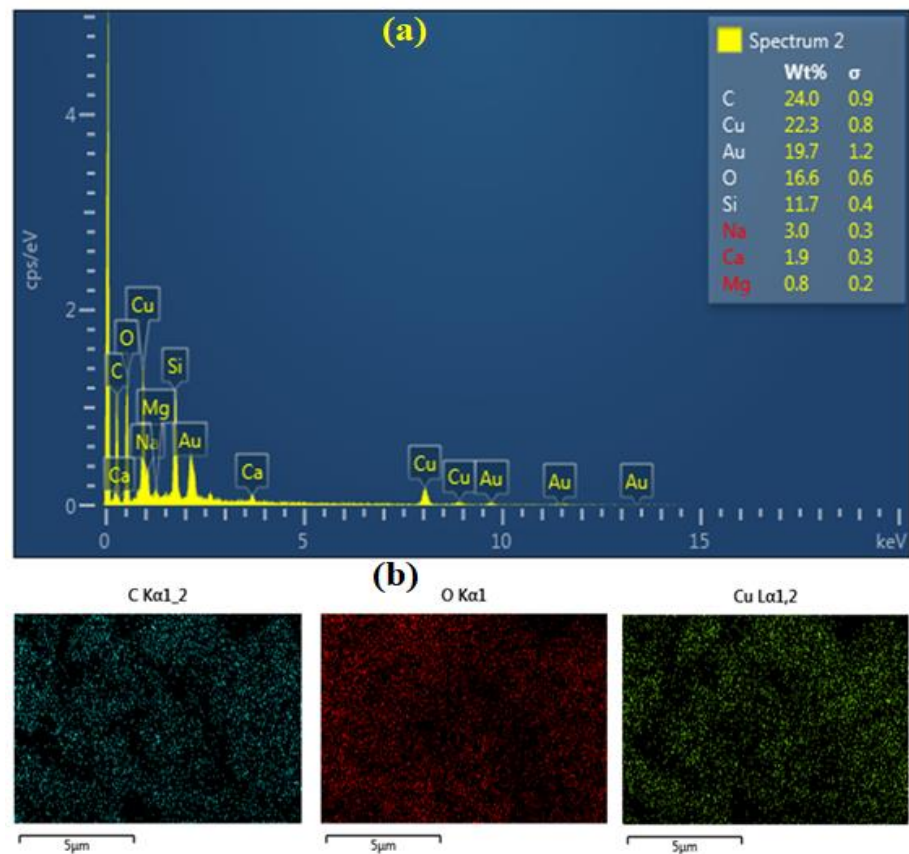


**Figure 2.7** (a) EDX spectra of MR. Apart from constituent elements (C, O, and Cu), the spectrum also shows trace amounts of Ca, Mg, Au, Na, and Si due to the glass slide substrate and gold coating. (b) Mapping of C, O, and Cu elements in **MR** composite

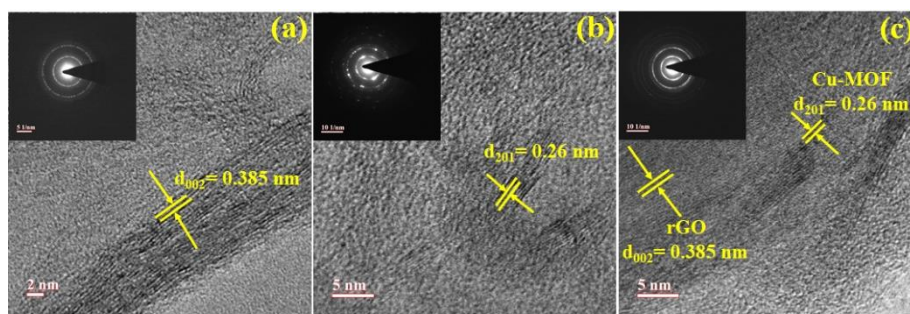


**Figure 2.8 (a,b,c).** HRTEM and corresponding SAED pattern (inset) of **R**, **M** and **MR**.

### 2.3.3 Electrochemical Properties

For supercapacitor application, the applicability of as-synthesized composite has been analyzed as an electrode material by casting it on the glassy carbon electrode (GCE). To achieve the best relative proportion of **M** and **R** for supercapacitor application, three composites of relative ratios of 1:3, 1:1, and 3:1 of **R** and **M**, respectively, were fabricated. The photographs of their ethanol suspensions are given in **Figure 2.9**. The cyclic voltammetry studies of three composites in the potential range -1.0 to -0.1V (scan rate 100 mVs<sup>-1</sup>) (**Figure 2.10**) suggest that the 1:3-composite shows the least current, which, upon addition of more rGO, reaches a maximum value for 1:1-composite because of augmentation of electrical conductivity of the overall composite. However, further addition of rGO reduces the current, as observed in the case of 3:1 composite, because of blockage of Cu-MOF channels due to wrapping of Cu-MOF by excess rGO [29]. It was further confirmed by comparing their specific surface areas calculated from their N<sub>2</sub> adsorption-desorption isotherms by BET analysis (**Figure 2.11**). The calculated specific areas of 1:3, 1:1 and 3:1 composites are 135.51 m<sup>2</sup>/g, 69.20 m<sup>2</sup>/g and 13.61 m<sup>2</sup>/g, respectively. It clearly indicates that increasing the rGO proportion in the composite decreases the overall specific surface area. Therefore, despite imparting more conductivity, the excess of rGO in the 3:1 composite reduces the current due to the decreased specific surface area. Considering the best electrochemical performance of 1:1 ratio, all subsequent electrochemical studies were

performed with 1:1 **R/M** composite (hereafter, **M/R** composite refers to the 1:1 ratio of its components).

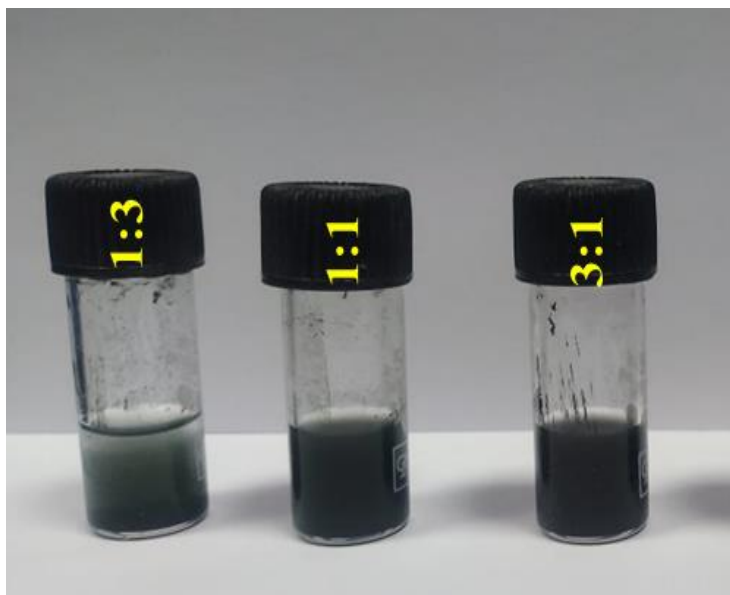


**Figure 2.9.** Digital photographs of three **MR** composites with different proportions of **R** and **M**.

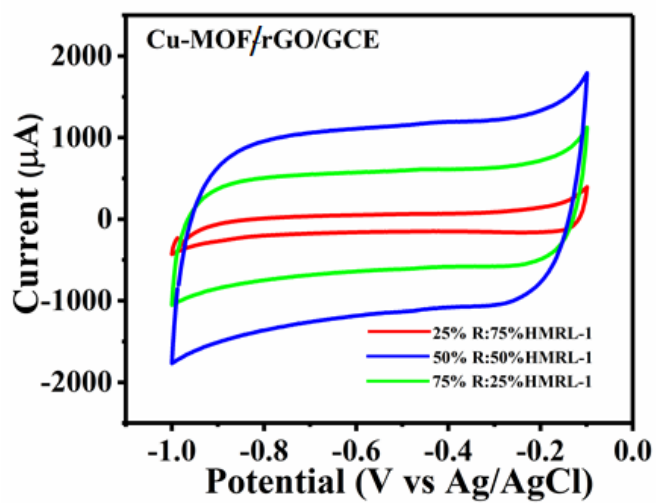


**Figure 2.10.** CV profiles of **MR** at different ratios.

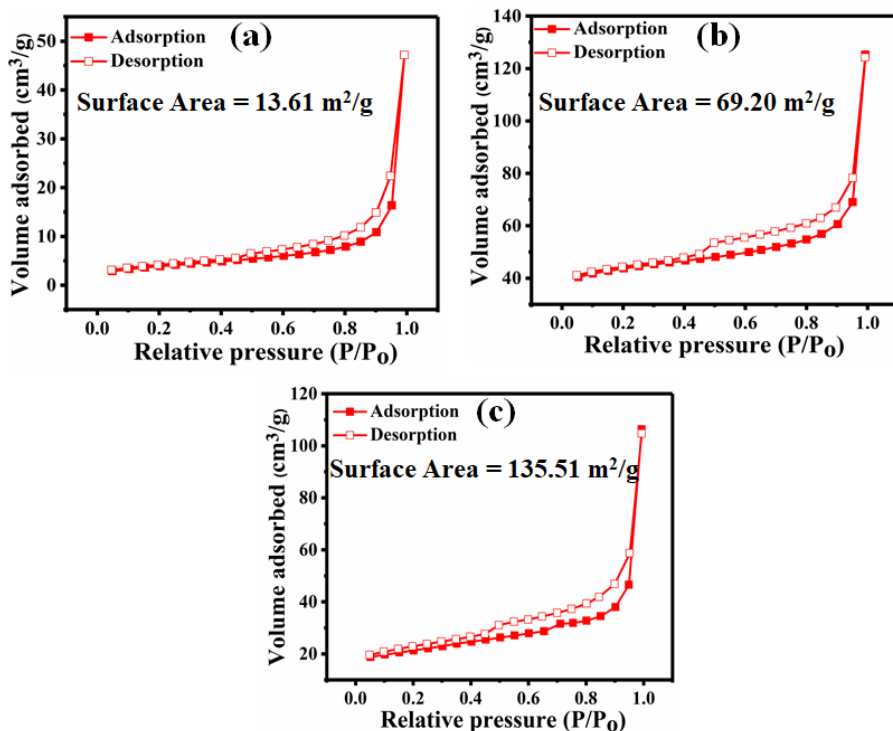


**Figure 2.11.** N<sub>2</sub> adsorption/desorption isotherms and specific surface area of (a) 3:1 of **RM** (b) 1:1 of **RM** (c) 1:3 of **RM**

To understand the comparative performance, supercapacitor properties of **M**, **R**, and **MR** were examined using cyclic voltammetry (CV), galvanostatic charge-discharge (GCD), and electrochemical impedance spectroscopy (EIS). The CV profiles of **M**, **R**, and **MR** were recorded in the potential range -1.0 to -0.1V at 100mVs<sup>-1</sup> scan rate to examine their comparative supercapacitive performance (**Figure 2.12a**). From cyclic voltammograms, the CV curve area is much higher for **MR** than individual **M** and **R**, which indicates that the association of **M** with **R** increases the current response of **MR**. Also, the calculated specific capacitances from their CVs are 8.1 Fg<sup>-1</sup>, 74.2 Fg<sup>-1</sup> and 206.6 Fg<sup>-1</sup> for M-GCE, R-GCE, and M/R -GCE, respectively. This is mainly due to the synergistic effects of the porous MOF having suitable channels with high ion holding capacity and high electrical conductivity of rGO.[51] Besides, MOFs in the rGO matrix also prevent the restacking of 2D rGO sheets and provide an enhanced effective area for ion adsorption [45].

Further, to understand the capacitive nature of **M**, **R**, and **MR**, their cyclic voltammograms were recorded at varying scan rates (10-500  $\text{mVs}^{-1}$ ) in the potential range of -1 to -0.1V (**Figure 2.12b-d**). At lower scan rates, the cyclic voltammogram of **M** (**Figure 2.12b**) shows a nonrectangular shape, indicating its pseudocapacitive behavior due to redox-active copper centres. However, at higher scan rates, the **M** voltammogram tends towards a semi-rectangular shape, indicating the dominance of EDLC behaviour due to sluggish electron transfer caused by the inherent low conductivity of MOF [52]. In the case of **R** (**Figure 12c**), the CV curve shows an almost rectangular shape at all scan rates, suggesting the EDLC behaviour of rGO. For composite material **MR**, a nearly rectangular voltammogram with the higher current was observed without any significant distortion at different scan rates (**Figure 2.12d**), indicating a hybrid charge storage mechanism due to faster electron transfer and ion diffusion. The unaltered voltammogram shape in **MR** indicates its excellent reversibility and electrochemical rate capability [53]. As expected, increasing scan rate ( $v$ ) in all cases led to the increase in current ( $i$ ); however, each material shows a different relationship between  $i$  and  $v$ , which also corroborates different charge storage mechanisms by three materials.

In **Figure 2.13**, linear plots of scan rate with peak current corresponding to EDLC ( $i$  vs.  $v$ ) and faradaic ( $i$  vs.  $v^{1/2}$ ) processes have been plotted for **M**, **R**, and **MR**. From the linear fitting plots of  $i$  vs.  $v$  for three materials, the order of regression values was found as **R** ( $R^2 = 0.997$ ) > **MR** ( $R^2 = 0.989$ ) > **M** ( $R^2 = 0.972$ ).

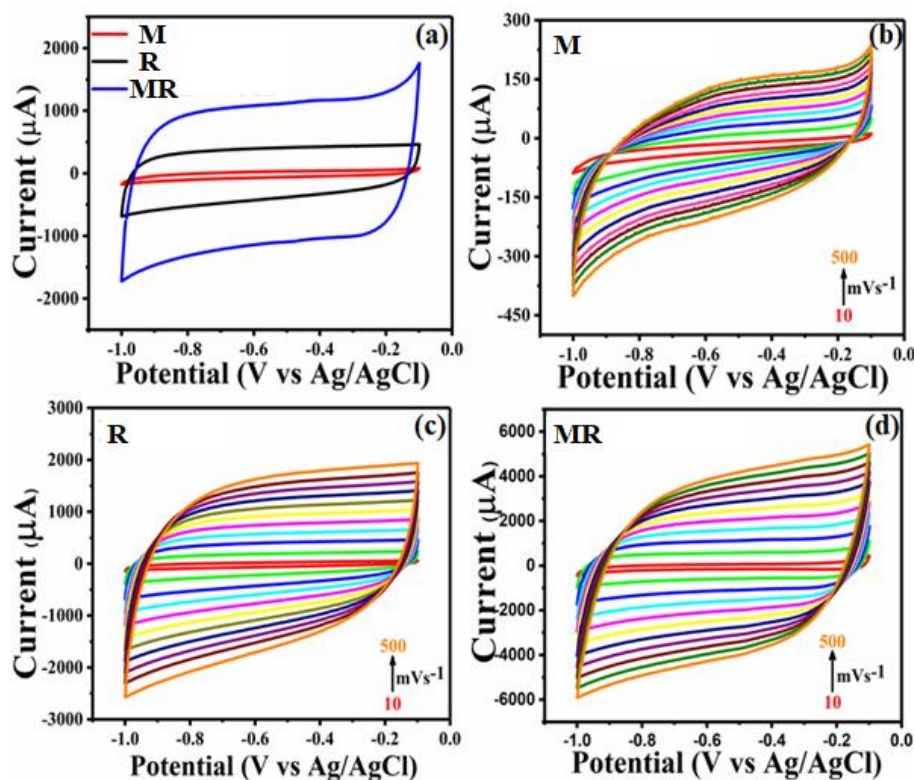


**Figure 2.12.** (a) Comparison of CVs of **M**-GCE, **R**-GCE, and **MR**-GCE at a scan rate of  $100 \text{ mV}\cdot\text{s}^{-1}$  in  $1\text{M Na}_2\text{SO}_4$ ; (b-c-d) CV profiles of the **M**-GCE, **R**-GCE, and **MR**-GCE at different scan rates ( $10\text{--}500 \text{ mV}\cdot\text{s}^{-1}$ ); (e) percentage EDLC and pseudocapacitive contributions to the overall capacitance of **MR** at different scan rates ( $50\text{--}250 \text{ mV}\cdot\text{s}^{-1}$ )

A reverse trend was observed in linear fitting plots of  $i$  vs.  $v^{1/2}$ , which follows **M** ( $R^2 = 0.996$ ) > **MR** ( $R^2 = 0.985$ ) > **R** ( $R^2 = 0.968$ ). From the comparison of  $R^2$  values, it can be understood that the EDLC is the best fit mechanism for the charge storage in **R**, whereas, for **M**, the pseudocapacitive charge storage is the most suitable model. The observed  $R^2$  values for **MR** composite fall between **R** and **M** for both types of plots, indicating its hybrid capacitive features, where charge storage occurs through EDLC as well as the faradaic process. Further to supplement this, the surface-controlled and diffusion-controlled charge storage behaviours of the electrode materials were also investigated by charge storage kinetic analysis using the Power-law relationship [54], given in equation 4.

$$i = av^b \quad (4)$$

where  $i$  is the peak current value,  $v$  is the scan rate,  $a$  and  $b$  are the variable constants.

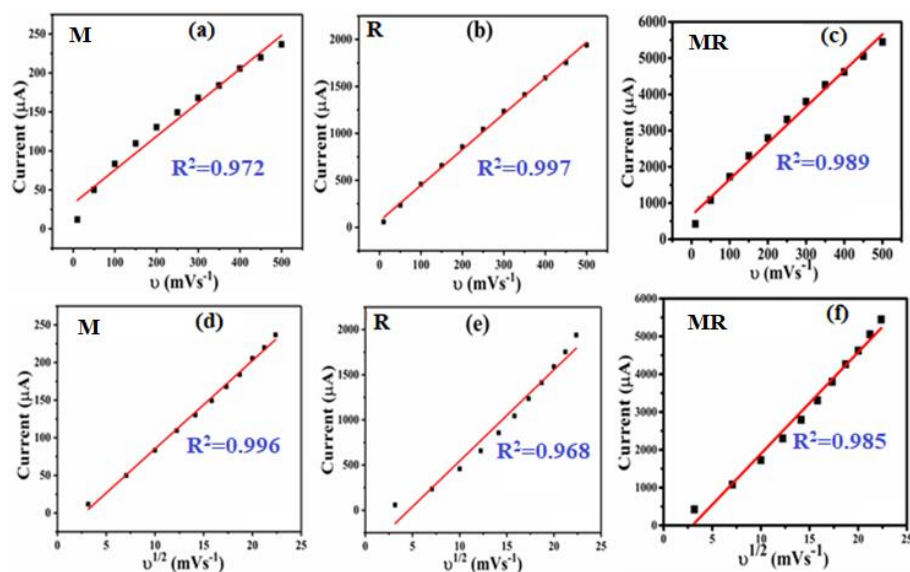


**Figure 2.13** Linear fitting of  $i$  vs.  $v$  (a-c) and  $i$  vs.  $v^{1/2}$  (d-e) for **M-GCE**, **R-GCE**, and **M/R-GCE**, respectively.

In the plot of  $\ln i$  vs.  $\ln v$  (from the linearized form of equation 4:  $\ln i = \ln a + b \ln v$ ), the slope of the plot gives the value of  $b$ , which provides the charge storage mechanism of an electrode. If  $b \approx 0.5$ , capacitive behavior is considered diffusion-controlled, while  $b \approx 1$  represents the surface-controlled capacitive performance. The linear plots of  $\ln i$  vs.  $\ln v$  for **M**, **R**, and **MR** are given in **Figure 2.14**. The values of  $b$  for **M**, **R**, and **MR** were found to be 0.24, 0.901, and 0.66, respectively. The values clearly indicate that the capacitive behaviour of **M** is mainly dominated by diffusion-controlled charge storage, whereas surface-controlled charge storage dominates in **R**. Unlike its components, the intermediate value of  $b$  in the case of composite suggests the operation of both charge storage mechanisms; thus, indicates its hybrid capacitive nature [55].

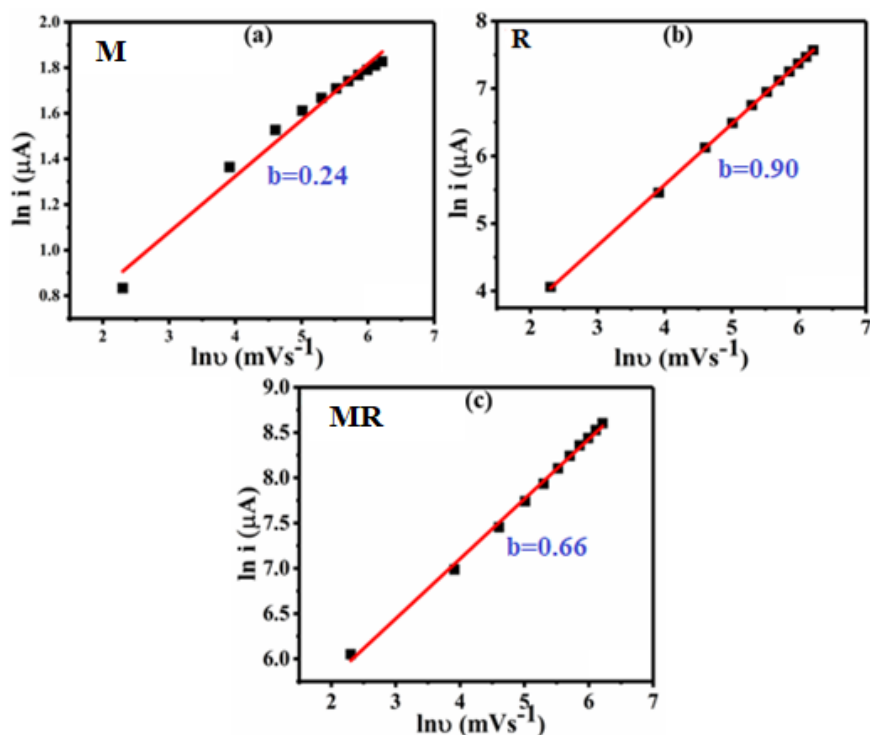


Figure 2.14. Charge storage kinetics  $\ln i$  ( $\mu A$ ) vs  $\ln v$  ( $mV/s$ ): estimation of values of  $b$  for **M** (a), **R** (b), and **M/R** (c)

The quantification of the percentage contribution of the surface and the diffusion-controlled capacitance to the overall specific capacitance of the **M**, **R**, and **MR** was also investigated by the Dunn method [56]. According to this method, the cyclic voltammetric current at a given potential as a function of scan rate can be expressed as a combination of surface-controlled and diffusion-controlled processes, given in equation 5.

$$i(V) = k_1 v + k_2 v^{1/2} \quad (5)$$

where  $i(V)$  is the current at a given potential  $V$ ,  $v$  is the scan rate,  $k_1$  and  $k_2$  are the constants for the surface and diffusion-controlled processes, respectively.

For **M**, the percentage contributions of the diffusion capacitance at lower scan rates are much higher than surface capacitance; however, it decreases with the increasing scan rate (10-250  $mVs^{-1}$ ) (**Figure 2.15a**). However, the diffusion-controlled process still dominates the overall capacitance of **M** due to the involvement of  $Cu^{2+/1+}$  redox centres. Contrary to Cu-MOF, the capacitance of **R** is mainly dominated by

surface-controlled processes, which increases further with increasing scan rate (**Figure 2.15b**), suggesting EDLC behaviour of rGO. **Figure 2.15c** shows the bar chart for the percentage capacitance contributions of the surface and diffusion processes, arising from rGO and Cu-MOF, respectively, to the overall capacitance of **MR** at different scan rates. The percentage contributions of the diffusion capacitance at lower scan rates are much higher than surface capacitance; however, at higher scan rates, surface capacitance dominates over the diffusion capacitance. From the contribution analysis, it can be understood that **MR** composite features as a hybrid supercapacitor at all scan rates; however, the extent of EDLC and pseudocapacitive characters to its overall capacitive performance varies with the scan rate. The reduction in the diffusion capacitance portion with increasing scan rate can be rationalized from the fact that, at higher scan rates, the diffusion rate is outmatched by the scan rate, leading to the dominance of surface capacitance.

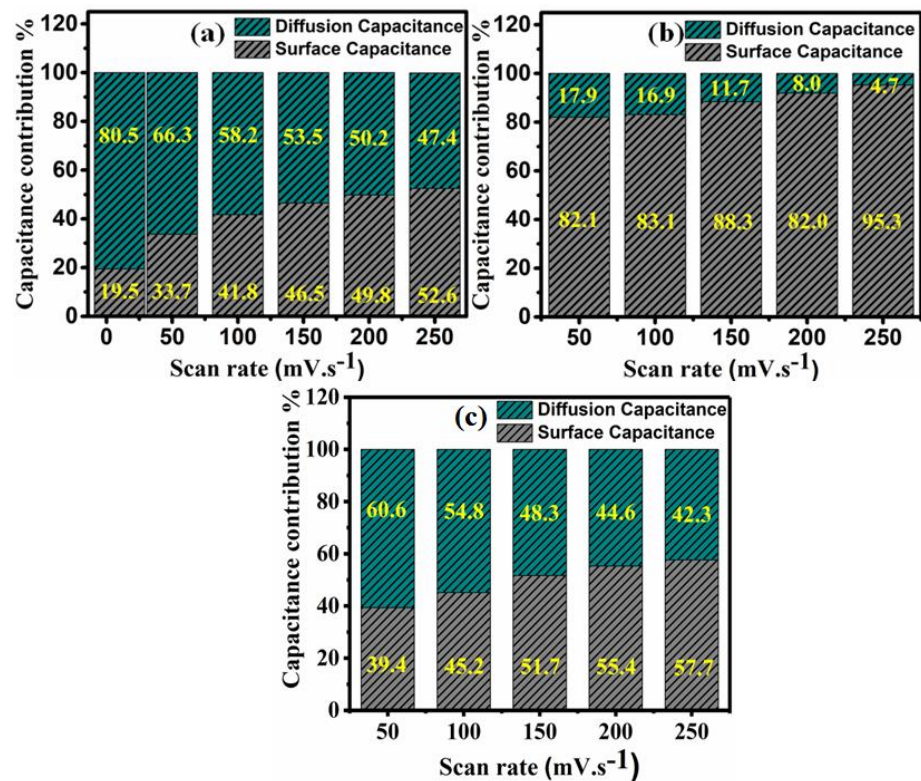


**Figure 2.15** (a-c) Percentage EDLC and pseudocapacitive contributions to the overall capacitance of **M,R** and **MR** at different scan rates (10-250 mV.s<sup>-1</sup>)

Galvanostatic charge-discharge (GCD) studies were performed for **M**, **R**, and **MR** in the potential window of -1 to -0.1V at different current densities ( $1.0 \text{ Ag}^{-1}$  to  $10 \text{ Ag}^{-1}$ ) to evaluate their specific capacitances. The GCD profiles of **M**, **R**, and **MR** at  $1 \text{ A.g}^{-1}$  current density have been depicted in **Figure 2.16a**, displaying the highest discharging time for **MR** composite compared to the individual components. Also, GCD profiles of **MR** at varying current densities are shown in **Figure 2.16b**, which indicates that the charging and discharging times decrease with increasing current density. This implies that the time required to build the same charge or voltage decreases with increasing current density, which is also applicable for the discharging step [57]. The specific capacitances of **M**, **R**, and **MR** at  $1 \text{ Ag}^{-1}$ , calculated using the discharge curve, are  $21 \text{ Fg}^{-1}$ ,  $201 \text{ Fg}^{-1}$ , and  $366 \text{ Fg}^{-1}$ , respectively (**Figure 2.16c**). It is evident that the blending of present Cu-MOF to rGO results in 82% augmentation in the specific capacitance of rGO, suggesting **M** is a promising material in composite fabrication with other matrices to derive superior capacitive performance. The increase in the specific capacitance of **MR**-GCE can be attributed to highly porous and functionalized Cu-MOF with compatible channels, providing additional surface area for ion transport and adsorption. In addition to this, redox metals centers present in the MOF skeleton also boost the capacitance by invoking pseudocapacitance. At the same time, the presence of the rGO matrix helps overcome the inherent poor electrical conductivity of MOF and facilitates ion diffusion besides its intrinsic EDLC contribution. Therefore, the blending of **M** and **R** in appropriate proportion leads to remarkable improvement in the electrochemical performance of the composite.

The variation in specific capacitance of **M**, **R**, and **MR** with the change in current density has been plotted and shown in **Figure 2.16d**. It is observed that, upon increasing current density, there is a rapid decrease in capacitance of the composite till  $4 \text{ A.g}^{-1}$ ; afterwards, a very gradual reduction in the capacitance is observed. This can be rationalized as, at low current density, the composite shows hybrid

capacitive features having EDLC as well as pseudocapacitive contributions. However, because of the diffusion limitation, the pseudocapacitive contribution reduces rapidly up to  $4 \text{ Ag}^{-1}$ , reducing the overall specific capacitance. Beyond  $4 \text{ Ag}^{-1}$ , the composite exhibits mainly EDLC features; therefore, further decrement in the capacitance is very slow. Further, coulombic efficiencies for **M-GCE**, **R-GCE** and **MR-GCE** were also calculated from the ratios of discharging and charging times obtained from their GCD curves at  $1 \text{ Ag}^{-1}$  current density (Figure 2.16a). At a fixed current density of  $1 \text{ Ag}^{-1}$ , coulombic efficiency of **M-GCE**, **R-GCE** and **MR-GCE** were found to be 38%, 88.051% and 79.61% for, respectively.

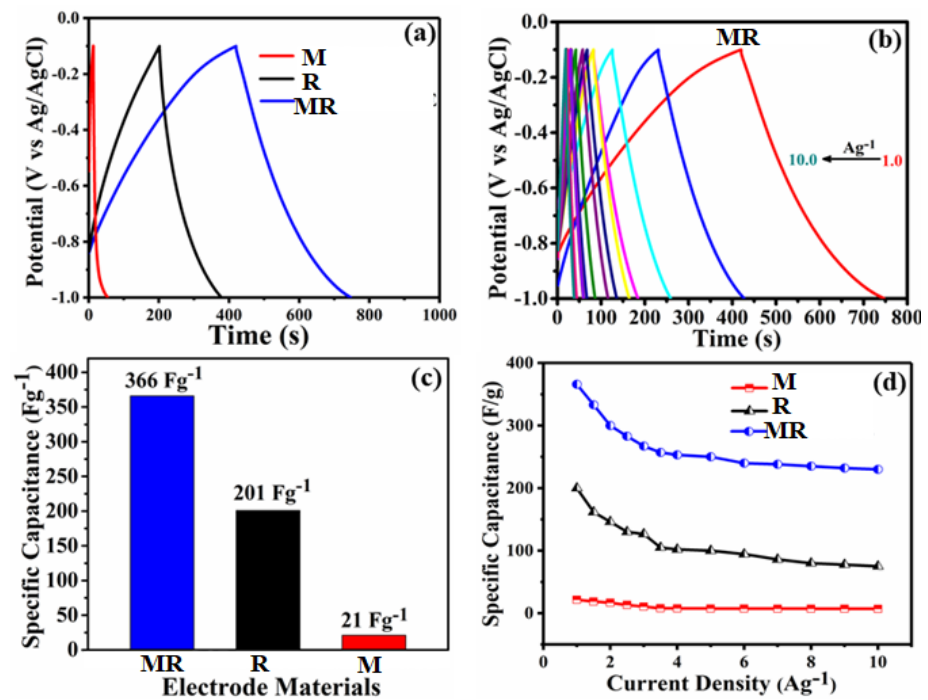


**Figure 2.16** (a) Comparison of GCD of **M-GCE**, **R-GCE**, and **MR-GCE** at a current density of  $1 \text{ A.g}^{-1}$  in  $1 \text{ M Na}_2\text{SO}_4$ ; (b) GCD profiles of the **M-GCE** at different scan rate ( $1\text{-}10 \text{ Ag}^{-1}$ ); (c) comparison of specific capacitance of **M-GCE**, **R-GCE**, and **MR** at  $1 \text{ A.g}^{-1}$ ; (d) comparison of the change in specific capacitance of **M-GCE**, **R-GCE**, and **MR** at varying current density.

Electrochemical impedance spectroscopy (EIS) was performed to understand the charge transfer kinetics, ion transportation, and charge storage mechanism. The resulting Nyquist plots for **M**, **R**, and **MR** in 10 mHz to 100 kHz frequency region with an AC amplitude of 10 mV have been shown in **Figure 2.17a**. In the Nyquist plot, an impedance line parallel to the imaginary axis suggests an exclusive EDLC behaviour. However, inclination towards the real axis indicates that faradaic processes are also operational besides the EDLC process. From **Figure 2.17a**, it can be observed that the impedance line corresponding to **R** is closest to the imaginary axis, which is followed by that of **MR** and **M**, in order. This corroborates that, among the three materials, **R** has the highest EDLC character, while **M** shows the highest pseudocapacitive behaviour. For **M/R**, the impedance line between **R** and **M** indicates a hybrid capacitive behaviour of the composite, having EDLC as well as pseudocapacitive features.

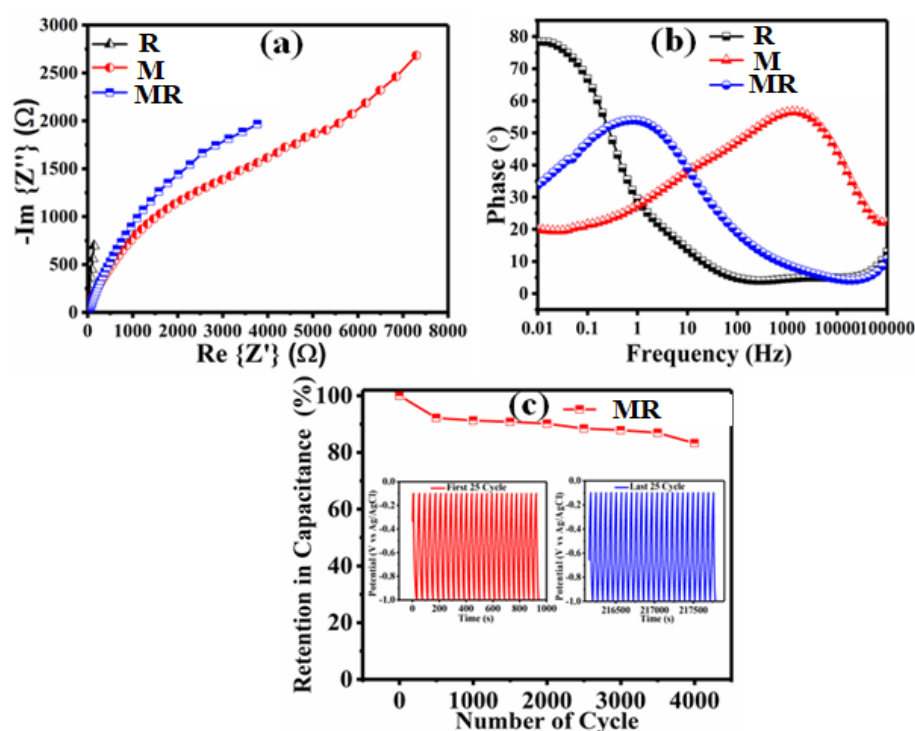


**Figure 2.17.** Nyquist plot (a) and bode phase angle plot (b) for **M**, **R**, and **MR**, (c) Cycling stability of **MR** at  $10 \text{ A.g}^{-1}$  for 4000 cycles (insets show first and last 25 GCD cycles).

The Bode plots for three electrode materials showing the variation of impedance phase angle with the frequency are given in **Figure 2.17b**. In the Bode plot,  $90^\circ$  phase angle at very low frequency represents the impedance originating due to the capacitive behaviour, whereas lower angles display the impedance resulting from the combination of capacitive and faradaic behaviours. The observed impedance phase angles for **R**, **M**, and **MR** at 0.01 Hz of  $78.4^\circ$ ,  $20.3^\circ$ , and  $34.8^\circ$ , respectively, support the conclusion drawn from the Nyquist plots. Overall, the EIS studies also indicate the hybrid supercapacitor nature of the composite, having charge storage taking place by EDLC as well as pseudocapacitive mechanisms [58].

For practical applications, recyclability is an important consideration that defines the stability of a material. Therefore, the performance retentivity and cyclic stability of **MR** composite for 4000 GCD cycles at a fixed current density of  $10 \text{ Ag}^{-1}$  were also evaluated. The change in specific capacitance of **MR** at  $10 \text{ Ag}^{-1}$  with the increasing number of cycles is shown in **Figure 2.17c**, along with GCD profiles of the first and last 25 cycles. The study reveals that even after 4000 cycles, composite shows excellent specific capacitance retention of 83.30%. After completing the recyclability experiment, no traces of electrode material stripping were observed, which corroborates that the marginal reduction in the capacitance is not due to the striping of the electrode material. It could be because of the irreversible adsorption of ions due to their entrapment in the MOF skeleton during multiple cycling. The GCD profiles of initial and later cycles remain almost unchanged, indicating the high stability of the composite material. The comparison of cyclic voltammogram of fresh composite and that after 4000 cycles also reveals only slight shrinkage of CV profile (**Figure 2.18**), again suggesting only a slight deterioration of the supercapacitive performance. The same was also confirmed by comparing the EIS of fresh and recycled composite (**Figure 2.19**), showing no significant alteration in the EIS profile.

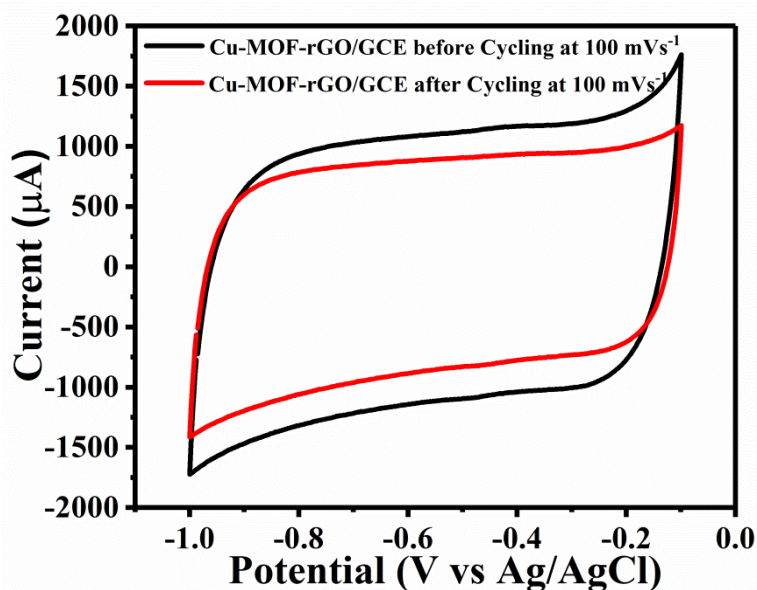


**Figure 2.18.** Comparison of CVs of fresh MR and the one retrieved after 4000 GCD cycles.

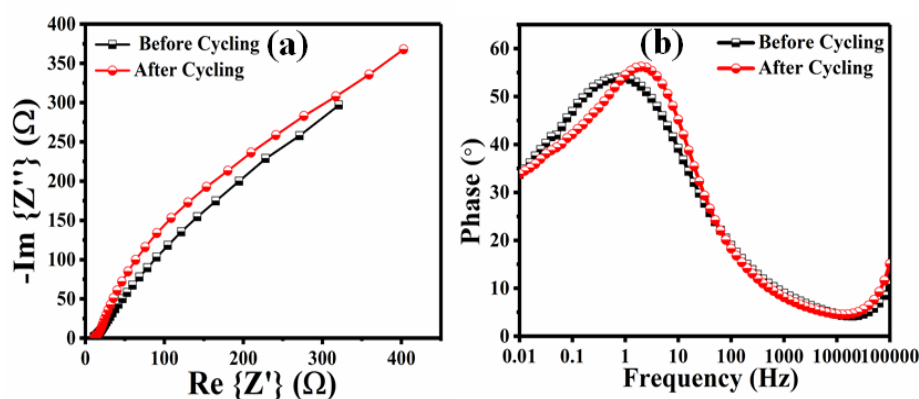


**Figure 2.19** Comparison of EIS of fresh MR and the one retrieved after 4000 GCD cycles.

To further investigate the practicability of the prepared electrode materials, solid-state symmetrical supercapacitor using the Swagelok cell was fabricated. For this, two identical MR electrodes were dipped in PVA- $\text{Na}_2\text{SO}_4$  gel electrolyte and sandwiched using a cellulose separator. The fabricated device was tested in a two-electrode symmetrical capacitor cell configuration (MR//MR).

The CV analysis of the device in two-electrode configuration at varying scan rates (10-500  $\text{mVs}^{-1}$ ) shows a nearly semi-rectangular

voltammogram (**Figure 2.20a**), which is consistent with the that of composite studied in three-electrode configuration. Further galvanostatic charge-discharge (GCD) studies were performed for the symmetrical device in the potential window of 0 to 1.2V at different current densities ( $1.0 \text{ Ag}^{-1}$  to  $10 \text{ Ag}^{-1}$ ) to evaluate its specific capacitances (**Figure 2.20b**). The calculated specific capacitance for the device at  $1.0 \text{ Ag}^{-1}$  current density is found to be  $156 \text{ Fg}^{-1}$ . The variation of the specific capacitance of the device at different current densities is plotted in **Figure 2.20c**. Similar to the observation in the three-electrode configuration, device capacitance also falls rapidly till  $4 \text{ Ag}^{-1}$ ; beyond that, a very slow capacitance reduction is observed. The GCD curve at different current densities was also used to calculate the rate performance of the device fabricated using MR, which was found to be 46.9% up to  $10 \text{ Ag}^{-1}$ .

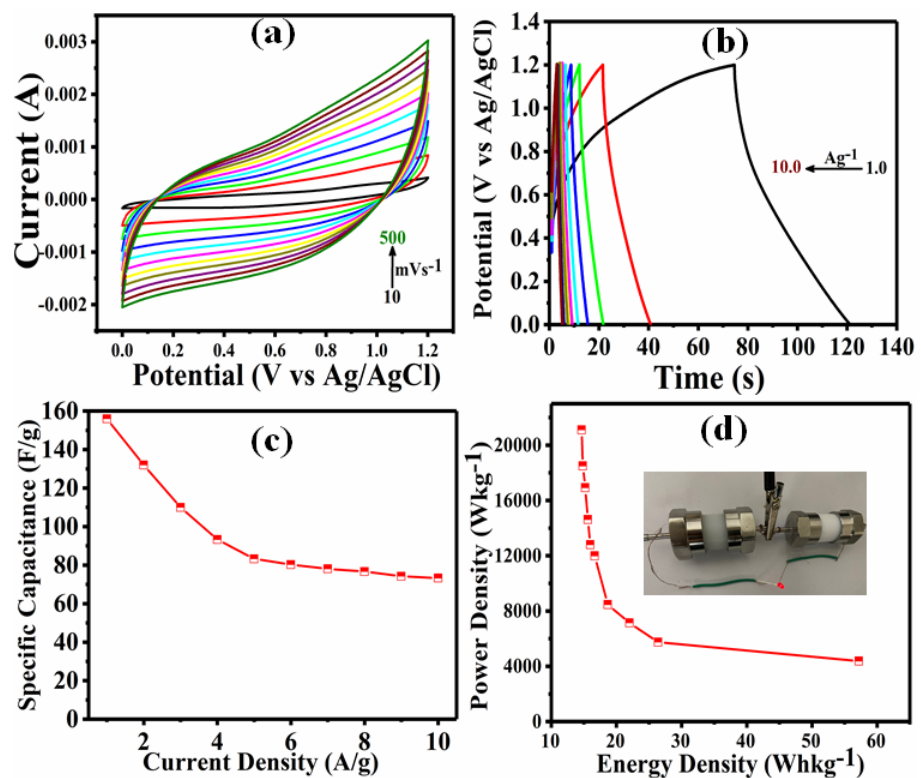


**Figure 2.20** a) CV profile of MR//MR at different scan rate (10—500  $\text{mV}\cdot\text{s}^{-1}$ ); (b) GCD profiles of the MR//M/R at different scan rate (1- $10\text{Ag}^{-1}$ ), (c) specific capacitance of MR//MR at varying current density,

(d) Ragone plot (energy density versus power density) of **MR//MR** (Photograph of the fabricated device in the inset of **Figure 20 d**).

The Ragone plot showing the energy density variation with the power density has also been plotted (**Figure 2.20d**). The plot reveals that the device exhibits a maximum power density of  $21.10 \text{ kWkg}^{-1}$  at  $14.66 \text{ Whkg}^{-1}$  energy density, and a maximum energy density of  $57.2 \text{ Whkg}^{-1}$  at  $4.38 \text{ kWkg}^{-1}$  power density. The above energy density and power density achievable with the present solid-state supercapacitor is much larger than many other MOF based supercapacitors. For comparison of supercapacitive performance of the present composite material with that of earlier reported MOF-based materials, a comparison table is given in **Table 3**. Based on the parameters like specific capacitance, current density, and the electrolyte used, it can be concluded that **MR** is a worthy candidate as an electrode material for supercapacitor application, which also displays excellent cyclic stability and performance retention in the absence of any expensive commercial binders.

**Table 3.** Comparison table of different MOFs and their derivatives with MR for supercapacitor performance.

<b>Electrode material</b>	<b>Electrolytes</b>	<b>Current density</b>	<b>Specific capacitance</b>	<b>References</b>
ZIF8@MWCNT	1M H <sub>2</sub> SO <sub>4</sub>	1 A/g	326 F/g	[59]
CNT@MnMOF	1M Na <sub>2</sub> SO <sub>4</sub>	1 A/g	203.1 F/g	[60]
NiMOF-CNT	6M KOH	0.5 A/g	1765 F/g	[39]
MOF-5/PANI	1M H <sub>2</sub> SO <sub>4</sub>	1 A/g	477F/g	[61]
MOF-NPC	1 M H <sub>2</sub> SO <sub>4</sub>	0.5 A/g	251 F/g	[62]
NiCOP@CNT@C	3M KOH	1 A/g	708.1 F/g	[63]
Polyoxometalate MOF-rGO	6M KOH	0.5 A/g	178 F/g	[64]
FeMOF-Graphene aerogel	1M H <sub>2</sub> SO <sub>4</sub>	20 A/g	353 F/g	[53]
rGO-NiMOF film	6M KOH	4 mA/cm <sup>2</sup>	260 mF/cm <sup>2</sup>	[65]
HKUST-1/CNT film	6M KOH	2 A/g	194.8 F/g	[66]
<b>MR</b>	1M Na <sub>2</sub> SO <sub>4</sub>	1 A/g	366 F/g	<b>This study</b>

## 2.4 Summary

In summary, the synthesis of a new Cu-MOF has been reported by a solvothermal method using a tetracarboxylic (5,5'-MDIP) linker and  $\text{Cu}^{2+}$  salt. Considering its 3D framework having suitable channels to facilitate ion transport and adsorption, the as-synthesized Cu-MOF has been composited with conductive 2D rGO sheets to fabricate a binder-free supercapacitor electrode material; which exhibits high specific capacitance, fast charge/discharge ability with good rate capability, and cyclic stability. The compositization of the new Cu-MOF with rGO leads to the augmentation in the specific capacitance of rGO by 82% through enhancement of EDLC capacitance by providing high surface area and also by invoking pseudocapacitance due to its redox-active  $\text{Cu}^{2+}$  centres. Consequently, the Cu-MOF/rGO composite exhibits a hybrid capacitive behaviour with high energy density because of the combined EDLC and pseudocapacitive manifestations of rGO and CuMOF, respectively. The gravimetric specific capacitance of the composite electrode material calculated by GCD is  $366 \text{ Fg}^{-1}$  at  $1 \text{ A.g}^{-1}$  current density, dropping to 83.30% after 4000 cycles. The electrochemical investigations reveal that the new Cu-MOF can be used as a promising component to be composited with other conducting matrices to derive improved charge storage performance.

## References

- [1] T.M. Gür, Review of electrical energy storage technologies, materials and systems: Challenges and prospects for large-scale grid storage, *Energy Environ. Sci.* 11 (2018) 2696–2767. <https://doi.org/10.1039/c8ee01419a>.
- [2] P.A. Owusu, S. Asumadu-Sarkodie, A review of renewable energy sources, sustainability issues and climate change mitigation, *Cogent Eng.* 3 (2016). <https://doi.org/10.1080/23311916.2016.1167990>.
- [3] P.J. Musgrove, Wind energy conversion: Recent progress and future prospects, *Sol. Wind Technol.* 4 (1987) 37–49. [https://doi.org/10.1016/0741-983X\(87\)90006-3](https://doi.org/10.1016/0741-983X(87)90006-3).
- [4] E. Kabir, P. Kumar, S. Kumar, A.A. Adelodun, K.H. Kim, Solar energy: Potential and future prospects, *Renew. Sustain. Energy Rev.* 82 (2018) 894–900. <https://doi.org/10.1016/j.rser.2017.09.094>.
- [5] O. Ellabban, H. Abu-Rub, F. Blaabjerg, Renewable energy resources: Current status, future prospects and their enabling technology, *Renew. Sustain. Energy Rev.* 39 (2014) 748–764. <https://doi.org/10.1016/j.rser.2014.07.113>.
- [6] M. Wu, J. Liao, L. Yu, R. Lv, P. Li, W. Sun, R. Tan, X. Duan, L. Zhang, F. Li, J. Kim, K.H. Shin, H. Seok Park, W. Zhang, Z. Guo, H. Wang, Y. Tang, G. Gorgolis, C. Galiotis, J. Ma, 2020 Roadmap on Carbon Materials for Energy Storage and Conversion, *Chem. - An Asian J.* 15 (2020) 995–1013. <https://doi.org/10.1002/asia.201901802>.
- [7] L. Trahey, F.R. Brushett, N.P. Balsara, G. Ceder, L. Cheng, Y.M. Chiang, N.T. Hahn, B.J. Ingram, S.D. Minteer, J.S. Moore, K.T. Mueller, L.F. Nazar, K.A. Persson, D.J. Siegel, K. Xu, K.R. Zavadil, V. Srinivasan, G.W. Crabtree, Energy storage emerging: A perspective from the Joint Center for Energy Storage Research,

- Proc. Natl. Acad. Sci. U. S. A. 117 (2020) 12550–12557.  
<https://doi.org/10.1073/pnas.1821672117>.
- [8] Z. Wang, J. Liu, X. Hao, Y. Wang, Y. Chen, P. Li, M. Dong, Enhanced power density of a supercapacitor by introducing 3D-interfacial graphene, *New J. Chem.* 44 (2020) 13377–13381.  
<https://doi.org/10.1039/d0nj02105a>.
- [9] A.D. Jagadale, G. Guan, X. Li, X. Du, X. Ma, X. Hao, A. Abudula, Ultrathin nanoflakes of cobalt-manganese layered double hydroxide with high reversibility for asymmetric supercapacitor, *J. Power Sources.* 306 (2016) 526–534.  
<https://doi.org/10.1016/j.jpowsour.2015.12.097>.
- [10] S.H. Park, J.M. Jeong, S.J. Kim, K.H. Kim, S.H. Lee, N.H. Bae, K.G. Lee, B.G. Choi, Large-Area and 3D Polyaniline Nanoweb Film for Flexible Supercapacitors with High Rate Capability and Long Cycle Life, *ACS Appl. Energy Mater.* 3 (2020) 7746–7755.  
<https://doi.org/10.1021/acsaem.0c01140>.
- [11] Y.M. Liu, C. Merlet, B. Smit, Carbons with Regular Pore Geometry Yield Fundamental Insights into Supercapacitor Charge Storage, *ACS Cent. Sci.* 5 (2019) 1813–1823.  
<https://doi.org/10.1021/acscentsci.9b00800>.
- [12] D. Chen, D. Ding, X. Li, G.H. Waller, X. Xiong, M.A. El-Sayed, M. Liu, Probing the Charge Storage Mechanism of a Pseudocapacitive MnO<sub>2</sub> Electrode Using in Operando Raman Spectroscopy, *Chem. Mater.* 27 (2015) 6608–6619.  
<https://doi.org/10.1021/acs.chemmater.5b03118>.
- [13] R. Srinivasan, E. Elaiyappillai, S. Anandaraj, B. kumar Duvaragan, P.M. Johnson, Study on the electrochemical behavior of BiVO<sub>4</sub>/PANI composite as a high performance supercapacitor material with excellent cyclic stability, *J. Electroanal. Chem.* 861 (2020) 113972. <https://doi.org/10.1016/j.jelechem.2020.113972>.
- [14] V.V.N. Obreja, On the performance of supercapacitors with

- electrodes based on carbon nanotubes and carbon activated material-A review, *Phys. E Low-Dimensional Syst. Nanostructures.* 40 (2008) 2596–2605. <https://doi.org/10.1016/j.physe.2007.09.044>.
- [15] A.C. Forse, C. Merlet, J.M. Griffin, C.P. Grey, New perspectives on the charging mechanisms of supercapacitors, *J. Am. Chem. Soc.* 138 (2016) 5731–5744. <https://doi.org/10.1021/jacs.6b02115>.
- [16] S. Osman, R.A. Senthil, J. Pan, W. Li, Highly activated porous carbon with 3D microspherical structure and hierarchical pores as greatly enhanced cathode material for high-performance supercapacitors, *J. Power Sources.* 391 (2018) 162–169. <https://doi.org/10.1016/j.jpowsour.2018.04.081>.
- [17] S. Sheng, W. Liu, K. Zhu, K. Cheng, K. Ye, G. Wang, D. Cao, J. Yan, Fe(3)O(4) nanospheres in situ decorated graphene as high-performance anode for asymmetric supercapacitor with impressive energy density., *J. Colloid Interface Sci.* 536 (2019) 235–244. <https://doi.org/10.1016/j.jcis.2018.10.060>.
- [18] J. Zhao, Z. Li, X. Yuan, Z. Yang, M. Zhang, A. Meng, Q. Li, A High-Energy Density Asymmetric Supercapacitor Based on Fe<sub>2</sub>O<sub>3</sub> Nanoneedle Arrays and NiCo<sub>2</sub>O<sub>4</sub>/Ni(OH)<sub>2</sub> Hybrid Nanosheet Arrays Grown on SiC Nanowire Networks as Free-Standing Advanced Electrodes, *Adv. Energy Mater.* 8 (2018) 1–14. <https://doi.org/10.1002/aenm.201702787>.
- [19] C.Y. Foo, H.N. Lim, M.A.B. Mahdi, K.F. Chong, N.M. Huang, High-performance supercapacitor based on three-dimensional hierarchical rGO/nickel cobaltite nanostructures as electrode materials, *J. Phys. Chem. C.* 120 (2016) 21202–21210. <https://doi.org/10.1021/acs.jpcc.6b05930>.
- [20] H. Mei, Z. Huang, B. Xu, Z. Xiao, Y. Mei, H. Zhang, S. Zhang, D. Li, W. Kang, D.F. Sun, NiSe<sub>2</sub>/Ni(OH)<sub>2</sub> Heterojunction

- Composite through Epitaxial-like Strategy as High-Rate Battery-Type Electrode Material, *Nano-Micro Lett.* 12 (2020) 1–15. <https://doi.org/10.1007/s40820-020-0392-8>.
- [21] R.A. Senthil, V. Yang, J. Pan, Y. Sun, A green and economical approach to derive biomass porous carbon from freely available feather finger grass flower for advanced symmetric supercapacitors, *J. Energy Storage.* 35 (2021) 102287. <https://doi.org/10.1016/j.est.2021.102287>.
- [22] Y. Sun, S. Guo, W. Li, J. Pan, C. Fernandez, R.A. Senthil, X. Sun, A green and template-free synthesis process of superior carbon material with ellipsoidal structure as enhanced material for supercapacitors, *J. Power Sources.* 405 (2018) 80–88. <https://doi.org/10.1016/j.jpowsour.2018.10.034>.
- [23] Z. Xiao, Y. Bao, Z. Li, X. Huai, M. Wang, P. Liu, L. Wang, Construction of Hollow Cobalt-Nickel Phosphate Nanocages through a Controllable Etching Strategy for High Supercapacitor Performances, *ACS Appl. Energy Mater.* 2 (2019) 1086–1092. <https://doi.org/10.1021/acsaem.8b01627>.
- [24] Z. Wang, Z. Xu, H. Huang, X. Chu, Y. Xie, D. Xiong, C. Yan, H. Zhao, H. Zhang, W. Yang, Unraveling and regulating self-discharge behavior of Ti<sub>3</sub>C<sub>2</sub>T<sub>x</sub> MXene-based supercapacitors, *ACS Nano.* 14 (2020) 4916–4924. <https://doi.org/10.1021/acsnano.0c01056>.
- [25] Y. Xiao, W. Wei, M. Zhang, S. Jiao, Y. Shi, S. Ding, Facile Surface Properties Engineering of High-Quality Graphene: Toward Advanced Ni-MOF Heterostructures for High-Performance Supercapacitor Electrode, *ACS Appl. Energy Mater.* 2 (2019) 2169–2177. <https://doi.org/10.1021/acsaem.8b02201>.
- [26] A.K. Gupta, D. De, K. Tomar, P.K. Bharadwaj, A Cu(II) metal-organic framework with significant H<sub>2</sub> and CO<sub>2</sub> storage capacity and heterogeneous catalysis for the aerobic oxidative amination

- of C(sp<sup>3</sup>)-H bonds and Biginelli reactions, *Dalt. Trans.* 47 (2018) 1624–1634. <https://doi.org/10.1039/c7dt04006g>.
- [27] A.K. Gupta, D. De, R. Katoch, A. Garg, P.K. Bharadwaj, Synthesis of a NbO Type Homochiral Cu(II) Metal-Organic Framework: Ferroelectric Behavior and Heterogeneous Catalysis of Three-Component Coupling and Pechmann Reactions, *Inorg. Chem.* 56 (2017) 4697–4705. <https://doi.org/10.1021/acs.inorgchem.7b00342>.
- [28] K. Tomar, M. Gupta, A.K. Gupta, A novel 2D porous Cd(II) MOF with a (4,4) connected binodal network: Synthesis and photoluminescence sensing of small molecules, *Inorg. Chem. Commun.* 64 (2016) 16–18. <https://doi.org/10.1016/j.inoche.2015.12.009>.
- [29] A.K. Gupta, M. Saraf, P.K. Bharadwaj, S.M. Mobin, Dual Functionalized CuMOF-Based Composite for High-Performance Supercapacitors, *Inorg. Chem.* 58 (2019) 9844–9854. <https://doi.org/10.1021/acs.inorgchem.9b00909>.
- [30] B. Xu, H. Zhang, H. Mei, D. Sun, Recent progress in metal-organic framework-based supercapacitor electrode materials, *Coord. Chem. Rev.* 420 (2020) 213438. <https://doi.org/10.1016/j.ccr.2020.213438>.
- [31] Z. Xiao, Y. Mei, S. Yuan, H. Mei, B. Xu, Y. Bao, L. Fan, W. Kang, F. Dai, R. Wang, L. Wang, S. Hu, D. Sun, H.C. Zhou, Controlled Hydrolysis of Metal-organic Frameworks: Hierarchical Ni/Co-Layered Double Hydroxide Microspheres for High-Performance Supercapacitors, *ACS Nano.* 13 (2019) 7024–7030. <https://doi.org/10.1021/acsnano.9b02106>.
- [32] S. Osman, R.A. Senthil, J. Pan, L. Chai, Y. Sun, Y. Wu, Hierarchically activated porous carbon derived from zinc-based fluorine containing metal-organic framework as extremely high specific capacitance and rate performance electrode material for

- advanced supercapacitors, *J. Colloid Interface Sci.* 591 (2021) 9–19. <https://doi.org/10.1016/j.jcis.2021.01.109>.
- [33] A.H. Assen, O. Yassine, O. Shekhah, M. Eddaoudi, K.N. Salama, MOFs for the Sensitive Detection of Ammonia: Deployment of fcu-MOF Thin Films as Effective Chemical Capacitive Sensors, *ACS Sensors*. 2 (2017) 1294–1301. <https://doi.org/10.1021/acssensors.7b00304>.
- [34] A.K. Gupta, N. Guha, S. Krishnan, P. Mathur, D.K. Rai, A Three-Dimensional Cu(II)-MOF with Lewis acid-base dual functional sites for Chemical Fixation of CO<sub>2</sub> via Cyclic Carbonate Synthesis, *J. CO<sub>2</sub> Util.* 39 (2020) 101173. <https://doi.org/10.1016/j.jcou.2020.101173>.
- [35] T.D. Burns, K.N. Pai, S.G. Subraveti, S.P. Collins, M. Krykunov, A. Rajendran, T.K. Woo, Prediction of MOF Performance in Vacuum Swing Adsorption Systems for Postcombustion CO<sub>2</sub> Capture Based on Integrated Molecular Simulations, Process Optimizations, and Machine Learning Models, *Environ. Sci. Technol.* 54 (2020) 4536–4544. <https://doi.org/10.1021/acs.est.9b07407>.
- [36] S.N. Ansari, M. Saraf, A.K. Gupta, S.M. Mobin, Functionalized Cu-MOF@CNT Hybrid: Synthesis, Crystal Structure and Applicability in Supercapacitors, *Chem. - An Asian J.* 14 (2019) 3566–3571. <https://doi.org/10.1002/asia.201900629>.
- [37] S. Osman, R.A. Senthil, J. Pan, Y. Sun, A novel coral structured porous-like amorphous carbon derived from zinc-based fluorinated metal-organic framework as superior cathode material for high performance supercapacitors, *J. Power Sources*. 414 (2019) 401–411. <https://doi.org/10.1016/j.jpowsour.2019.01.026>.
- [38] G. Nagaraju, S.C. Sekhar, B. Ramulu, S.K. Hussain, D. Narsimulu, J.S. Yu, Ternary MOF-Based Redox Active Sites Enabled 3D-on-2D Nanoarchitected Battery-Type Electrodes

- for High-Energy-Density Supercapatteries, *Nano-Micro Lett.* 13 (2021) 1–18. <https://doi.org/10.1007/s40820-020-00528-9>.
- [39] P. Wen, P. Gong, J. Sun, J. Wang, S. Yang, Design and synthesis of Ni-MOF/CNT composites and rGO/carbon nitride composites for an asymmetric supercapacitor with high energy and power density, *J. Mater. Chem. A.* 3 (2015) 13874–13883. <https://doi.org/10.1039/c5ta02461g>.
- [40] C. Qu, L. Zhang, W. Meng, Z. Liang, B. Zhu, D. Dang, S. Dai, B. Zhao, H. Tabassum, S. Gao, H. Zhang, W. Guo, R. Zhao, X. Huang, M. Liu, R. Zou, MOF-derived  $\alpha$ -NiS nanorods on graphene as an electrode for high-energy-density supercapacitors, *J. Mater. Chem. A.* 6 (2018) 4003–4012. <https://doi.org/10.1039/c7ta11100b>.
- [41] P.C. Banerjee, D.E. Lobo, R. Middag, W.K. Ng, M.E. Shaibani, M. Majumder, Electrochemical capacitance of Ni-doped metal organic framework and reduced graphene oxide composites: More than the sum of its parts, *ACS Appl. Mater. Interfaces.* 7 (2015) 3655–3664. <https://doi.org/10.1021/am508119c>.
- [42] M.S. Rahmanifar, H. Hesari, A. Noori, M.Y. Masoomi, A. Morsali, M.F. Mousavi, A dual Ni/Co-MOF-reduced graphene oxide nanocomposite as a high performance supercapacitor electrode material, *Electrochim. Acta.* 275 (2018) 76–86. <https://doi.org/10.1016/j.electacta.2018.04.130>.
- [43] N. Cao, Y. Zhang, Study of Reduced Graphene Oxide Preparation by Hummers' Method and Related Characterization, *J. Nanomater.* 2015 (2015). <https://doi.org/10.1155/2015/168125>.
- [44] G.M. Sheldrick, Crystal structure refinement with SHELXL, *Acta Crystallogr. Sect. C Struct. Chem.* 71 (2015) 3–8. <https://doi.org/10.1107/S2053229614024218>.
- [45] L.G. Beka, X. Bu, X. Li, X. Wang, C. Han, W. Liu, A 2D metal-organic framework/reduced graphene oxide heterostructure for

- supercapacitor application, *RSC Adv.* 9 (2019) 36123–36135.  
<https://doi.org/10.1039/c9ra07061c>.
- [46] P. Wen, Z. Li, P. Gong, J. Sun, J. Wang, S. Yang, Design and fabrication of carbonized rGO/CMOF-5 hybrids for supercapacitor applications, *RSC Adv.* 6 (2016) 13264–13271.  
<https://doi.org/10.1039/c5ra27893g>.
- [47] P. Chithaiah, M.M. Raju, G.U. Kulkarni, C.N.R. Rao, Simple synthesis of nanosheets of rGO and nitrogenated rGO, *Beilstein J. Nanotechnol.* 11 (2020) 68–75.  
<https://doi.org/10.3762/bjnano.11.7>.
- [48] S. Krishnan, S. Chatterjee, A. Solanki, N. Guha, M.K. Singh, A.K. Gupta, D.K. Rai, Aminotetrazole-Functionalized SiO<sub>2</sub>Coated MgO Nanoparticle Composites for Removal of Acid Fuchsin Dye and Detection of Heavy Metal Ions, *ACS Appl. Nano Mater.* 3 (2020) 11203–11216.  
<https://doi.org/10.1021/acsanm.0c02351>.
- [49] N.R. Dhumal, M.P. Singh, J.A. Anderson, J. Kiefer, H.J. Kim, Molecular Interactions of a Cu-Based Metal-Organic Framework with a Confined Imidazolium-Based Ionic Liquid: A Combined Density Functional Theory and Experimental Vibrational Spectroscopy Study, *J. Phys. Chem. C.* 120 (2016) 3295–3304.  
<https://doi.org/10.1021/acs.jpcc.5b10123>.
- [50] U. Kamran, Y.J. Heo, B.G. Min, I. In, S.J. Park, Effect of nickel ion doping in MnO<sub>2</sub>/reduced graphene oxide nanocomposites for lithium adsorption and recovery from aqueous media, *RSC Adv.* 10 (2020) 9245–9257. <https://doi.org/10.1039/c9ra10277a>.
- [51] M. Saraf, R. Rajak, S.M. Mobin, A fascinating multitasking Cu-MOF/rGO hybrid for high performance supercapacitors and highly sensitive and selective electrochemical nitrite sensors, *J. Mater. Chem. A.* 4 (2016) 16432–16445.  
<https://doi.org/10.1039/c6ta06470a>.

- [52] Y. Zhou, Z. Mao, W. Wang, Z. Yang, X. Liu, In-Situ Fabrication of Graphene Oxide Hybrid Ni-Based Metal-Organic Framework (Ni-MOFs@GO) with Ultrahigh Capacitance as Electrochemical Pseudocapacitor Materials, *ACS Appl. Mater. Interfaces*. 8 (2016) 28904–28916. <https://doi.org/10.1021/acsami.6b10640>.
- [53] L. Liu, Y. Yan, Z. Cai, S. Lin, X. Hu, Growth-Oriented Fe-Based MOFs Synergized with Graphene Aerogels for High-Performance Supercapacitors, *Adv. Mater. Interfaces*. 5 (2018) 1–8. <https://doi.org/10.1002/admi.201701548>.
- [54] B. Kirubasankar, P. Palanisamy, S. Arunachalam, V. Murugadoss, S. Angaiah, 2D MoSe<sub>2</sub>-Ni(OH)<sub>2</sub> nanohybrid as an efficient electrode material with high rate capability for asymmetric supercapacitor applications, *Chem. Eng. J.* 355 (2019) 881–890. <https://doi.org/10.1016/j.cej.2018.08.185>.
- [55] M. Liang, M. Zhao, H. Wang, J. Shen, X. Song, Enhanced cycling stability of hierarchical NiCo<sub>2</sub>S<sub>4</sub>@Ni(OH)<sub>2</sub>@PPy core-shell nanotube arrays for aqueous asymmetric supercapacitors, *J. Mater. Chem. A*. 6 (2018) 2482–2493. <https://doi.org/10.1039/c7ta10413h>.
- [56] H. Peng, B. Yao, X. Wei, T. Liu, T. Kou, P. Xiao, Y. Zhang, Y. Li, Pore and Heteroatom Engineered Carbon Foams for Supercapacitors, *Adv. Energy Mater.* 9 (2019) 1–9. <https://doi.org/10.1002/aenm.201803665>.
- [57] F. Wang, S. Sun, Y. Xu, T. Wang, R. Yu, H. Li, High performance asymmetric supercapacitor based on Cobalt Nickel Iron-layered double hydroxide/carbon nanofibres and activated carbon, *Sci. Rep.* 7 (2017) 1–11. <https://doi.org/10.1038/s41598-017-04807-1>.
- [58] L. Code, Development of Advanced Nanostructured Electrode Materials for High-Performance Supercapacitors and Self-Charging Power Cell, (n.d.).

- [59] Y. Wang, B. Chen, Y. Zhang, L. Fu, Y. Zhu, L. Zhang, Y. Wu, ZIF-8@MWCNT-derived carbon composite as electrode of high performance for supercapacitor, *Electrochim. Acta.* 213 (2016) 260–269. <https://doi.org/10.1016/j.electacta.2016.07.019>.
- [60] Y. Zhang, B. Lin, Y. Sun, X. Zhang, H. Yang, J. Wang, Carbon nanotubes@metal–organic frameworks as Mn-based symmetrical supercapacitor electrodes for enhanced charge storage, *RSC Adv.* 5 (2015) 58100–58106. <https://doi.org/10.1039/c5ra11597c>.
- [61] S.N. Guo, Y. Zhu, Y.Y. Yan, Y.L. Min, J.C. Fan, Q.J. Xu, H. Yun, (Metal-Organic Framework)-Polyaniline sandwich structure composites as novel hybrid electrode materials for high-performance supercapacitor, *J. Power Sources.* 316 (2016) 176–182. <https://doi.org/10.1016/j.jpowsour.2016.03.040>.
- [62] R.R. Salunkhe, Y. Kamachi, N.L. Torad, S.M. Hwang, Z. Sun, S.X. Dou, J.H. Kim, Y. Yamauchi, Fabrication of symmetric supercapacitors based on MOF-derived nanoporous carbons, *J. Mater. Chem. A.* 2 (2014) 19848–19854. <https://doi.org/10.1039/c4ta04277h>.
- [63] J. Gu, L. Sun, Y. Zhang, Q. Zhang, X. Li, H. Si, Y. Shi, C. Sun, Y. Gong, Y. Zhang, MOF-derived Ni-doped CoP@C grown on CNTs for high-performance supercapacitors, *Chem. Eng. J.* 385 (2020) 123454. <https://doi.org/10.1016/j.cej.2019.123454>.
- [64] L. Tan, D. Guo, J. Liu, X. Song, Q. Liu, R. Chen, J. Wang, In-situ calcination of polyoxometallate-based metal organic framework/reduced graphene oxide composites towards supercapacitor electrode with enhanced performance, *J. Electroanal. Chem.* 836 (2019) 112–117. <https://doi.org/10.1016/j.jelechem.2019.01.051>.
- [65] C. Cheng, J. Xu, W. Gao, S. Jiang, R. Guo, Preparation of flexible supercapacitor with RGO/Ni-MOF film on Ni-coated polyester

fabric, *Electrochim. Acta.* 318 (2019) 23–31.  
<https://doi.org/10.1016/j.electacta.2019.06.055>.

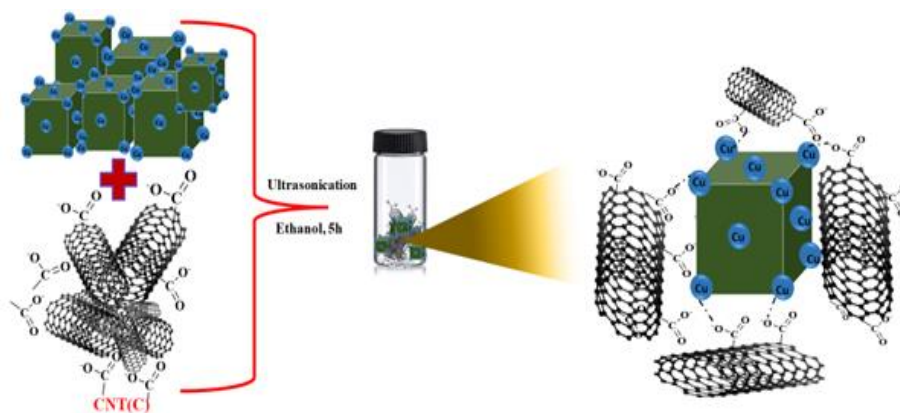
- [66] Y. Liu, G. Li, Y. Guo, Y. Ying, X. Peng, Flexible and Binder-Free Hierarchical Porous Carbon Film for Supercapacitor Electrodes Derived from MOFs/CNT, *ACS Appl. Mater. Interfaces.* 9 (2017) 14043–14050. <https://doi.org/10.1021/acsami.7b03368>.

## Chapter 2 - Section 2

Building on the remarkable electrochemical performance observed in Cu-MOF/rGO (MR), this section introduces a novel Cu-MOF/CNT (MC) composite as an electrode material for supercapacitors. Herein, the presence of redox-active  $\text{Cu}^{2+}$  centers in the Cu-MOF enables charge storage by the faradaic process, which is supported by a three-dimensional (3D) channeled structure of MOF to facilitate the access of electrolyte ions throughout the bulk of the electrode. On the other hand, the CNTs in the composite provide a conductive network that promotes efficient charge transport and enhances the overall electrical conductivity of the composite. Owing to the synergistic effect of the advantages offered by Cu-MOF (pseudo type charge storage) and CNT (EDLC type charge storage), the Cu-MOF/CNT (MC) composite material exhibits excellent charge storage for supercapacitor applications.

### 2.5 Results and Discussion

Synthesis of Cu-MOF/CNT (MC) was achieved by ultrasonication of Cu-MOF (M) and CNT(C) in different proportions. During the compositization process, the free carboxylate groups on CNT resulting from the activation coordinate with the peripheral Cu(II) centers of MOF, resulting in the firm anchorage of two components to yield a stable MC composite (Scheme 1).



Scheme 1. Synthesis of MC

Additionally, it also improves the hydrophilic characteristics of the resulting MC, which in turn increases electrolyte contact with the electrode material. Eventually, the effective compositzation of the two components leads to an enhanced synergism, which causes an improved supercapacitive and electrocatalytic performance.

### 2.5.1 Physical and Morphological Characterization

In **Figure 2.1**, we present the PXRD patterns for the as-synthesized C, M, and MC samples, providing insight into the crystalline nature and phase purity of each. Notably, the PXRD pattern of C exhibits distinctive peaks corresponding to the (002) and (100) planes of multi-walled carbon nanotubes (MWCNT) at 26.13° and 43.32°, respectively.[1] In the composite MC, peaks related to both components can be seen without any alteration, confirming the successful formation of the composite and the structural integrity of its components during compositzation by ultrasonication. In summary, PXRD data confirms the formation of an MC composite consisting of pure phases of M and C.

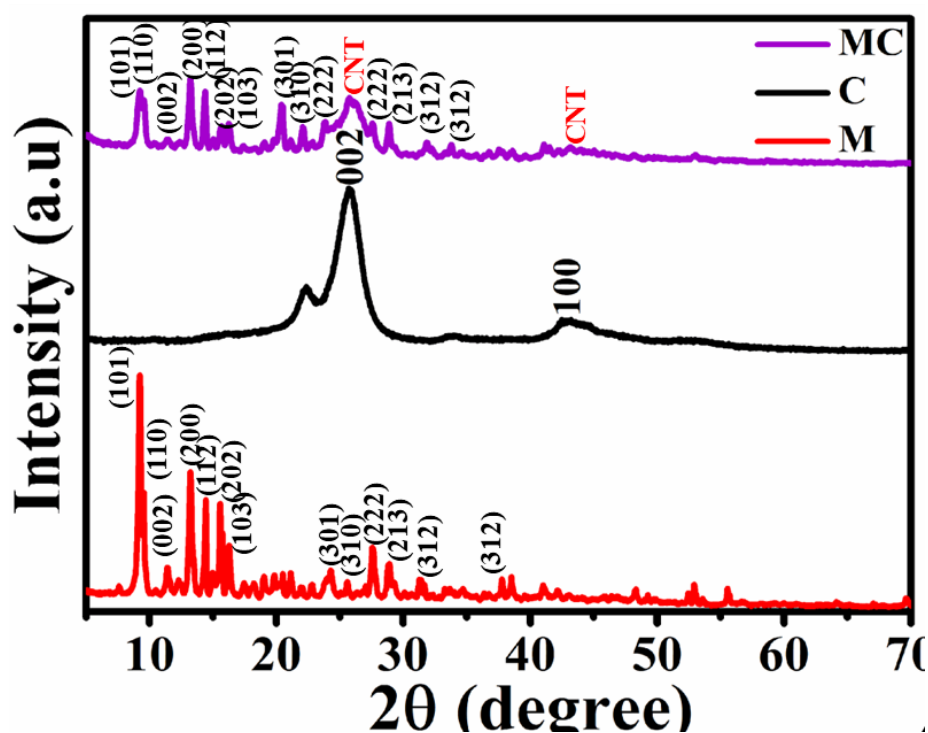


**Figure 2.1** PXRD patterns of M, C, and MC.

The thermal stability and decomposition characteristics were assessed by subjecting them to thermogravimetric analysis (TGA) under a nitrogen (N<sub>2</sub>) atmosphere (**Figure 2.2**). **Table 4** provides information on the weight loss regions and corresponding weight percentages for each material. The TGA profile of **CNT (C)** exhibits a two-step weight loss, primarily attributed to the desorption and decarboxylation of adsorbed water and carboxylate groups (2.81% weight loss upto 465°C), which are followed by decarbonization step. In the case of **M**, weight loss occurs in multiple steps. The first step involves the desorption of adsorbed water (up to 130°C, 9.13%), followed by the removal of apically bound water and solvent molecules present in the MOF voids (150-290°C, 47.97%). The subsequent steps involve the decarboxylation of carboxylate groups and the decomposition of aromatic moieties (290-430°C, 15.68%).[2] For the composite **MC**, a combined decomposition behavior of both components was observed (up to 110°C (4.9%), 150-290°C (17.21%), and 290-350°C (13.47%)), indicating the successful formation of the composite. Overall the TGA profile of **MC** confirms its successful formation and thermal stability up to 150 °C.

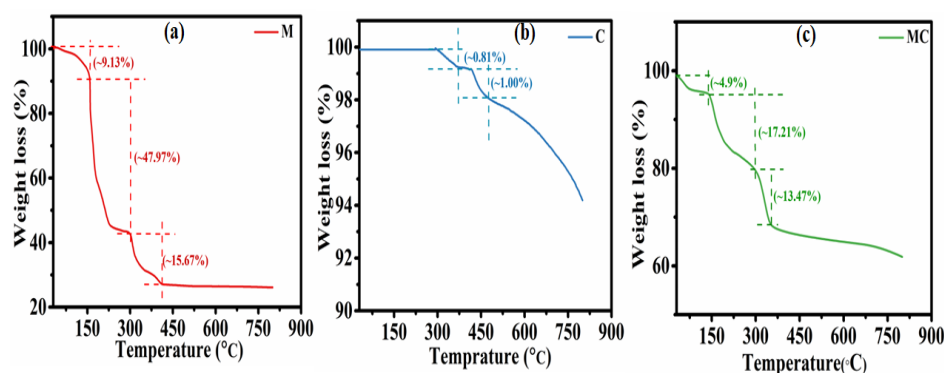


**Figure 2.2** TGA curve of **M**, **C**, and **MC** nanocomposite.

**Table 4.** Comparison table of weight loss percentage of **MC** with temperature.

Sample	Weight loss in %		
	1	2	3
<b>M</b>	9.13 %	47.97 %	15.67 %
<b>C</b>	0.81 %	1.0%	-
<b>MC</b>	4.90 %	17.21 %	13.47 %

The presence of different functional groups in the synthesized materials was analyzed using FTIR spectroscopy. **Figure. 2.3** shows the FTIR spectra of **M**, **C**, and the **MC** composite. For Cu-MOF (**M**), the spectrum exhibits a peak at  $510\text{ cm}^{-1}$  corresponding to the Cu-O vibration. Peaks between  $600$  and  $900\text{ cm}^{-1}$  are attributed to the rocking vibrations of methylene group ( $\text{CH}_2$ ) moiety, while the appearance of very weak peaks around  $2850\text{ cm}^{-1}$  are related to its stretching vibrations. The asymmetric and symmetric vibrations of carboxylate groups of the MOF are observed at  $1560$  and  $1350\text{ cm}^{-1}$ , respectively. The strong peak around  $3400$  is due to the coordinated water molecules. In **CNT (C)**, a broad peak centered around  $3300\text{ cm}^{-1}$  arises from the water molecules adsorbed on the CNT surface due to strong hydrogen bonding between carboxylate groups of CNT and water molecules ( $\text{CNT-COO}^-\dots\text{H-OH}$ ). Besides, a sharp peak at  $3650\text{ cm}^{-1}$  and a medium peak at around  $1360\text{ cm}^{-1}$  can be seen due to the presence of free hydroxyl ( $\nu_{\text{O-H}}$ ) and carboxylate groups ( $\nu_{\text{C-O}}$ ), respectively, on the CNT surface generated as a result of hydrothermal oxidation. A peak at  $1640\text{ cm}^{-1}$  corresponds to C=C bond vibrations of the CNT framework. The FTIR spectrum of the **MC** composite displays all the characteristic peaks observed in **M** and **C**; however, peaks corresponding to free

hydroxyl and carboxylates of CNT are absent, indicating their coordination with the peripheral Cu(II) centers of the MOF.

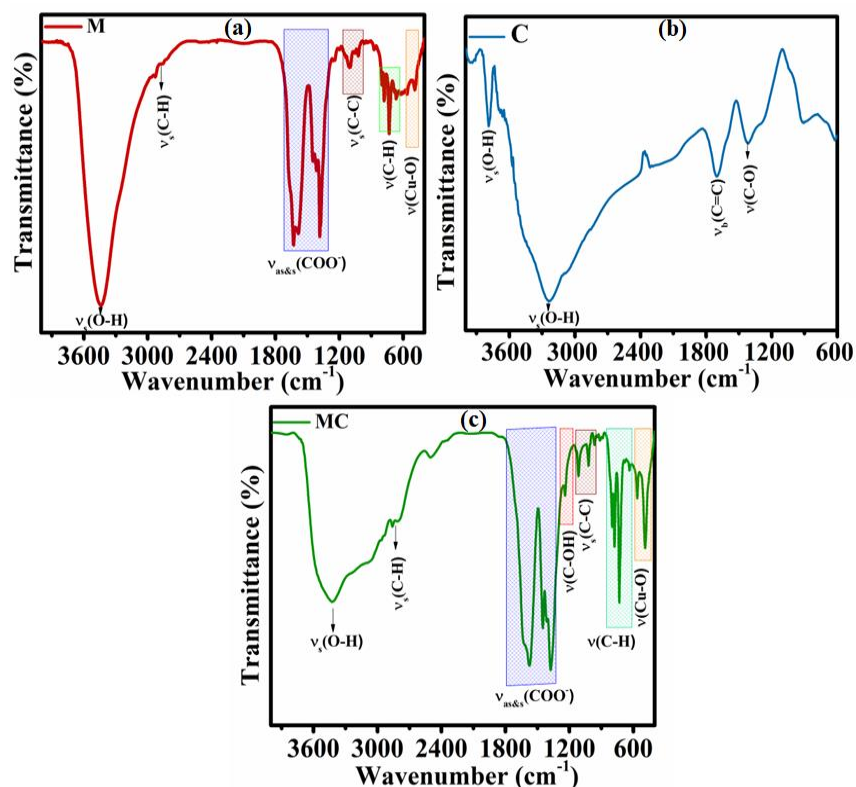


**Figure 2.3** FTIR spectra of **M**, **C**, and **MC** nanocomposite.

The X-Ray photoelectron spectroscopy (XPS) was performed to investigate the surface valence states and the presence of elements in the **MC** composite, which is shown in **Figure 2.4**. The full survey spectrum (**Figure. 2.4a**) confirms the presence of Cu, C, and O in the **MC** composite. In **Figure. 4b**, the high-resolution spectrum of Cu 2p shows two characteristic peaks corresponding to Cu 2p<sup>3/2</sup> and Cu 2p<sup>1/2</sup> at the binding energies of 934.9 and 954.9 eV, respectively, confirming the Cu in divalent (+2) oxidation state.[3] Additionally, the satellite peaks can also be observed at the binding energies of 939.8, 944.2, and 960.3 eV. The high-resolution C 1s spectrum (**Figure. 2.4c**) reveals the peaks at the binding energies around 284.4, 285.1, and 289.5 eV, which are associated with C-C, C-O, and C=O, respectively.[4.5] The O 1s spectrum shows three peaks at 532.1, 533.2, and 535.4 eV, which are related to C-OH, C=O, and chemisorbed water molecules, respectively.[6]

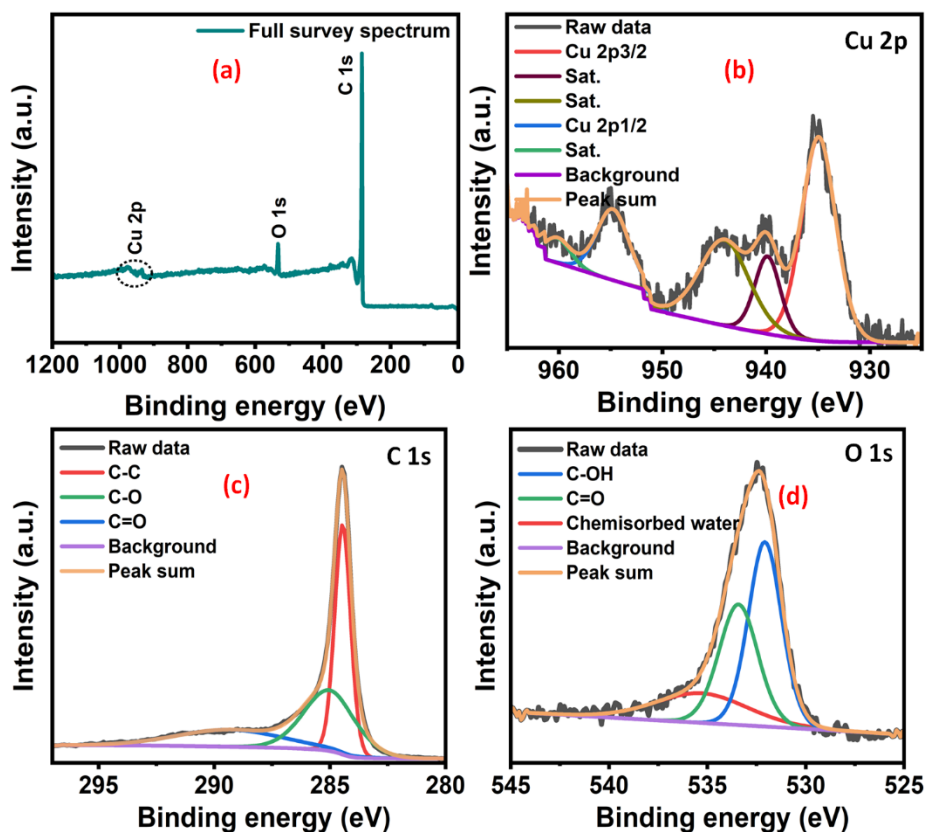


**Figure 2.4** XPS spectra of MC (a) Full survey spectrum, high-resolution spectra of (b) Cu 2p, (c) C 1s, and (d) O 1s.

Morphological investigations of **M**, **C**, and the **MC** were conducted using FE-SEM and TEM, as shown in **Figure 2.5**. **Figure 2.5a** shows an irregular-shaped particle of **M**. **Figure 2.5b** depicts the tube-like structure of **C**, where multiple interwoven tubes can be seen. SEM micrograph of **MC** composite (**Figure 2.5c**) reveals an extensive coverage of MOF surface by CNT. Such an effective anchorage of CNT on the MOF surface is mainly supported by coordinative interactions between peripheral Cu(II) centers on MOF with the carboxylate groups of CNT.

The EDX spectrum and elemental mapping of the **MC** composite are depicted in **Figure 2.6 (a,b)**, showing the presence of C, O, and Cu elements in appropriate proportions. Furthermore, an even distribution of these elements is observed in the elemental mapping, suggesting a uniform coverage of CNT on the MOF. The TEM images of **M** and **C** are consistent with their SEM images, as shown in **Figure 2.5(d-i)**. The TEM image of **M** reveals irregularly shaped crystals with varying crystallite sizes. In the TEM image of **C**, the thick wall corresponding to multi-wall carbon nanotubes of approximately 27 nm diameter can be easily seen. The TEM images of the **MC** composite show an extension dispersion of CNT on **M** crystals. The selected area electron diffraction (SAED) pattern of **M** exhibits prominent concentric rings, indicating its crystalline nature.[7] However, **C** displays diffused rings in its SAED pattern, suggesting its disordered structure.[8] For the **MC** composite, the SAED pattern shows a combined nature of both crystalline and amorphous structure.

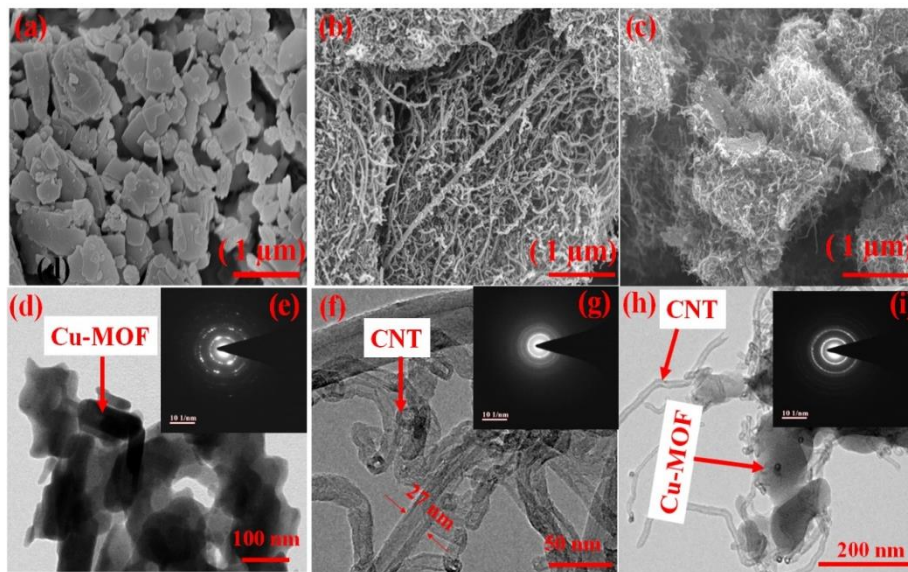


**Figure 2.5** FE-SEM of (a) **M** (b) **C** and (c) **MC** composite. TEM of (d) **M** and (f) **C** (h) **MC** (e,g,h) SAED pattern (inset) of **M**, **C** and **MC**.

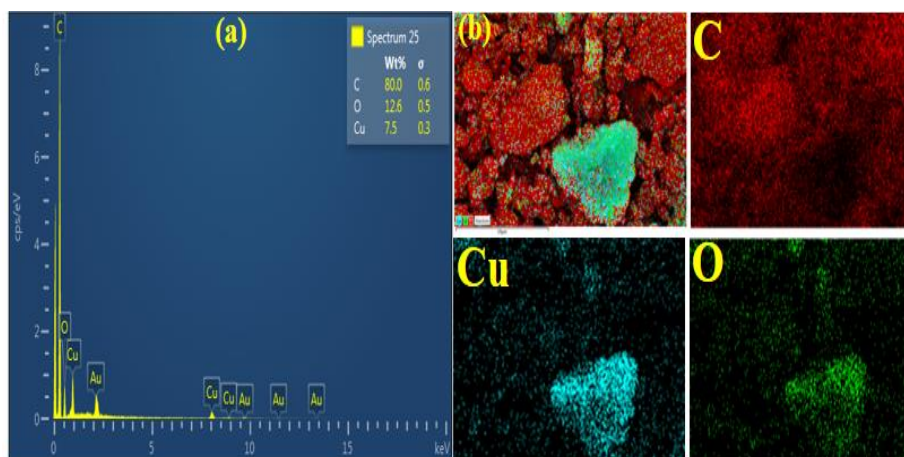


**Figure 2.6.** (a) EDX and (b) Mapping of MC composite.

The textural properties, including specific surface areas and porous characteristics, of as-prepared **M**, **C**, and **MC** were investigated through N<sub>2</sub> adsorption-desorption isotherms at 77 K (**Figure. 2.7** and **Table. 5**). According to the IUPAC classification, the isotherms of all three-materials exhibit type IV behavior with a type-3 hysteresis loop. In terms of specific surface area, the **M** exhibits a BET surface area of 599.38 m<sup>2</sup>/g, while the **C** has a surface area of 193.20 m<sup>2</sup>/g. The **MC** composite displays a BET surface area of 293.32 m<sup>2</sup>/g, which is significantly less than the gravimetric average of both components. The reduction in the specific surface area of **MC** is because some of the channels of MOF are covered by CNT during compositization.

**Table 5.** Comparison table of BET curve of **M**, **C**, and **MC** nanocomposite.

Materials	BET surface area (m <sup>2</sup> /g)
<b>M</b>	599.31
<b>C</b>	193.20
<b>MC</b>	293.32

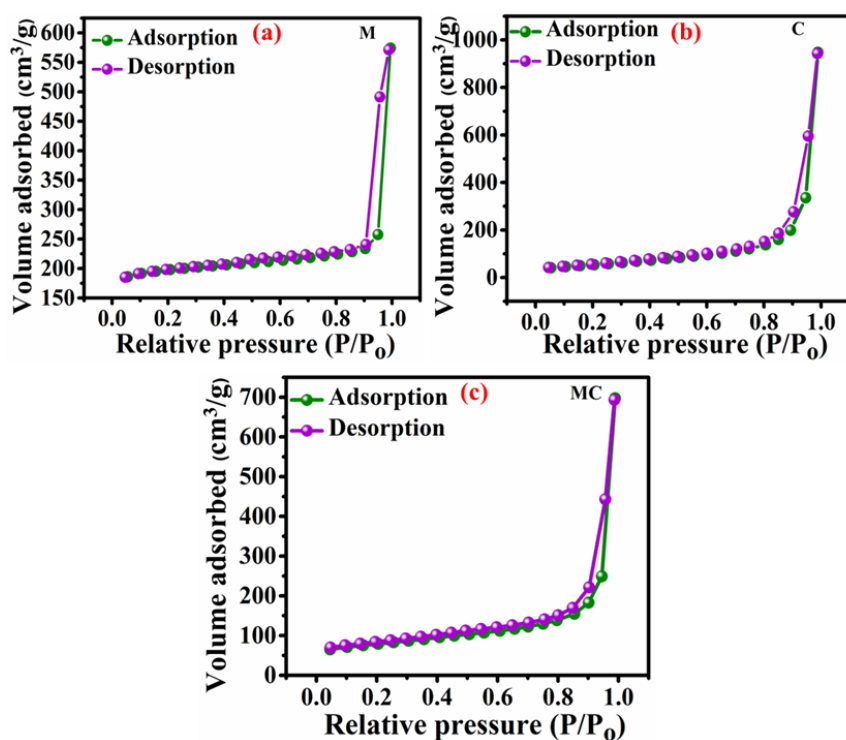


**Figure 2.7** BET curve of **M**, **C**, and **MC** nanocomposite.

## 2.5.2 Electrochemical performance

The supercapacitor characteristics of the **M**, **C**, and **MC** electrodes were assessed through cyclic voltammetry (CV), galvanostatic charge-discharge (GC D), and electrochemical impedance spectroscopy (EIS) methods. To derive the best supercapacitive performance of the **MC** composite, the working potential window and the relative ratio of **M** and **C** were systematically optimized. To determine the optimal potential window, CVs of the **MC** composite was recorded in the positive (0.0 to 0.6 V) as well as in negative (-1.0 to 0.0 V) potential windows at a scan rate of  $10 \text{ mVs}^{-1}$  (**Figure. 2.8a**). The analysis of the cyclic voltammograms showed that the area under the curve in the negative potential window was significantly larger ( $2.09 \times 10^{-4} \text{ A}\cdot\text{V}$ ) compared to the positive potential window ( $4.18 \times 10^{-5} \text{ A}\cdot\text{V}$ ). Also, the maximum current value obtained was higher in the negative potential range. Further GCD results also show higher discharging time in the negative range (**Figure. 2.8b, c**). These results indicate that the composite electrode material exhibits superior supercapacitive

performance in the negative potential range. Based on these findings, all further electrochemical investigations were conducted within the negative potential window of -0.1 to 0.0 V.

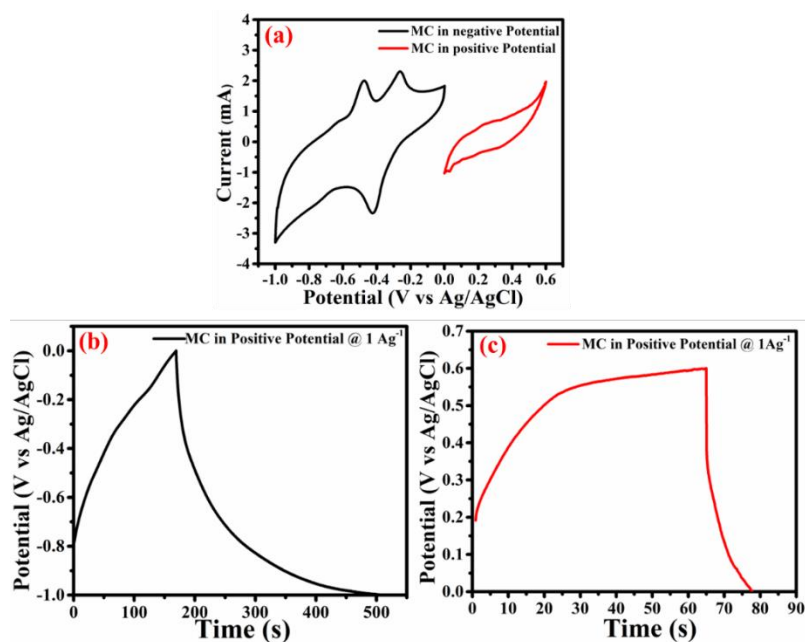


**Figure 2.8** (a) CV and (b,c) GCD profiles of MC in Positive and Negative Potential range at  $50 \text{ mVs}^{-1}$  and  $1 \text{ Ag}^{-1}$ .

Further, we also optimized the relative ratio **M** and **C** in **MC** to achieve the suitable proportion for the best supercapacitive performance. For this, CV investigations of six ratios of **M** and **C** (10:90, 20:80, 30:70, 40:60, 50:50, and 60:40) (**Figure. 9**) were carried out at  $10 \text{ mVs}^{-1}$ .



**Figure 2.9** Digital photographs of three MC composites with different proportions of **M** and **C**.

**Figure. 2.10** depicts cyclic voltammograms of **MC** composites comprising six different ratios. The study reveals that increasing the relative proportion of **C** in the **MC** composite to a ratio up to 50% results in an increase in the current response as well as in the CV curve area. Further increasing the **C** content beyond 50% in the composite leads to a decline in both parameters. This makes perfect sense because the overall electrochemical performance of a material depends not only on its conductivity but also on its specific surface area. When the **C** content is more than 50%, aggregation occurs, which causes the pores in MOF to get blocked, resulting in the reduction of the specific surface of the composite and eventually degrading the supercapacitive performance. Based on the potential window and M:C ratio optimization studies, 1:1 ratio of **MC** was chosen for further study in the negative potential window.

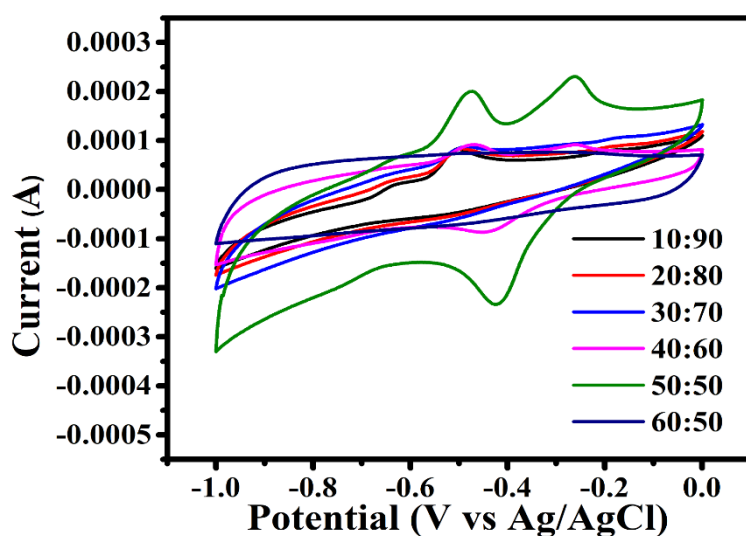


**Figure 2.10** Cyclic Voltammetry of **MC** in different ratio of **M** and **C**

To investigate the supercapacitive behaviors of **M**, **C**, and **MC**, their cyclic voltammetry studies were performed. **Figure. 2.11a** presents a comparison of the cyclic voltammetry (CV) curves of **M**, **C**, and **MC** at 10 mVs<sup>-1</sup> scan rate. Among these materials, **MC** exhibits the highest current response and a larger CV area, suggesting its superior supercapacitive performance. The enhanced electrochemical performance of **MC** can be attributed to the synergistic behavior of the

**M** and **C** components. The **M** component provides a porous structure with a high surface area, facilitating enhanced ion adsorption. Moreover, the Cu(II) centers in MOF impart redox activity leading to increased capacitance and improved energy storage capabilities. The presence of **C** increases the conductivity of the overall material and thereby facilitates charge transfer. Overall, the combination of the high surface area and redox activity from **M**, along with the conductive properties of **C**, result in the superior electrochemical performance observed in the **MC** composite.[9]

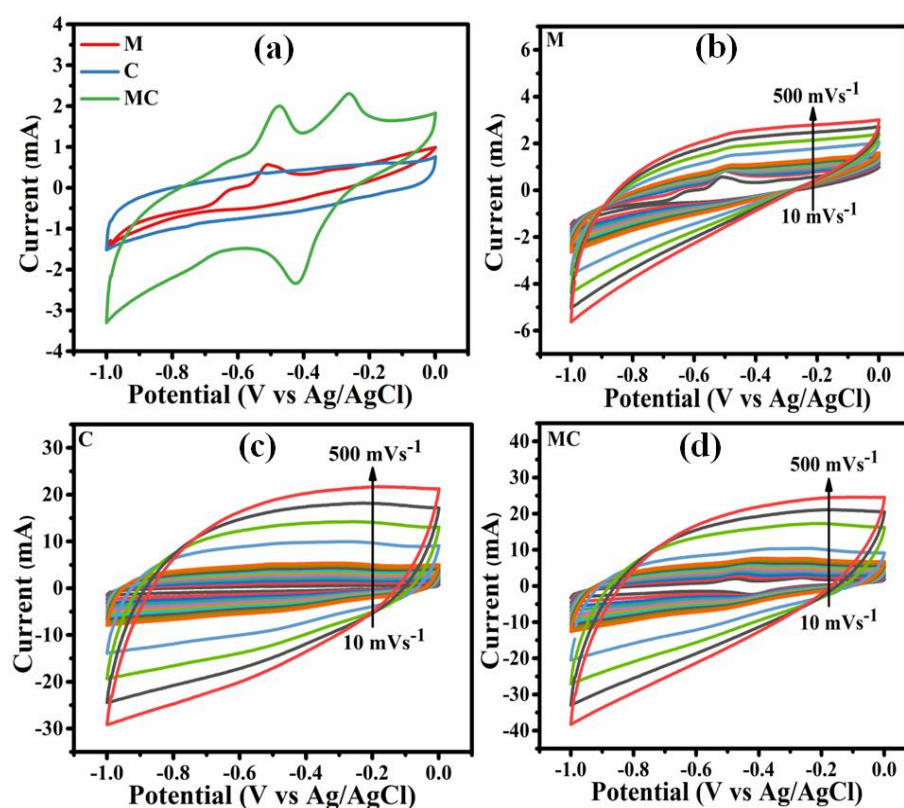


**Figure 2.11** (a) Comparison of CVs of **M**, **C**, and **MC** at  $10 \text{ mVs}^{-1}$  scan rate in  $1\text{M KOH}$ ; (b, c,d) CV profiles of the **M**, **C**, and **MC** at different scan rates ( $10\text{-}500 \text{ mVs}^{-1}$ ).

The charge storage mechanism and kinetics of **M**, **C**, and **MC** materials were assessed by recording their CVs at different scan rates ranging from  $10$  to  $500 \text{ mVs}^{-1}$  (**Figure 2.11b-d**). The cyclic voltammogram for **M** (**Figure 2.11b**) shows discernable redox peaks indicating the occurrence of the faradaic process due to the redox active Cu(II), indicating the pseudocapacitive behavior of the Cu-MOF.[10]

For **C**, the voltammogram shape resembles a typical EDLC-type behavior (**Figure 2.11c**). In the case of **MC** composite, redox peaks are observable at a low scan rate, which gradually disappears as the scan rate is increased, indicating a combined effect of EDLC and faradaic processes (**Figure 2.11d**). With increasing scan rate, increase in the current density was observed for each material; however, the relationship between peak current ( $i$ ) and scan rate ( $v$ ) was found to be different for each material, suggesting different charge storage mechanisms. To further investigate the charge storage mechanism, the Power law approach was utilized. [11] The value of  $b$  can be determined from the slope of the plot of  $\ln i$  vs  $\ln v$ , which indicates the charge storage mechanism of the electrode material ( $b \approx 0.5$  suggests diffusion-controlled charge storage involving the faradaic process, while  $b \approx 1$  indicates surface-controlled charge storage, involving EDL formation). The linear plots of  $\ln(i)$  versus  $\ln(v)$  for the electrode materials **M**, **C**, and **MC** are provided in **Figure 2.12**, showing the  $b$  values of 0.39, 0.83, and 0.67, respectively. These findings indicate that the charge storage mechanisms for **M**, **C**, and **MC** are primarily influenced by diffusion phenomena, surface phenomena, and a blend of both surface and diffusion processes, respectively.

To quantify the contribution of surface-controlled and diffusion-controlled capacitance to the overall specific capacitance of the **MC** composite, Dunn's method was employed. [12]

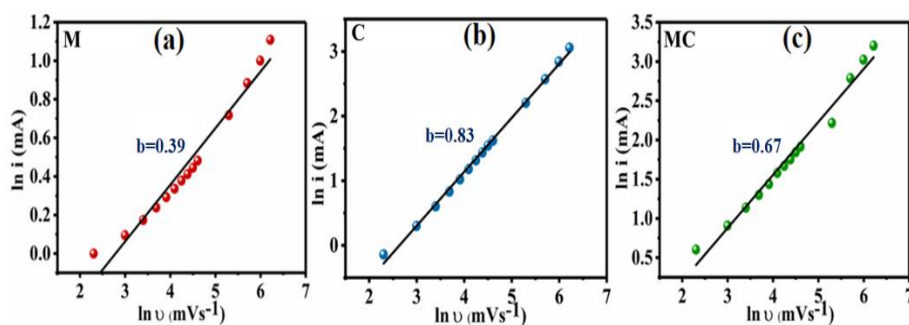


**Figure 2.12** Charge storage kinetics  $\ln i$  ( $\mu\text{A}$ ) vs  $\ln v$  ( $\text{mV/s}$ ): estimation of values of  $b$  for **M** (a), **C** (b), and **MC** (c)

**Figure 2.13a** presents the percentage capacitance contributions of the surface-controlled and diffusion-controlled processes at various scan

rates. The bar diagram clearly indicates the diffusion-dominant supercapacitor features of **MC**, whose contribution gradually decreases upon increasing the scan rates due to the limitation of the electrolyte diffusion.[12,13] For comparison, the contributions of EDLC capacitance in the overall cyclic voltammograms of **MC** at scan rates 10 and 50  $\text{mVs}^{-1}$  are shown in **Figure 1.13b,c**.

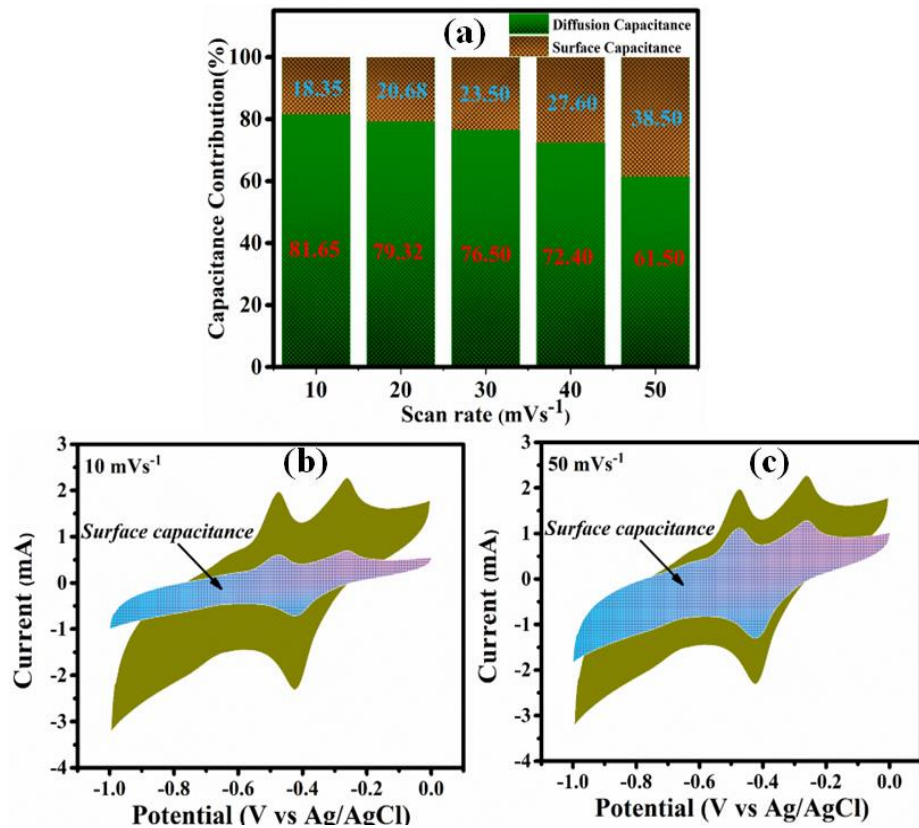


**Figure 2.13** (a) Percentage EDLC and pseudocapacitive contributions to the overall capacitance of **MC** at different scan rates (10-50  $\text{mVs}^{-1}$ ) (b, c) comparison of calculated CV profile of **MC** for surface only capacitance and overall experimental at 10 and 50  $\text{mVs}^{-1}$ .

The charge storage capabilities, specifically the specific capacitances, of the electrode materials were evaluated through galvanostatic charge-discharge (GCD) studies at different current densities ranging from 1 to 10  $\text{Ag}^{-1}$  within a potential window of -1.0 to 0 V. **Figure 2.14a** shows the comparison of the GCD profiles of **M**, **C**, and **MC** at a current density of 1  $\text{Ag}^{-1}$ . The specific capacitances of **M**, **C**, and **MC** calculated from the discharge responses were found to be

48.52  $\text{Fg}^{-1}$ , 75.41  $\text{Fg}^{-1}$ , and 348.62  $\text{Fg}^{-1}$ , respectively, at a current density of 1  $\text{Ag}^{-1}$ . **Figure 2.14b** presents the measured capacitances of different electrode materials as a bar chart. Notably, the specific capacitance of **MC** is more than two times the sum of the specific capacitances of its constituents **M** and **C**. The notable enhancement can be ascribed to the synergistic interplay between **M** and **C**, yielding reduced internal resistance, accelerated charge transfer kinetics, improved ion diffusion, and an expanded active surface area. These cumulative effects ultimately culminate in outstanding charge storage performance. The results obtained from the Galvanostatic Charge-Discharge (GCD) studies corroborate those derived from Cyclic Voltammetry (CV) measurements, reaffirming the superior suitability of **MC** as an electrode material for supercapacitor applications.

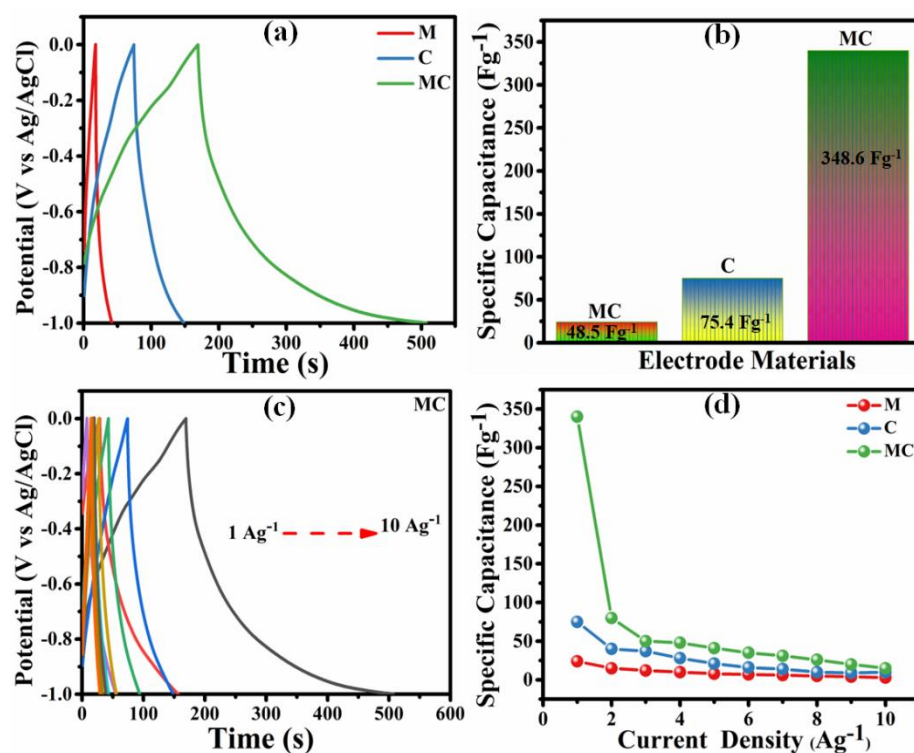


**Figure 2.14** (a) Comparison of GCD of **M**, **C**, and **MC** at a current density of 1  $\text{Ag}^{-1}$  in 1M KOH; (b) Specific capacitance value at 1  $\text{Ag}^{-1}$  **M**, **C**, and **MC** (c) GCD of **MC** at different current density(1-10 $\text{Ag}^{-1}$ ) and (d) Specific capacitance value of **M**, **C**, and **MC** at different current density (1-10 $\text{Ag}^{-1}$ )

**Fig 14.** (a) Comparison of GCD of **M**, **C**, and **MC** at a current density of  $1 \text{ Ag}^{-1}$  in  $1\text{M KOH}$ ; (b) Specific capacitance value at  $1 \text{ Ag}^{-1}$  **M**, **C**, and **MC** (c) GCD of **MC** at different current density( $1\text{-}10\text{Ag}^{-1}$ ) and (d) Specific capacitance value of **M**, **C**, and **MC** at different current density ( $1\text{-}10\text{Ag}^{-1}$ )

The GCD profiles of **MC** at different current densities are depicted in **Figure 2.14c**, which indicate that charging and discharging time decrease with increasing current density. It implies that increasing current density decreases the time required to build and drain the stored charge in the charging and discharging step. **Figure 2.14d** demonstrates the variation of the specific capacitances of **M**, **C**, and **MC** with increasing current density. It is observed that in the case of **MC**, upon increasing the current density, there is a sudden decrease in the specific capacitance up to  $2 \text{ Ag}^{-1}$ . Afterward, a gradual reduction in the capacitance is observed. This is mainly because, with increasing current density, the diffusion process fails to match up with the current, i.e., the rate of charge transfer. And beyond  $2 \text{ Ag}^{-1}$ , EDLC is the main contributor to the overall capacitance of the composite.

Electrochemical impedance spectroscopy (EIS) was employed to gain deeper insights into the conductivity and charge storage mechanisms of the electrode materials. **Figure 2.15a** illustrates Nyquist plots for **M**, **C**, and **MC** over a frequency range spanning from  $100 \text{ mHz}$  to  $100 \text{ kHz}$ , with an AC amplitude of  $10 \text{ mV}$ . The inset provides an enlarged view of the Nyquist plots in the high-frequency domain. In the Nyquist plot, the point where the impedance curve intersects the real axis corresponds to the equivalent series resistance ( $R_s$ ), encompassing the resistance of the electrolyte and the contact resistance at the electrode-electrolyte interface. The observed  $R_s$  values for **M**, **C**, and **MC** were  $13.78 \text{ }\Omega$ ,  $11.43 \text{ }\Omega$ , and  $12.01 \text{ }\Omega$ , respectively. The reduction in  $R_s$  value observed in the **MC** composite, in comparison to **M** alone, suggests that the combined presence of **M** and **C** enhances the accumulation of ions at the electrode-electrolyte interface. This effect is achieved by diminishing the overall resistance to ion mobility and their

adsorption onto the electrode surface. The alignment of the impedance curve on the Nyquist plot offers insights into the capacitive characteristics of the materials.[14] In the Nyquist plots, it becomes evident that the impedance line associated with **C** aligns most closely with the imaginary axis, indicating its predominant EDLC behavior. Conversely, the impedance line associated with **M** aligns closer to the real axis, signifying its pseudocapacitive nature. For **MC**, the impedance line falls between those of **C** and **M**, indicating a combination of both EDLC and pseudocapacitive behavior. In the Bode plot, the phase angle at lower frequencies is a parameter used to determine the capacitive nature of the electrode materials.[15] Ideally, a 90° phase angle at a low frequency represents ideal capacitor behavior. At a low frequency of 0.1 Hz, the impedance phase angles for **M**, **C**, and **MC** are 48.65°, 72.38°, and 65.49°, respectively (**Figure 2.15b**).

These values indicate that the behavior of **C** is very close to that of a capacitor, confirming its EDLC characteristics. The lowest phase angle for **M** suggests the involvement of a faradaic process in the charge storage mechanism. In the case of **MC**, the observed phase angle value falls between that of **M** and **C**, indicating its hybrid capacitive behavior, combining both EDLC and pseudocapacitive features. The rates of charging and discharging of the electrode materials were evaluated by measuring the phase relaxation time constants ( $t_0$ ), which can be calculated using the equation 1:[16]

$$t_0 = 1/f_0 \quad (1)$$

where  $t_0$  denotes the phase relaxation constant and  $f_0$  denotes the AC frequency at which the capacitive and resistive impedances are equal in magnitude, which occurs at 45° phase angle.

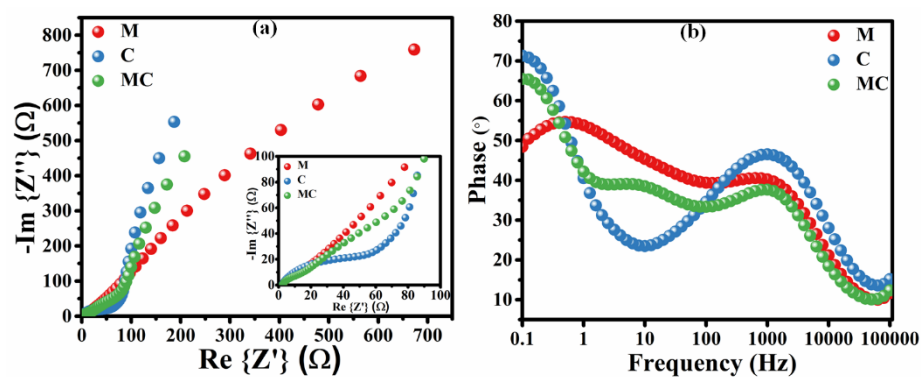


**Figure 2.15** (a) Nyquist plots for **M**, **C** and **MC** with magnification (inset) and (b) Bode plots for **M**, **C** and **MC**.

The  $45^\circ$  phase angle frequencies for **M**, **C**, and **MC** were measured to be 0.11, 0.54, and 0.74 Hz, corresponding to  $t_0$  values of 9.09, 1.85, and 1.35s, respectively. The smaller  $t_0$  value of **MC** compared to **M** and **C** highlights the significance of the synergy between **M** and **C**, causing better rate capability due to improved conductivity and lowered charge transfer resistance during the charge/discharge process. Overall, EIS investigations confirm **MC** composite is a promising material for energy storage, occurring combinedly via surface and diffusion processes.

The retention of performance and cyclic stability of the **MC** composite was assessed through 5000 galvanostatic charge-discharge (GCD) cycles at a current density of  $10 \text{ Ag}^{-1}$ . **Figure 2.16a** illustrates the change in specific capacitance of the **MC** composite at  $10 \text{ Ag}^{-1}$  as the cycle count increases, accompanied by GCD profiles for the initial and final five cycles (inset in **Figure 2.16a**). The results indicate that, even after 5000 cycles, the composite preserves 84.50% of its initial specific capacitance. Notably, there were no detectable traces of electrode material found in the electrolyte following the completion of the recycling experiment, ruling out electrode material stripping as the cause of capacitance reduction. Instead, this phenomenon is likely attributed to the irreversible adsorption of ions within the MOF framework during repeated cycling. Furthermore, a comparison of cyclic voltammograms between the fresh composite and the one subjected to 5000 cycles reveals only minor alterations in the CV profile, confirming the cyclic stability of the electrode material (**Figure 2.17**). This is further

supported by comparing the electrochemical impedance spectroscopy (EIS) of the fresh and recycled composite, which also shows no considerable change in the EIS profile (Nyquist plot (**Figure 2.16b**) and Bode plot (**inset Figure 2.16b**)).

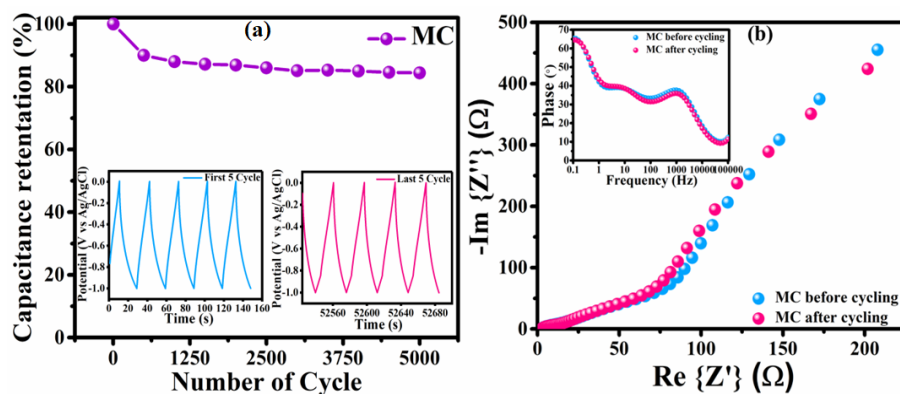


**Figure 2.16** (a) Cycling performance of MC at  $10 \text{ A.g}^{-1}$  for 5000 cycles (insets show first and last five cycles), (b & c) Nyquist and (inset) Bode plots of fresh MC after 5000.

To assess the morphological and compositional changes after 5000 cycles, field-emission scanning electron microscopy (FE-SEM) images, energy-dispersive X-ray spectroscopy (EDX) spectrum, and elemental mapping were recorded. The FE-SEM images reveal that the MC composite exhibits a slightly agglomerated morphology compared to the freshly prepared composite (**Figure 2.18a**). The EDX spectrum and elemental mapping confirm the presence of all the elements of the composite (Cu, O, and C) as well as the electrolyte element (K), confirming the compositional integrity of the electrode materials after multiple cycles (**Figure 2.18b, c**). These observations indicate the promising cyclic stability and structural integrity of the MC composite, making it suitable for practical applications.

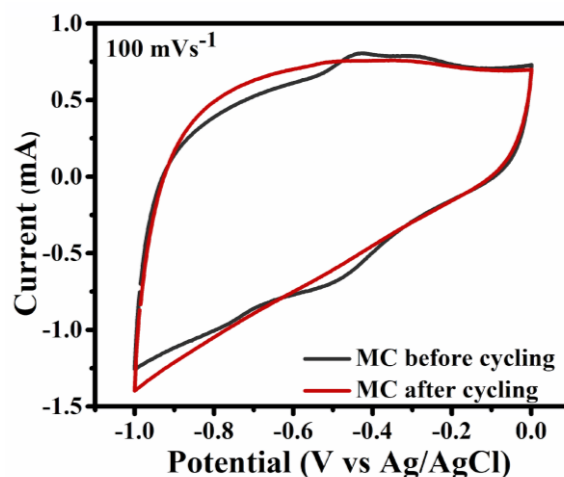


**Figure 2.17** CV profiles of MC before and after 5000 cycles at 100 mVs<sup>-1</sup>.

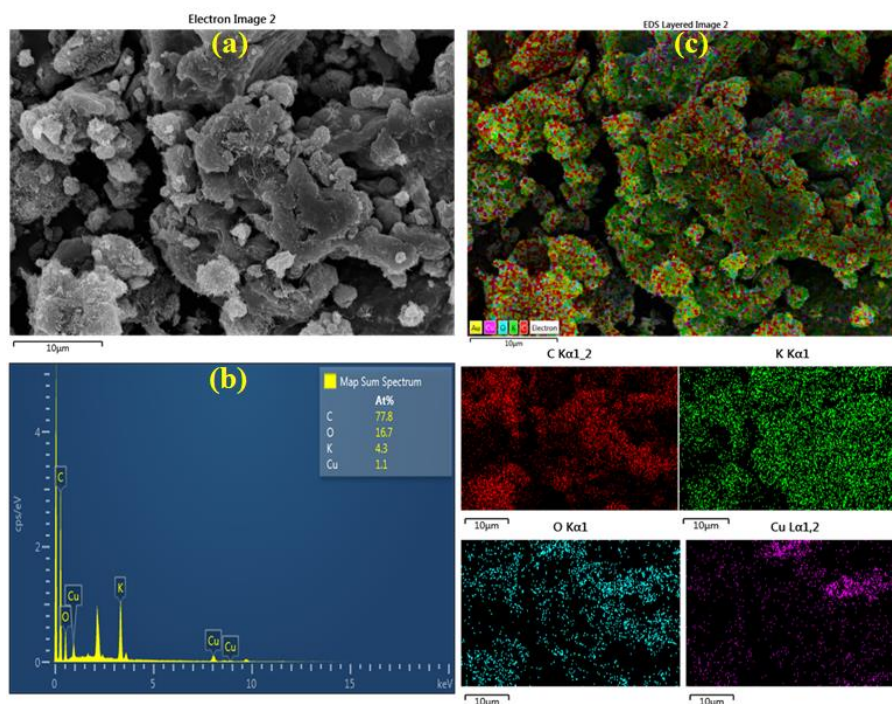


**Figure 2.18** (a) FE-SEM of MC after 5000 cycles (b,c) EDX and elemental mapping of MC after 5000 cycles.

To assess the practical applicability of the MC composite, a symmetric supercapacitor device was assembled using a cellulose membrane separator. The device was characterized in a two-electrode configuration with an optimum cell voltage of 1.0 V (**Figure 2.19**). CV curves of the device at various scan rates (10 to 100 mVs<sup>-1</sup>) were recorded. Except for the increase in current density, the shapes of the cyclic voltammogram are maintained at all scan rates (**Figure 2.19 a**),

suggesting the high-rate capability of the device. The GCD studies were conducted at different current densities (1.0 to 10  $\text{Ag}^{-1}$ ) to determine the specific capacitance of the device (**Figure 2.19 b**). The non-symmetric nature of the GCD curves suggests that the overall capacitance combines both EDLC and diffusion capacitances. The variation of specific capacitance of the device with increasing current density is given in **Figure 2.19c**, showing a maximum value of 152.79  $\text{Fg}^{-1}$  at 1  $\text{Ag}^{-1}$ , which is reduced to 47.7  $\text{Fg}^{-1}$  at 10  $\text{Ag}^{-1}$ . The cyclic stability of the device was evaluated by performing 10,000 GCD cycles at a current density of 10  $\text{Ag}^{-1}$  within the potential window of 0-1.0 V. The device exhibited a capacity retention of 90.07% after 10,000 cycles, demonstrating exceptional cyclic stability (**Figure 2.19 d**, the inset shows the first and last cycle).

A Ragone plot was constructed to analyze the energy density ( $E_d$ ) and power density ( $P_d$ ) of the symmetric supercapacitor device (**Figure 2.19 e**). The plot depicts the expected trend of increasing energy density with decreasing power density and vice versa. The device delivers a maximum energy density of 30.56  $\text{Whkg}^{-1}$  at a power density of 0.6  $\text{kWkg}^{-1}$  and a maximum power density of 12  $\text{kWkg}^{-1}$  at 14.59  $\text{Whkg}^{-1}$  energy density. To showcase the practical use of the device, two similar symmetric supercapacitor devices connected in series were demonstrated to power a red-light emitting diode (LED) and operate a DC motor fan (**Figure 2.19 f**). Overall, the MC composite-based supercapacitor device exhibited excellent electrochemical performance, including high-rate capability, cyclic stability, and desirable energy and power densities, making it suitable for practical applications. To compare the performance of the current electrode material with the previously reported MOF-CNT systems, a comparison of different performance parameters is given in **Table 6**. The table suggests that, in collective consideration of energy density, specific capacitance, and cyclic stability, the current MC electrode shows better supercapacitive performance than the previously reported similar systems.

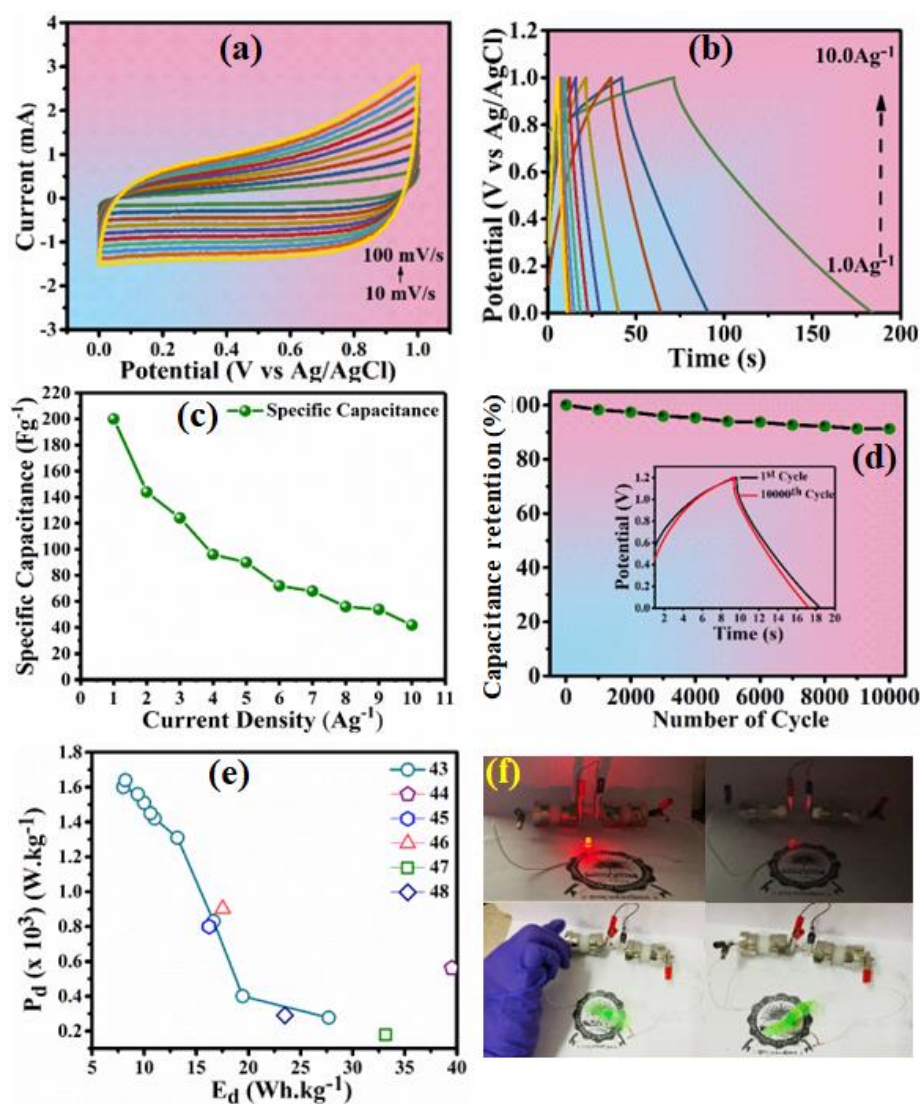


**Figure 2.19** (a) CV performance at different scan rates (b) GCD profiles at different current densities (1-10 Ag<sup>-1</sup>) (c) Specific capacitance variations with changing current densities. (d) Cycling stability of the device for 10000 consecutive cycles (insets show first and last cycle of the device), (e) Ragone plot (energy density vs. power density) of the fabricated device [36–41] (f) Glowing LED and running FAN using the fabricated device.

**Table 6.** Comparison table for efficiency in devices. [1–5]

<b>Electrode</b>	<b>Energy density(Wh Kg<sup>-1</sup>)</b>	<b>Specific capacity/capacitance</b>	<b>Cycling stability</b>	<b>Reference</b>
Cu-MOF/CNT	-	380 Fg <sup>-1</sup> @ 1.6 A g <sup>-1</sup>	63.63 %, 4000 cycles	1
Cu-MOF/CNT	23.6	166.4 Fg <sup>-1</sup> @ 1 A g <sup>-1</sup>	79.2 %, 10000 cycles	2
MOF(Ni)/CNT	32.6	97 Fg <sup>-1</sup> @ 0.5 A g <sup>-1</sup>	83.2 %, 5000 cycles	3
Ni-Co-MOF/MWCNT	20.2	120 Fg <sup>-1</sup> @ 1.0 A g <sup>-1</sup>	93%, 3000 cycles	4
Mn-NiMOF/CNT	33.2	793.6 F g <sup>-1</sup> @ 1 A g <sup>-1</sup>	78.3 %, 2000 cycles	5
Cu-MOF/CNT	<b>30.56</b>	<b>348.56 Fg<sup>-1</sup> @ 1 A g<sup>-1</sup></b>	<b>90.04%, 10000 cycles</b>	<b>This work</b>

## 2.6 Summary

In conclusion, this chapter demonstrates the potential of a synergistic electrochemical approach using CNT (**C**) interwoven Cu-MOF (**M**) for achieving high performance in solid-state supercapacitors. For supercapacitors, the **MC** composite exhibited excellent electrochemical properties, including high specific capacitance ( $348.62 \text{ F.g}^{-1}$  at  $1 \text{ A.g}^{-1}$ ) and good rate capability. The presence of **Cu-MOF** facilitated the redox reaction, while the **CNTs** provided excellent electronic conductivity and rapid ion transport. The symmetric device composed of **MC** showed high energy and power densities ( $30.56 \text{ Wh.kg}^{-1}$  and  $12 \text{ kW.kg}^{-1}$ ) with excellent cyclic stability, retaining 90.07% of its capacity after 10,000 charging-discharging cycles. The successful integration of Cu-MOF and CNTs in a synergistic manner led to the enhancement of supercapacitive performance compared to individual components. This approach offers a versatile and efficient solution for energy storage applications. The findings of this study contribute to the development of cost-effective, and high-performance electrochemical electrode materials.

## References

- [1] M.K. Singh, A.K. Gupta, S. Krishnan, N. Guha, S. Marimuthu, D.K. Rai, A new hierarchically porous Cu-MOF composited with rGO as an efficient hybrid supercapacitor electrode material, *Journal of Energy Storage* 43 (2021) 103301. <https://doi.org/10.1016/j.est.2021.103301>.
- [2] H. Sandhu, D. Gangacharyulu, An experimental study on stability and some thermophysical properties of multiwalled carbon nanotubes with water–ethylene glycol mixtures, *Particulate Science and Technology* 35 (2017) 547–554. <https://doi.org/10.1080/02726351.2016.1180335>.
- [3] S. Krishnan, S. Chatterjee, A. Solanki, N. Guha, M.K. Singh, A.K. Gupta, D.K. Rai, Aminotetrazole-Functionalized SiO<sub>2</sub> Coated MgO Nanoparticle Composites for Removal of Acid Fuchsin Dye and Detection of Heavy Metal Ions, *ACS Appl. Nano Mater.* 3 (2020) 11203–11216. <https://doi.org/10.1021/acsanm.0c02351>.
- [4] J.-X. Wu, C.-T. He, G.-R. Li, J.-P. Zhang, An inorganic-MOF-inorganic approach to ultrathin CuO decorated Cu–C hybrid nanorod arrays for an efficient oxygen evolution reaction, *J. Mater. Chem. A* 6 (2018) 19176–19181. <https://doi.org/10.1039/C8TA06069J>.
- [5] Q. Li, H. Guo, R. Xue, M. Wang, M. Xu, W. Yang, J. Zhang, W. Yang, Self-assembled Mo doped Ni-MOF nanosheets based electrode material for high performance battery-supercapacitor hybrid device, *International Journal of Hydrogen Energy* 45 (2020) 20820–20831. <https://doi.org/10.1016/j.ijhydene.2020.05.143>.
- [6] J. Chen, Y. Chen, S. Li, J. Yang, J. Dong, X. Lu, MXene/CNTs/Cu-MOF electrochemical probe for detecting tyrosine, *Carbon* 199 (2022) 110–118. <https://doi.org/10.1016/j.carbon.2022.07.021>.
- [7] T.V.M. Sreekanth, G.R. Dillip, P.C. Nagajyothi, K. Yoo, J. Kim, Integration of Marigold 3D flower-like Ni-MOF self-assembled on MWCNTs via microwave irradiation for high-performance

- electrocatalytic alcohol oxidation and oxygen evolution reactions, *Applied Catalysis B: Environmental* 285 (2021) 119793. <https://doi.org/10.1016/j.apcatb.2020.119793>.
- [8] H. Zhao, J. Sun, Y. Du, M. Zhang, Z. Yang, J. Su, X. Peng, X. Liu, G. Sun, Y. Cui, In-situ immobilization of CuMOF on sodium alginate/chitosan/cellulose nanofibril composite hydrogel for fast and highly efficient removal of Pb<sup>2+</sup> from aqueous solutions, *Journal of Solid-State Chemistry* 322 (2023) 123928. <https://doi.org/10.1016/j.jssc.2023.123928>.
- [9] J. Wang, M. Rao, C. Ye, Y. Qiu, W. Su, S. Zheng, J. Fan, S. Cai, W.-G. Zhang, Cu-MOF derived Cu-C nanocomposites towards high performance electrochemical supercapacitors, *RSC Adv.* 10 (2020) 4621–4629. <https://doi.org/10.1039/C9RA09738D>.
- [10] J. Sui, C. Zhang, D. Hong, J. Li, Q. Cheng, Z. Li, W. Cai, Facile synthesis of MWCNT–ZnFe<sub>2</sub>O<sub>4</sub> nanocomposites as anode materials for lithium ion batteries, *J. Mater. Chem.* 22 (2012) 13674. <https://doi.org/10.1039/c2jm31905e>.
- [11] J. Zhou, J. Lian, L. Hou, J. Zhang, H. Gou, M. Xia, Y. Zhao, T.A. Strobel, L. Tao, F. Gao, Ultrahigh volumetric capacitance and cyclic stability of fluorine and nitrogen co-doped carbon microspheres, *Nat Commun* 6 (2015) 8503. <https://doi.org/10.1038/ncomms9503>.
- [12] S. Jana, S. Saha, A. Chandra, S. El Fallah, S. Das, C. Sinha, A Cu(II) Metal Organic Framework with a Tetranuclear Core: Structure, Magnetism, and Supercapacitor Activity, *Crystal Growth & Design* 22 (2022) 1172–1181. <https://doi.org/10.1021/acs.cgd.1c01109>.
- [13] T. Qin, S. Dang, J. Hao, Z. Wang, H. Li, Y. Wen, S. Lu, D. He, G. Cao, S. Peng, Carbon fabric supported 3D cobalt oxides/hydroxide nanosheet network as cathode for flexible all-solid-state asymmetric supercapacitor, *Dalton Trans.* 47 (2018) 11503–11511. <https://doi.org/10.1039/C8DT02371A>.
- [14] W. Chen, X. Yu, Z. Zhao, S. Ji, L. Feng, Hierarchical architecture of coupling graphene and 2D WS<sub>2</sub> for high-performance

- supercapacitor, *Electrochimica Acta* 298 (2019) 313–320.  
<https://doi.org/10.1016/j.electacta.2018.12.096>.
- [15] S. Krishnan, A.K. Gupta, M.K. Singh, N. Guha, D.K. Rai, Nitrogen-rich Cu-MOF decorated on reduced graphene oxide nanosheets for hybrid supercapacitor applications with enhanced cycling stability, *Chemical Engineering Journal* 435 (2022) 135042. <https://doi.org/10.1016/j.cej.2022.135042>.
- [16] Z. Wu, L. Li, J. Yan, X. Zhang, *Materials Design and System Construction for Conventional and New-Concept Supercapacitors*, *Adv. Sci.* 4 (2017) 1600382. <https://doi.org/10.1002/advs.201600382>.
- [17] H. Peng, B. Yao, X. Wei, T. Liu, T. Kou, P. Xiao, Y. Zhang, Y. Li, Pore and Heteroatom Engineered Carbon Foams for Supercapacitors, *Adv. Energy Mater.* 9 (2019) 1803665. <https://doi.org/10.1002/aenm.201803665>.
- [18] S.C. Wechsler, F.Z. Amir, Superior Electrochemical Performance of Pristine Nickel Hexaaminobenzene MOF Supercapacitors Fabricated by Electrophoretic Deposition, *ChemSusChem* 13 (2020) 1491–1495. <https://doi.org/10.1002/cssc.201902691>.
- [19] U.A. Khan, N. Iqbal, T. Noor, R. Ahmad, A. Ahmad, J. Gao, Z. Amjad, A. Wahab, Cerium based metal organic framework derived composite with reduced graphene oxide as efficient supercapacitor electrode, *Journal of Energy Storage* 41 (2021) 102999. <https://doi.org/10.1016/j.est.2021.102999>.
- [20] A.A. Ensafi, R. Fazel, B. Rezaei, J.-S. Hu, Electrochemical properties of modified poly(4-aminothiophenol)-Zn-Ni MOF-reduced graphene oxide nanocomposite for high-performance supercapacitors, *Fuel* 324 (2022) 124724. <https://doi.org/10.1016/j.fuel.2022.124724>.
- [21] Q. Yang, R. Song, Y. Wang, X. Hu, Z. Chen, Z. Li, W. Tan, One-pot synthesis of Zr-MOFs on MWCNTs for high-performance electrochemical supercapacitor, *Colloids and Surfaces A: Physicochemical and Engineering Aspects* 631 (2021) 127665. <https://doi.org/10.1016/j.colsurfa.2021.127665>.

- [22] B. Ramasubramanian, C. Chinglenthoba, X. Huiqing, N. Xiping, H.K. Hui, S. Valiyaveetil, S. Ramakrishna, V. Chellappan, Sustainable Fe-MOF@carbon nanocomposite electrode for supercapacitor, *Surfaces and Interfaces* 34 (2022) 102397. <https://doi.org/10.1016/j.surfin.2022.102397>.
- [23] Significantly Enhanced Ultrathin NiCo-based MOF Nanosheet Electrodes Hybridized with Ti<sub>3</sub>C<sub>2</sub>T<sub>x</sub> MXene for High Performance Asymmetric Supercapacitors, *Eng. Sci.* (2020). <https://doi.org/10.30919/es8d903>.
- [24] P. Wen, P. Gong, J. Sun, J. Wang, S. Yang, Design and synthesis of Ni-MOF/CNT composites and rGO/carbon nitride composites for an asymmetric supercapacitor with high energy and power density, *J. Mater. Chem. A* 3 (2015) 13874–13883. <https://doi.org/10.1039/C5TA02461G>.



## Chapter 3

# NiO-rGO Heterostructures as Supercapattery: Bridging Battery and EDLC Behavior

### 3.1 Introduction

Our discussion on the development of ultra-efficient electrochemical energy storage in Section 2.1 of Chapter 1 highlights the need for electrochemical energy storage devices. From this discussion, it is evident that supercapacitors are vital electrochemical energy devices categorized into two types: Electrical double-layer capacitors (EDLCs) and pseudocapacitors. Lately, a third category, “supercapattery,” has been coined, featuring combined characteristics of batteries as well as supercapacitors.[1–5]

Among the various electroactive materials, transitional metal oxides are known to be ubiquitously employed as energy storage because they tend to exhibit reversible surface redox reactions, leading to improved energy density.[6,7] In this regard, the first-row transition metals (Fe, Co, Ni, and Mn) compounds, particularly, have been used as promising electrode materials[8–11] owing to their low cost, and environmentally benignancy. Among these, nickel-based materials, particularly nickel oxide, are well-established for energy storage [12]. Nickel oxide's exceptional attributes, including its high theoretical capacity, multiple oxidation states, abundance, easily attainable synthesis process, cyclic reversibility, and outstanding durability, make it a superior choice as an electrode for supercapacitors. Despite these positive characteristics, NiO's intrinsic inferior electronic conductivity compromises its efficacy as an electroactive material. To address this, many prudent approaches have been adopted to boost its efficiency,

which include compositionalization with conducting carbonaceous materials,[13] surface engineering[14], heteroatom doping[15], and heterostructure formation[16]. Among them, blending 2D carbonaceous materials such as graphene, rGO, graphitic carbon, carbon nanotubes, nitrogen, and phosphorous-doped carbon to obtain heterostructures is known to improve electron transport and overall stability.[17–19]

In particular, 2D carbonaceous layered nanostructures offer high accessible surface area, leading to diminished path length for charge carriers and, thereby, enhancing the charge storage performance.[20] Y Hu et al. synthesized an rGO composite with hydrothermally obtained NiO, which showed a specific capacitance of  $171.3 \text{ Fg}^{-1}$ . [21] A very high specific capacitance of  $1027.27 \text{ Fg}^{-1}$  was realized by Zhao et al. from a self-assembled Ni/NiO-rGO heterostructure.[22] Zhou et al. reported on the fabrication of a supercapacitor device using a NiO-rGO electrode with a specific capacitance of  $782 \text{ Fg}^{-1}$ . [23] In another work, Karuppuchamy et al. adopted microwave synthesis of CNT/NiO assembly and showed a specific capacitance of  $258 \text{ Fg}^{-1}$  [24]. Despite the progress achieved in synthesizing NiO and carbon materials composites, most of the resulting composite electrode materials have not been able to exhibit outstanding capacitance to be adopted for practical applications. Moreover, many previously reported materials require electrochemically inactive binders to function as stable electrodes, which compromises their specific charge storage capacity.

This chapter demonstrates the synthesis and application of **NiO-rGO** heterostructure as a supercapattery, which exhibits a remarkable specific capacity due to the efficient compositionalization of **NiO** (battery-type electrode) and **rGO** (EDLC type electrode) components. The synthesis of **NiO** has been done using a precipitation-aging-calcination approach starting with nickel carbonate ( $\text{NiCO}_3$ ) precipitate. Obtaining **NiO** by calcination of  $\text{NiCO}_3$  is advantageous over the hydrothermal approach as the removal of gaseous  $\text{CO}_2$  during calcination leaves a NiO structure with more pore density and higher specific surface area. Therefore, such structures are expected to feature better electrochemical

performances for the processes occurring at the electrode-electrolyte interface, such as supercapacitor charging-discharging. Although such approaches are reported for the synthesis of other metal oxides [25,26] it is the first attempt for **NiO** synthesis. To overcome the intrinsic lower conductivity of the **NiO**, the effective compositization of **NiO** and **rGO** has been achieved by ultrasonication. It leads to the disruption of interlayer of **rGO** causing suppression of restacking **rGO** layers resulting in increased specific surface area of the resulting **NiO-rGO** composite compared to its individual components. Moreover, the presence of **rGO** activates the  $\text{Ni}^{2+}$  redox centers in **NiO** by providing a conducting medium for electron transfer between **NiO** and the current collector. In this way, **rGO** facilitates the redox process and renders improved energy storage performance.

Owing to the above-mentioned attributes and synergistic effect of **NiO** and **rGO**, the reported binder-free **NiO-rGO** composite electrode material exhibits an ultra-high charge storage capacity of  $850 \text{ Cg}^{-1}$  at  $1 \text{ Ag}^{-1}$  with excellent capacity retention of 91% after 5000 charge/discharge cycles. Moreover, the assembled symmetric device shows a superior energy density ( $56.6 \text{ W h kg}^{-1}$ ) and power density ( $9.65 \text{ kW kg}^{-1}$ ) at an operating voltage window of 1.2V with stable performance up to 10000 charge/discharge cycles. Finally, the experimental data of charge storage capacity have also been rationalized and supported by the first principle DFT methods through investigation of ion-electrode interaction energetics. All results suggest that the as-synthesized **NiO-rGO** functions as an excellent electrode material for charge storage.

## 3.2 Experimental Section

### 3.2.1 Chemicals

Graphite flakes-99.5%, potassium permanganate ( $\text{KMnO}_4$ )-98%, sodium nitrate ( $\text{NaNO}_3$ )-99%, hydrogen peroxide ( $\text{H}_2\text{O}_2$ )-35%, and hydrochloric acid ( $\text{HCl}$ )-35% were purchased from SRL Chemical and TCI Chemical. Sodium carbonate ( $\text{Na}_2\text{CO}_3$ )-94% and nickel

chloride hexahydrate ( $\text{NiCl}_2 \cdot 6\text{H}_2\text{O}$ )-98% were purchased from Advent Biochemicals. Throughout the synthesis, deionized water (Millipore DI water,  $18.2 \text{ M}\Omega\text{cm}^{-1}$ ) was used. The digital ultrasonic cleaner of LMUC SERIES (Labman Scientific Instruments) was used throughout the experiment.

### 3.2.2 Synthesis of reduced graphene oxide (rGO)

Synthesis of reduced graphene oxide (rGO) was done using previously reported literature[27] and elaborated as:

The synthesis of graphene oxide and reduced graphene oxide (R) were done using the modified Hummer's method. Graphite with an average flake size of  $\leq 35 \mu\text{m}$  was used to synthesize GO using modified Hummer's Method. In this method, 2g of graphite was mixed with 1g of  $\text{NaNO}_3$  and then added to 60 mL of sulfuric acid ( $\text{H}_2\text{SO}_4$ , 98 %) in a 100 mL beaker kept on an ice bath. Subsequently, 6g  $\text{KMnO}_4$  was added slowly with vigorous stirring while maintaining the temperature between 5- 10 °C. After continuously stirring the mixture for 6 h, the mixture turned viscous and brownish. Afterwards, the addition of 100 mL of DI water followed by 10 mL of  $\text{H}_2\text{O}_2$  (30 wt% aqueous solution) was done slowly. The GO thus obtained was filtered and washed using DI water and ethanol. The as-synthesized GO was dried in a vacuum oven for 6 h to get the dry powder.

For reduction of GO to obtain rGO, 100 mg of GO was dispersed in 10mL DI water. To this dispersion, a solution of 1g of  $\text{NaBH}_4$  in 6 mL DI water was added gradually, and the resulting mixture was refluxed for 24 h. Afterward, the product was filtered and washed thoroughly with DI water and ethanol and dried in a vacuum oven.

### 3.2.3 Synthesis of nickel oxide (NiO)

NiO nanoparticles were synthesized by optimizing the precipitation-aging-calcination technique. The details of the optimization of aging time and calcination temperature are given in the supplementary information. In this approach, 12.5 mL of 1M  $\text{Na}_2\text{CO}_3$

aqueous solution was dropwise added (2 drops/second flow rate) to another 12.5 mL of 1M aqueous solution of  $\text{NiCl}_2 \cdot 6\text{H}_2\text{O}$ , which resulted in a green precipitate. The resulting precipitate-containing reaction mixture- was kept in a hot air oven for aging for 2 h at 80 °C. Afterward, the reaction mixture was allowed to cool to room temperature and the precipitate was washed several times with deionized water and ethanol by centrifugation. Finally, the green powder was transferred to a ceramic boat and kept in a muffle furnace for calcination at 500 °C for 5 h, which led to the formation of highly crystalline NiO particles.

### **3.2.4 Synthesis of nickel oxide-reduced graphene oxide (NiO-rGO) Composite**

NiO-rGO composites of three different compositions were prepared by taking different weight proportions of NiO and rGO (1:3, 1:1, and 3:1). For the synthesis of the composite, 40 mg of NiO and rGO mixture were taken in the desired proportion, and the mixture was pulverized in a mortar and pestle. Subsequently, the mixture was dispersed in a 5 mL reaction vessel containing 3 mL of ethanol and subjected to ultrasonication at room temperature for 1 h using a frequency of 33kHz at 60W power. The resulting suspension was kept in the oven to obtain the composite.

### **3.2.5 Preparation of Electrodes for Electrochemical Testing**

First, 1 x 3 cm<sup>2</sup> Ni-Foam strips were cleaned three times with DI water and ethanol using ultrasonication (PCi Analytics) for 30 min. Subsequently, all the strips were baked at 60°C overnight in an electric oven. The slurries of electrode materials were prepared by dispersing 10 mg of electrode materials in 1 mL of ethanol and kept under sonication for 2 h. Finally, the as-obtained slurry was uniformly coated on 1x1 cm<sup>2</sup> portion of the cleaned Ni-Foam and then dried in a vacuum oven for 4 h. All electrochemical measurements were carried out in a 1 M KOH electrolyte solution.

## 3.3 Characterization

### 3.3.1 Physiochemical Characterization

Powder X-ray diffraction (PXRD) patterns were recorded on an X-ray diffractometer (Bruker's AXA D8 Advance system) having monochromatic Cu K $\alpha$  radiation (1.54 Å) in the 2 $\theta$  range of 5 to 80° at a scanning rate of 0.02° min<sup>-1</sup>. Raman spectra were recorded at room temperature with a Horiba LabRam HR evolution spectrometer. To understand the sample's phase characteristics and stability, thermogravimetric analyses (TGA) were carried out on Perkin-Elmer gravimetric analyzer instrument under an N<sub>2</sub> atmosphere from room temperature to 1200 °C with a heating rate of 10 °C/min. Nitrogen gas adsorption/desorption isotherms were recorded on an Autosorb iQ apparatus, version 1.11 (Quanta chrome Instruments). Morphological and elemental analyses were done using field emission scanning electron microscopy (FE-SEM) (JEOL -7610F Plus) equipped with Energy Dispersive Spectroscopy (EDS). Transmission electron microscopy (TEM) was done using FEI TECNAI 20 at an operating voltage of 200 kV.

### 3.3.2 Electrochemical Characterization

**Charge storage Studies:** All electrochemical testing was performed on a computer controlled Autolab PGSTAT 204N using NOVA software (version 1.10) at room temperature. Three electrode configurations were utilized, which included Ag/AgCl as a reference electrode, platinum as a counter electrode, and Ni-Foam coated with the electrode material as a working electrode. Cyclic voltammetry (CV) and galvanostatic charge/discharge (GCD) studies at different scan rates and current densities were performed in the potential range of 0 to 0.6 V. Electrochemical impedance spectroscopy (EIS) studies were performed in a frequency range of 10 mHz to 100 kHz with 10 mV AC amplitude. Calculations of the specific capacities were done utilizing discharging curve of GCD using the following equation:

$$C = \frac{I \Delta t}{m} \quad (1)$$

Where  $C$  is specific capacity ( $\text{Cg}^{-1}$ ),  $I$  is current (A),  $\Delta t$  is the discharge time (s),  $m$  is mass of the coated active material (g).

**Solid-state device fabrication:** Specific capacity, energy density (E), and power density (P) of the fabricated device were calculated from the GCD curves using the following equations.[28]

$$C = \frac{2I \Delta t}{m} \quad (2)$$

$$E \left( \frac{\text{Wh}}{\text{kg}} \right) = \frac{0.5 \times C \Delta V}{3.6} \quad (3)$$

$$P \left( \frac{\text{W}}{\text{kg}} \right) = \frac{3600 \times E}{\Delta t} \quad (4)$$

Where  $C$  is specific capacity ( $\text{C.g}^{-1}$ ),  $I$  is current (A),  $\Delta t$  is the discharge time (s),  $m$  is mass of the coated active material (g), and  $\Delta V$  is the potential range.

### 3.3.3 Computational Study

Theoretical investigations have been carried out using the Vienna ab initio simulation package (VASP) for density functional theory (DFT) based first-principles electronic structure calculations.[29,30] For electronic and structural optimizations, generalized gradient approximation (GGA) with projector-augmented wave (PAW) potentials have been considered. [31]The energy convergence criteria were fixed to  $10^{-4}$  eV, and the plane wave basis sets were taken as 450 eV of energy cut-off. The geometry optimization force convergence criteria were taken as 0.03 eV/ Å. The K point grid of  $2 \times 2 \times 1$  was taken for geometry relaxations, while for electronic properties, K point meshes were further increased to  $10 \times 10 \times 1$ .

## 3.4 Results and discussion

### 3.4.1 Synthesis

The NiO nanoparticles were synthesized by calcination of the aged nickel carbonate ( $\text{NiCO}_3$ ) precipitate obtained by the reaction of

nickel chloride ( $\text{NiCl}_2$ ) and sodium carbonate ( $\text{Na}_2\text{CO}_3$ ). The formation of  $\text{NiCO}_3$  was confirmed by PXRD, which matches very well with JCPDS No. 12-0771 (**Figure 3.1**).[32] The aging of  $\text{NiCO}_3$  precipitate allows the growth of the particles, while the subsequent calcination causes  $\text{CO}_2$  removal, leaving **NiO** nanoparticles with high porosity. The duration of aging and calcination temperature play an important role in getting **NiO** of superior performance. The optimization of aging time and calcination temperature reveals that **NiO** obtained from 2 h aging of  $\text{NiCO}_3$  and subsequent calcination at  $500\text{ }^\circ\text{C}$  features the best charge storage performance (**Figure 3.2**). The overall reaction for the formation of **NiO** can be given by the following reaction:

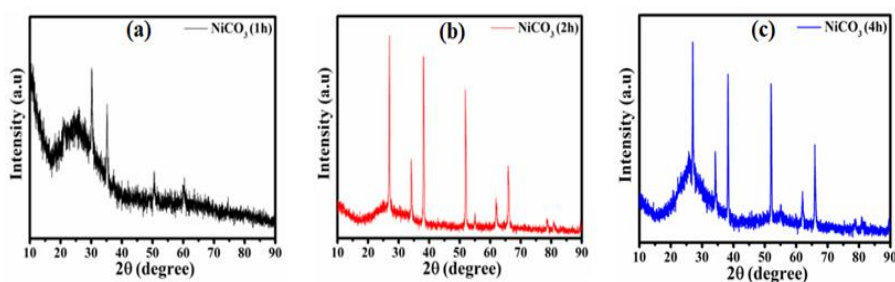
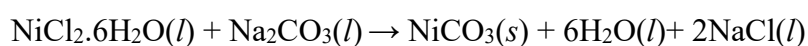


**Figure 3.1** Comparison of PXRD patterns of  $\text{NiCO}_3$  at different aging time.

The compositionalization of **NiO** and **rGO** was achieved by ultrasonication of an ethanol suspension containing both components (**Scheme 1**). The cavitation effect caused by ultrasonic treatment disrupts the interlayer interactions of the **rGO** sheets and facilitates the interaction of **NiO** particles on **rGO** sheets. The structural, morphological, and electrochemical characterizations of the as-synthesized **NiO**, **rGO**, and **NiO-rGO** heterostructures were done using different characterization techniques.

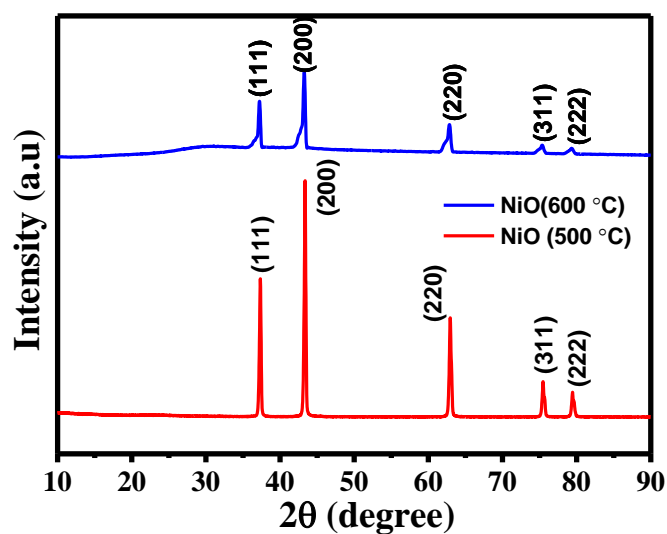
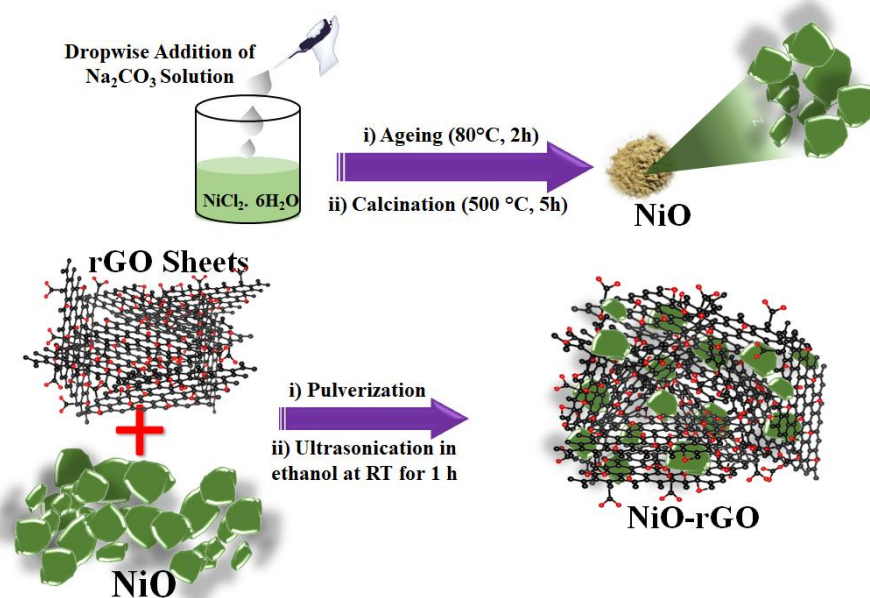


**Figure 3.2** Comparison of PXRD patterns of NiO at different calcination temperatures.



**Scheme 1.** Synthesis of NiO and NiO-rGO

### 3.4.2 Structural, Physical and Morphological Characterization

Crystallinity and phase analysis of NiO, rGO, and NiO-rGO were examined using Powder X-ray diffraction (PXRD) analysis in the range 5-80° (Figure 3.3a). For pure NiO, the sharp diffraction peaks can

be indexed as (111), (200), (220), (311) and (222) crystal planes of the face-centered-cubic **NiO** phase (JCPDS Card No- 78-0643) without any impurity.[33] For **rGO**, peaks located at  $2\theta \approx 24.24^\circ$  and  $42.83^\circ$  correspond to (002) and (100) planes. [34]In the case of **NiO-rGO**, the PXRD pattern shows the presence of the peaks from both **NiO** and **rGO**, indicating the successful compositionalization of the two components. Overall, the PXRD data confirms the successful formation of **NiO-rGO** heterostructures.

Raman Spectroscopy provides a better understanding of different vibrational frequencies in the materials (**Figure 3.3b**). Raman spectrum of **NiO** reveals a characteristic band of pristine **NiO** at  $600 \text{ cm}^{-1}$  that relates to the first order longitudinal optical phonon mode (1P) of Ni-O lattice vibration mode while the peak at  $1545 \text{ cm}^{-1}$  is ascribed to magneton mode (2M) of **NiO**. [35] Similar to most of the carbonaceous material, **rGO** displays two major Raman-active modes of vibration at low frequency; an  $A_{1g}$  mode around  $\sim 1350 \text{ cm}^{-1}$  (D band), and a high-frequency  $E_{2g}$  mode around  $\sim 1580 \text{ cm}^{-1}$  (G band). [36] Raman Spectrum of **NiO-rGO** includes all the vibrational modes related to **NiO** and **rGO**, confirming the heterostructure formation. The calculated  $I_D/I_G$  ratio of **NiO-rGO** composite is higher (1.56) as compared to **rGO** (1.50), indicating more disordering of composite structure because of disruption of **rGO** layer due to ultrasonication.

The thermal stabilities of **NiO**, **rGO**, and **NiO-rGO** were studied by thermogravimetric analysis (TGA) under  $N_2$  atmosphere from 30 to  $1200^\circ\text{C}$  (**Figure 3.3c-e**). In the case of **NiO**, only one small weight loss of 1.25 % is observed because of the loss of water molecules. The TGA profile of **rGO** shows a typical three weight loss steps. The first weight loss of 4.5% up to  $180^\circ\text{C}$  corresponds to the desorption of adsorbed water. The second (6.5% up to  $\sim 800^\circ\text{C}$ ) and third (30% up to  $1200^\circ\text{C}$ ) weight loss steps correspond to the decomposition of organic functionalities and carbon network of **rGO**, respectively. The TGA profile of **NiO-rGO** heterostructure shows a combined decomposition behavior of both **NiO** and **rGO** with three-step weight loss (1: upto

120°C (3.0%), 2: upto 705°C (5%), and 3: upto 1200°C (29%)). For supercapacitor applications, the specific surface area of the electrode material is an important consideration. Therefore, specific surface areas of as prepared **NiO**, **rGO**, and **NiO-rGO** were examined using N<sub>2</sub> adsorption-desorption isotherm at 77K (**Figure 3.3f-h**). Their N<sub>2</sub> adsorption isotherms match with Type-IV BET classification. [37] The calculated BET surface areas of pure **NiO**, **rGO**, and **NiO-rGO** were found to be 5.38 m<sup>2</sup>/g, 54.82 m<sup>2</sup>/g, and 68.91 m<sup>2</sup>/g, respectively. In most reports, the specific surface area of a composite is observed to be a gravimetric average of the specific surface areas of the individual components. [38] However, in the present case, **NiO-rGO** specific surface area was found to be more than the sum of **NiO** and **rGO**, which is a rare observation. This is perhaps due to disruption in the layered rGO structure due to the ultrasonication, which allows effective interaction with **NiO**, preventing restacking of the rGO layer and thereby exposing the inaccessible portion of the **rGO** surface for N<sub>2</sub> adsorption. Moreover, such arrangements also thwart the agglomeration of **NiO** particles. Collectively, these two effects considerably increase the specific surface area of the composite compared to its components and thereby render improved electrochemical performances.

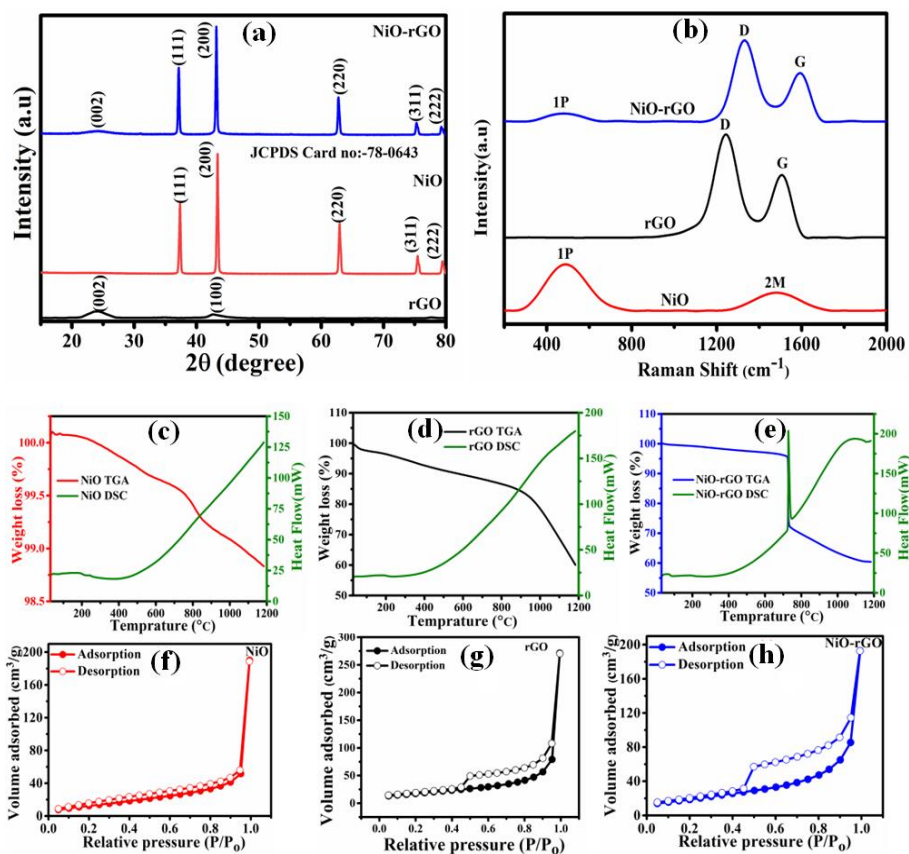


**Figure 3.3** (a) PXRD patterns of NiO, rGO, and NiO-rGO (b) Raman Spectra of NiO, rGO, and NiO-rGO (c,d,e) TGA and DSC curve of

Morphological investigations were performed using FE-SEM and TEM. FE-SEM micrographs of NiO, rGO, and NiO-rGO are depicted in **Figure 3.4a-c**. It is observed that NiO forms nanoparticles of the quasi-spherical shape of varying sizes (**Figure 3.4a**). The rGO micrograph reveals a layered sheet structure with exfoliated edges (**Figure 3.4b**). In the case of composite, NiO nanoparticles dispersed throughout the rGO surface as well as along the exfoliated edges of the sheets can be clearly seen (**Figure 3.4c**). The TEM images of NiO, rGO, and NiO-rGO are given in **Figure 3.4f-h**, showing NiO particles and a transparent sheet of rGO. For the NiO-rGO composite, the presence of NiO nanoparticles on rGO sheets is clearly visible (**Figure 3.4h**). The high-resolution TEM images of NiO, rGO, and NiO-rGO and their corresponding SAED patterns were also examined (**Figure 3.4 i-k**).

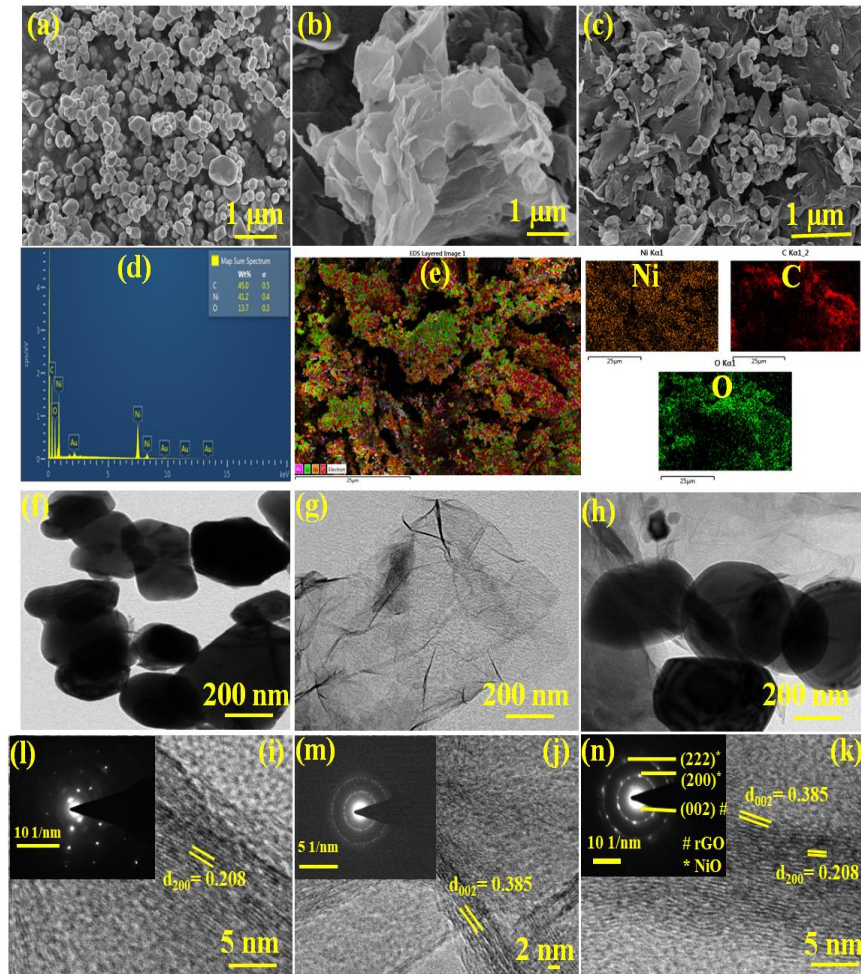


**Figure 3.4** FE-SEM of (a) **NiO** (b) **rGO** and (c) **NiO-rGO** (d) EDX spectra of **NiO-rGO** and (e) Mapping of Ni, C, and O elements in **NiO-rGO** composite. TEM of (f) **NiO** and (g) **rGO** (h) **NiO-rGO** (i-k) HRTEM and corresponding SAED pattern (inset) of **NiO**, **rGO** and **NiO-rGO**.

The observed interplanar spacing (d) value of 0.208 nm for **NiO** corresponds to its 200 planes, while that of **rGO** at 0.385 nm relates to its 002 planes. In the case of **NiO-rGO** composite, the d values corresponding to both of its components were observed. The SAED pattern of **NiO** exhibits multiple diffraction lines denoting its polycrystalline nature, while that of **rGO** reveals diffused rings, suggesting its disordered structure. For the **NiO-rGO** composite, the SAED pattern shows a characteristic of **NiO** as well as **rGO**, suggesting a combined nature of crystalline as well as an amorphous structure.

### 3.4.3 Electrochemical Properties

#### 3.4.3.1 Charge storage study.

The usefulness of as-synthesized **NiO-rGO** heterostructures towards charge storage application has been analyzed by three-electrode cell configuration and solid-state device using **NiO-rGO** modified Ni-Foam electrode. Prior to the extensive electrochemical study, potential window optimization was done to achieve the best performance. In this regard, we have performed cyclic voltammetry (CV) and galvanostatic charge-discharge (GCD) studies in positive and negative potential ranges (**Figure 3.5**). The observed cyclic voltammogram area as well as the GCD discharge time in the positive potential range were found to be significantly higher than those recorded in the negative potential range. This observation confirms the suitability of the electrode material for a positive potential range. The observed cyclic voltammogram area as well as the GCD discharge time in the positive potential range were found to be significantly higher than those recorded in the negative potential range. This observation confirms the suitability of the electrode material for a positive potential range. Further, to achieve the suitable mass ratio of **rGO** and **NiO** for the best charge storage performance, three relative ratios of 3:1, 1:1, and 1:3 of **rGO** and **NiO**, respectively, were studied. The CV studies of three different ratios reveal the highest voltammogram area for the 1:1 ratio, suggesting an equal proportion of **NiO** and **rGO** to be the most appropriate composition for the best composite performance (**Figure 3.6**). The best performance for this particular composition may be attributed to an appropriate balance of conductivity, imparted from **rGO**, and redox-active sites for high charge storage, offered by **NiO**, in the resulting composite. Therefore, for further detailed electrochemical studies, the heterostructure having a 1:1 ratio has been chosen.

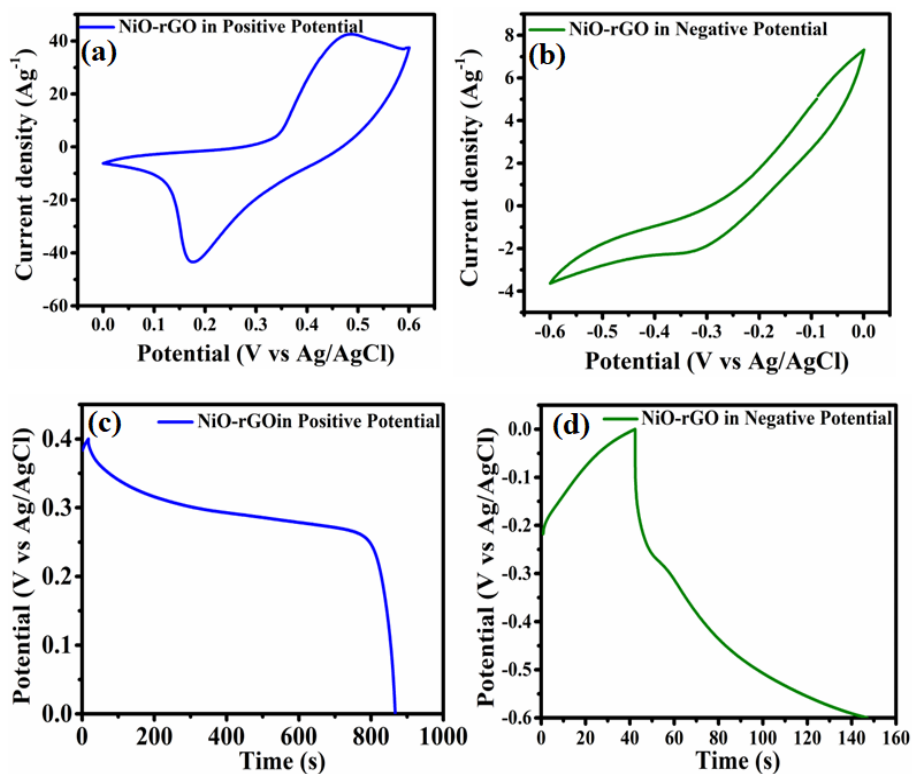


**Figure 3.5** CV and GCD profiles of NiO-rGO in Positive and Negative Potential range at  $50 \text{ mVs}^{-1}$

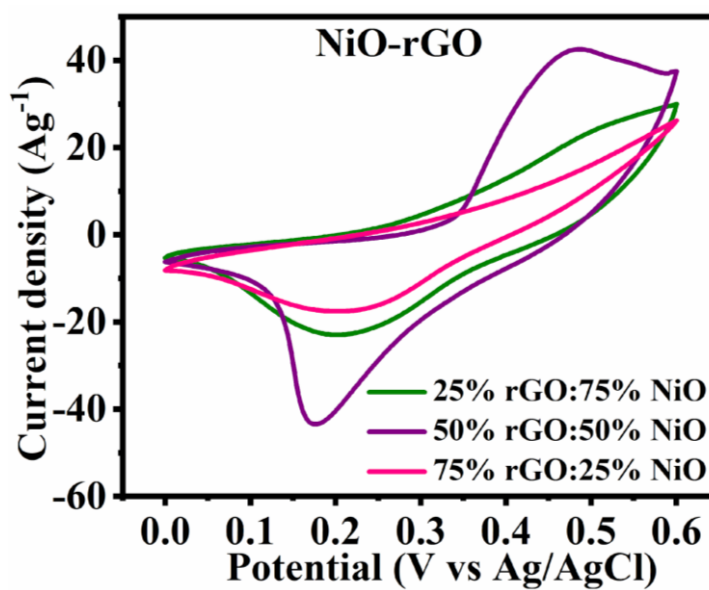


**Figure 3.6** CV profiles of composite with three different ratios of components at  $50 \text{ mVs}^{-1}$

The cyclic voltammetry of bare Ni-Foam was also investigated to know the contribution of Ni-Foam (**Figure 3.7**). Compared to the NiO-rGO composite, the bare Ni-Foam showed a very less current value,

corroborating that the active coated material is the sole contributor to the overall performance.

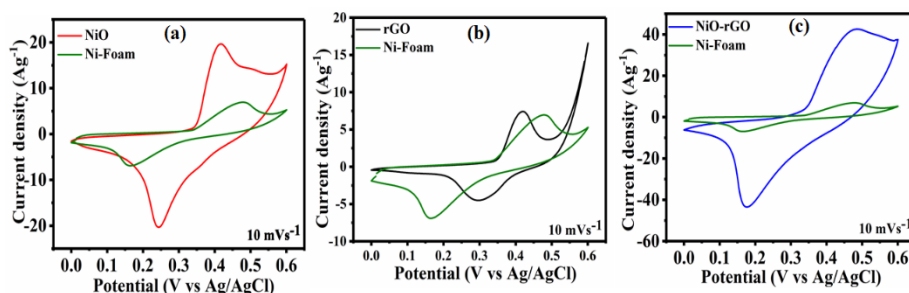
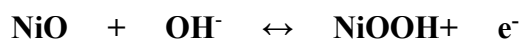


**Figure 3.7** CV profile comparison of Ni-Foam with (a) **NiO**, (b) **rGO**, and (c) **NiO-rGO** at  $10 \text{ mVs}^{-1}$  scan rate.

The systematic charge storage behavior of each electrode material was studied by cyclic voltammetry. CV curves comparison of **NiO**, **rGO**, and **NiO-rGO** at  $10 \text{ mVs}^{-1}$  scan rate is shown in **Figure 3.8a**.

The CV profiles of **NiO** and **NiO-rGO** show a typical pattern of a battery-type electrode with well-discernable anodic and cathodic peaks arising from  $\text{Ni}^{2+}$  centers.[39,40] The redox peaks in **NiO-rGO** are relatively broader compared to pure **NiO**, indicating that the **NiO-rGO** also has a contribution from EDLC behavior in the total capacity. The observed redox peak in the case of **rGO** is due to the underlying Ni-Foam, otherwise, it should show a rectangular pattern, typical of a supercapacitor.

The redox peaks in **NiO** and **NiO-rGO** correspond to the following electrochemical reaction of **NiO** in an aqueous KOH electrolyte, involving a reversible  $\text{Ni}^{2+}/\text{Ni}^{3+}$  redox couple.[41]



(6)

Among the three electrode materials, **NiO-rGO** exhibits maximum current response and CV area. This high performance is due to the synergistic effect of **NiO** and **rGO**. In this synergism, **rGO** renders high surface area and conductivity, thereby, enhancing the ions accessibility to the electrode and boosting the charge transfer.[42] On

the other hand, **NiO** provides redox activity for improved charge storage and energy density.

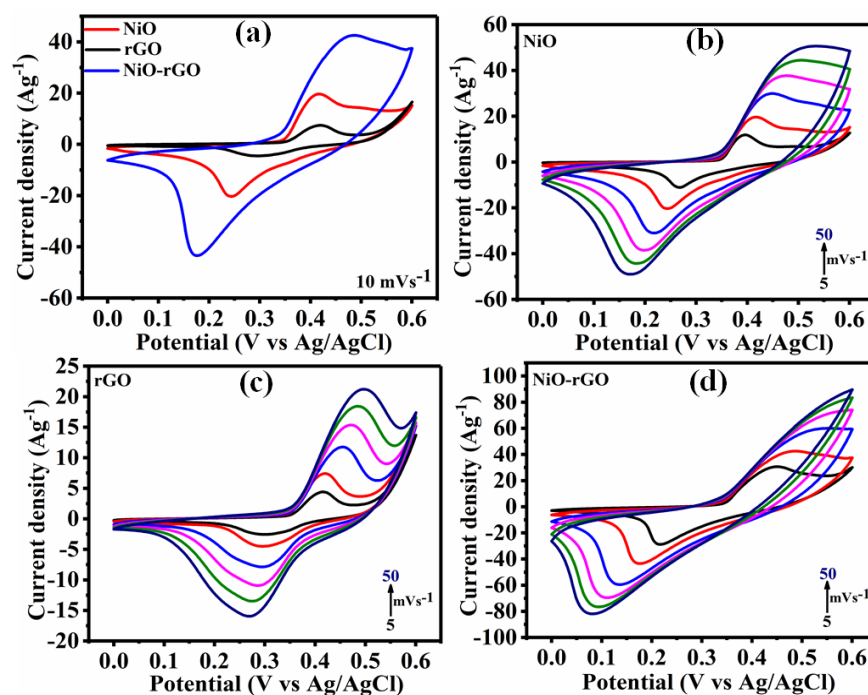


**Figure 3.8** (a) Comparison of CVs of **NiO**, **rGO**, and **NiO-rGO** at 10 mV.s<sup>-1</sup> scan rate in 1M KOH; (b,c,d) CV profiles of the **NiO**, **rGO**, and **NiO-rGO** at different scan rates (5-50 mV.s<sup>-1</sup>).

To understand the charge storage mechanism in **NiO**, **rGO**, and **NiO-rGO** electrodes, their cyclic voltammetry studies were performed at varying scan rates ranging from 5-50 mV.s<sup>-1</sup> (**Figure 3.8b-d**). All three materials show an increase in the current with increasing scan rates. Moreover, increasing the scan rate also causes separation between anodic and cathodic peaks due to the internal resistance of the electrodes and diffusion limitation, characteristics of battery-type electrodes.[43] The charge storage mechanisms in each electrode were assessed using the Power law. The *b* values for **NiO**, **rGO**, and **NiO-rGO** are given in **Figure 3.9a-c**, giving their respective *b* values of 0.47, 0.67, and 0.61. A comparison of *b* values suggests that, in **NiO**, charge storage is mainly controlled by diffusion; however, **rGO** has a dominant surface-controlled character. Despite having EDLC-type charge storage, the reason for **rGO** not showing a *b* value close to 1 is because of the redox-active Ni-Foam substrate. In the case of **NiO-rGO**, the *b* value is

observed to be in between its components **NiO** and **rGO**, suggesting a combined diffusion and surface-controlled charge storage mechanism. As **NiO-rGO** features a combined battery and supercapacitor-type charge storage, it is appropriate to term it as a supercapattery-type electrode.

The quantification of the surface and the diffusion-controlled charge storage contribution to the overall specific capacity of **NiO-rGO** was calculated using the Dunn's method. The percentage charge storage capacity contribution in **NiO-rGO** due to the two processes at three different scan rates is shown in **Figure 3.9d-f**. It is evident that the charge storage due to the diffusion process to the overall capacity is much higher than the surface process at all scan rates, indicating that **NiO-rGO** shows dominant battery-type features. Moreover, the contribution from diffusion-controlled processes decreases with the increasing scan rates because of the limitation of diffusion rate at higher scan rates. For the comparison, contributions of surface and diffusion-controlled processes to the overall CV profile of **NiO-rGO** at 5 mVs<sup>-1</sup> and 20 mVs<sup>-1</sup> are given in **Figure 3.9e&f**.

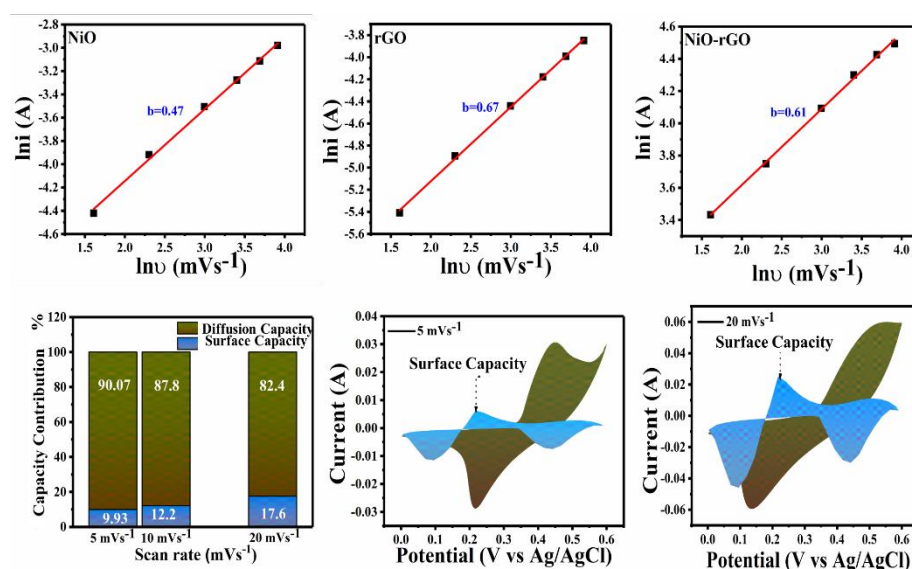


**Figure 3.9 (a-f).** Charge storage kinetics:  $\ln i$  vs.  $\ln v$  plots of (a) **NiO**, (b) **rGO**, and (c) **NiO-rGO**. The slope of each plot represents the value of  $b$  and (d) Percentage surface and diffusion-controlled capacity contributions at different scan rates to the overall capacity of **NiO-rGO**;

(e, f) Contributions of surface and diffusion-controlled processes to the overall CV profile of **NiO-rGO** at  $5 \text{ mVs}^{-1}$  and  $20 \text{ mVs}^{-1}$ .

Galvanostatic charge-discharge (GCD) studies were performed for **NiO**, **rGO** and **NiO-rGO** in the potential window of 0 to 0.4 V at different current densities ( $1.0 \text{ Ag}^{-1}$  to  $5 \text{ Ag}^{-1}$ ) to evaluate their specific capacities. The comparison of the GCD profiles of **NiO**, **rGO** and **NiO-rGO** at a current density of  $1 \text{ Ag}^{-1}$  is shown in **Figure 3.10a**. From the discharge time responses, specific capacities of **NiO**, **rGO** and **NiO-rGO** were calculated to be  $23 \text{ Cg}^{-1}$ ,  $184.8 \text{ Cg}^{-1}$ , and  $612 \text{ Cg}^{-1}$  respectively, at  $1 \text{ Ag}^{-1}$  current density. The bar chart of the measured specific capacities of different electrode materials (**Figure 3.10b**) shows that the specific capacity of **NiO-rGO** is more than four-fold of the sum of its constituents (**NiO** and **rGO**) specific capacities. Such an outstanding augmentation in the performance of the composite is due to extensive synergy between its **NiO** and **rGO** individual components. This ultimately leads to faster ion diffusion, increased charge transfer kinetics, and rate capability.[45] A detailed comparison of the charge storage performance of the present **NiO-rGO** composite with recently reported various metal-oxide-carbonaceous composites is given in **Table 7**, showing the much better performance of the present **NiO-rGO** compared to other composites.

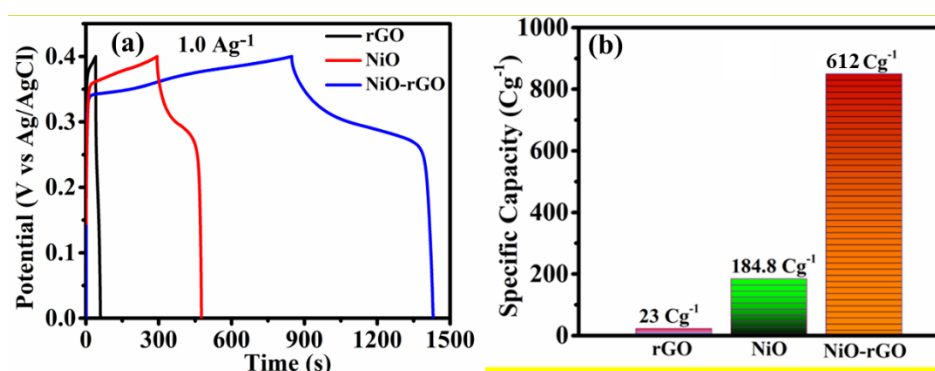


**Figure 3.10** (a) Comparison of GCD and Specific capacity of **NiO**, **rGO**, and **NiO-rGO** at a current density of  $1 \text{ Ag}^{-1}$  in  $1 \text{ M KOH}$ .

**Table 7.** Comparison table of the charge storage performance of the present NiO-rGO with various metal-oxide carbonaceous composites

Electrode material	Synthetic conditions	Electrolytes	Specific capacitance
Co <sub>3</sub> O <sub>4</sub> /rGO	Hydrothermal	3M KOH	754 F/g
rGO/Co <sub>3</sub> O <sub>4</sub>	Hydrothermal	1M H <sub>2</sub> SO <sub>4</sub>	278 F/g
CNT/CuO	CVD followed by Sonication	6M KOH	60 F/g
GO/CuO	Coprecipitation	1M Na <sub>2</sub> SO <sub>4</sub>	245 F/g
rGO/CuO/PANI	Single-step Chemical method	1M KOH	684.93 F/g

CO <sub>3</sub> O <sub>4</sub> /MWCNT	Coprecipitation followed by simple heat treatment	2M KOH	418 F/g
CO <sub>3</sub> O <sub>4</sub> /C	Precipitation	1M KOH	567 F/g
Fe <sub>3</sub> O <sub>4</sub> /rGO	Chemical reduction	6M KOH	416 F/g
Fe <sub>3</sub> O <sub>4</sub> /2D carbon Sheets	Green synthesis	3M KOH	820 F/g
ZnO/rGO	Chemical reduction method	0.1M Na <sub>2</sub> SO <sub>4</sub>	280 F/g
ZnO/rGO	Hydrothermal	1.0 M Na <sub>2</sub> SO <sub>4</sub>	275 F/g
Fe <sub>3</sub> O <sub>4</sub> /CNT	Solvothermal	1.0 M Na <sub>2</sub> SO <sub>4</sub>	145.4 F/g
MoO <sub>3</sub> /rGO	Ultrasonication	1M KOH	331.0 F/g
MnO <sub>2</sub> /rGO	Microwave	1M KOH	140.3 F/g
MnO <sub>2</sub> /CNT	Electrodeposition	1M KOH	2539m F/cm <sup>2</sup>
<b>NiO/rGO</b>	Precipitation- Ageing- calcination Technique	1M KOH	2125 F/g* (850 Cg <sup>-1</sup> )

---

\*\*Here the calculated specific capacity value for **NiO/rGO** is converted into specific capacitance for the sake of comparison.

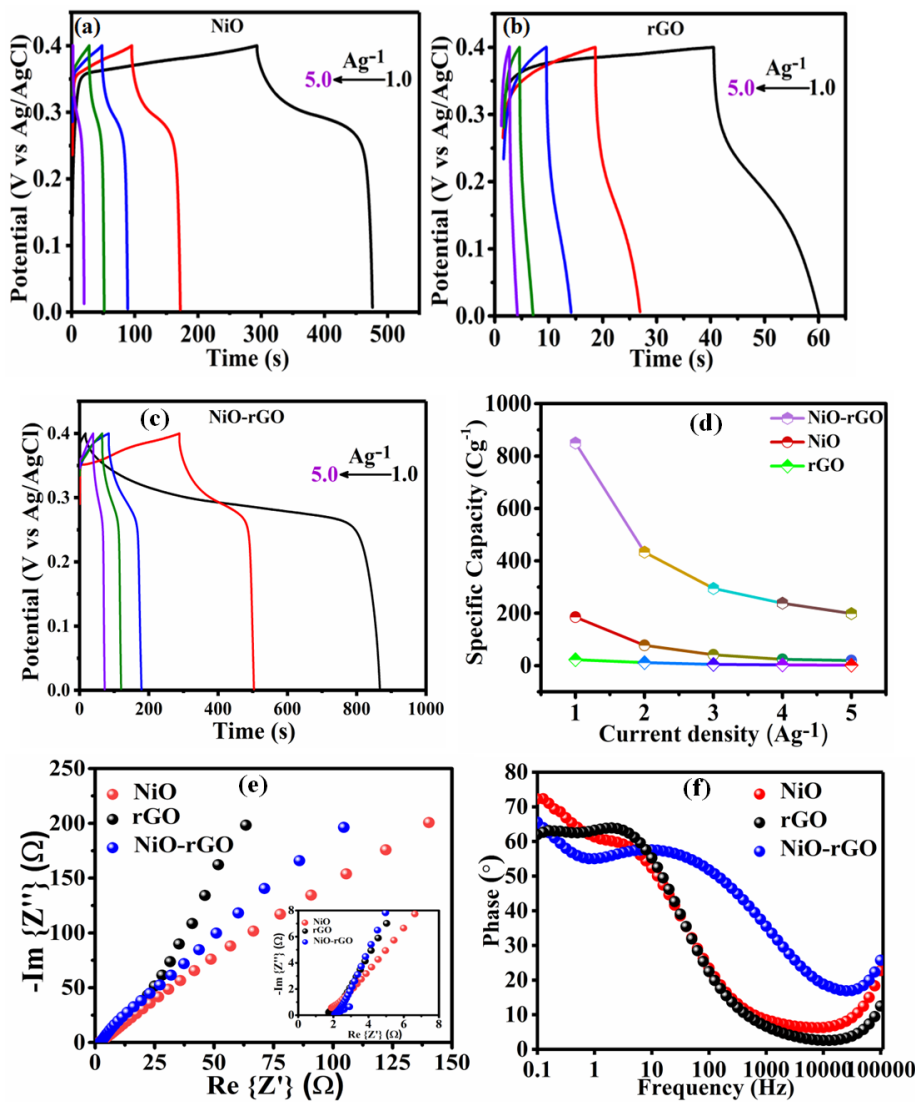


**Figure 3.11.** (a-c) GCD of NiO, rGO, and NiO-rGO at a different current density; (b) Specific (d) Specific capacity value of NiO, rGO, and NiO-rGO at different current density (1-5Ag<sup>-1</sup>), (e&f) Nyquist and Bode plots for NiO, rGO and NiO-rGO.

The GCD profiles of NiO-rGO, NiO, and rGO at different current densities are shown in Figure 3.11a-c, respectively. The variation in their specific capacities with changing current densities is also shown in Figure 3.11d. All three materials show a decrease in their specific capacities with increasing current density, however, at different rates. While rGO shows an almost negligible reduction in storage capacity, the specific capacities NiO and NiO-rGO drop rapidly up to 2 Ag<sup>-1</sup> and then gradually decrease with increasing current densities. This

observation may be rationalized by the fact that the charge storage in **rGO** is primarily due to the surface-controlled process involving very fast electrolyte (de)adsorption, thus independent of current densities. However, for **Ni-rGO** and **NiO**, the charge storage is mainly due to a relatively slow diffusion-controlled process, which becomes a limiting factor at higher current densities.[27,28]

To understand the conductive nature and ion transport mechanism of the as-prepared electrode materials, electrochemical impedance spectroscopy (EIS) has been carried out. Nyquist plots for **NiO**, **rGO**, and **NiO-rGO** in the frequency region of 10 mHz to 100 kHz have been depicted in **Figure 3.11e**. [46] In the Nyquist plot, the intercept on the real axis by the impedance line shows the equivalent series resistance ( $R_s$ ). The observed average  $R_s$  values for **NiO**, **rGO**, and **NiO-rGO** are 2.48 ( $s = 0.031$ ), 2.07 ( $s = 0.046$ ), and 2.29 ( $s = 0.036$ )  $\Omega$ , respectively, indicating a decrease in the resistance of the composite compared to neat **NiO** due to the blending of conductive **rGO**. Among the Nyquist plots of three materials, the impedance line of **NiO** is closest to the real axis, suggesting the charge storage due to charge transfer, i.e. battery-type electrode. On the other hand, the impedance line for **rGO** is closest to the imaginary axis, indicating it has the highest EDLC character compared to the other two materials. In the case of **NiO-rGO**, the impedance line lies in between that of its components, corroborating that it possesses characteristics of both **NiO** and **rGO**. **Figure 3.11f** depicts the Bode plots for **NiO**, **rGO**, and **NiO-rGO**, showing the change in their impedance phase angles with applied AC frequency (10 MHz to 100 kHz). At a lower frequency, a phase angle of  $-90^\circ$  refers to an ideal capacitor behavior, where a reduction in its magnitude indicates the mixing of the diffusion-controlled process. The observed phase angles for **NiO**, **rGO**, and **NiO** are 72.35, 61.23, and 66.39 $^\circ$ , respectively, supplementing the conclusion from the Nyquist plots.

The cyclic stability of as-synthesized electrode material is an essential measure for practical applications. The cyclic performance of **NiO-rGO** has been evaluated for 5000 charge-discharge cycles at 10

A.g<sup>-1</sup> current density in the potential window of 0 to 0.4 V. The plot showing the change in percentage capacity retention of **NiO-rGO** with the number of cycles is depicted in **Figure 3.12a**, along with the first and last 10 cycles in the inset. The study shows that even after 5000 cycles, **NiO-rGO** heterostructure shows excellent capacity retention of 88.40%. The GCD profiles of initial and later cycles remain shows a change in the behavior, indicating loss of capacitance at 50 mVs<sup>-1</sup> in **NiO-rGO** heterostructures material. Moreover , a comparison of Nyquist and Bode plots was also done after 5000 cycles (**Figure 3.12b-c**). Both Nyquist plots show similar intercepts on the real axis, indicating  $R_s$  value remains almost unchanged after 5000 charge-discharge cycles. However, after 5000 cycles, the impedance profile was observed to be inclined towards the real axis, implying an increase in the faradaic process. A similar conclusion can be drawn by comparing the Bode plots, in which the phase angle is observed to reduce from 66.39° to 44.35° after 5000 cycles. Moreover, the cyclic voltammetry of **NiO-rGO** was performed after 5000 cycles and compared with the fresh one (**Figure 3.12d**), which shows an insignificant change in the observed current and CV area, indicating stable electrochemical performance of the composite material.

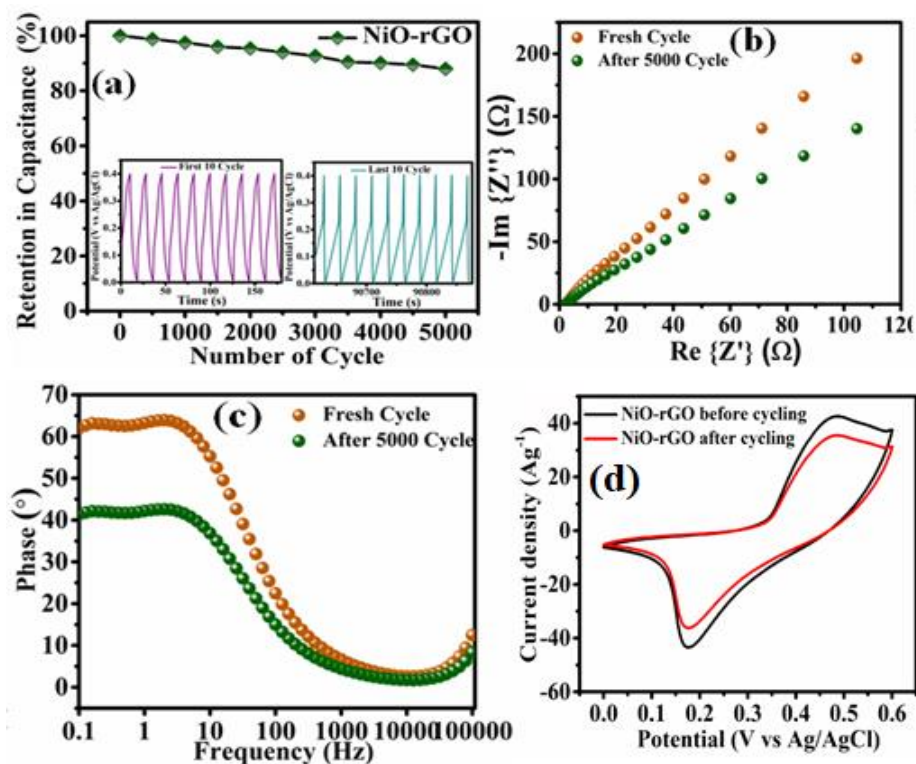


**Figure 3.12** (a) Cycling performance of NiO-rGO at 10 A.g-1 for 5000 cycles (insets show first and last 10 cycles), (b& c) Nyquist and Bode plots of fresh NiO-rGO after 5000.(d) CV profiles of NiO-rGO of before and after 5000 cycles at 50 mVs<sup>-1</sup>.

Further to assess the morphological and compositional change after 5000 cycles, FE-SEM images, EDX spectrum and elemental mapping were also recorded (**Figure 3.13a-d**). The FE-SEM images reveal that, after 5000 cycles, NiO-rGO shows a slightly agglomerated morphology compared to that of the freshly prepared composite. The EDX spectrum and elemental mapping feature all the elements of the composite (Ni, O,

and C) along with that of the electrolyte (K), confirming the compositional integrity of the electrode materials after multiple cycles.

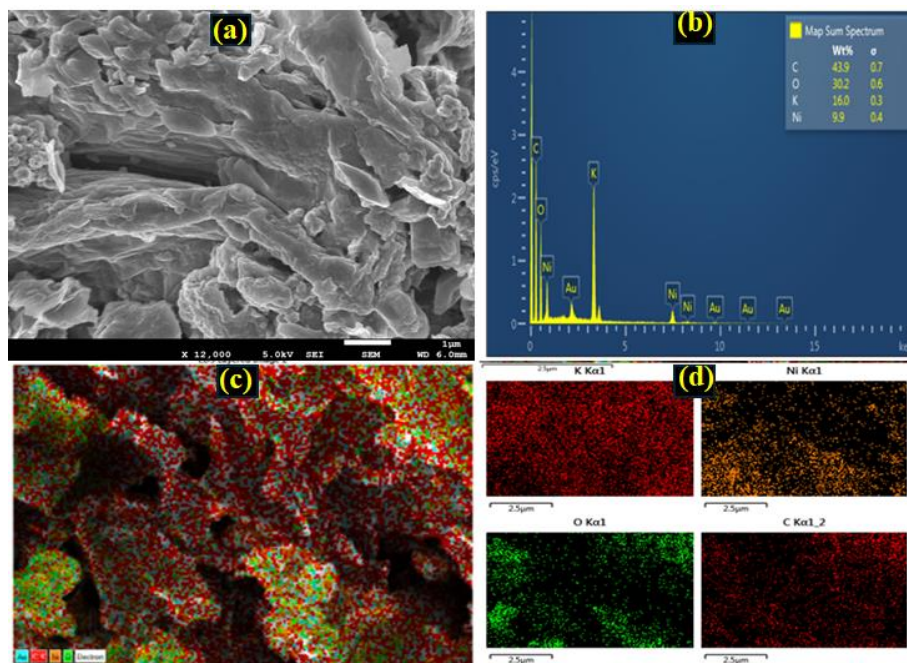


**Figure 3.13** FE-SEM of NiO-rGO after 5000 cycles. **(b-d)** EDX and elemental mapping of NiO/rGO after 5000 cycles.

To understand the applicability of NiO-rGO heterostructures in practical applications, a solid-state symmetric prototype device (NiO-rGO//NiO-rGO) was assembled using a cellulose membrane separator in a Swagelok cell. The cell voltage in the two-electrode configuration was 1.2 V for the as-prepared prototype device. CV curves of the device, recorded within 1.2 V cell voltage at various scan rates (5 to 500 mVs<sup>-1</sup>), show a more of rectangular shape compared to the three-electrode configuration wherein redox peaks are discernable (**Figure 3.14a**). The absence of redox peaks in the case of device, signifies that the supercapacitor undergoes charging and discharging at a pseudo-constant rate because of restrictive ion movement in gel electrolyte as compared to the free movement of ions in aqueous electrolytes. The free movement of electrolyte ions in an aqueous medium allows ion movement to be diffusion controlled.

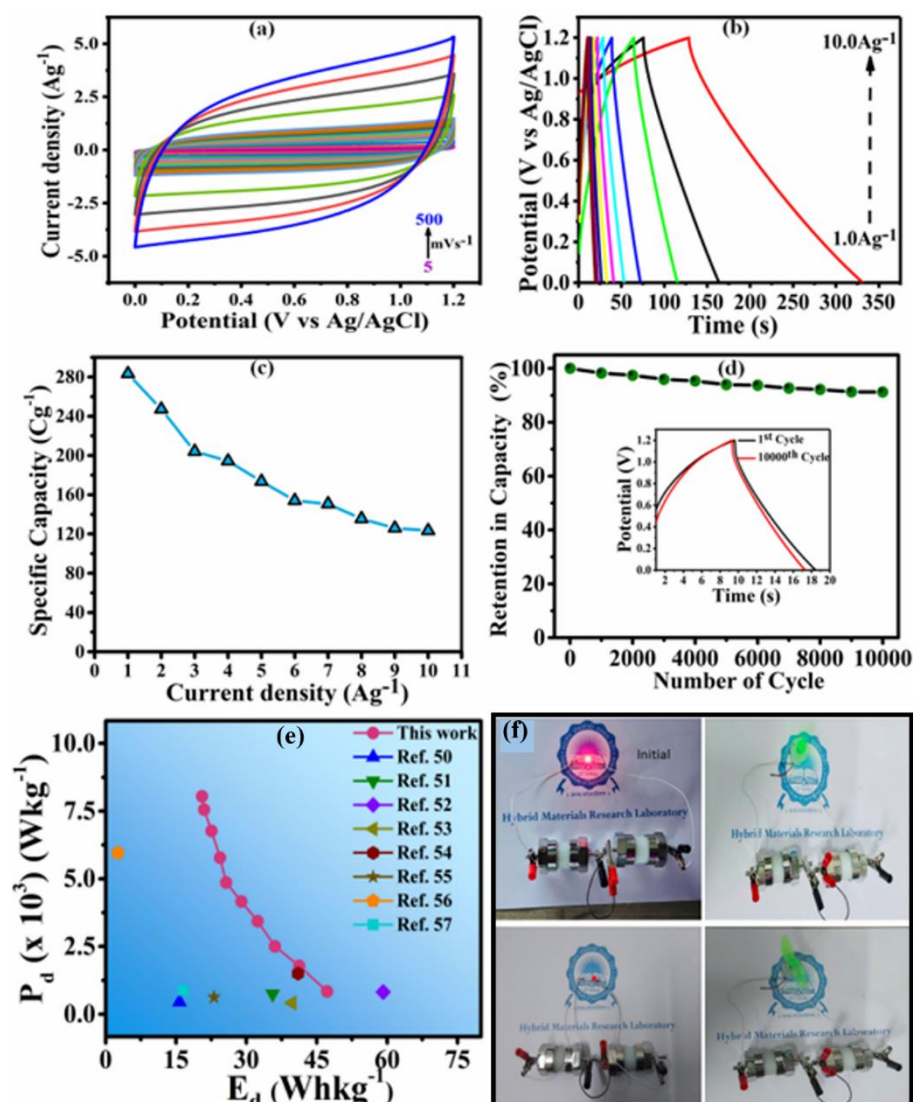


**Figure 3.14** (a) CV profiles at different scan rates (b) GCD profiles at different current densities (1-10 Ag-1) (c) Specific capacitance variations with changing current densities. (d) Cycling performance for 10000 consecutive cycles (insets show first and last cycle of the device), (e) Ragone plot (energy density vs. power density) of the fabricated device [51–58] (f) Glowing LED and running FAN using the fabricated device.

However, due to the restricted movement of ions imposed by steric hindrance in gel electrolyte medium, ion movement can not be exclusively governed by diffusion, which leads to a pseudo-constant rate for charge storage, resembling EDLC-type behavior [47–50]. The specific capacity of the device was calculated using the GCD studies at

various current densities (1–10 A.g<sup>-1</sup>) (**Figure 3.14b**). The change in specific capacity at different current densities is given in **Figure 3.14c**, showing a decreasing trend with the increasing current density due to diffusion limitation. The device displays a maximum specific capacity of 283.3 Cg<sup>-1</sup> at 1 Ag<sup>-1</sup>, which reduces to 123.1 Cg<sup>-1</sup> at 10 Ag<sup>-1</sup> current density. The cyclic stability of the fabricated prototype device has been investigated for 10000 GCD cycles at 10 Ag<sup>-1</sup> current density in the potential window of 0 - 1.2 V (**Figure 3.14d**). After 10000 charging-discharging cycles the device shows a capacity retention of 91.24%, confirming exceptional cyclic stability. Moreover, GCD profiles of the first and 10000<sup>th</sup> cycle show an almost similar pattern (**Figure 3.14d inset**), corroborating its robust electrochemical character. Energy density and power density are essential criteria for the practical applications of any energy storage device. The Ragone plot of the energy density (E<sub>d</sub>) vs. power density (P<sub>d</sub>) for the fabricated device is given in **Figure 3.14e**, which shows an expected pattern of increasing energy density with a decrease in the power density and vice versa. The as-prepared device shows a maximum energy density of 56.6 Wh.kg<sup>-1</sup> at a power density of 1.00 kW.kg<sup>-1</sup> and a maximum power density of 9.6 kW.kg<sup>-1</sup> at 24.66 Wh.kg<sup>-1</sup> energy density. The obtained results are comparable to or higher than the recently reported metal oxide carbonaceous heterostructures for energy storage applications (**Figure 3.14e**). The practical demonstration has been done by connecting two similar devices in a series combination for illuminating a red-light emitting diode and running a DC motor fan (**Figure 3.14f**).

#### 3.4.3.2 Theoretical studies:

To rationalize the superior charge storage and electrocatalytic performance of **NiO-rGO** heterostructure compared to its components **NiO** and **rGO**, theoretical studies have been performed using DFT calculations. The structure of **NiO** was optimized considering it as a face-centered cubic crystal with the Fm-3m space group. DFT optimized lattice parameters of **NiO** are  $a = 10.55 \text{ \AA}$ ,  $b = 10.50 \text{ \AA}$ ,  $c = 10.10 \text{ \AA}$ , and  $\alpha = 90.3312^\circ$ ,  $\beta = 89.4564^\circ$ ,  $\gamma = 89.7326^\circ$  with a unit cell volume of 1120

$\text{\AA}^3$ . Instead of optimizing the **rGO** structure, a graphene model has been chosen for the sake of simplicity, which is a common practice in DFT calculations of composite materials containing rGO.[59] For the optimization of **NiO-graphene** heterostructure (mimic of **NiO-rGO**), the (200) plane of **NiO** has been chosen as the interface plane with graphene since it corresponds to the highest peak intensity in the X-ray diffraction pattern of **NiO**. The lattice mismatch at the boundary area was minimized by considering the **NiO** surface and graphene layer as close as possible. The DFT-optimized structures of **NiO**, **graphene**, and **NiO-graphene** are displayed in **Figure 3.15a-c**.

In order to bring theoretical insight into the orbital interactions, the total density of states (TDOS) for the **NiO** and **graphene** are presented in **Figure 3.16a&b**. Moreover, the TDOS of **NiO-graphene**, along with its partial density of states (PDOS) contributed from Ni-3*d*, O-2*p*, and C-2*p* are also given in **Figure 3.16c**. Compared to **graphene** and **NiO**, an enhanced TDOS was observed near the fermi level of the composite, mainly consisting of Ni-3*d*, O-2*p*, and C-2*p*. This may be attributed to the shift of bonding  $\pi$ -electron density of graphene towards Ni-3*d* as a result of coordinative interaction of graphene with the Ni metal center. The enhanced TDOS close to the Fermi level in **NiO-graphene** causes it to have better conductivity[60] as well as facilitates the transfer of electrons from the composite electrode.[61] Moreover, it eases the  $\text{Ni}^{2+} \leftrightarrow \text{Ni}^{3+}$  redox process, thereby, improves the supercapattery performance of the composite.

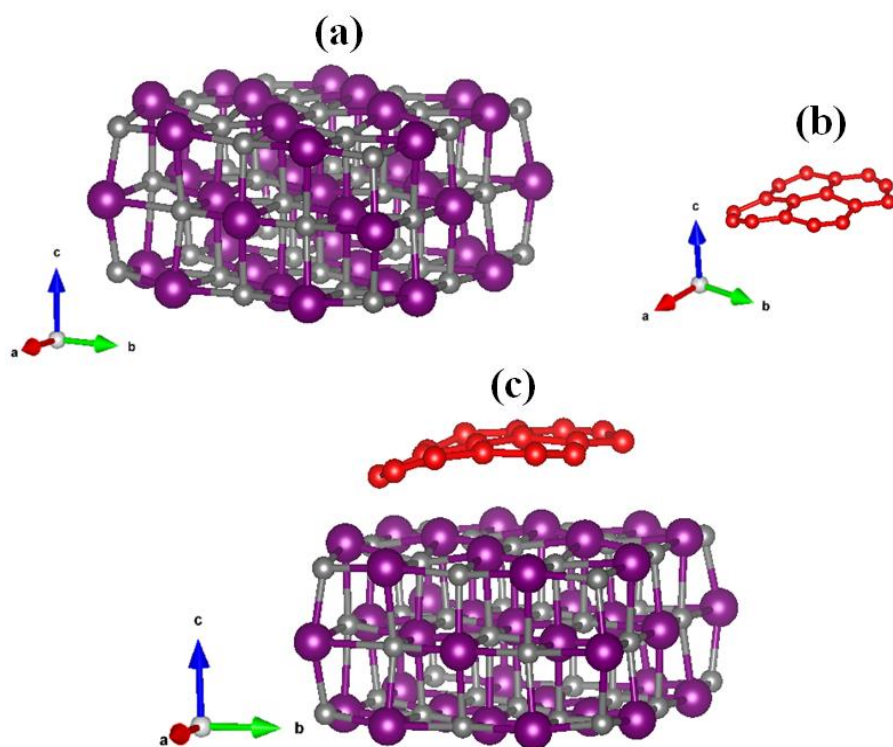


**Figure 3.15** DFT optimized structure of (a) NiO (b) graphene (c) NiO-graphene; violet, grey and red represent nickel, oxygen, and carbon respectively.

The charge storage property of an electrode greatly depends on the adsorption of electrolyte ions on the electrode during the charge-discharge process. [62,63] Therefore, to understand the adsorption behavior of electrolyte ions on electrodes, OH\* ion adsorption energies ( $\delta_{OH}$ ) on all three optimized electrode structures have been calculated using equation 7.

$$\delta_{OH} = E_{e-OH} - \{E_e - E_{OH}\} \text{ eV} \quad (7)$$

where,  $\delta_{OH}$  is the OH adsorption energy,  $E_{e-OH}$  represents the total energy of the OH-adsorbed electrode, whereas  $E_e$  and  $E_{OH}$  are the total energies of the electrode and OH molecule.

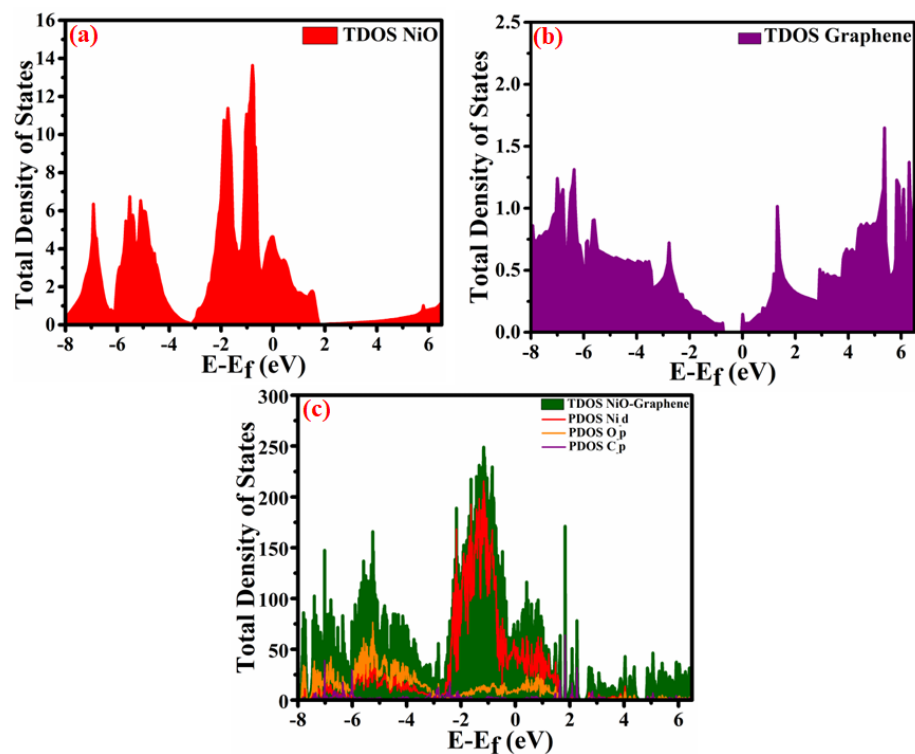


**Figure 3.16** Density of States (DOS) for the **NiO** and **graphene**, with Partial Density of states (PDOS) for **NiO/graphene**.

The calculated  $\delta_{OH}$  values were -1.21 eV, -1.69 eV, and -1.85 eV for **NiO**, **graphene**, and **NiO/graphene**, respectively. It clearly signifies that the  $OH^*$  adsorption is most favorable in the case of **NiO/graphene** heterostructure, leading to a superior performance, which matches well with the experimental observations.

### 3.5 Summary

In summary, **NiO-rGO** heterostructure was synthesized using the facile precipitation-aging-calcination and ultrasonication technique, which resulted in outstanding charge storage performance. Due to the enhanced synergistic interaction between **NiO** and **rGO** nanosheets, the resulting **NiO-rGO** heterostructure exhibited a charge storage capacity of more than four times the sum of its constituents with excellent cyclic stability. The fabricated symmetrical device (**NiO-rGO // NiO-rGO**) showed the highest energy and power densities of 68 Wh.kg<sup>-1</sup> and 11.58 kW.kg<sup>-1</sup>, respectively, with a capacity retention of 91.24 % over 10000 charge/discharge cycles. Justifications of experimental charge storage of composite and its components were done by the first principle DFT approach. Theoretical results indicated that OH adsorptions are more favorable on the composite due to its enhanced total density of states near the Fermi level compared to **NiO** and **rGO**. The theoretical conclusions were found to be in good agreement with the experimental results. This work offers a facile approach to enhance the synergism between 3D-metal oxides-2D-layered materials-based heterostructures to derive maximum electrochemical performance. We believe the use of a material obtained from a facile route and consisting of non-noble and earth-abundant elements to achieve such an excellent performance is indeed a sustainable approach for energy storage.

## References

- [1] M. Winter, R.J. Brodd, What Are Batteries, Fuel Cells, and Supercapacitors? *Chem. Rev.* 104 (2004) 4245–4270. <https://doi.org/10.1021/cr020730k>.
- [2] M.K. Singh, S. Krishnan, D.K. Rai, Rational design of Ti<sub>3</sub>C<sub>2</sub>T<sub>x</sub> MXene coupled with hierarchical CoS for a flexible supercapattery, *Electrochimica Acta.* 441 (2023) 141825. <https://doi.org/10.1016/j.electacta.2023.141825>.
- [3] S. Raj, P. Kar, P. Roy, Facile synthesis of flower-like morphology Cu<sub>0.27</sub>Co<sub>2.73</sub>O<sub>4</sub> for a high-performance supercapattery with extraordinary cycling stability, *Chem. Commun.* 54 (2018) 12400–12403. <https://doi.org/10.1039/C8CC04625E>.
- [4] Y. Yan, Y. Luo, J. Ma, B. Li, H. Xue, H. Pang, Facile Synthesis of Vanadium Metal-Organic Frameworks for High-Performance Supercapacitors, *Small.* 14 (2018) 1801815. <https://doi.org/10.1002/sml.201801815>.
- [5] Q. Hu, M. Tang, M. He, N. Jiang, C. Xu, D. Lin, Q. Zheng, Core-shell MnO<sub>2</sub>@CoS nanosheets with oxygen vacancies for high-performance supercapattery, *J. Power Sources.* 446 (2020) 227335. <https://doi.org/10.1016/j.jpowsour.2019.227335>.
- [6] C. An, Y. Zhang, H. Guo, Y. Wang, Metal oxide-based supercapacitors: progress and perspectives, *Nanoscale Adv.* 1 (2019) 4644–4658. <https://doi.org/10.1039/C9NA00543A>.
- [7] Y. Zhu, Q. Lin, Y. Zhong, H.A. Tahini, Z. Shao, H. Wang, Metal oxide-based materials as an emerging family of hydrogen evolution electrocatalysts, *Energy Environ. Sci.* 13 (2020) 3361–3392. <https://doi.org/10.1039/D0EE02485F>.
- [8] R.K. Nare, S. Ramesh, P.K. Basavi, V. Kakani, C. Bathula, H.M. Yadav, P.B. Dhanapal, R.K.R. Kotanka, V.R. Pasupuleti, Sonication-supported synthesis of cobalt oxide assembled on an N-MWCNT composite for electrochemical supercapacitors via three-electrode configuration, *Sci. Rep.* 12 (2022) 1998. <https://doi.org/10.1038/s41598-022-05964-8>.

- [9] M. Gong, W. Zhou, M.-C. Tsai, J. Zhou, M. Guan, M.-C. Lin, B. Zhang, Y. Hu, D.-Y. Wang, J. Yang, S.J. Pennycook, B.-J. Hwang, H. Dai, Nanoscale nickel oxide/nickel heterostructures for active hydrogen evolution electrocatalysis, *Nat. Commun.* 5 (2014) 4695. <https://doi.org/10.1038/ncomms5695>.
- [10] C. Guan, J. Liu, Y. Wang, L. Mao, Z. Fan, Z. Shen, H. Zhang, J. Wang, Iron Oxide-Decorated Carbon for Supercapacitor Anodes with Ultrahigh Energy Density and Outstanding Cycling Stability, *ACS Nano.* 9 (2015) 5198–5207. <https://doi.org/10.1021/acsnano.5b00582>.
- [11] J.B. Gerken, J.G. McAlpin, J.Y.C. Chen, M.L. Rigsby, W.H. Casey, R.D. Britt, S.S. Stahl, Electrochemical Water Oxidation with Cobalt-Based Electrocatalysts from pH 0–14: The Thermodynamic Basis for Catalyst Structure, Stability, and Activity, *J. Am. Chem. Soc.* 133 (2011) 14431–14442. <https://doi.org/10.1021/ja205647m>.
- [12] U.K. Chime, A.C. Nkele, S. Ezugwu, A.C. Nwanya, N.M. Shinde, M. Kebede, P.M. Ejikeme, M. Maaza, F.I. Ezema, Recent progress in nickel oxide-based electrodes for high-performance supercapacitors, *Curr. Opin. Electrochem.* 21 (2020) 175–181. <https://doi.org/10.1016/j.coelec.2020.02.004>.
- [13] W. Chen, D. Gui, J. Liu, Nickel oxide/graphene aerogel nanocomposite as a supercapacitor electrode material with extremely wide working potential window, *Electrochimica Acta.* 222 (2016) 1424–1429. <https://doi.org/10.1016/j.electacta.2016.11.120>.
- [14] S.T. Navale, V.V. Mali, S.A. Pawar, R.S. Mane, M. Naushad, F.J. Stadler, V.B. Patil, Electrochemical supercapacitor development based on electrodeposited nickel oxide film, *RSC Adv.* 5 (2015) 51961–51965. <https://doi.org/10.1039/C5RA07953E>.
- [15] H. Wang, H. Yi, X. Chen, X. Wang, Asymmetric supercapacitors based on nano-architected nickel oxide/graphene foam and hierarchical porous nitrogen-doped carbon nanotubes with

- ultrahigh-rate performance, *J Mater Chem A*. 2 (2014) 3223–3230.  
<https://doi.org/10.1039/C3TA15046A>.
- [16] Y. Jiao, Y. Liu, B. Yin, S. Zhang, F. Qu, X. Wu, Hybrid  $\alpha$ -Fe<sub>2</sub>O<sub>3</sub>@NiO heterostructures for flexible and high performance supercapacitor electrodes and visible light driven photocatalysts, *Nano Energy*. 10 (2014) 90–98.  
<https://doi.org/10.1016/j.nanoen.2014.09.002>.
- [17] S. Vijayakumar, S. Nagamuthu, G. Muralidharan, Porous NiO/C Nanocomposites as Electrode Material for Electrochemical Supercapacitors, *ACS Sustain. Chem. Eng.* 1 (2013) 1110–1118.  
<https://doi.org/10.1021/sc400152r>.
- [18] L. Yu, G. Wang, G. Wan, G. Wang, S. Lin, X. Li, K. Wang, Z. Bai, Y. Xiang, Highly effective synthesis of NiO/CNT nanohybrids by atomic layer deposition for high-rate and long-life supercapacitors, *Dalton Trans.* 45 (2016) 13779–13786.  
<https://doi.org/10.1039/C6DT01927G>.
- [19] X. Zhu, H. Dai, J. Hu, L. Ding, L. Jiang, Reduced graphene oxide–nickel oxide composite as high performance electrode materials for supercapacitors, *J. Power Sources*. 203 (2012) 243–249.  
<https://doi.org/10.1016/j.jpowsour.2011.11.055>.
- [20] E. Frackowiak, Carbon materials for supercapacitor application, *Phys. Chem. Chem. Phys.* 9 (2007) 1774.  
<https://doi.org/10.1039/b618139m>.
- [21] J. Xu, L. Wu, Y. Liu, J. Zhang, J. Liu, S. Shu, X. Kang, Q. Song, D. Liu, F. Huang, Y. Hu, NiO-rGO composite for supercapacitor electrode, *Surf. Interfaces*. 18 (2020) 100420.  
<https://doi.org/10.1016/j.surfin.2019.100420>.
- [22] Y. Zhu, W. Chu, N. Wang, T. Lin, W. Yang, J. Wen, X.S. Zhao, Self-assembled Ni/NiO/RGO heterostructures for high-performance supercapacitors, *RSC Adv.* 5 (2015) 77958–77964.  
<https://doi.org/10.1039/C5RA14790E>.
- [23] Q. Li, Q. Wei, L. Xie, C. Chen, C. Lu, F.-Y. Su, P. Zhou, Layered NiO/reduced graphene oxide composites by heterogeneous assembly with enhanced performance as high-performance

- asymmetric supercapacitor cathode, RSC Adv. 6 (2016) 46548–46557. <https://doi.org/10.1039/C6RA04998B>.
- [24] V. Sannasi, K.U. Maheswari, C. Karthikeyan, S. Karuppuchamy, H<sub>2</sub>O<sub>2</sub>-assisted microwave synthesis of NiO/CNT nanocomposite material for supercapacitor applications, Ionics. 26 (2020) 4067–4079. <https://doi.org/10.1007/s11581-020-03563-z>.
- [25] D. Patiño-Ruiz, L. Sánchez-Botero, L. Tejeda-Benitez, J. Hinestroza, A. Herrera, Green synthesis of iron oxide nanoparticles using Cymbopogon citratus extract and sodium carbonate salt: Nanotoxicological considerations for potential environmental applications, Environ. Nanotechnol. Monit. Manag. 14 (2020) 100377. <https://doi.org/10.1016/j.enmm.2020.100377>.
- [26] Synthesis and Characterization of MgO Nanoparticles by Orange Fruit Waste through Green Method, Int. J. Adv. Res. Chem. Sci. 4 (2017). <https://doi.org/10.20431/2349-0403.0409005>.
- [27] M.K. Singh, A.K. Gupta, S. Krishnan, N. Guha, S. Marimuthu, D.K. Rai, A new hierarchically porous Cu-MOF composited with rGO as an efficient hybrid supercapacitor electrode material, J. Energy Storage. 43 (2021) 103301. <https://doi.org/10.1016/j.est.2021.103301>.
- [28] S. Krishnan, A.K. Gupta, M.K. Singh, N. Guha, D.K. Rai, Nitrogen-rich Cu-MOF decorated on reduced graphene oxide nanosheets for hybrid supercapacitor applications with enhanced cycling stability, Chem. Eng. J. 435 (2022) 135042. <https://doi.org/10.1016/j.cej.2022.135042>.
- [29] G. Kresse, J. Furthmüller, Efficiency of ab-initio total energy calculations for metals and semiconductors using a plane-wave basis set, Comput. Mater. Sci. 6 (1996) 15–50. [https://doi.org/10.1016/0927-0256\(96\)00008-0](https://doi.org/10.1016/0927-0256(96)00008-0).
- [30] G. Kresse, J. Hafner, *Ab initio* molecular-dynamics simulation of the liquid-metal–amorphous-semiconductor transition in germanium, Phys. Rev. B. 49 (1994) 14251–14269. <https://doi.org/10.1103/PhysRevB.49.14251>.

- [31] J.P. Perdew, K. Burke, M. Ernzerhof, Generalized Gradient Approximation Made Simple, *Phys. Rev. Lett.* 77 (1996) 3865–3868. <https://doi.org/10.1103/PhysRevLett.77.3865>.
- [32] X. Qin, M. Zhou, B. Zong, J. Guo, J. Gong, L. Wang, G. Liang, Urea-assisted hydrothermal synthesis of a hollow hierarchical  $\text{LiNi}_{0.5}\text{Mn}_{1.5}\text{O}_4$  cathode material with tunable morphology characteristics, *RSC Adv.* 8 (2018) 30087–30097. <https://doi.org/10.1039/C8RA05817B>.
- [33] M.A. Peck, M.A. Langell, Comparison of Nanoscaled and Bulk NiO Structural and Environmental Characteristics by XRD, XAFS, and XPS, *Chem. Mater.* 24 (2012) 4483–4490. <https://doi.org/10.1021/cm300739y>.
- [34] S.N. Alam, N. Sharma, L. Kumar, Synthesis of Graphene Oxide (GO) by Modified Hummers Method and Its Thermal Reduction to Obtain Reduced Graphene Oxide (rGO)\*, *Graphene.* 06 (2017) 1–18. <https://doi.org/10.4236/graphene.2017.61001>.
- [35] N. Mironova-Ulmane, A. Kuzmin, I. Steins, J. Grabis, I. Sildos, M. Pärs, Raman scattering in nanosized nickel oxide NiO, *J. Phys. Conf. Ser.* 93 (2007) 012039. <https://doi.org/10.1088/1742-6596/93/1/012039>.
- [36] N. Bala, H.K. Singh, S. Verma, S. Rath, Magnetic-order induced effects in nanocrystalline NiO probed by Raman spectroscopy, *Phys. Rev. B.* 102 (2020) 024423. <https://doi.org/10.1103/PhysRevB.102.024423>.
- [37] F. Ambroz, T.J. Macdonald, V. Martis, I.P. Parkin, Evaluation of the BET Theory for the Characterization of Meso and Microporous MOFs, *Small Methods.* 2 (2018) 1800173. <https://doi.org/10.1002/smt.201800173>.
- [38] M. Saraf, R. Rajak, S.M. Mobin, A fascinating multitasking Cu-MOF/rGO hybrid for high performance supercapacitors and highly sensitive and selective electrochemical nitrite sensors, *J. Mater. Chem. A.* 4 (2016) 16432–16445. <https://doi.org/10.1039/C6TA06470A>.

- [39] T. Brousse, D. Bélanger, J.W. Long, To Be or Not To Be Pseudocapacitive?, *J. Electrochem. Soc.* 162 (2015) A5185–A5189. <https://doi.org/10.1149/2.0201505jes>.
- [40] P. Simon, Y. Gogotsi, B. Dunn, Where Do Batteries End and Supercapacitors Begin?, *Science*. 343 (2014) 1210–1211. <https://doi.org/10.1126/science.1249625>.
- [41] S.D. Dhas, P.S. Maldar, M.D. Patil, A.B. Nagare, M.R. Waikar, R.G. Sonkawade, Annasaheb.V. Moholkar, Synthesis of NiO nanoparticles for supercapacitor application as an efficient electrode material, *Vacuum*. 181 (2020) 109646. <https://doi.org/10.1016/j.vacuum.2020.109646>.
- [42] R.K. Mishra, G.J. Choi, Y. Sohn, S.H. Lee, J.S. Gwag, A novel RGO/N-RGO supercapacitor architecture for a wide voltage window, high energy density and long-life *via* voltage holding tests, *Chem. Commun.* 56 (2020) 2893–2896. <https://doi.org/10.1039/D0CC00249F>.
- [43] N. Elgrishi, K.J. Rountree, B.D. McCarthy, E.S. Rountree, T.T. Eisenhart, J.L. Dempsey, A Practical Beginner's Guide to Cyclic Voltammetry, *J. Chem. Educ.* 95 (2018) 197–206. <https://doi.org/10.1021/acs.jchemed.7b00361>.
- [44] K. Brezesinski, J. Wang, J. Haetge, C. Reitz, S.O. Steinmueller, S.H. Tolbert, B.M. Smarsly, B. Dunn, T. Brezesinski, Pseudocapacitive Contributions to Charge Storage in Highly Ordered Mesoporous Group V Transition Metal Oxides with Iso-Oriented Layered Nanocrystalline Domains, *J. Am. Chem. Soc.* 132 (2010) 6982–6990. <https://doi.org/10.1021/ja9106385>.
- [45] M. Zhi, C. Xiang, J. Li, M. Li, N. Wu, Nanostructured carbon–metal oxide composite electrodes for supercapacitors: a review, *Nanoscale*. 5 (2013) 72–88. <https://doi.org/10.1039/C2NR32040A>.
- [46] B.-A. Mei, O. Munteshari, J. Lau, B. Dunn, L. Pilon, Physical Interpretations of Nyquist Plots for EDLC Electrodes and Devices, *J. Phys. Chem. C*. 122 (2018) 194–206. <https://doi.org/10.1021/acs.jpcc.7b10582>.

- [47] L. Yang, S. Cheng, Y. Ding, X. Zhu, Z.L. Wang, M. Liu, Hierarchical Network Architectures of Carbon Fiber Paper Supported Cobalt Oxide Nanonet for High-Capacity Pseudocapacitors, *Nano Lett.* 12 (2012) 321–325. <https://doi.org/10.1021/nl203600x>.
- [48] X. Lang, A. Hirata, T. Fujita, M. Chen, Nanoporous metal/oxide hybrid electrodes for electrochemical supercapacitors, *Nat. Nanotechnol.* 6 (2011) 232–236. <https://doi.org/10.1038/nnano.2011.13>.
- [49] Q. Liao, N. Li, S. Jin, G. Yang, C. Wang, All-Solid-State Symmetric Supercapacitor Based on  $\text{Co}_3\text{O}_4$  Nanoparticles on Vertically Aligned Graphene, *ACS Nano.* 9 (2015) 5310–5317. <https://doi.org/10.1021/acsnano.5b00821>.
- [50] H. Du, F. Ding, J. Zhao, X. Zhang, Y. Li, Y. Zhang, J. Li, X. Yang, K. Li, Y. Yang, Core-shell structured  $\text{Ni}_3\text{S}_2@ \text{VO}_2$  nanorods grown on nickel foam as battery-type materials for supercapacitors, *Appl. Surf. Sci.* 508 (2020) 144876. <https://doi.org/10.1016/j.apsusc.2019.144876>.
- [51] A. Viswanathan, A.N. Shetty, Single step synthesis of rGO, copper oxide and polyaniline nanocomposites for high energy supercapacitors, *Electrochimica Acta.* 289 (2018) 204–217. <https://doi.org/10.1016/j.electacta.2018.09.033>.
- [52] A. Viswanathan, A.N. Shetty, Facile in-situ single step chemical synthesis of reduced graphene oxide-copper oxide-polyaniline nanocomposite and its electrochemical performance for supercapacitor application, *Electrochimica Acta.* 257 (2017) 483–493. <https://doi.org/10.1016/j.electacta.2017.10.099>.
- [53] S. Jadhav, R.S. Kalubarme, C. Terashima, B.B. Kale, V. Godbole, A. Fujishima, S.W. Gosavi, Manganese dioxide/ reduced graphene oxide composite an electrode material for high-performance solid state supercapacitor, *Electrochimica Acta.* 299 (2019) 34–44. <https://doi.org/10.1016/j.electacta.2018.12.182>.
- [54] A.J.C. Mary, C.I. Sathish, A. Vinu, A.C. Bose, Electrochemical Performance of  $\text{rGO}/\text{NiCo}_2\text{O}_4 @ \text{ZnCo}_2\text{O}_4$  Ternary Composite

- Material and the Fabrication of an all-Solid-State Supercapacitor Device, *Energy Fuels*. 34 (2020) 10131–10141. <https://doi.org/10.1021/acs.energyfuels.0c01427>.
- [55] S. Mondal, U. Rana, S. Malik, Reduced Graphene Oxide/Fe<sub>3</sub>O<sub>4</sub>/Polyaniline Nanostructures as Electrode Materials for an All-Solid-State Hybrid Supercapacitor, *J. Phys. Chem. C*. 121 (2017) 7573–7583. <https://doi.org/10.1021/acs.jpcc.6b10978>.
- [56] A.M. Zardkhoshoui, S.S.H. Davarani, Flexible asymmetric supercapacitors based on CuO@MnO<sub>2</sub>-rGO and MoS<sub>2</sub>-rGO with ultrahigh energy density, *J. Electroanal. Chem.* 827 (2018) 221–229. <https://doi.org/10.1016/j.jelechem.2018.08.023>.
- [57] J. Yuan, D. Yao, L. Jiang, Y. Tao, J. Che, G. He, H. Chen, Mn-Doped NiMoO<sub>4</sub> Mesoporous Nanorods/Reduced Graphene Oxide Composite for High-Performance All-Solid-State Supercapacitor, *ACS Appl. Energy Mater.* 3 (2020) 1794–1803. <https://doi.org/10.1021/acsaem.9b02238>.
- [58] P. Makkar, N.N. Ghosh, Facile Synthesis of MnFe<sub>2</sub>O<sub>4</sub> Hollow Sphere-Reduced Graphene Oxide Nanocomposites as Electrode Materials for All-Solid-State Flexible High-Performance Asymmetric Supercapacitors, *ACS Appl. Energy Mater.* 3 (2020) 2653–2664. <https://doi.org/10.1021/acsaem.9b02360>.
- [59] R. Samal, P. Mane, M. Bhat, B. Chakraborty, D.J. Late, C.S. Rout, Stabilization of Orthorhombic CoSe<sub>2</sub> by 2D-rGO/MWCNT Heterostructures for Efficient Hydrogen Evolution Reaction and Flexible Energy Storage Device Applications, *ACS Appl. Energy Mater.* 4 (2021) 11386–11399. <https://doi.org/10.1021/acsaem.1c02205>.
- [60] K. Pal, S. Anand, U.V. Waghmare, Thermoelectric properties of materials with nontrivial electronic topology, *J. Mater. Chem. C*. 3 (2015) 12130–12139. <https://doi.org/10.1039/C5TC02344K>.
- [61] Y. Cui, C. Zhou, X. Li, Y. Gao, J. Zhang, High performance electrocatalysis for hydrogen evolution reaction using nickel-doped CoS<sub>2</sub> nanostructures: experimental and DFT insights,

Electrochimica Acta. 228 (2017) 428–435.  
<https://doi.org/10.1016/j.electacta.2017.01.103>.

- [62] X. Shi, S.L. Bernasek, A. Selloni, Formation, Electronic Structure, and Defects of Ni Substituted Spinel Cobalt Oxide: a DFT+U Study, *J. Phys. Chem. C.* 120 (2016) 14892–14898.  
<https://doi.org/10.1021/acs.jpcc.6b03096>.
- [63] R. Hu, J. Shang, Quantum capacitance of transition metal and nitrogen co-doped graphenes as supercapacitors electrodes: A DFT study, *Appl. Surf. Sci.* 496 (2019) 143659.  
<https://doi.org/10.1016/j.apsusc.2019.143659>.



## Chapter 4

# **Ti<sub>3</sub>C<sub>2</sub>T<sub>x</sub> MXene Coupled with Hierarchical CoS for Flexible Supercapattery: Exploring Pseudo and Battery-like Behavior**

### 4.1 Introduction

In the prospect of high demands for portable electronic devices, flexible energy storage devices have recently gained enormous attention and have brought a paradigm shift in energy storage devices.[1-10]. Because of their appreciable features, such as portability, efficiency, excellent mechanical stability, and low cost, flexible energy storage devices find particular research interest among all the different electronic devices. There are various flexible energy storage devices, including supercapacitors, which work under varying mechanical stress (bending and twisting states) for next-generation flexible electronics.[11] For flexible supercapacitors, different conducting flexible substrates, including Ni-foam, carbon cloth, carbon paper, and PET (polyethylene terephthalate), have been used for growing active electrode materials. Among them, carbon cloth (CC), possessing excellent flexibility, good stretchability, and high conductivity, has become the most promising substrate in flexible supercapacitor device fabrications.[12] The common methods that have been adopted to conduct the electrode materials on carbon cloth (CC) include the electrophoretic deposition process,[13] hydrothermal growth,[14] electrodeposition,[15] dip coating,[16] and normal drop-casting.[17]

Apart from the synthetic method of the electrode, selecting suitable electrode materials with inherent supercapacitive properties such as excellent electrochemical activity, high conductivity, and a high surface area must also be considered.[18] In choosing such electrode

materials, metal sulfides have aroused particular attention due to their inherent properties favorable for higher electrochemical activities, including different crystal structures, valence states, and different possible stoichiometric compositions.[19] Moreover, metal sulfides also show higher electrical conductivity than metal oxides because the energy difference between the S 3p levels is lower than O 2p levels, which conduces the fast charge transfer.[20] Besides, sulfur also has a lower electronegativity than oxygen which facilitates electron transport in the microstructure. Considering all the above superior properties, unambiguously sulfides are better materials as an electrodes for supercapacitors. Cobalt sulfides have attracted more attention due to their low cost, excellent physical and electrochemical properties, high theoretical capacitance, and weak Co-S bond favorable for conversion reactions. However, the neat cobalt sulfide as an electrode significantly changes the volume during the redox process, leading to reduced electrochemical performance and poor rate capability.[21] To overcome this problem, hybridizing metal sulfides with layered 2D structures, such as rGO[22], graphene[23], CNTs[24], and MXene[25], has been recognized as an important approach.

MXenes are transition metal carbides, nitrides, or carbonitrides, a family of two-dimensional (2D) ceramic materials, abbreviated as  $M_{n+1}X_nT_x$  (M = early transition metals; X = C or N; n = 1, 2, or 3; T = surface functional groups -OH, -O, and -F). Due to their layered 2D structure, high conductivity, and redox-active Ti-framework, they facilitate ion (de)intercalation and, therefore, have been widely employed as electrode materials for batteries and supercapacitors.[26,27] Among several reported MXenes,  $Ti_3C_2T_x$  is the most studied MXene synthesized by selectively etching aluminium from its parent  $Ti_3AlC_2$  MAX phase. Different strategies have also been used to customize its electrochemical properties. It includes the introduction of intercalants, such as metal oxides and sulfides, between the conductive MXene ( $Ti_3C_2T_x$ ) sheets[28], and forming a composite for targeted applications[29]. Of note is the use of metal sulfides because of

their superior electrochemical properties, as discussed above. For example, Wei et al. reported an MXene/CoS<sub>2</sub> composite as a supercapacitor electrode material with a specific capacitance of 1320 Fg<sup>-1</sup> at 1 A g<sup>-1</sup>. [30] In another work, Pan et al. synthesized a CuS/Ti<sub>3</sub>C<sub>2</sub> composite for supercapacitor application yielding a specific capacitance of 169.5 Cg<sup>-1</sup> at 1 A g<sup>-1</sup>. [31] These studies corroborate that combining metal sulfides with MXene to form a composite improves the overall performance of the electrode materials.

In this chapter, a flexible supercapattery device was fabricated by synthesizing **Ti<sub>3</sub>C<sub>2</sub>T<sub>x</sub>/CoS** on a carbon cloth (CC) substrate using a simple in-situ hydrothermal cum drop-casting technique. Overall, the prepared hierarchical material combines the effect of pseudocapacitors and battery with multiple attributes, such as high conductivity, rapid charge/discharge, improved electrochemical stability, and high surface area, features excellent performance. The comparative electrochemical properties of carbon cloth supported as-prepared composite (**Ti<sub>3</sub>C<sub>2</sub>T<sub>x</sub>/CoS@CC**) and its components (**CoS@CC** and **Ti<sub>3</sub>C<sub>2</sub>T<sub>x</sub>@CC**) have been investigated using cyclic voltammetry (CV), galvanostatic charge/discharge (GCD), and electrochemical impedance spectroscopy (EIS). The composite material **Ti<sub>3</sub>C<sub>2</sub>T<sub>x</sub>/CoS@CC** shows a much higher specific capacity of 120 Cg<sup>-1</sup> at 1 Ag<sup>-1</sup> compared to its constituent components (60 Cg<sup>-1</sup> and 10.4 Cg<sup>-1</sup> for **CoS@CC** and **Ti<sub>3</sub>C<sub>2</sub>T<sub>x</sub>@CC**, respectively). Such high electrochemical performance of **Ti<sub>3</sub>C<sub>2</sub>T<sub>x</sub>/CoS@CC** can be attributed to the synergistic effect of its components. The cyclic stability test for **Ti<sub>3</sub>C<sub>2</sub>T<sub>x</sub>/CoS@CC** was carried out using GCD for 1000 charge/discharge cycles, which shows **88.6%** capacity retention. The flexible symmetrical supercapacitor device fabricated using **Ti<sub>3</sub>C<sub>2</sub>T<sub>x</sub>/CoS@CC** electrode also shows good capacity retention after 10000 cycles. The results suggest that as-prepared material could be a promising candidate for the next-generation flexible supercapacitor device.

## 4.2 Experimental Section

### 4.2.1 Chemicals

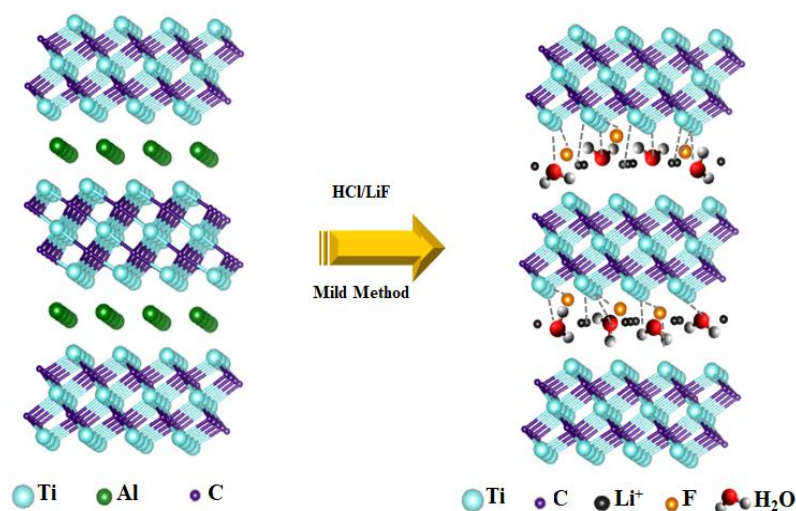
Cobalt chloride hexahydrate ( $\text{CoCl}_2 \cdot 6\text{H}_2\text{O}$ ) was purchased from SRL chemicals with < 99% purity and was stored in a vacuum desiccator. Thiourea was purchased from spectrochemical with <99% purity. MAX ( $\text{Ti}_3\text{AlC}_2$ ) phase precursor for synthesizing MXene ( $\text{Ti}_3\text{C}_2\text{T}_x$ ) was purchased from CARBON-Ukraine Ltd. All the other chemicals used were procured from SRL and TCI chemicals. Deionized water (DI water,  $18.2 \text{ M}\Omega\text{cm}^{-1}$ ) was used throughout the synthesis. Carbon cloth as the substrate was purchased from Vinpro Technologies (Hyderabad, India). All the chemicals were used as received without further purification.

### 4.2.2 Preparation of carbon cloth (CC) substrate

Initially, 1 x 3 cm carbon cloth (CC) strips were successively sonicated in acetone, ethanol, and DI water for 30 min in an ultrasonicator (PCI Analytics). Afterward, to further increase CC's hydrophilicity, the substrates were placed in 2 M nitric acid in a Teflon-lined autoclave and hydrothermally treated at  $130^\circ\text{C}$  for 2 h.[32] Finally, all the strips were cleaned using DI water and ethanol and baked at  $60^\circ\text{C}$  overnight in a vacuum oven.

### 4.2.3 Synthesis of MXene ( $\text{Ti}_3\text{C}_2\text{T}_x$ )

MXene ( $\text{Ti}_3\text{C}_2\text{T}_x$ ) was synthesized using selective etching of the Al layer from its corresponding MAX ( $\text{Ti}_3\text{AlC}_2$ ) phase (**Scheme 1**) [33]. Initially, 5 mL deionized water was added to a Teflon container, then 15 mL HCl (12 M) and 1.6 g LiF were added to it. Afterward, 1.0 g  $\text{Ti}_3\text{AlC}_2$  (MAX Phase) was added slowly into the solution over 5 min while stirring at 300 RPM. The reaction was allowed to proceed for 24 h. Afterward, the suspension was centrifuged at 5000 rpm for 10 minutes in a repeated manner until the pH was nearly neutral (>6). Finally, the obtained  $\text{Ti}_3\text{C}_2\text{T}_x$  was filtered and dried at  $60^\circ\text{C}$  for 8 h in a vacuum oven.



**Scheme 1.** Synthesis of  $\text{Ti}_3\text{C}_2\text{T}_x$  from  $\text{Ti}_3\text{AlC}_2$

#### 4.2.4 Synthesis of carbon cloth coated cobalt sulfide (CoS@CC)

A simple in-situ hydrothermal technique was used to deposit CoS on the CC substrate (**Scheme 2**). Firstly, 1.785g of  $\text{CoCl}_2 \cdot 6\text{H}_2\text{O}$  was dissolved in 70 mL of DI water and stirred for 1h at  $50^\circ\text{C}$ . Afterward, 3.045g of thiourea was slowly added to the above solution at  $30^\circ\text{C}$  and stirred for 30 more minutes. After that, the above solution was poured into a 100 mL Teflon autoclave containing CC ( $1 \times 3$  cm) substrate stuck on a glass slide. Finally, the autoclave was kept in an oven for 6 h at  $200^\circ\text{C}$ . After the cooling period, CoS-coated carbon cloth (CC) was removed from the autoclave, washed carefully with DI water and ethanol several times, and dried at  $60^\circ\text{C}$  overnight in a vacuum oven.

#### 4.2.5 Synthesis of carbon cloth-coated cobalt sulfide (CoS) and $\text{Ti}_3\text{C}_2\text{T}_x$ (MXene) ( $\text{Ti}_3\text{C}_2\text{T}_x/\text{CoS@CC}$ )

MXene ( $\text{Ti}_3\text{C}_2\text{T}_x$ ) suspension was prepared by grinding and dispersing 10 mg of  $\text{Ti}_3\text{C}_2\text{T}_x$  in 1 mL of ethanol under sonication for one h to obtain a homogeneous slurry. The appropriate amounts of the as-obtained suspension were uniformly drop-casted on three separate CoS@CC substrates to obtain  $\text{Ti}_3\text{C}_2\text{T}_x/\text{CoS@CC}$  having 1:3, 1:1 and 3:1 ratios of CoS and  $\text{Ti}_3\text{C}_2\text{T}_x$  (**Scheme 2**) (total sum amount of both materials was kept constant). Each electrode was dried in a vacuum oven for 2 h. For

the comparative study,  $\text{Ti}_3\text{C}_2\text{T}_x@\text{CC}$  was also fabricated by drop-casting of  $\text{Ti}_3\text{C}_2\text{T}_x$  suspension on carbon cloth of the same dimension.

#### **4.2.6 Material characterizations**

Powder X-ray diffraction (PXRD, Bruker's AXA D8 Advance system) in the  $2\theta$  range of 5 to  $60^\circ$  at a scanning rate of  $0.02^\circ \text{ min}^{-1}$  with  $\text{CuK}_\alpha$  ( $\lambda = 1.54 \text{ \AA}$ ) as the source was carried out. Morphological and elemental mapping has been done using field emission scanning electron microscopy (FE-SEM) (Jeol -7610F Plus) equipped with energy-dispersive spectroscopy (EDS) setup. Raman spectroscopy (Lab RAM HR Evolution) was done using Nd: YAG LASER with wavelength  $\lambda = 532 \text{ nm}$ .

#### **4.2.7 Electrochemical measurements**

The electrochemical measurements were done using Autolab 204 potentiostat in a standard three-electrode cell setup. It consists of Pt as a counter electrode, Ag/AgCl as a reference electrode, and carbon cloth (CC) of size  $1 \times 1 \text{ cm}$  deposited with our desired materials as a working electrode. All the measurements were carried out in a 1 M KOH electrolyte. Cyclic voltammetry (CV) and constant current charge-discharge (GCD) were performed in the potential range of -0.1 to 0.5 V at different scan rates and current densities. Electrochemical impedance spectroscopy (EIS) was carried out in the frequency range of 0.1 Hz to 100 kHz with 10 mV AC amplitude.

#### **4.2.8 Fabrication of flexible symmetric supercapacitor (SSC) device**

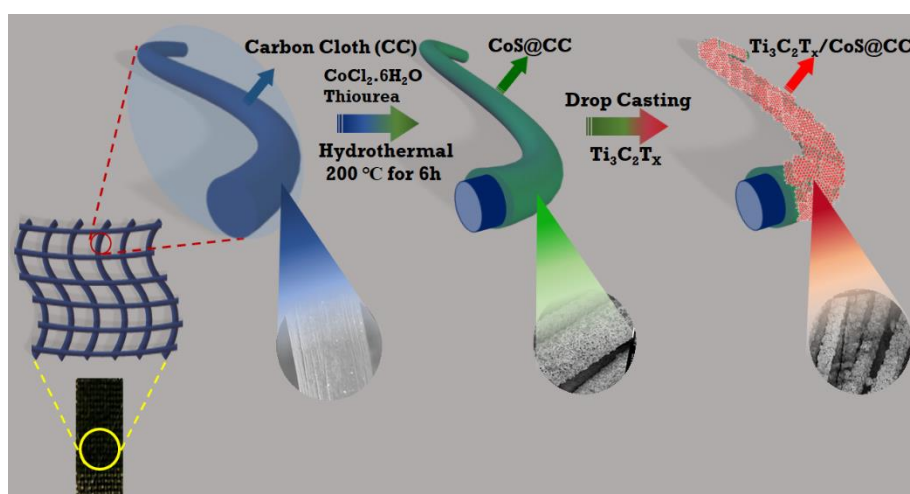
The flexible symmetric supercapacitor was fabricated using  $\text{Ti}_3\text{C}_2\text{T}_x/\text{CoS}@\text{CC}$  as the electrode, polyvinyl alcohol-potassium hydroxide (PVA-KOH) as an electrolyte, and cellulose paper as a separator. PVA-KOH electrolyte solution was prepared by adding 1g of PVA in 10 mL of DI water; subsequently, the resultant solution was heated at  $90^\circ\text{C}$  for 3 hr with continuous stirring, followed by the addition of 1M KOH solution. Afterward, the flexible device was fabricated by

sandwiching the cellulose paper with two electrodes wetted with the electrolyte solution, followed by drying of the assembly. After fabrication, electrochemical measurements such as CV and GCD of the flexible symmetrical device were investigated.

## 4.3 Results and Discussion

### 4.3.1 Synthesis and Characterization

A hydrothermal synthetic approach was used to grow **CoS** nanostructure on carbon cloth using cobalt chloride and urea as precursors (**Scheme 2**). The hydrothermally deposited CoS on CC (**CoS@CC**) serves as the substrate for further deposition of  $\text{Ti}_3\text{C}_2\text{T}_x$  by drop-casting, which leads to the formation of  **$\text{Ti}_3\text{C}_2\text{T}_x/\text{CoS@CC}$** . For the purpose of comparison,  $\text{Ti}_3\text{C}_2\text{T}_x$  deposited carbon cloth ( **$\text{Ti}_3\text{C}_2\text{T}_x@CC$** ) was also fabricated by drop-casting  $\text{Ti}_3\text{C}_2\text{T}_x$  suspension on CC. The structural and morphological characterizations of the as-synthesized **CoS@CC**,  **$\text{Ti}_3\text{C}_2\text{T}_x@CC$** , and  **$\text{Ti}_3\text{C}_2\text{T}_x/\text{CoS@CC}$**  were done using different characterization techniques. Besides imparting conductivity,  $\text{Ti}_3\text{C}_2\text{T}_x$  also augments the specific surface area of the overall composite. Therefore, because of their synergistic effects, both components,  $\text{Ti}_3\text{C}_2\text{T}_x$  and CoS, improve the supercapacitor performance of the  **$\text{Ti}_3\text{C}_2\text{T}_x/\text{CoS@CC}$**  composite.



**Scheme 2.** Synthesis of **CoS@CC** and  **$\text{Ti}_3\text{C}_2\text{T}_x/\text{CoS@CC}$**

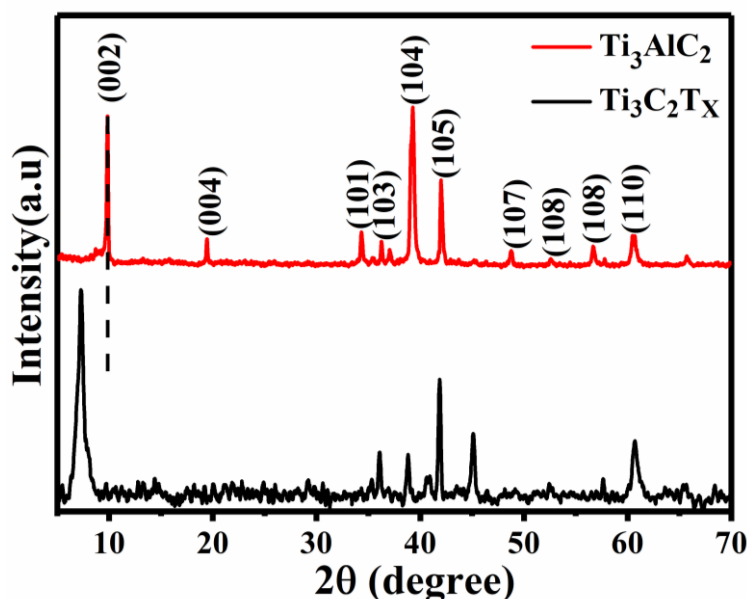


**Figure 4.1** PXRD pattern of  $\text{Ti}_3\text{AlC}_2$  and  $\text{Ti}_3\text{C}_2\text{T}_x$

To confirm the MAX to MXene transformation, the powder X-ray diffraction patterns of  $\text{Ti}_3\text{C}_2\text{T}_x$  and  $\text{Ti}_3\text{AlC}_2$  have been compared (**Figure 4.1**). The figure indicates that, in  $\text{Ti}_3\text{C}_2\text{T}_x$ , the intensity of the characteristic (104) peak, due to aluminum, at  $39^\circ$  is significantly reduced, suggesting the etching of the large fraction of Al from the  $\text{Ti}_3\text{AlC}_2$  phase. Moreover, due to an increase in the interplanar distance, the (002) peak in  $\text{Ti}_3\text{C}_2\text{T}_x$  ( $6.38^\circ$ ) is observed to be shifted towards a lower angle compared to that in  $\text{Ti}_3\text{AlC}_2$  ( $9.6^\circ$ ). Both observations collectively confirm the successful transformation of  $\text{Ti}_3\text{AlC}_2$  phase into  $\text{Ti}_3\text{C}_2\text{T}_x$  MXene.[34] The diffraction patterns of as-prepared  $\text{Ti}_3\text{C}_2\text{T}_x@CC$ ,  $\text{CoS}@CC$ , and  $\text{Ti}_3\text{C}_2\text{T}_x/\text{CoS}@CC$  are depicted in **Figure 4.2a**. The  $\text{Ti}_3\text{C}_2\text{T}_x@CC$  diffraction pattern shows the (002) peaks of  $\text{Ti}_3\text{C}_2\text{T}_x$  at  $6.38^\circ$  along with (004) and (110) plane peaks at  $22^\circ$  and  $60^\circ$ , respectively. In the case of  $\text{CoS}@CC$ , diffraction peaks centered at  $2\theta$  values of  $31.08^\circ$ ,  $35.54^\circ$ ,  $44.64^\circ$ ,  $54.9^\circ$ ,  $64.77^\circ$ , corresponding to (100), (101), (102), (110), and (200) planes, respectively, were observed for CoS, perfectly matching with JCPDS No # 65-3418.[35] The PXRD pattern of  $\text{Ti}_3\text{C}_2\text{T}_x/\text{CoS}@CC$  shows diffraction peaks at  $2\theta$  values  $6.5^\circ$ ,  $22.7^\circ$ ,  $35.18^\circ$ ,  $45.04^\circ$ ,  $60.1^\circ$ , and

65.24°, corresponding to both  $\text{Ti}_3\text{C}_2\text{T}_x$  and CoS components. Additionally, in all the samples, peaks at 25° and 43° correspond to (002) and (101) planes of carbon cloth, which has been used as a flexible substrate. [36] In all the samples, the absence of any additional peak confirms their phase purity.

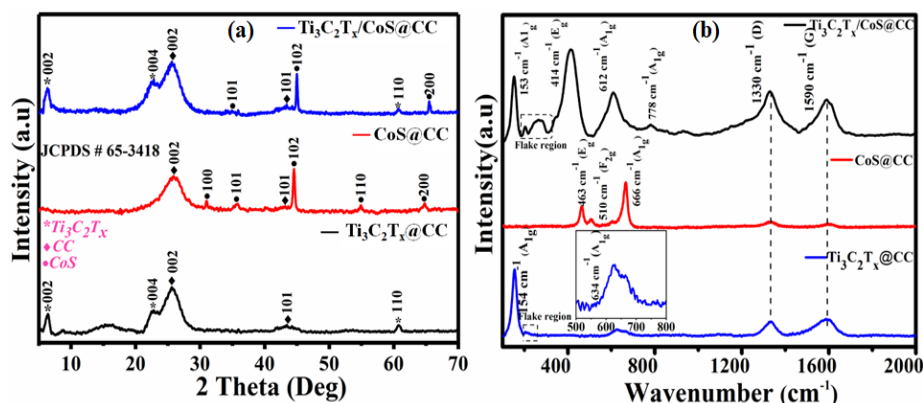


**Figure 4.2** (a) P-XRD pattern of  $\text{Ti}_3\text{C}_2\text{T}_x@CC$ ,  $\text{CoS}@CC$ , and  $\text{Ti}_3\text{C}_2\text{T}_x/\text{CoS}@CC$ ; (b) Raman Spectra of  $\text{Ti}_3\text{C}_2\text{T}_x@CC$ ,  $\text{CoS}@CC$ , and  $\text{Ti}_3\text{C}_2\text{T}_x/\text{CoS}@CC$

To probe the different vibrational modes and structural fingerprints, Raman spectroscopy for all the materials was performed (**Figure 4.2b**). For comparison, the Raman spectrum of bare carbon cloth was recorded, which showed typical D, G, and 2D bands at 1350, 1590, and 2642  $\text{cm}^{-1}$ , respectively, explaining its disordered graphitic nature (**Figure 4.3**). [37]

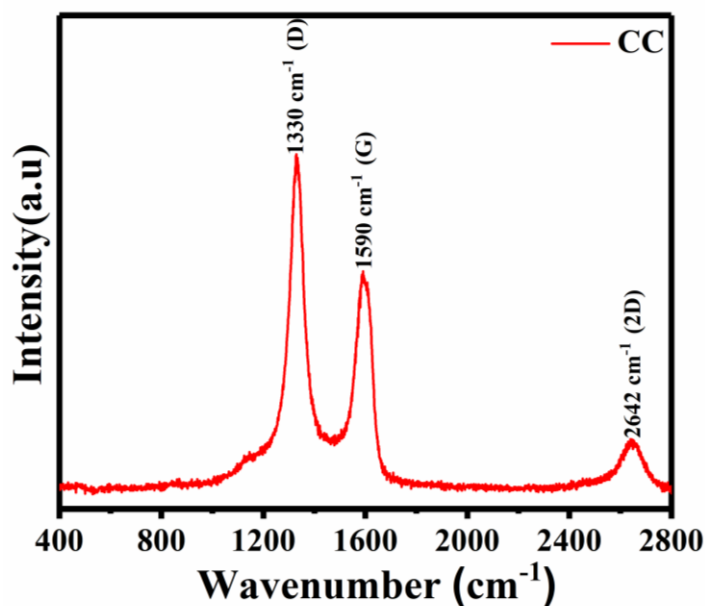


**Figure 4.3** Raman Spectrum of carbon cloth (CC)

For  $\text{Ti}_3\text{C}_2\text{T}_x@CC$ , besides carbon cloth peaks, two  $A_{1g}$  out-of-plane vibration modes for the titanium outer layer and carbon layer of  $\text{Ti}_3\text{C}_2\text{T}_x$  were observed at 154 and 634  $\text{cm}^{-1}$ , respectively, along with the flake vibration. As the Raman spectra were recorded using a 532 nm laser source, the resonant peak of  $\text{Ti}_3\text{C}_2\text{T}_x$  was not observed (observed only for a 785 nm laser source).[38] In the case of  $\text{CoS}@CC$ , peaks at 463, 510, and 666  $\text{cm}^{-1}$  were observed, indicating  $E_g$ ,  $F_{2g}$ , and  $A_{1g}$  modes of vibration, respectively, of CoS.[39] In  $\text{Ti}_3\text{C}_2\text{T}_x/\text{CoS}@CC$ , the vibrational mode corresponding to both  $\text{Ti}_3\text{C}_2\text{T}_x$  and CoS were observed, confirming the presence of both components.

Field emission scanning electron microscopy (FE-SEM) has been done to understand the sample morphologies. **Figure 4.4a** shows the SEM image of  $\text{Ti}_3\text{C}_2\text{T}_x$ , in which layers of  $\text{Ti}_3\text{C}_2\text{T}_x$  sheets can be clearly seen. The SEM image of CoS (from the residue powder settled on the bottom of the Teflon reactor during its insitu deposition on carbon cloth) is given in **Figure 4.4b**, revealing a hierarchical flower-like morphology of CoS. Such morphology is always beneficial in electrochemical energy storage as it offers most of its surface area accessible to the electrolyte, allowing enhanced Faradaic and capacitive processes. The EDX spectra of  $\text{Ti}_3\text{C}_2\text{T}_x$  and CoS (**Figure 4.5a&b**) show

an appropriate proportion of the corresponding elements ( $\text{Ti}_3\text{C}_2\text{T}_x$  also shows traces of unetched Al).

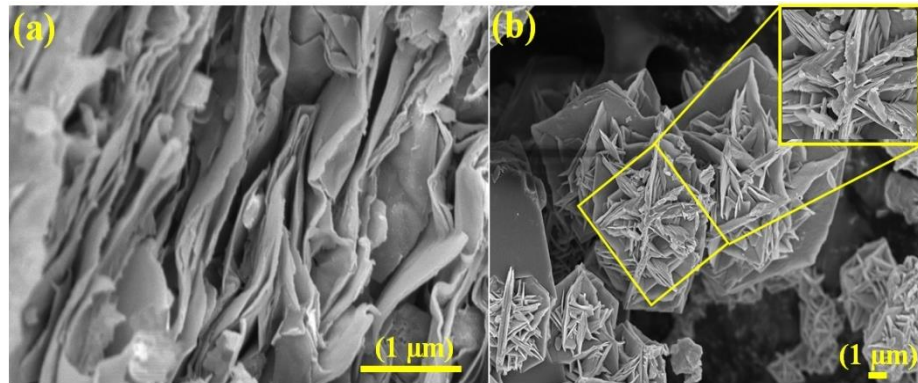


Figure 4.4 (a, b). FESEM of  $\text{Ti}_3\text{C}_2\text{T}_x$  and  $\text{CoS}$

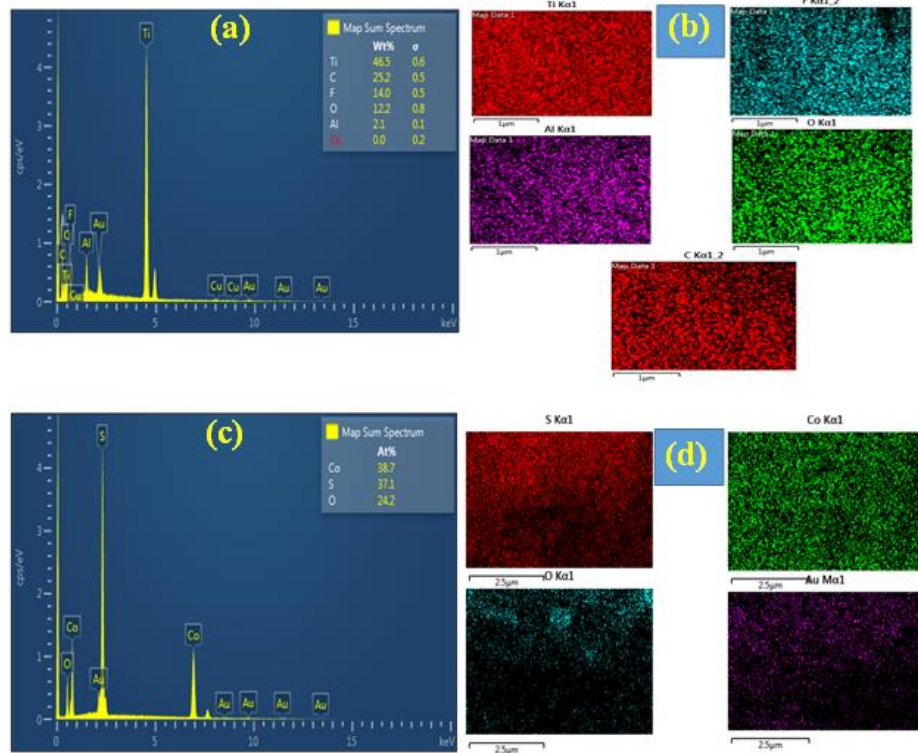
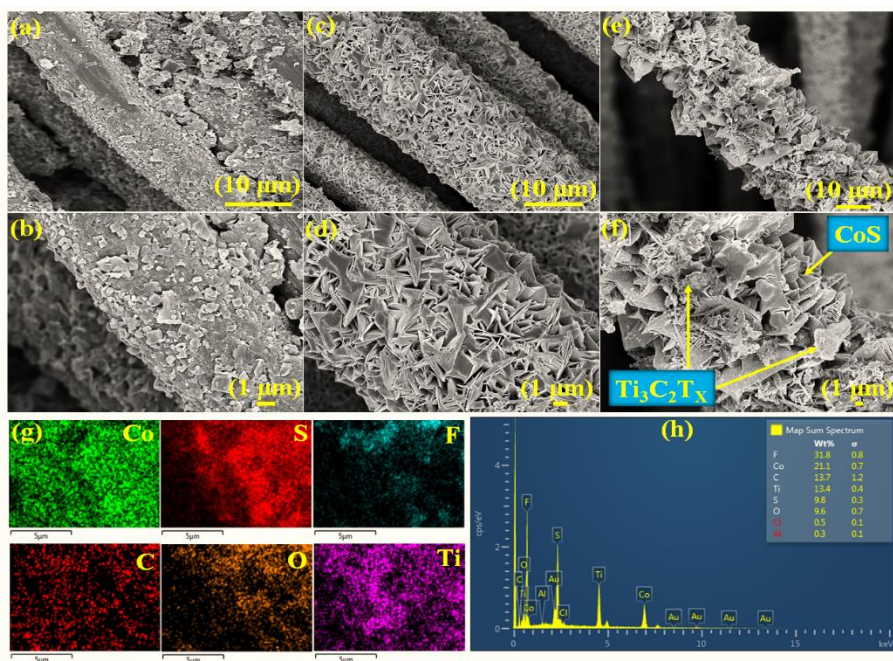


Figure 4.5 (a, b, c, d). EDX and elemental mapping of  $\text{Ti}_3\text{C}_2\text{T}_x$  and  $\text{CoS}$

The micrographs of  $\text{Ti}_3\text{C}_2\text{T}_x@\text{CC}$  indicate the uniform deposition of  $\text{Ti}_3\text{C}_2\text{T}_x$  sheets on each fiber of the carbon cloth (**Figure 4.6a, b**). The SEM images of  $\text{CoS}@\text{CC}$  are depicted in **Figure 4.6c&d**, showing consistent growth of flower-type CoS on individual fibers of the carbon cloth. In the SEM images of  $\text{Ti}_3\text{C}_2\text{T}_x/\text{CoS}@\text{CC}$ , uniform deposition of both  $\text{Ti}_3\text{C}_2\text{T}_x$  sheets and CoS flowers on CC fibers can be observed.. The same is further supplemented by EDX and elemental mapping studies of  $\text{Ti}_3\text{C}_2\text{T}_x/\text{CoS}@\text{CC}$ . In the EDX spectrum (**Figure 4.6g**), the presence of suitable proportions of F, C, Ti, O, Co, and S, along with traces of Al, are evident. The elemental mapping from a selected area of a carbon fiber reveals the homogeneous distribution of Co, S, F, C, O, and Ti (**Figure 4.6h**). This suggests an effective compositionalization between two components with enhanced CoS/ $\text{Ti}_3\text{C}_2\text{T}_x$  interfaces to maximize the synergy.



**Figure 4.6** FE-SEM images of (a,b)  $\text{Ti}_3\text{C}_2\text{T}_x@\text{CC}$ , (c,d)  $\text{CoS}@\text{CC}$ , (e,f)  $\text{Ti}_3\text{C}_2\text{T}_x/\text{CoS}@\text{CC}$  at lower and higher magnification; (g) Elemental mapping of  $\text{Ti}_3\text{C}_2\text{T}_x/\text{CoS}@\text{CC}$  (h) EDX spectra of  $\text{Ti}_3\text{C}_2\text{T}_x/\text{CoS}@\text{CC}$

### 4.3.2 Electrochemical studies

The applicability of as-synthesized  $\text{Ti}_3\text{C}_2\text{T}_x/\text{CoS}@CC$  composite has been investigated as electrode material in supercapattery applications. Before performing the extensive electrochemical studies, the operational potential window for  $\text{Ti}_3\text{C}_2\text{T}_x/\text{CoS}@CC$  was optimized using cyclic voltammetry in the negative (-0.1 to -0.1V) as well as in positive (-0.1 to 0.5V) potential windows at  $100 \text{ mVs}^{-1}$  (**Figure 4.7a,b**). The cyclic voltammogram in the -0.1 to 0.5V potential window shows a much higher CV curve area ( $2.32 \times 10^{-2} \text{ A.V}$ ) and current response compared to those in the -0.8 to -0.1V potential window (CV curve area =  $6.89 \times 10^{-4} \text{ A.V}$ ). This confirms the best electrochemical performance of the  $\text{Ti}_3\text{C}_2\text{T}_x/\text{CoS}@CC$  electrode in the positive potential window. The upper limit of positive potential was determined by LSV experiment, in which the onset of OER was observed between 0.5 and 0.6 V (**Figure 4.7c**). Therefore, 0.5 V potential was fixed as an upper limit of the best performance operational potential window (-0.1 to 0.5 V). Therefore, all the electrochemical studies have been done in the -0.1 to 0.5V potential window.

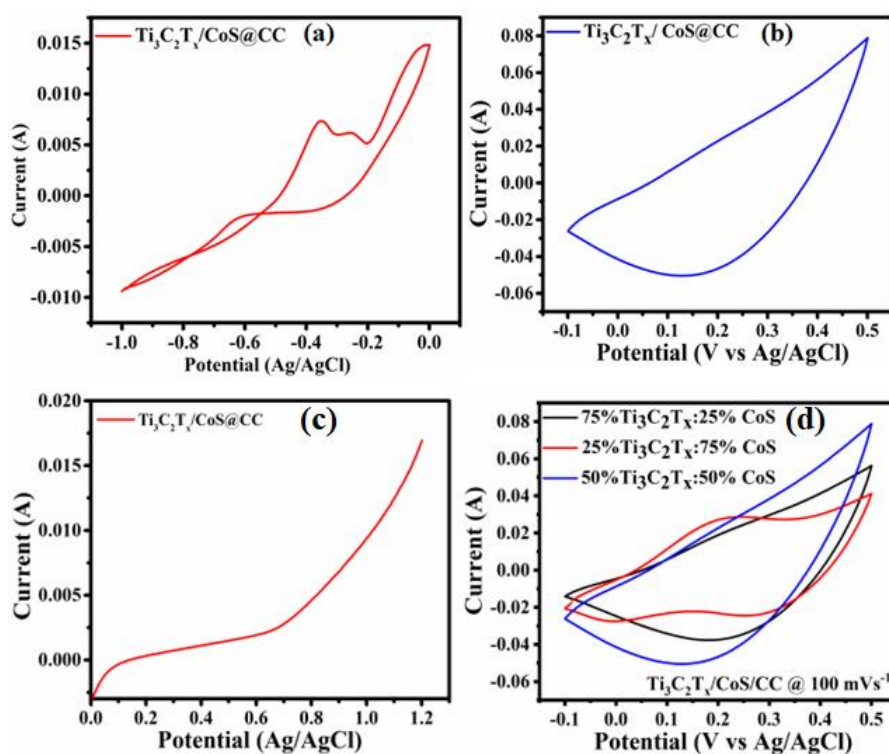


**Figure 4.7** CV curves of  $\text{Ti}_3\text{C}_2\text{T}_x/\text{CoS}@CC$  in negative and positive potential windows at  $100 \text{ mVs}^{-1}$ . (c) Linear Sweep Voltammetry of  $\text{Ti}_3\text{C}_2\text{T}_x/\text{CoS}@CC$  positive potential. (d) CV profiles of different ratios of  $\text{Ti}_3\text{C}_2\text{T}_x/\text{CoS}@CC$

Further, to achieve the suitable proportion of CoS and  $\text{Ti}_3\text{C}_2\text{T}_x$  for the best performance of the composite, three relative ratios of 3:1, 1:1, and 1:3 of  $\text{Ti}_3\text{C}_2\text{T}_x$  and CoS were deposited on CC. The cyclic voltammetry studies of the three electrodes in the potential range  $-0.1 \text{ V}$  to  $0.5 \text{ V}$  at  $100 \text{ mVs}^{-1}$  scan rate (**Figure 4.7d**) suggest that the electrode having 1:3 ratio of  $\text{Ti}_3\text{C}_2\text{T}_x$  and CoS shows the least current. Upon increasing the relative proportion of  $\text{Ti}_3\text{C}_2\text{T}_x$ , the current increases up to a 1:1 ratio because of the increase in the overall electrical conductivity imparted by  $\text{Ti}_3\text{C}_2\text{T}_x$ , which facilitates the Faradaic process in CoS. However, further increasing the  $\text{Ti}_3\text{C}_2\text{T}_x$  proportion beyond the 1:1 ratio leads to a current reduction, as observed with the electrode having a 3:1 ratio. This is because the excess  $\text{Ti}_3\text{C}_2\text{T}_x$  hinders the direct connections between CoS and  $\text{Ti}_3\text{C}_2\text{T}_x$ , reducing the overall electrochemical performance.[40] Therefore, the composite with a 1:1 ratio was selected

for further electrochemical studies (throughout this paper, the notation **Ti<sub>3</sub>C<sub>2</sub>T<sub>x</sub>/CoS@CC** represents the 1:1 mass ratio of Ti<sub>3</sub>C<sub>2</sub>T<sub>x</sub> and CoS).

The comparative electrochemical behavior of **Ti<sub>3</sub>C<sub>2</sub>T<sub>x</sub>@CC**, **CoS@CC**, and **Ti<sub>3</sub>C<sub>2</sub>T<sub>x</sub>/CoS@CC** was investigated using cyclic voltammetry (CV), galvanostatic charge–discharge (GCD), and electrochemical impedance spectroscopy (EIS) techniques in 1 M aqueous KOH electrolyte. **Figure 4.8a** presents the comparison of CV profiles of **Ti<sub>3</sub>C<sub>2</sub>T<sub>x</sub>@CC**, **CoS@CC**, and **Ti<sub>3</sub>C<sub>2</sub>T<sub>x</sub>/CoS@CC** in the potential range of -0.1 to 0.5V at a scan rate of 100 mVs<sup>-1</sup>. The shape of each voltammogram indicates the occurrence of some redox processes, which are associated with their respective electrode material coated on the carbon cloth. The faradaic reactions involved in Ti<sub>3</sub>C<sub>2</sub>T<sub>x</sub> and CoS in the alkaline electrolytes can be proposed as [31]:



The comparison of CV profiles of three electrodes reveals the highest current value for **Ti<sub>3</sub>C<sub>2</sub>T<sub>x</sub>/CoS@CC**. This suggests that the electrochemical performance of the composite electrode is better than the electrodes loaded with the individual component, mainly because of the fast charge propagation and minimized internal resistance arising from the synergistic effect of the two components.[30] Further, to understand the charge storage mechanism, CVs of **Ti<sub>3</sub>C<sub>2</sub>T<sub>x</sub>@CC**, **CoS@CC**, and **Ti<sub>3</sub>C<sub>2</sub>T<sub>x</sub>/CoS@CC** were also recorded at varying scan rates (5–100 mVs<sup>-1</sup>) (**Figure 4.8b,c&d**). As expected, an increase in the current was observed for each electrode with an increasing scan rate. The CVs of **CoS@CC**, with increasing scan rate, show a gradual increase in separation between anodic and cathodic peaks. This could be attributed to slow electron kinetics in CoS due to its inferior conductivity, leading to a quasi-reversible redox process.[41] However, this effect is less pronounced in the composite electrode

$\text{Ti}_3\text{C}_2\text{T}_x/\text{CoS}@CC$  because of its improved conductivity due to the blending of highly conducting  $\text{Ti}_3\text{C}_2\text{T}_x$ .

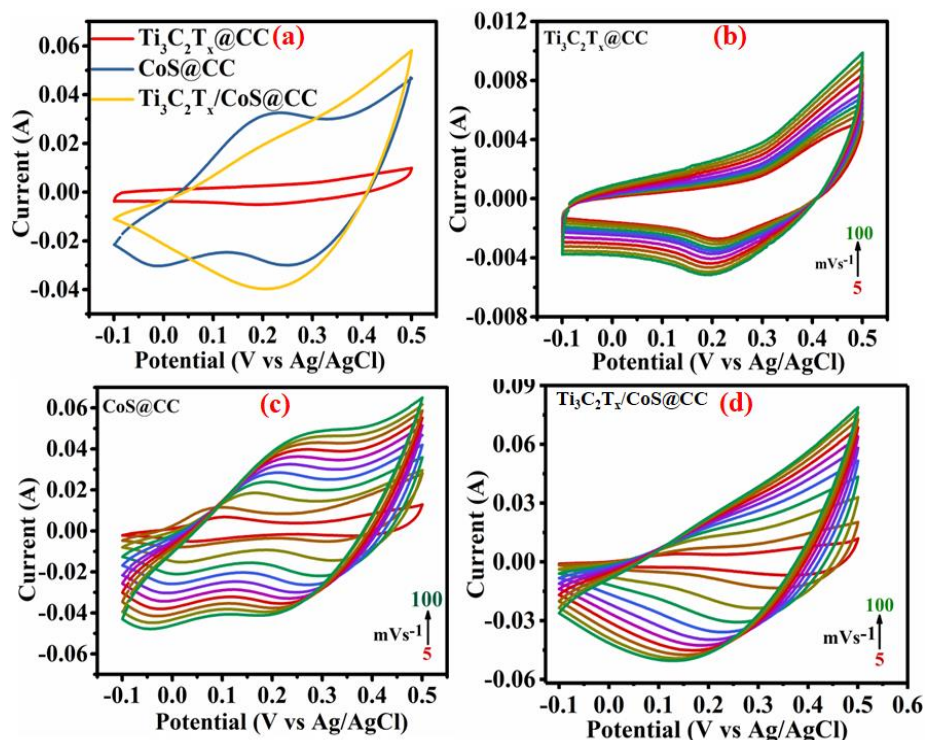


**Figure 4.8** (a) Comparison of CVs of  $\text{Ti}_3\text{C}_2\text{T}_x@CC$ ,  $\text{CoS}@CC$ , and  $\text{Ti}_3\text{C}_2\text{T}_x/\text{CoS}@CC$  at a scan rate of 100 mVs<sup>-1</sup> in 1M KOH; (b,c,d) CV profiles of  $\text{Ti}_3\text{C}_2\text{T}_x@CC$ ,  $\text{CoS}@CC$  and  $\text{Ti}_3\text{C}_2\text{T}_x/\text{CoS}@CC$  at different scan rates (5—100 mVs<sup>-1</sup>).

The cyclic voltammetric data at different scan rates were used to understand the percentage contribution of the diffusion-controlled capacitance (due to the Faradic process) and the surface capacitance (due to EDLC) to the overall capacitance of the  $\text{Ti}_3\text{C}_2\text{T}_x@CC$ ,  $\text{CoS}@CC$  and  $\text{Ti}_3\text{C}_2\text{T}_x/\text{CoS}@CC$  using Dunn's method.[42]

The bar charts for the percentage capacitance contributions of the capacitive and diffusion processes for  $\text{Ti}_3\text{C}_2\text{T}_x@CC$ ,  $\text{CoS}@CC$ , and  $\text{Ti}_3\text{C}_2\text{T}_x/\text{CoS}@CC$  at various scan rates (20 - 100 mVsec<sup>-1</sup>) are given in **Figures 4.9a**, **4.10a**, and **4.11a**, respectively. The calculated diffusion contribution to their overall CV profiles at 20 mVsec<sup>-1</sup> and 100 mVsec<sup>-1</sup> scan rates are also depicted in **Figures 4.9b&c**, **4.10b&c**, and **4.11b&c**, respectively. For all three electrodes, as the scan rate is

increased, the diffusion capacitance contribution decreases with an increase in the percentage contribution of the capacitive process.

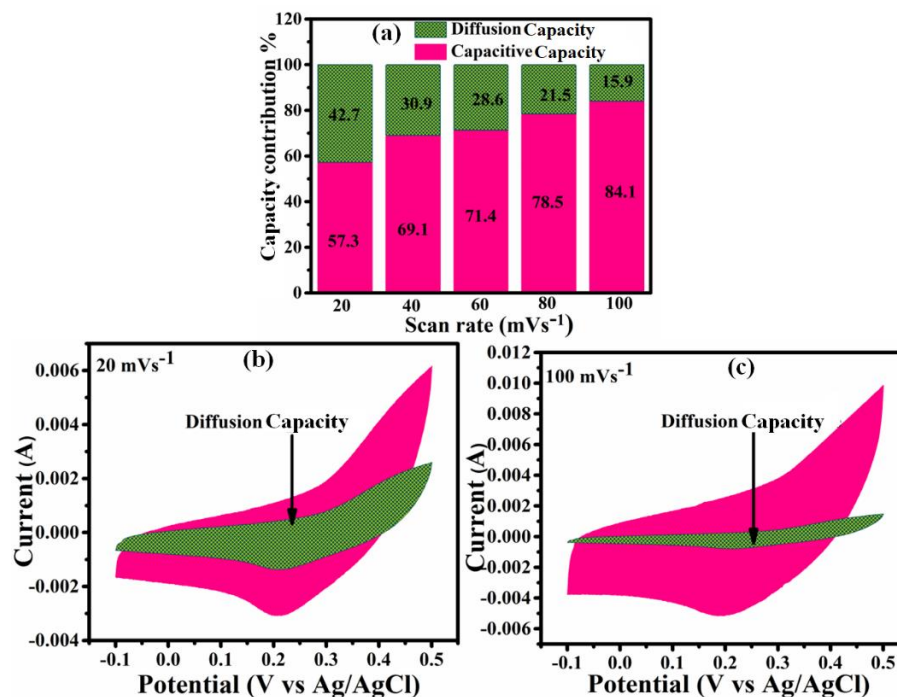


**Figure 4.9** (a) Percentage EDLC and pseudocapacitance contributions at different scan rates to the overall capacity of  $\text{Ti}_3\text{C}_2\text{T}_x@\text{CC}$ ; (b, c) Comparison of calculated CV profile of  $\text{Ti}_3\text{C}_2\text{T}_x@\text{CC}$  composite for diffusion only capacity and overall experimental CV at 20 and 100  $\text{mVs}^{-1}$  scan rates.

This is due to the fact that, at higher scan rates, double-layer formation out speeds the faradic process due to diffusion limitation. The overall capacitance of  $\text{Ti}_3\text{C}_2\text{T}_x@\text{CC}$  is mainly dominated by surface-controlled capacitance, behaving as an EDLC electrode. The small contribution from the diffusion process is due to the redox processes mentioned in equations 2 and 3. Unlike  $\text{Ti}_3\text{C}_2\text{T}_x@\text{CC}$ , for  $\text{CoS}@\text{CC}$ , almost the entire capacitance is due to the diffusion-controlled process, featuring a battery-type behavior due to the conversion reactions mentioned in equation 1. The charge storage in  $\text{Ti}_3\text{C}_2\text{T}_x/\text{CoS}@\text{CC}$  composite is mainly due to the Faradaic processes of the CoS component; however, it is further boosted due to enhanced conductivity imparted by the  $\text{Ti}_3\text{C}_2\text{T}_x$  component. Overall, from Dunn's analysis, it can be concluded

that the composite  $\text{Ti}_3\text{C}_2\text{T}_x/\text{CoS}@CC$  features a net behavior of a battery-type electrode, despite consisting of the two components showing EDLC and battery-type behaviors independently.

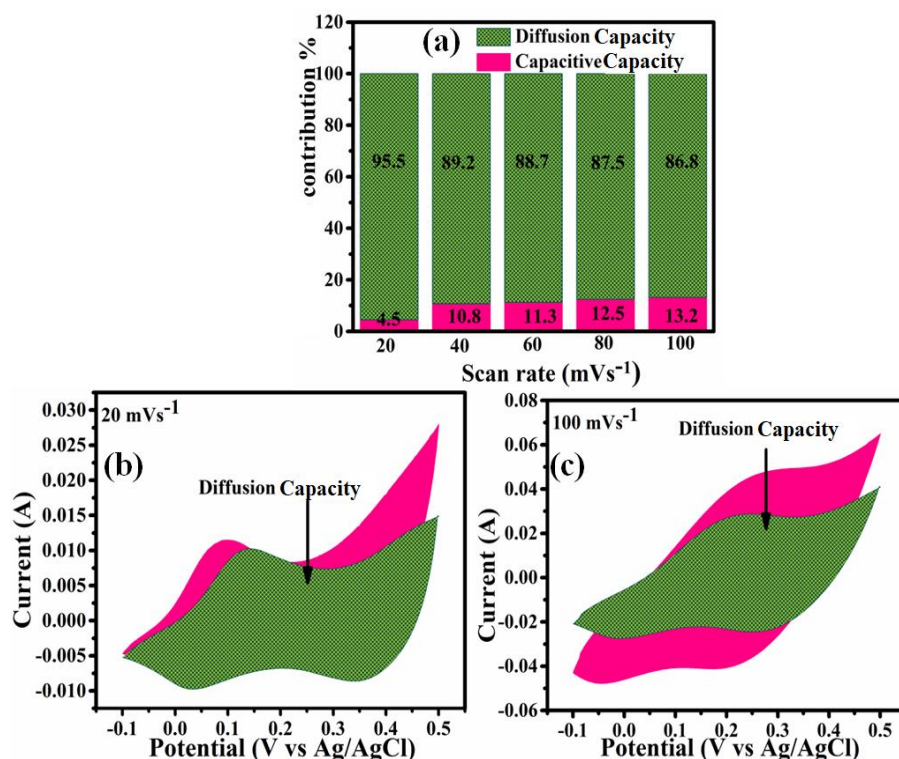


**Figure 4.10** (a) Percentage EDLC and pseudocapacity contributions at different scan rates to the overall capacity of  $\text{CoS}@CC$ ; (b, c) Comparison of calculated CV profile of  $\text{CoS}@CC$  composite for diffusion only capacity and overall experimental CV at 20 and 100  $\text{mVs}^{-1}$  scan rates.

To evaluate the specific capacity, galvanostatic charge-discharge (GCD) studies were performed for  $\text{Ti}_3\text{C}_2\text{T}_x@CC$ ,  $\text{CoS}@CC$ , and  $\text{Ti}_3\text{C}_2\text{T}_x/\text{CoS}@CC$ . The GCD profiles of  $\text{Ti}_3\text{C}_2\text{T}_x@CC$ ,  $\text{CoS}@CC$ , and  $\text{Ti}_3\text{C}_2\text{T}_x/\text{CoS}@CC$  at  $1 \text{ Ag}^{-1}$  have been shown in **Figure 4.12a**. The figure shows that the composite electrode  $\text{Ti}_3\text{C}_2\text{T}_x/\text{CoS}@CC$  shows the highest discharging time compared to its components  $\text{Ti}_3\text{C}_2\text{T}_x@CC$  and  $\text{CoS}@CC$ . The obtained specific capacities at  $1 \text{ Ag}^{-1}$ , calculated using the discharge curve of the GCD profile, were found to be  $10.4 \text{ Cg}^{-1}$ ,  $60 \text{ Cg}^{-1}$ , and  $120 \text{ Cg}^{-1}$  for  $\text{Ti}_3\text{C}_2\text{T}_x@CC$ ,  $\text{CoS}@CC$ , and  $\text{Ti}_3\text{C}_2\text{T}_x/\text{CoS}@CC$  respectively (**Figure 4.12b**). It is evident from the

specific capacity values that the synergistic effect between  $\text{Ti}_3\text{C}_2\text{T}_x$  and  $\text{CoS}$  leads to a significant increase in the specific capacity of  $\text{Ti}_3\text{C}_2\text{T}_x/\text{CoS}@CC$  compared to  $\text{CoS}@CC$  and  $\text{Ti}_3\text{C}_2\text{T}_x@CC$  alone.

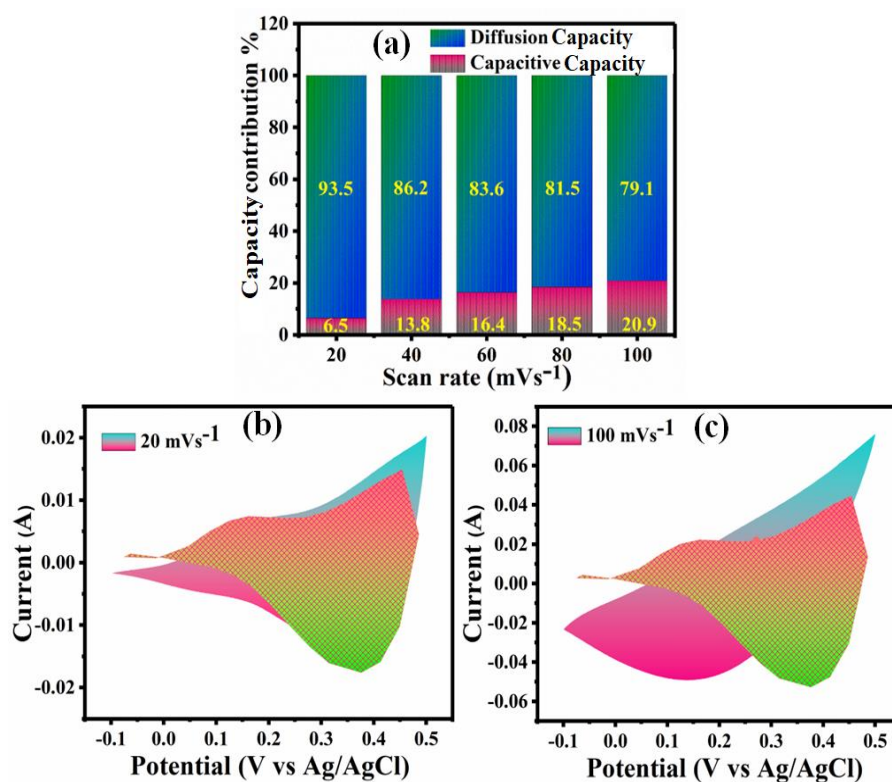


**Figure 4.11** (a) Percentage EDLC and pseudocapacity contributions at different scan rates to the overall capacity of  $\text{Ti}_3\text{C}_2\text{T}_x/\text{CoS}@CC$ ; (b, c) Comparison of calculated CV profile of  $\text{Ti}_3\text{C}_2\text{T}_x/\text{CoS}@CC$  composite for diffusion only capacity and overall experimental CV at 20 and 100  $\text{mVs}^{-1}$  scan rates.

The GCD studies were also performed at different current densities (Figure 4.13a-c), for  $\text{Ti}_3\text{C}_2\text{T}_x@CC$ ,  $\text{CoS}@CC$ , and  $\text{Ti}_3\text{C}_2\text{T}_x/\text{CoS}@CC$  to understand the rate capabilities of the materials. The change in specific capacities of  $\text{Ti}_3\text{C}_2\text{T}_x@CC$ ,  $\text{CoS}@CC$ , and  $\text{Ti}_3\text{C}_2\text{T}_x/\text{CoS}@CC$  with varying current densities has been given in Figure 4.13d. Except for  $\text{Ti}_3\text{C}_2\text{T}_x@CC$ , specific capacity values fall rapidly with increasing current density in  $\text{CoS}@CC$  and  $\text{Ti}_3\text{C}_2\text{T}_x/\text{CoS}@CC$ . This is because the specific capacities of electrode materials with predominant diffusion-controlled charge storage are known to exhibit such behavior due to the limited diffusion/electron

transfer rate at higher current density.[43,44] For  $\text{Ti}_3\text{C}_2\text{T}_x@\text{CC}$ , this effect is not much pronounced due to its high conductivity (facilitating electron transfer) and relatively higher proportion of surface-controlled capacitance.

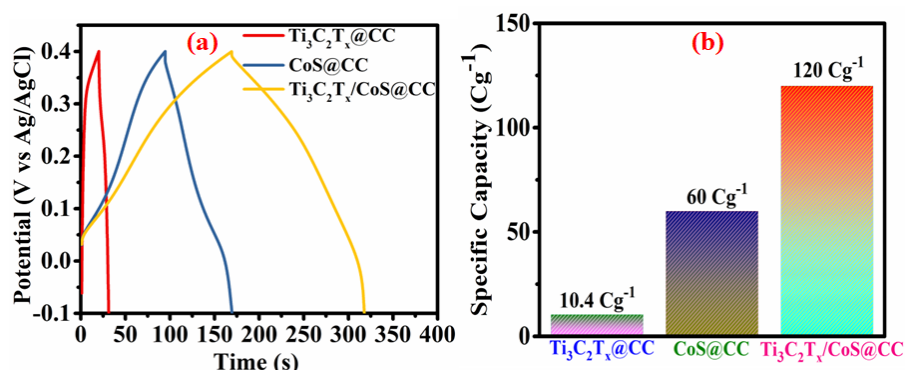


**Figure 4.12** (a) Comparison of GCD of  $\text{Ti}_3\text{C}_2\text{T}_x@\text{CC}$ ,  $\text{CoS}@\text{CC}$ , and  $\text{Ti}_3\text{C}_2\text{T}_x/\text{CoS}@\text{CC}$  at a current density of  $1 \text{ Ag}^{-1}$  in  $1 \text{ M KOH}$ ; (b) Comparison of specific capacity of  $\text{Ti}_3\text{C}_2\text{T}_x@\text{CC}$ ,  $\text{CoS}@\text{CC}$ , and  $\text{Ti}_3\text{C}_2\text{T}_x/\text{CoS}@\text{CC}$  at  $1 \text{ Ag}^{-1}$  in  $1 \text{ M KOH}$  (c) GCD profiles of  $\text{Ti}_3\text{C}_2\text{T}_x/\text{CoS}@\text{CC}$  at various current density.

Electrochemical impedance spectroscopy (EIS) in the frequency range of  $0.1 \text{ Hz}$ – $100 \text{ kHz}$  with a  $10 \text{ mV}$  AC amplitude was performed to understand the charge storage behavior and impedance of the three electrodes. [45,46] The Nyquist plots for  $\text{Ti}_3\text{C}_2\text{T}_x@\text{CC}$ ,  $\text{CoS}@\text{CC}$ , and  $\text{Ti}_3\text{C}_2\text{T}_x/\text{CoS}@\text{CC}$  are given in **Figure 4.14a**. From the Nyquist plot, it can be observed that the impedance line corresponding to  $\text{Ti}_3\text{C}_2\text{T}_x@\text{CC}$  is closest to the imaginary axis, which is followed by  $\text{Ti}_3\text{C}_2\text{T}_x/\text{CoS}@\text{CC}$  and  $\text{CoS}@\text{CC}$ . This observation suggests that, among three electrodes,  $\text{Ti}_3\text{C}_2\text{T}_x@\text{CC}$  has the relatively highest EDLC character, whereas  $\text{CoS}@\text{CC}$  has the lowest. The composite electrode  $\text{Ti}_3\text{C}_2\text{T}_x/\text{CoS}@\text{CC}$  falls in between its component electrodes. This observation is in accordance with the Dunn's method analysis performed on the three electrodes.

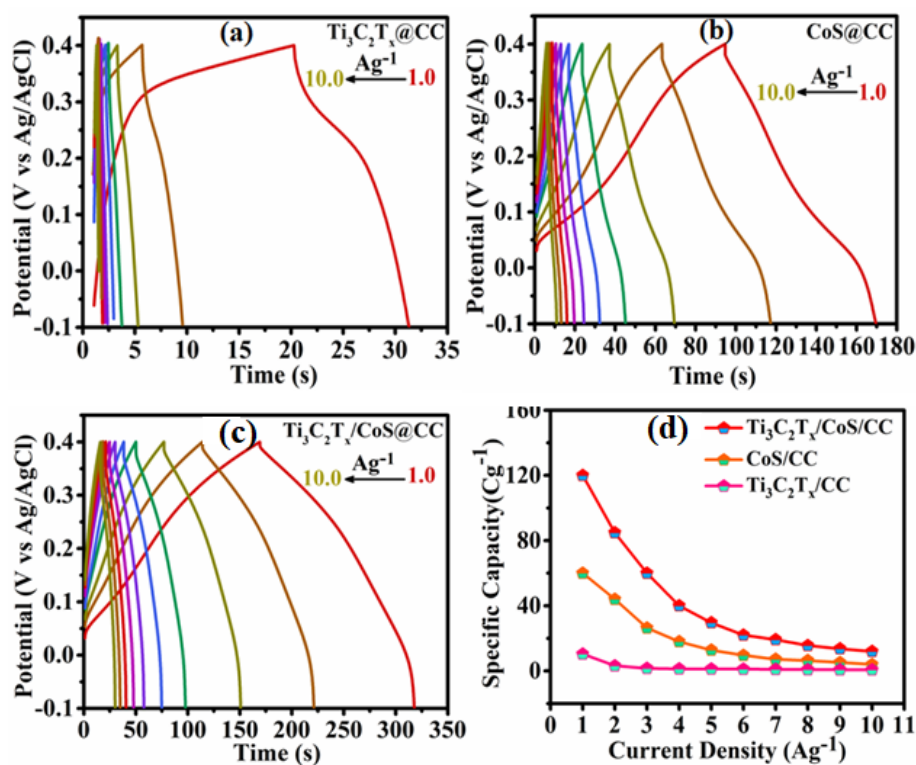


**Figure 4.13 (a-d).** GCD profiles of (a)  $\text{Ti}_3\text{C}_2\text{T}_x@CC$  (b)  $\text{CoS}@CC$  and (c)  $\text{Ti}_3\text{C}_2\text{T}_x/\text{CoS}@CC$  at various current density ranging from 1 to 10  $\text{A.g}^{-1}$  (d) Comparison of change in specific capacities of  $\text{Ti}_3\text{C}_2\text{T}_x@CC$ ,  $\text{CoS}@CC$ , and  $\text{Ti}_3\text{C}_2\text{T}_x/\text{CoS}@CC$  at various current density.

Cyclic stability is an important consideration for the practical application of any electrode material. Therefore, the cyclic stability of  $\text{Ti}_3\text{C}_2\text{T}_x/\text{CoS}@CC$  was studied for 1000 GCD cycles at a current density of 10  $\text{Ag}^{-1}$  (Figure 4.14b). The study reveals that, after 1000 cycles,  $\text{Ti}_3\text{C}_2\text{T}_x/\text{CoS}@CC$  shows 88.6% capacity retention, which is an acceptable value for practical ability. Moreover, the shapes of GCD profiles of the initial and last 25 cycles (given in the inset of Figure 4.14b) are almost unchanged, indicating the high stability of the  $\text{Ti}_3\text{C}_2\text{T}_x/\text{CoS}@CC$  electrode.

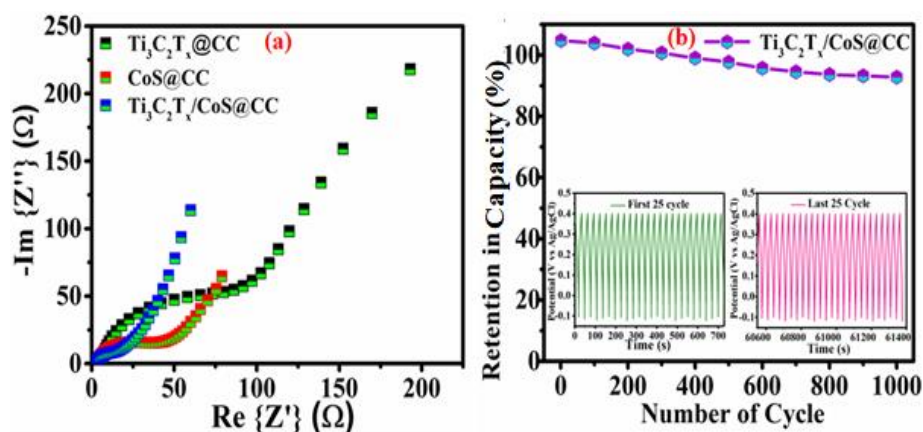


**Figure 4.14** (a) Nyquist plot of  $\text{Ti}_3\text{C}_2\text{T}_x@CC$ ,  $\text{CoS}@CC$ , and  $\text{Ti}_3\text{C}_2\text{T}_x/\text{CoS}@CC$ ; (b) Cycling stability of  $\text{Ti}_3\text{C}_2\text{T}_x/\text{CoS}@CC$  at  $10 \text{ Ag}^{-1}$  for 1000 cycles (insets show first and last 25 GCD cycles).

Furthermore, the cyclic voltammograms of the fresh electrode and that after 1000 cycles were also compared (**Figure 4.15a**), showing only a slight reduction in CV area after 1000 cycles. Also, the Nyquist plots of the fresh and after 1000 cycles  $\text{Ti}_3\text{C}_2\text{T}_x/\text{CoS}@CC$  show an almost similar pattern (**Figure 4.15b**). These observations corroborate that the cyclic stability and reversibility of the composite electrode material are maintained for the long run, even in the absence of any conducting additives or expensive commercial binders. To further investigate the compositional and morphological changes after cycling, FE-SEM, EDX, and elemental mapping (**Figure 4.16 a-c**) of the recycled  $\text{Ti}_3\text{C}_2\text{T}_x/\text{CoS}@CC$  were also done. Compared to the fresh electrode, the FESEM image of the recycled electrode shows an almost similar morphology of the coated carbon fiber. The EDX spectrum also shows the presence of all the elements of the electrode material (C, O, Ti, C, F, S and Al) along with the electrolyte(K), indicating that the electrode material maintains its compositional integrity after multiple cycles. Moreover, the elemental mapping of Na shows its uniform distribution, suggesting the accessibility of the electrolyte ions to the entire matrix of the electrode, which is beneficial for the diffusion and surface-controlled process occurring at the electrode.

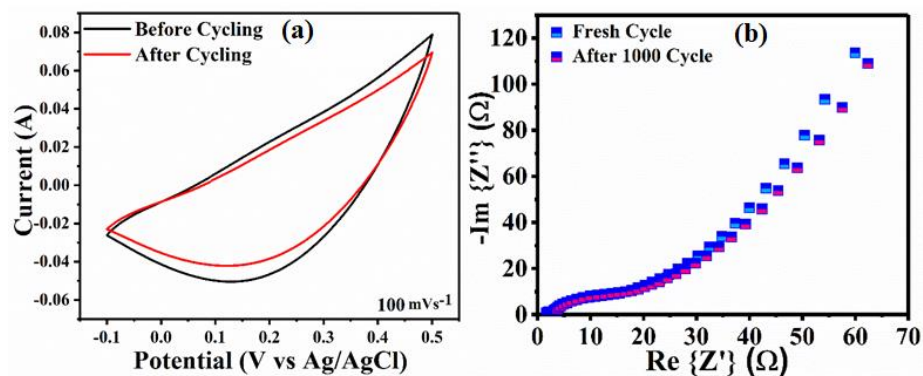


**Figure 4.15 (a,b).** Comparison of CVs of  $\text{Ti}_3\text{C}_2\text{T}_x/\text{CoS}/\text{CC}$  before after 1000 GCD cycles.

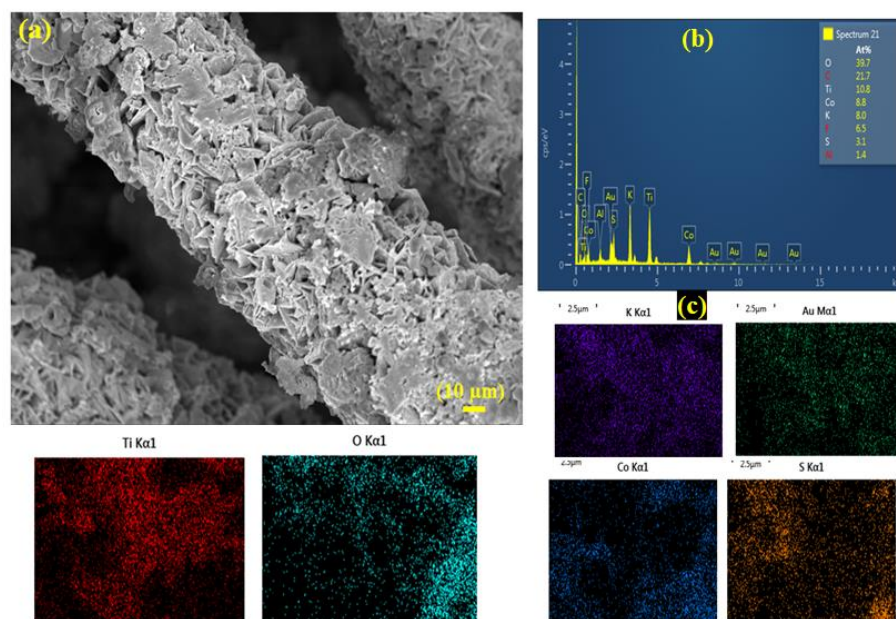


**Figure 4.16 (a)** FE-SEM images of  $\text{Ti}_3\text{C}_2\text{T}_x/\text{CoS}/\text{CC}$  after 1000 charge-discharge cycles. (b,c) EDX spectrum and elemental mapping of  $\text{Ti}_3\text{C}_2\text{T}_x/\text{CoS}/\text{CC}$  after 1000 charge-discharge cycles.

To demonstrate the practical applicability of the electrode, a flexible symmetric device ( $\text{Ti}_3\text{C}_2\text{T}_x/\text{CoS}@CC//\text{Ti}_3\text{C}_2\text{T}_x/\text{CoS}@CC$ ) was fabricated by sandwiching and a cellulose paper with composite electrodes wetted with PVA-KOH electrolyte, as depicted in **Figure 4.17a**. The CV curves of the device at various scan rates ranging from 5 to  $500 \text{ mV}\cdot\text{s}^{-1}$  in the potential window of 0 to 0.8V are shown in **Figure 4.17b**. It shows the non-rectangular shapes of curves with their area getting increased with increasing scan rate while maintaining their

shapes even at high scan rate. This observation indicates the excellent rate capability of the device. To further emphasize the flexible character of the device, CVs of the device were recorded under stretching, bending, and twisting conditions (**Figure 17c,d&e**). As evident from the figure, the shapes and areas of CVs recorded under different mechanical stresses remain almost unaltered, confirming the excellent flexible behavior of the device without any compromise in the electrochemical performance. This is due to the robust and effective  $\text{Ti}_3\text{C}_2\text{T}_x/\text{CoS}$  interface showing synergy, which is not hampered by mechanical stress.

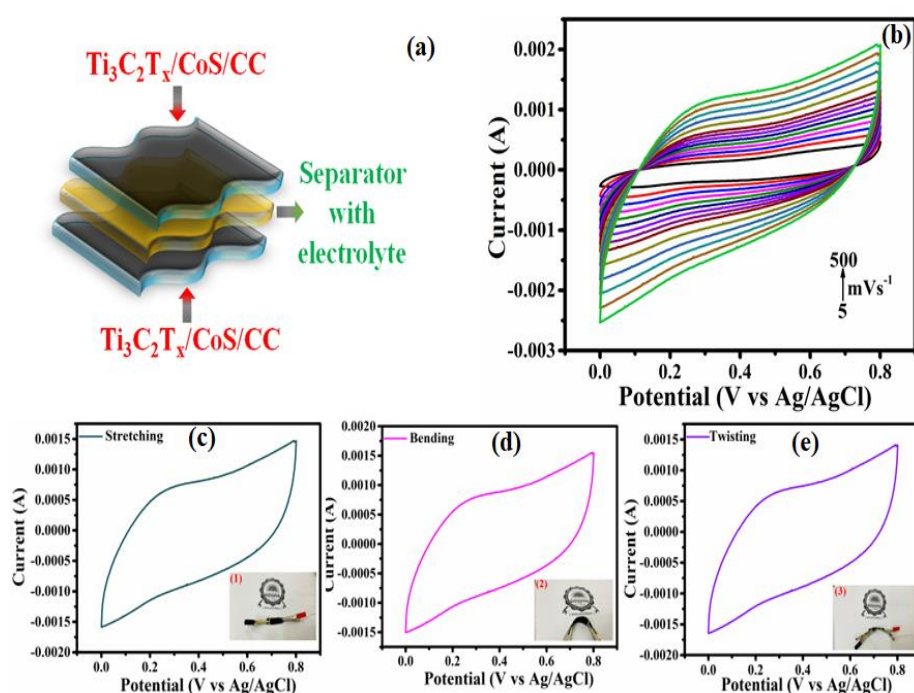


**Figure 4.17** (a) Schematic of the flexible symmetric device (b) CV profiles of the flexible symmetric device at different scan rates (5-500  $\text{mVs}^{-1}$ ), (c,d,e) comparison of CV profiles in stretching, bending, and twisting condition.

The GCD studies for the device at various current densities (1 – 10  $\text{A.g}^{-1}$ ) were conducted to determine its rate capability (**Figure 4.18a**). The non-symmetric nature of GCD curves suggests the overall capacitance mainly originating from the quasi-reversible faradic processes. At 1  $\text{A.g}^{-1}$  current density, the device shows a maximum specific capacity of 117.2  $\text{C.g}^{-1}$  (**Figure 4.18b**). Upon increasing current

density, unlike a gradual reduction in specific capacitance observed in the three-electrode configuration (having aqueous KOH electrolyte), in the device (having semisolid PVA-KOH electrolyte), the specific capacity is lost drastically up to  $2 \text{ A.g}^{-1}$ , and afterward remains almost constant up to  $10 \text{ A.g}^{-1}$ . This can be explained by the fact that, in a semisolid electrolyte, the diffusion-controlled process is severely restricted.[44] Therefore, pseudocapacitive contribution wanes relatively quickly upon increasing the current density, and the residual EDLC capacitance becomes the dominant contributor to the overall capacitance, which remains almost unaltered even at higher current densities.

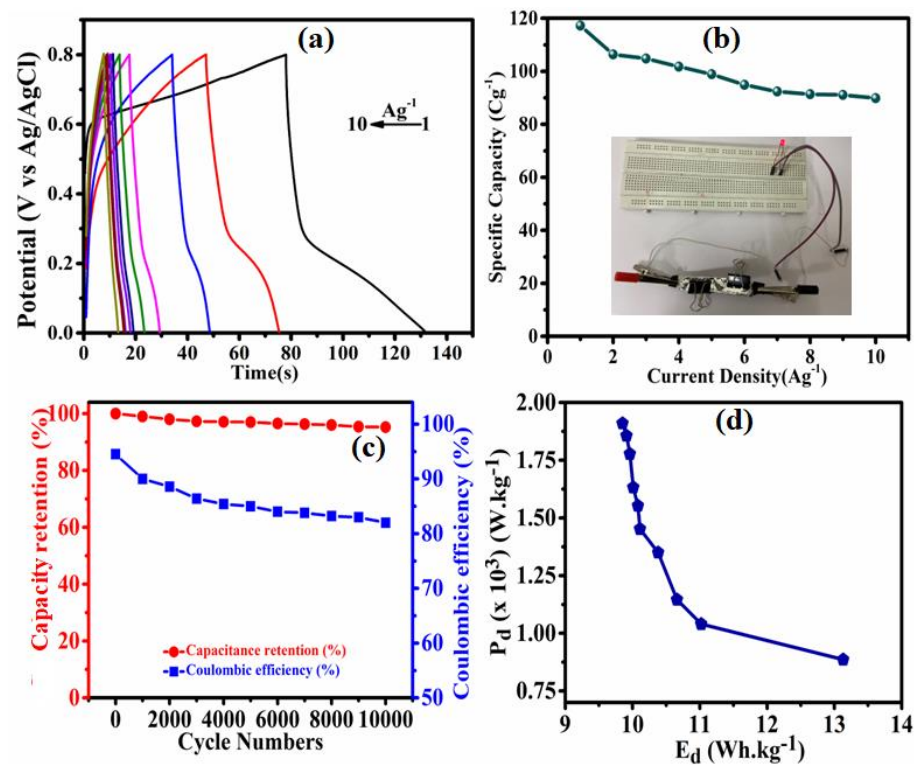


**Figure 4.18** (a) GCD profiles of the flexible symmetric device at different current densities ( $1\text{-}10 \text{ A.g}^{-1}$ ), (b) Specific capacity variations of the device with changing current densities ( $1\text{-}10 \text{ A.g}^{-1}$ ), (c) Cycling performance and Coulombic efficiency of the device at  $10 \text{ A.g}^{-1}$  for 10000 consecutive cycles (d) Ragone plot of energy density vs. power density of the device along with some similar electrode materials reported recently.

The cyclic stability of the device has been carried out for 10000 consecutive cycles at  $10 \text{ A.g}^{-1}$  current density in the potential window of 0-0.8 V (**Figure 4.18c**). It shows a capacity retention of 93.41 % after 10000 charging-discharging cycles, confirming the excellent cyclic stability of the fabricated device. Further, the initial coulombic efficiency of 91.63 % reduces only by 8 % after 10000 cycles. **Figure 4.18d** depicts the Ragone plot of the flexible symmetric supercapacitor device. The as-prepared flexible symmetric device shows a maximum energy density of  $13.3 \text{ Wh.kg}^{-1}$  at a power density of  $0.86 \text{ kW.kg}^{-1}$  and a maximum power density of  $1.91 \text{ kW.kg}^{-1}$  at an energy density of  $0.98 \text{ Wh.kg}^{-1}$ . To assess the current standing of  $\text{Ti}_3\text{C}_2\text{T}_x/\text{CoS}@CC$  electrode, a performance comparison table (in terms of energy density, power density, and retentivity) of some recently reported metal sulfide/MXene-based supercapacitor electrodes is given in **Table 8**. The table shows that the collective energy storage performance of the present flexible electrode is better than many materials reported in the table. Though some of the materials mentioned in the table have higher energy and power densities, none of them have been investigated as flexible electrodes. It is worth considering that  $\text{Ti}_3\text{C}_2\text{T}_x/\text{CoS}@CC$  electrode performance remains uncompromised under any mechanical stress. Finally, to demonstrate the practical use of this device, three similar symmetric flexible devices, connected in series, have been shown to illuminate a red light-emitting diode (**Inset Figure 4.18b**).

**Table 8.** Comparison of different Metal Sulfide MXene Composite for supercapacitor performance.

Electrode material	Potential Window (V)	Electrolytes	Energy density	Power density	Retentivity
CoS @ MXene/CF	0-1.5 V	6 M KOH	10.66 Wh.kg <sup>-1</sup>	135 W.kg <sup>-1</sup>	80.99% (5000 cycles)
Nickel Sulfide/Ti <sub>3</sub> C <sub>2</sub>	0-2.0 V	6 M KOH	20.0 Wh.kg <sup>-1</sup>	10 kW.kg <sup>-1</sup>	71.4% (10000 cycles)
MoS <sub>2</sub> /MXene	0-1.6 V	3 M KOH	54 Wh.kg <sup>-1</sup>	0.86 kW.kg <sup>-1</sup>	90 % (10000 cycles)
MXene/ MoS <sub>2</sub>	0-0.6V	1 M H <sub>2</sub> SO <sub>4</sub>	5.1 Wh.kg <sup>-1</sup>	298 W.kg <sup>-1</sup>	72.34% (10000 cycles)
MXene/CoNi <sub>2</sub> S <sub>4</sub>	0-1.6 V	3 M KOH	30.5 Wh.kg <sup>-1</sup>	1587 W.kg <sup>-1</sup>	80.5 % (10000 cycles)
MXene/ MoS <sub>2</sub>	-1.5-1.5 V	1 M H <sub>2</sub> SO <sub>4</sub>	355 Wh.kg <sup>-1</sup>	758 W.kg <sup>-1</sup>	-----
MXene-NiCo <sub>2</sub> S <sub>4</sub>	0-0.6 V	3M KOH	27.2 Wh.kg <sup>-1</sup>	0.48 kW.kg <sup>-1</sup>	80 % (3000 cycles)
Ni <sub>1.5</sub> Co <sub>1.5</sub> S <sub>4</sub> @Ti <sub>3</sub> C	0- 1.5 V	2M KOH	49.8 Wh.Kg <sup>-1</sup>	800 W.kg <sup>-1</sup>	90 % (8000 cycles)
Ti <sub>3</sub> C <sub>2</sub> T <sub>x</sub> /CoS <sub>2</sub> /CuCo <sub>2</sub> S <sub>4</sub>	0- 1.8 V	1 M TEABF <sub>4</sub> /DMSO	42.2Wh.kg <sup>-1</sup>	1801.5 W.kg <sup>-1</sup>	96 % (10000 cycles)
Ti <sub>3</sub> C <sub>2</sub> T <sub>x</sub> /CoS@CC	0-1.0 V	1 M KOH	13.13 Wh.kg <sup>-1</sup>	1.91 kW.kg <sup>-1</sup>	93.41 % (10000 cycles)

## 4.4 Summary

A fabric-based flexible supercapattery electrode material  $\text{Ti}_3\text{C}_2\text{T}_x/\text{CoS}@CC$  has been prepared by in-situ growth of CoS on carbon cloth fibers followed by drop-casting of  $\text{Ti}_3\text{C}_2\text{T}_x$  MXene. Due to the synergistic effect of highly conducting MXene and redox-active CoS, the resulting  $\text{Ti}_3\text{C}_2\text{T}_x/\text{CoS}@CC$  electrode shows a specific capacity of  $120 \text{ Cg}^{-1}$  at  $1 \text{ Ag}^{-1}$ , which is much higher than the sum of the specific capacities of its components ( $\text{Ti}_3\text{C}_2\text{T}_x@CC$  ( $10.4 \text{ Cg}^{-1}$ ) and  $\text{CoS}@CC$  ( $60 \text{ Cg}^{-1}$ )). The charge storage mechanism studies by Dunn's method and EIS confirmed that the  $\text{Ti}_3\text{C}_2\text{T}_x@CC$  electrode exhibits a dominant EDLC character, whereas the CoS and the composite  $\text{Ti}_3\text{C}_2\text{T}_x/\text{CoS}@CC$  mainly feature battery-type behavior. The fabrication of a flexible symmetrical device has also been demonstrated using  $\text{Ti}_3\text{C}_2\text{T}_x/\text{CoS}@CC$  electrode. The device shows a maximum energy density of  $13.3 \text{ Wh.kg}^{-1}$  and a maximum power density of  $1.91 \text{ kW.kg}^{-1}$  with 93.41% retention in capacity after 10000 cycles. Because of the abundant and robust interphase interactions between  $\text{Ti}_3\text{C}_2\text{T}_x$  and CoS in the composite, its pseudocapacitive performance remains unaltered under any mechanical stress (stretching, bending, and twisting), which highlights its flexible character. The electrochemical features exhibited by the present composite electrode material make it a promising candidate to be considered for flexible energy storage devices.

## References

- [1] T.M. Gür, Review of electrical energy storage technologies, materials and systems: challenges and prospects for large-scale grid storage, *Energy Environ. Sci.* 11 (2018) 2696–2767. <https://doi.org/10.1039/C8EE01419A>.
- [2] S. Liu, K.S. Hui, K.N. Hui, Flower-like copper cobaltite nanosheets on graphite paper as high-performance supercapacitor electrodes and enzymeless glucose sensors, *ACS Appl. Mater. Interfaces.* 8 (2016) 3258–3267. <https://doi.org/10.1021/acsami.5b11001>.
- [3] S. Dai, Z. Liu, B. Zhao, J. Zeng, H. Hu, Q. Zhang, D. Chen, C. Qu, D. Dang, M. Liu, A high-performance supercapacitor electrode based on N-doped porous graphene, *J. Power Sources.* 387 (2018) 43–48. <https://doi.org/10.1016/j.jpowsour.2018.03.055>.
- [4] S. Zhu, J. Ni, Y. Li, Carbon nanotube-based electrodes for flexible supercapacitors, *Nano Res.* 13 (2020) 1825–1841. <https://doi.org/10.1007/s12274-020-2729-5>.
- [5] C.A. Tseng, P.K. Sahoo, C.P. Lee, Y.T. Lin, J.H. Xu, Y.T. Chen, Synthesis of CoO-Decorated Graphene Hollow Nanoballs for High-Performance Flexible Supercapacitors, *ACS Appl. Mater. Interfaces.* 12 (2020) 40426–40432. <https://doi.org/10.1021/acsami.0c12898>.
- [6] K. Wang, R. Bi, M. Huang, B. Lv, H. Wang, C. Li, H. Wu, Q. Zhang, Porous Cobalt Metal-Organic Frameworks as Active Elements in Battery-Supercapacitor Hybrid Devices, *Inorg. Chem.* 59 (2020) 6808–6814. <https://doi.org/10.1021/acs.inorgchem.0c00060>.
- [7] Q. Hu, M. Tang, M. He, N. Jiang, C. Xu, D. Lin, Q. Zheng, Core-shell MnO<sub>2</sub>@CoS nanosheets with oxygen vacancies for high-performance supercapattery, *J. Power Sources.* 446 (2020)

227335. <https://doi.org/10.1016/j.jpowsour.2019.227335>.
- [8] S. Raj, P. Kar, P. Roy, Facile synthesis of flower-like morphology  $\text{Cu}_{0.27}\text{Co}_{2.73}\text{O}_4$  for a high-performance supercapattery with extraordinary cycling stability, *Chem. Commun.* 54 (2018) 12400–12403. <https://doi.org/10.1039/c8cc04625e>.
- [9] Y. Yan, Y. Luo, J. Ma, B. Li, H. Xue, H. Pang, Facile Synthesis of Vanadium Metal-Organic Frameworks for High-Performance Supercapacitors, *Small.* 14 (2018) 1–8. <https://doi.org/10.1002/sml.201801815>.
- [10] L. Li, Z. Wu, S. Yuan, X.B. Zhang, Advances and challenges for flexible energy storage and conversion devices and systems, *Energy Environ. Sci.* 7 (2014) 2101–2122. <https://doi.org/10.1039/c4ee00318g>.
- [11] M. Yu, X. Feng, Thin-Film Electrode-Based Supercapacitors, *Joule.* 3 (2019) 338–360. <https://doi.org/10.1016/j.joule.2018.12.012>.
- [12] M. Hu, T. Hu, R. Cheng, J. Yang, C. Cui, C. Zhang, X. Wang, MXene-coated silk-derived carbon cloth toward flexible electrode for supercapacitor application, *J. Energy Chem.* 27 (2018) 161–166. <https://doi.org/10.1016/j.jechem.2017.10.030>.
- [13] S. Wang, B. Pei, X. Zhao, R.A.W. Dryfe, Highly porous graphene on carbon cloth as advanced electrodes for flexible all-solid-state supercapacitors, *Nano Energy.* 2 (2013) 530–536. <https://doi.org/10.1016/j.nanoen.2012.12.005>.
- [14] P. Yu, W. Duan, Y. Jiang, Porous  $\text{Fe}_2\text{O}_3$  Nanorods on Hierarchical Porous Biomass Carbon as Advanced Anode for High-Energy-Density Asymmetric Supercapacitors, *Front. Chem.* 8 (2020) 1–9. <https://doi.org/10.3389/fchem.2020.611852>.
- [15] Y.C. Chen, Y.K. Hsu, Y.G. Lin, Y.K. Lin, Y.Y. Horng, L.C. Chen, K.H. Chen, Highly flexible supercapacitors with manganese

- oxide nanosheet/carbon cloth electrode, *Electrochim. Acta.* 56 (2011) 7124–7130. <https://doi.org/10.1016/j.electacta.2011.05.090>.
- [16] S. Su, L. Lai, R. Li, Y. Lin, H. Dai, X. Zhu, Annealing-Assisted Dip-Coating Synthesis of Ultrafine Fe<sub>3</sub>O<sub>4</sub> Nanoparticles/Graphene on Carbon Cloth for Flexible Quasi-Solid-State Symmetric Supercapacitors, *ACS Appl. Energy Mater.* 3 (2020) 9379–9389. <https://doi.org/10.1021/acsaem.0c01745>.
- [17] J. Cincy, T.E. Milja, K.P. Prathish, Fabrication of a flexible carbon cloth based solid contact iodide selective electrode, *Anal. Methods.* 9 (2017) 2947–2956. <https://doi.org/10.1039/c7ay00733g>.
- [18] K.V.G. Raghavendra, R. Vinoth, K. Zeb, C.V.V. Muralee Gopi, S. Sambasivam, M.R. Kummara, I.M. Obaidat, H.J. Kim, An intuitive review of supercapacitors with recent progress and novel device applications, *J. Energy Storage.* 31 (2020) 101652. <https://doi.org/10.1016/j.est.2020.101652>.
- [19] R. Barik, P.P. Ingole, Challenges and prospects of metal sulfide materials for supercapacitors, *Curr. Opin. Electrochem.* 21 (2020) 327–334. <https://doi.org/10.1016/j.coelec.2020.03.022>.
- [20] S. Chandrasekaran, L. Yao, L. Deng, C. Bowen, Y. Zhang, S. Chen, Z. Lin, F. Peng, P. Zhang, Recent advances in metal sulfides: From controlled fabrication to electrocatalytic, photocatalytic and photoelectrochemical water splitting and beyond, *Chem. Soc. Rev.* 48 (2019) 4178–4280. <https://doi.org/10.1039/c8cs00664d>.
- [21] J. Shi, X. Li, G. He, L. Zhang, M. Li, Electrodeposition of high-capacitance 3D CoS/graphene nanosheets on nickel foam for high-performance aqueous asymmetric supercapacitors, *J. Mater. Chem. A.* 3 (2015) 20619–20626.

<https://doi.org/10.1039/c5ta04464b>.

- [22] K. Zhang, Y. Wei, J. Huang, Y. Xiao, W. Yang, T. Hu, K. Yuan, Y. Chen, A generalized one-step in situ formation of metal sulfide/reduced graphene oxide nanosheets toward high-performance supercapacitors, *Sci. China Mater.* 63 (2020) 1898–1909. <https://doi.org/10.1007/s40843-020-1371-y>.
- [23] P. Geng, S. Zheng, H. Tang, R. Zhu, L. Zhang, S. Cao, H. Xue, H. Pang, Transition Metal Sulfides Based on Graphene for Electrochemical Energy Storage, *Adv. Energy Mater.* 8 (2018) 1–26. <https://doi.org/10.1002/aenm.201703259>.
- [24] H. Tong, W. Bai, S. Yue, Z. Gao, L. Lu, L. Shen, S. Dong, J. Zhu, J. He, X. Zhang, Zinc cobalt sulfide nanosheets grown on nitrogen-doped graphene/carbon nanotube film as a high-performance electrode for supercapacitors, *J. Mater. Chem. A.* 4 (2016) 11256–11263. <https://doi.org/10.1039/c6ta02249a>.
- [25] J.Q. Qi, C.C. Zhang, H. Liu, L. Zhu, Y.W. Sui, X.J. Feng, W.Q. Wei, H. Zhang, P. Cao, MXene-wrapped ZnCo<sub>2</sub>S<sub>4</sub> core-shell nanospheres via electrostatic self-assembly as positive electrode materials for asymmetric supercapacitors, *Rare Met.* (2022). <https://doi.org/10.1007/s12598-021-01956-1>.
- [26] Y. Yu, J. Zhou, Z. Sun, Modulation engineering of 2D MXene-based compounds for metal-ion batteries, *Nanoscale.* 11 (2019) 23092–23104. <https://doi.org/10.1039/c9nr08217d>.
- [27] M. Hu, H. Zhang, T. Hu, B. Fan, X. Wang, Z. Li, Emerging 2D MXenes for supercapacitors: Status, challenges and prospects, *Chem. Soc. Rev.* 49 (2020) 6666–6693. <https://doi.org/10.1039/d0cs00175a>.
- [28] H. Zhou, Y. Lu, F. Wu, L. Fang, H.J. Luo, Y.X. Zhang, M. Zhou, MnO<sub>2</sub> nanorods/MXene/CC composite electrode for flexible supercapacitors with enhanced electrochemical performance, *J. Alloys Compd.* 802 (2019) 259–268.

<https://doi.org/10.1016/j.jallcom.2019.06.173>.

- [29] I. Ayman, A. Rasheed, S. Ajmal, A. Rehman, A. Ali, I. Shakir, M.F. Warsi, CoFe<sub>2</sub>O<sub>4</sub>Nanoparticle-Decorated 2D MXene: A Novel Hybrid Material for Supercapacitor Applications, *Energy and Fuels*. 34 (2020) 7622–7630. <https://doi.org/10.1021/acs.energyfuels.0c00959>.
- [30] H. Liu, R. Hu, J. Qi, Y. Sui, Y. He, Q. Meng, F. Wei, Y. Ren, Y. Zhao, W. Wei, One-Step Synthesis of Nanostructured CoS<sub>2</sub> Grown on Titanium Carbide MXene for High-Performance Asymmetrical Supercapacitors, *Adv. Mater. Interfaces*. (n.d.). <https://doi.org/10.1002/admi.201901659>.
- [31] Z. Pan, F. Cao, X. Hu, X. Ji, A facile method for synthesizing CuS decorated Ti<sub>3</sub>C<sub>2</sub> MXene with enhanced performance for asymmetric supercapacitors, *J. Mater. Chem. A*. 7 (2019) 8984–8992. <https://doi.org/10.1039/c9ta00085b>.
- [32] D. Ye, Y. Yu, J. Tang, L. Liu, Y. Wu, Electrochemical activation of carbon cloth in aqueous inorganic salt solution for superior capacitive performance, *Nanoscale*. 8 (2016) 10406–10414. <https://doi.org/10.1039/c6nr00606j>.
- [33] M. Alhabeb, K. Maleski, B. Anasori, P. Lelyukh, L. Clark, S. Sin, Y. Gogotsi, Guidelines for Synthesis and Processing of Two-Dimensional Titanium Carbide (Ti<sub>3</sub>C<sub>2</sub>T<sub>x</sub> MXene), *Chem. Mater.* 29 (2017) 7633–7644. <https://doi.org/10.1021/acs.chemmater.7b02847>.
- [34] T.S. Kvashina, N.F. Uvarov, M.A. Korchagin, Y.L. Krutskiy, A. V. Ukhina, Synthesis of MXene Ti<sub>3</sub>C<sub>2</sub> by selective etching of MAX-phase Ti<sub>3</sub>AlC<sub>2</sub>, *Mater. Today Proc.* 31 (2020) 592–594. <https://doi.org/10.1016/j.matpr.2020.07.107>.
- [35] Q. Wang, L. Jiao, H. Du, W. Peng, Y. Han, D. Song, Y. Si, Y. Wang, H. Yuan, Novel flower-like CoS architectures: One-pot synthesis and electrochemical properties, *J. Mater. Chem.* 21

- (2011) 327–329. <https://doi.org/10.1039/c0jm03121f>.
- [36] H. Long, T. Shi, H. Hu, S. Jiang, S. Xi, Z. Tang, Growth of hierarchal mesoporous NiO nanosheets on carbon cloth as binder-free anodes for high-performance flexible lithium-ion batteries, *Sci. Rep.* 4 (2014) 1–9. <https://doi.org/10.1038/srep07413>.
- [37] Z.C. Xiang, Z. Zhang, X.J. Xu, Q. Zhang, C. Yuan, MoS<sub>2</sub> nanosheets array on carbon cloth as a 3D electrode for highly efficient electrochemical hydrogen evolution, *Carbon N. Y.* 98 (2016) 84–89. <https://doi.org/10.1016/j.carbon.2015.10.071>.
- [38] A. Sarycheva, Y. Gogotsi, Raman Spectroscopy Analysis of the Structure and Surface Chemistry of Ti<sub>3</sub>C<sub>2</sub>T<sub>x</sub> MXene, *Chem. Mater.* 32 (2020) 3480–3488. <https://doi.org/10.1021/acs.chemmater.0c00359>.
- [39] D. Ma, B. Hu, W. Wu, X. Liu, J. Zai, C. Shu, T. Tadesse Tsega, L. Chen, X. Qian, T.L. Liu, Highly active nanostructured CoS<sub>2</sub>/CoS heterojunction electrocatalysts for aqueous polysulfide/iodide redox flow batteries, *Nat. Commun.* 10 (2019). <https://doi.org/10.1038/s41467-019-11176-y>.
- [40] Z. Wu, L. Li, J. Yan, X. Zhang, Materials Design and System Construction for Conventional and New-Concept Supercapacitors, *Adv. Sci.* 4 (2017) 1600382. <https://doi.org/10.1002/advs.201600382>.
- [41] C.K. Ranaweera, Z. Wang, E. Alqurashi, P.K. Kahol, P.R. Dvornic, B.K. Gupta, K. Ramasamy, A.D. Mohite, G. Gupta, R.K. Gupta, Highly stable hollow bifunctional cobalt sulfides for flexible supercapacitors and hydrogen evolution, *J. Mater. Chem. A.* 4 (2016) 9014–9018. <https://doi.org/10.1039/c6ta03158g>.
- [42] P. Tiwari, J. Jaiswal, R. Chandra, Hierarchal growth of MoS<sub>2</sub>@CNT heterostructure for all solid-state symmetric supercapacitor: Insights into the surface science and storage mechanism, *Electrochim. Acta.* 324 (2019) 134767.

<https://doi.org/10.1016/j.electacta.2019.134767>.

- [43] M.K. Singh, A.K. Gupta, S. Krishnan, N. Guha, S. Marimuthu, D.K. Rai, A new hierarchically porous Cu-MOF composited with rGO as an efficient hybrid supercapacitor electrode material, *J. Energy Storage*. 43 (2021) 103301. <https://doi.org/10.1016/j.est.2021.103301>.
- [44] S. Krishnan, A.K. Gupta, M.K. Singh, N. Guha, D.K. Rai, Nitrogen-rich Cu-MOF decorated on reduced graphene oxide nanosheets for hybrid supercapacitor applications with enhanced cycling stability, *Chem. Eng. J.* 435 (2022). <https://doi.org/10.1016/j.cej.2022.135042>.
- [45] Z. Wu, L. Li, J.M. Yan, X.B. Zhang, Materials Design and System Construction for Conventional and New-Concept Supercapacitors, *Adv. Sci.* 4 (2017). <https://doi.org/10.1002/advs.201600382>.
- [46] J. Hong, S.J. Park, S. Kim, Synthesis and electrochemical characterization of nanostructured Ni-Co-MOF/graphene oxide composites as capacitor electrodes, *Electrochim. Acta*. 311 (2019) 62–71. <https://doi.org/10.1016/j.electacta.2019.04.121>.

# **Chapter 5**

## **Enhanced Sodium-Ion Storage via High-Entropy Metal-Organic Frameworks: Battery-like Behaviour**

### **5.1 Introduction**

In order to address the limitations of batteries and supercapacitors, Hybrid Ion Capacitors (HICs), specifically Hybrid Li-ion capacitors (HLCs), were introduced in 2001.[1] These devices combine the benefits of batteries and supercapacitors, thereby reducing the performance gap between batteries and supercapacitors. HLCs have successfully bridged the performance gap between batteries and supercapacitors but they encounter the issue of limited natural lithium resources. Further, abundant sodium sources, with their favorable redox potential, offer a promising alternative for Sodium-ion-Capacitors (SICs), ensuring cost-effectiveness, environmental sustainability, safety, stability, and scalability.[2] SICs are composed of a battery-type cathode (dominated by intercalation/deintercalation behavior) and a capacitor-type anode (controlled by physical adsorption/desorption behavior) in a Na-salt-containing electrolyte.[3]

One of the most significant obstacles in Sodium-ion-Capacitors research is the search for electrode materials that facilitate high energy density storage while retaining its capacity. Recently Prussian blue analogs (PBAs) have attracted great interest and have been investigated as the positive electrode in sodium-ion capacitors.[4–6] PBAs are a

coordination structure interconnected by hexacyanometalate, denoted by the chemical formula  $A_xM[Fe(CN)_6]_y \square Fe(CN)_6 \cdot zH_2O$ , where A represents an alkali metal ion such as  $K^+$  or  $Na^+$ , while M denotes transition metals like Mn, Fe, Co, Ni, Cu, or Zn and  $\square Fe(CN)_6$  denotes the vacancy in the  $[Fe(CN)_6]$  group. The M site cation can vary within the coordination framework, thus imparting the PBA with intriguing electrochemical and morphological properties. Because of their fascinating redox characteristics, remarkable chemical stability, easy synthesis approach, and cheap cost, they have sparked substantial interest. [4,7,8] Recently, Jiang et al. have developed high additive-free Co-FePBA for sodium-ion capacitors, which showed an energy density of  $33.8 \mu Wh \text{ cm}^{-2}$  at a power density of  $200 \mu W \text{ cm}^{-2}$  and 85.6% capacitance retention after 5000 cycles. [9] Similarly, Miao et al. synthesized a composite of Ni-FePBA with rGO for a sodium ion hybrid supercapacitor and achieved a capacity of  $451 \text{ Fg}^{-1}$  and remarkable rate performance in aqueous  $Na_2SO_4$  electrolyte. Impressively, the aqueous Na-ion HSC assembled with the composite cathode and activated carbon (AC) anode also shows a high energy density of  $51.11 \text{ Wh kg}^{-1}$ , and a superb power density of  $10 \text{ kW kg}^{-1}$ . [5] In another work Jian et al. synthesized  $Co(OH)_2$  nanosheets grown on activated carbon cloth (CC) by electrodeposition, which is subsequently embedded with Prussian blue analog (PBA) nanocubes by the ion exchange, obtaining  $Co(OH)_2/PBA/CC$  electrodes which shows a high specific capacitance ( $1175.7 \text{ mF cm}^{-2}$  at  $1 \text{ mA cm}^{-2}$ ) and high energy density of  $0.4 \text{ mWh cm}^{-2}$  at a power density of  $1.5 \text{ mW cm}^{-2}$ . [10] The high specific capacity of the above-mentioned PBAs as electrode materials is the manifestation of enhanced electrochemical features arising due to the metal center responsible for the faradaic reaction.

Despite showing exceptional performance in Na-ion capacitors and batteries, metal dissolution has been a severe problem with PBA electrode materials, which leads to capacity fading and, thus, limits their longer cyclability. [11,12] To improve the electrochemical performance of PBA electrodes, researchers have recently attempted the synthesis of PBAs containing multiple redox-active transition metals and termed

them as High Entropy Prussian Blue Analogs (HEPBAs), inspired by the concept of high-entropy alloys.[13] The concept of "high entropy" in this context is related to the incorporation of multiple metal ions into the crystal lattice resulting in enhanced configuration entropy compared to regular PBAs. Based on the number of principle metal ions and configurational entropy, the concept of low, medium, and high entropy PBAs has been postulated. Low entropy Prussian blue analogs (LEPBAs) generally consist of 2 or 3 metal-ions, exhibiting configurational entropy typically less than  $1R$  ( $R$  is universal gas constant). Medium entropy PBAs (MEPBAs) consist of 4 or 5 metal ions, showing configurational entropy between  $1R$  to  $1.5R$ , while high entropy PBAs (HEPBAs) contain five or more metal ions, having configurational entropy greater than  $1.5R$ . [14]

In HEPBAs, the increased entropy not only mitigates metal dissolution due to enhanced stability, but also induces improved electrochemical features through cocktail effects, resulting in improved energy density, charge-discharge efficiency, and cycle performance of the electrodes. For example, Zhao et al. reported MnCoNiCuZnPBA as cathode material for sodium-ion batteries with a specific capacity of  $75 \text{ mA h g}^{-1}$  at  $0.5C$  and 87% capacity retention after 1000 cycles.[13] In another work, Ma et. al synthesized HEPBA for a Na-ion battery and achieved a capacity of  $102.4 \text{ mA h g}^{-1}$  with 84.4% capacity retention after undergoing 3448 cycles. Similarly, Wang et.al investigate a NaMnCoCuNiFe[Fe(CN)<sub>6</sub>]@C cathode for a sodium-ion battery, which featured an impressive charge storage performance of  $120.2 \text{ mA h g}^{-1}$  at  $10 \text{ mA g}^{-1}$ . [15] Though HEPBAs have shown great promise in the field of energy storage, their exploration is still in the infancy stage. There are still many HEPBA combinations yet to be explored in order to push the performance limit of the material. Despite the fact that metal-ion capacitors are known to bridge the performance gap between supercapacitors and batteries, surprisingly, HEPBAs have not been explored for metal-ion capacitors to the best of our knowledge.

In continuation of this innovative approach, herein, we report the synthesis and systematic investigation of a series of new multi-metallic

binary, ternary, and quinary Prussian blue analogs (PBAs), synthesized via a co-precipitation method employing metal salt precursors (Co, Ni, Cu, Mg, Zn) and  $K_3[Fe(CN)_6]$ , for Na-ion hybrid capacitor. The three-electrode study reveals that by increasing the entropy (number of transition metal ions), a significant increase in the charge storage performance is observed, with HEPBA (quinary PBA) featuring the best performance ( $435\text{ Cg}^{-1}$ ). Further, an asymmetrical Na-ion hybrid capacitor device has been fabricated using a HEPBA cathode and activated carbon (AC) anode in a Swagelok cell using  $Na_2SO_4$  gel electrolyte, which shows maximum energy density ( $^{max}E_d = 252\text{ Whkg}^{-1}$ ) and maximum power density ( $^{max}P_d = 20\text{ kWkg}^{-1}$ ) with excellent capacity retention of 93.2% after 10000 charge-discharge cycles. Overall, our investigations clearly corroborate that HEPBAs hold great promise in the field of electrochemical storage with the ability to render high energy density without compromising the power density.

## 5.2 Experimental Section

### 5.2.1 Chemicals

The following chemicals were utilized in the experiment without additional purification: Sodium citrate ( $C_6H_5Na_3O_7 \cdot 2H_2O$ ,  $\geq 99.0\%$ , SRL), potassium ferricyanide ( $K_3FeCN_6$ ,  $\geq 99.5\%$ , SRL), cobalt chloride hexahydrate ( $CoCl_2 \cdot 6H_2O$ ,  $\geq 99.0\%$ , SRL), nickel chloride hexahydrate ( $NiCl_2 \cdot 6H_2O$ ,  $\geq 99.0\%$ , SRL), manganese chloride tetrahydrate ( $MgCl_2 \cdot 4H_2O$ ,  $\geq 99.5\%$ , SRL), copper chloride dihydrate ( $CuCl_2 \cdot 2H_2O$ ,  $\geq 99.0\%$ , SRL), and zinc chloride ( $ZnCl_2 \cdot 6H_2O$ ,  $\geq 99.0\%$ , SRL). Throughout the synthesis, deionized water (Millipore DI water,  $18.2\text{ M}\Omega\text{cm}^{-1}$ ) was used.

### 5.2.2 Synthesis

A variety of multi-metal Prussian Blue Analogs (PBAs) was prepared via a co-precipitation method employing metal salt precursors and  $K_3[Fe(CN)_6]$  at room temperature. In a simple procedure for the synthesis of high entropy Prussian blue analog (HEPBAs), solution A was initially prepared by dissolving 9 mmol of sodium citrate and an

equimolar amount (6 mmol each) of  $\text{CoCl}_2 \cdot 6\text{H}_2\text{O}$ ,  $\text{NiCl}_2 \cdot 6\text{H}_2\text{O}$ ,  $\text{MgCl}_2 \cdot 4\text{H}_2\text{O}$ ,  $\text{CuCl}_2 \cdot 2\text{H}_2\text{O}$ , and  $\text{ZnCl}_2 \cdot 6\text{H}_2\text{O}$  in 50 mL of deionized (DI) water. Simultaneously, 4 mmol of  $\text{K}_3[\text{Fe}(\text{CN})_6]$  was dispersed in 50 mL of DI water to create solution B. Subsequently, solution A and solution B were mixed together and stirred for 15 minutes. The resulting solution was allowed to age for 24 h to form precipitates, which were subsequently collected via centrifugation and finally dried in a vacuum oven at  $60^\circ\text{C}$  for 12 h. Similar methods were employed for the synthesis of ternary and quaternary PBAs.

### 5.2.3 Preparation of Electrodes

The as-synthesized multi-metal Prussian Blue Analogs (PBAs) materials were coated on different carbon paper (2x1 cm). Before coating, carbon paper of equal size is cut and cleaned in ethanol for 2 h. Afterward, they were dried in a vacuum oven. Later, 10 mg of each synthesized PBA was dispersed in 1.0 ml of ethanol in different glass vials with the aid of ultrasonic agitation to give 10 mg/mL suspension. Finally, 200  $\mu\text{L}$  of each suspension was drop-cast on carbon paper with the help of a micropipette, and the solvent was allowed to evaporate in an oven. All electrochemical measurements were carried out in a 1 M  $\text{Na}_2\text{SO}_4$  electrolyte solution.

## 5.3 Characterization

### 5.3.1 Physiochemical Characterization

The crystallinity and phase analyses were done using an Empyrean, Malvern PANalytical diffractometer with  $\text{Cu-K}\alpha$  radiation source at room temperature in the  $2\theta$  range of  $10$  to  $70^\circ$  at a scanning rate of  $0.02^\circ \text{min}^{-1}$ . To understand the stability of the sample, thermogravimetric analysis (TGA) was carried out on a Perkin-Elmer gravimetric instrument under  $\text{N}_2$  atmosphere from room temperature to  $800^\circ\text{C}$  at a heating rate of  $10^\circ\text{C}$ . FTIR spectra were recorded using Bruker Tensor 27 spectrometer in the wavelength range  $400 \text{ cm}^{-1}$  to  $4000 \text{ cm}^{-1}$ . Morphological and elemental analyses were done using Field Emission Scanning Electron Microscopy (FESEM) (JEOL-7610F Plus) equipped

with Energy Dispersive Spectroscopy (EDS). Transmission electron microscopy (TEM) was done using FEI TECNAI 20 at an operating voltage of 200 kV. X-ray photoelectron spectroscopy (XPS) was investigated by a Shimadzu spectrometer using an Al K $\alpha$  source (1486.7 eV).

### 5.3.2 Electrochemical Measurements

For three-electrode electrochemical testing, Autolab 204 potentiostat was used to do all the electrochemical measurements using a standard three-electrode cell setup, consisting of our electrode materials as working electrodes, Pt as a counter electrode, and Ag/AgCl as a reference electrode. The potential range of 0.0 to 1.0 V was used to perform CV and GCD at different scan rates and current densities. EIS studies were performed at a frequency range of 10 mHz to 100 kHz in 10 mV AC amplitude.

GCD curves were used to calculate the specific capacity using the following equation: [16]

$$C = \frac{I \Delta t}{m} \quad (1)$$

Where C is the specific capacity (C.g<sup>-1</sup>), I is current (A),  $\Delta t$  is the discharge time (s), and m is the mass of the coated active material (g).

For the two-electrode system, the mass ratio of the positive and negative electrodes was balanced according to the following equations:[17]

$$\frac{m^+}{m^-} = \frac{C^-}{C^+} \quad (2)$$

where m<sup>-</sup>, and C<sup>-</sup>, are the mass and specific capacity of the negative electrodes, and m<sup>+</sup> and C<sup>+</sup> are the mass and specific capacity of the positive electrode, respectively.

The specific capacity, energy density (E), and power density (P) of the fabricated device were calculated using the following equations from the GCD curves.

$$C = \frac{2I \Delta t}{m} \quad (3)$$

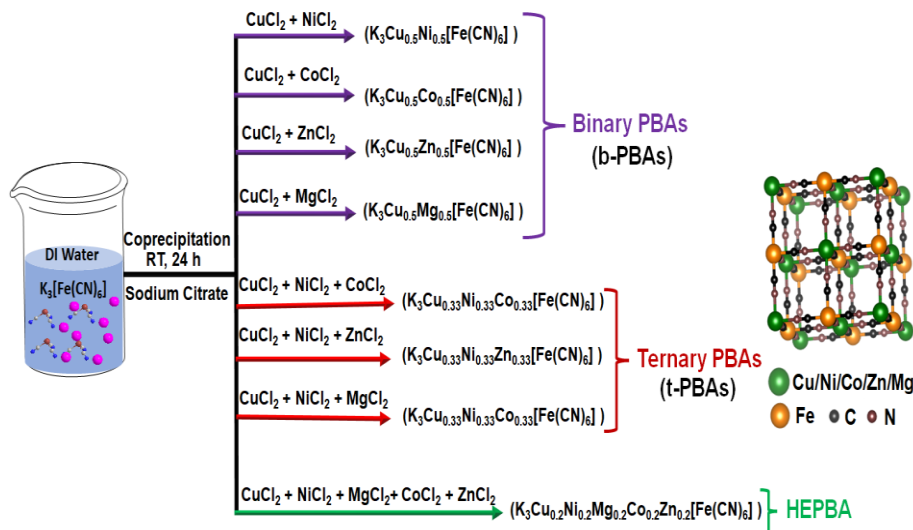
$$E \left( \frac{Wh}{kg} \right) = \frac{0.5 \times C \Delta V}{3.6} \quad (4)$$

$$P \left( \frac{W}{kg} \right) = \frac{3600 \times E}{\Delta t} \quad (5)$$

Where  $C$  is the specific capacity ( $Cg^{-1}$ ),  $I$  is current (A),  $\Delta t$  is the discharge time (s),  $m$  is mass of the coated active material (g), and  $\Delta V$  is the potential range.

## 5.4 Result and Discussion

Synthesis of multi-metal Prussian blue was achieved by co-precipitation method which offers a simple cost-effective approach. During the addition of the metal salt solution to the  $[Fe(CN)_6]^{3-}$  solution under stirring, insoluble metal  $[Fe(CN)_6]^{3-}$  complexes precipitate out of the solution. This co-precipitation reaction forms the basis for the synthesis of multi-metal PBAs, wherein metal ions from the precursor salts react with  $[Fe(CN)_6]^{3-}$  ions to produce the desired complex. The use of citrate salt ensures the slow release of salt through coordination, leading to the slow nucleation of PBAs, which is essential for the growth of ordered cubic PBA crystals.[18]



**Scheme. 1** Synthesis of multi-metal Prussian blue analogue.

From statistical thermodynamics, the configurational entropy of multi-metal PBAs can be given as. [19]

$$\Delta S_{\text{mix}} = -R \sum_{i=1}^m x_i \ln x_i$$

where  $R$  is the universal gas constant,  $i$  and  $m$  are the element and number of transition metals located at the M site in  $K_x M [Fe(CN)_6]_{1-y} \square_y \cdot nH_2O$ , and  $x_i$  is the mole fraction of the elements present in the M site.

The calculated configurational entropy for equimolar fraction ternary (three different metals at M site, **t-PBAs**), quaternary (four different metals at M site, **q-PBAs**), and quinary (five different metals at M site, **HEPBA**) PBAs are  $0.69R$ ,  $1.09R$ , and  $1.61R$ , respectively. According to the literature, materials with a configurational entropy below  $1 R$ , between  $1$  and  $1.5 R$ , and greater than  $1.5 R$  are categorized as low entropy, medium entropy, and high entropy, respectively. Our calculations indicate that the configurational entropy of quinary PBA stands at  $1.61 R$ , exceeding the threshold of  $1.5 R$ ; therefore, it is appropriate to consider it a high-entropy PBA (**HEPBA**).

#### 5.4.1 Structural, Physical, and Morphological Characterization

The crystallinity and phase purity of all synthesized materials were analyzed using PXRD (Powder X-ray Diffraction). The PXRD patterns of all PBAs (b-, t-, and HE-PBA) exhibit a set of characteristic diffraction peaks of a typical cubic PBA material with no additional peaks, indicating a single-phase PBA structure (**Figure 5.1, Figure 5.2** for **b-PBAs** and **t-PBAs** and **Figure 5.3a** for **HEPBA**). The PXRD pattern for each shows many peaks that correspond to JCPDS number: 01-075-4637. The crystallographic planes denoted as (200), (220), and (400) with corresponding angles of  $17.32^\circ$ ,  $24.65^\circ$ , and  $35.10^\circ$ , respectively, provide evidence supporting the assertion that HEPBA has a cubic crystal lattice.[20]

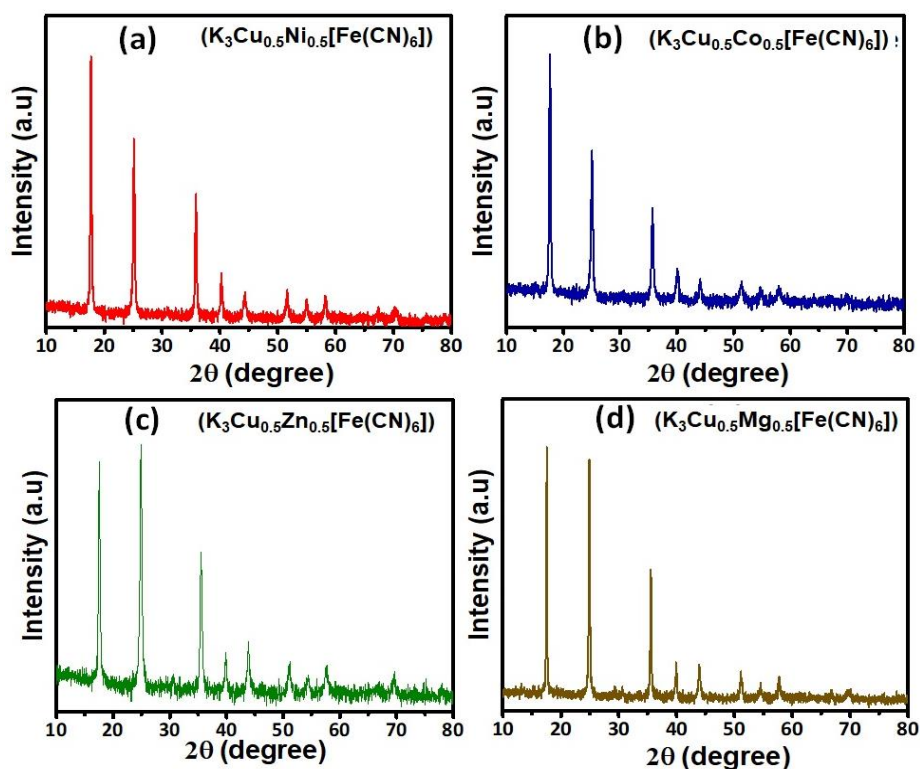


**Figure 5.1** PXRD patterns of Binary PBAs.

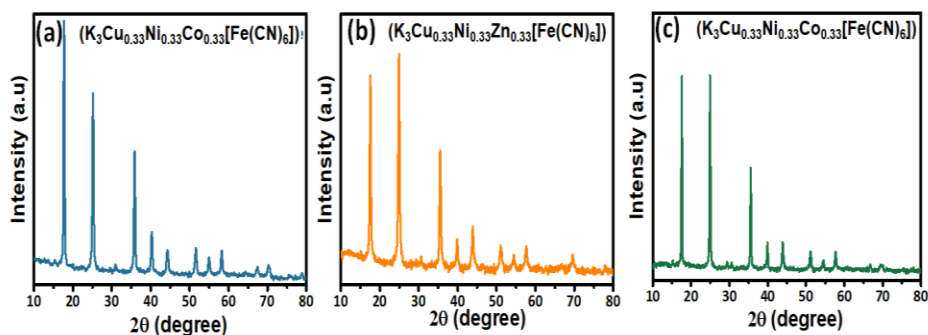


**Figure 5.2** PXRD patterns of Ternary PBAs.

FTIR spectroscopy of HEPBA was performed to examine the different functional groups as shown in **Figure 5.3b**. The peaks between 480 and 600  $\text{cm}^{-1}$  are related to the  $\nu$  (Metal-C/N) vibration mode. Cyano-bridged complexes can be readily identified by a distinctive sharp band stretching ( $\nu$ -CN) in the range of 2000–2250  $\text{cm}^{-1}$ , with two characteristic peaks at 2104  $\text{cm}^{-1}$ , assigned to  $\nu(\text{Fe}^{2+}\text{-CN})$  and 2216  $\text{cm}^{-1}$   $\nu(\text{Fe}^{3+}\text{-CN})$ , indicative of a reduction of fraction of  $\text{Fe}^{3+}\text{-CN}$  to  $\text{Fe}^{2+}\text{-CN}$ . The peak at 1604  $\text{cm}^{-1}$  is attributed to the bending vibration

of zeolitic water molecules. Further, a broad peak in the 3200-3403  $\text{cm}^{-1}$  region may be ascribed to the stretching modes of the hydroxyl(-OH) group of the surface-bound water molecules. In summary, the FTIR spectrum of HEPBA shows all the typical peaks of PBAs (CN and Fe-CN-M), confirming its successful synthesis. [21]

The thermogravimetric analysis (TGA) results shown in **Figure 5.3c** are obtained under a nitrogen atmosphere from room temperature to 800 °C to understand the thermal stability of HEPBA. The analysis indicates a weight loss of 23.4 wt.% till 200 °C, which is commonly associated with the removal of zeolitic water and coordinated water. The second weight loss of 29.7% from 200°C to 600°C is related to the decomposition of the coordination framework. [22]

X-ray photoelectron spectroscopy (XPS) was performed to investigate the surface valence states and the presence of elements in the **HEPBA (Figure 5.3d and Figure 5.4a-j)**. The full survey spectrum (confirms the presence of Zn, Cu, Ni, Mg, Co, Fe, N, K C, and O in the **HEPBA**. The high-resolution C 1s spectrum (**Figure 5.4a**) reveals the peaks at the binding energies around 284.4, 285.2, 287.5 eV, and 294 eV, which are associated with C-C, C-N, C=O, and N-C=O respectively. The high-resolution spectrum of Zn 2p (**Figure 5.4b**) shows two characteristic peaks corresponding to Zn 2p<sup>3/2</sup> and Zn 2p<sup>1/2</sup> at the binding energies of 1021.4 and 1045.3 eV, respectively, confirming the Zn in divalent (+2) oxidation state. In the high-resolution spectrum of Cu 2p (**Figure 5.4c**), two characteristic peaks corresponding to Cu(II) 2p<sup>3/2</sup> and Cu(II) 2p<sup>1/2</sup> at the binding energies of 933.4 and 952.5 eV, respectively, were observed along with a satellite peak. The Co 2p core-level spectrum (**Figure 5.4d**) presents clear spin-orbital components at 777.5 eV (Co 2p<sup>3/2</sup>) and 793.6 eV (Co 2p<sup>1/2</sup>). [R] These are accompanied by intense satellite peaks at 787.0 and 796.7 eV. Additionally, the peaks corresponding to Co<sup>2+</sup> and Co<sup>3+</sup> at 781.6 eV and 776.3 eV can also be seen. [R] In the Fe 2p spectrum (**Figure 5.4e**), two distinct peaks at 722.5 and 709.6 eV, are observed, which correspond to the 2p<sup>1/2</sup> and 2p<sup>3/2</sup>, respectively, of the Fe<sup>2+</sup> state. in the orbitals, respectively with

the presence of  $\text{Fe}^{2+}$  (708eV) and  $\text{Fe}^{3+}$  (723.1 eV). The presence of  $\text{K}2\text{p}^{3/2}$  and  $\text{K}2\text{p}^{1/2}$  at 239.1 eV and 297 eV are observed in **Figure 5.4f** respectively. The Mg 2p spectrum (**Figure 5.4g**) reveals a peak at 53.2 eV of Mg and a peak at 55.3 eV of MgO. Moreover two peaks originated from N1s is assigned as  $\text{sp}^2$  and  $\text{sp}^3$  at 398.2 and 399.6 eV respectively. The Ni 2p spectrum (**Figure 5.4i**) displays distinguishable signals that can be deconvoluted into two major contributions with binding energies of 853.5 and 872.0 eV, corresponding to  $\text{Ni}^{2+}$   $2\text{p}^{3/2}$  and  $2\text{p}^{1/2}$ , respectively. Also, a signal corresponding to  $\text{Ni}^{3+}$   $2\text{p}^{3/2}$  at 857 eV is observed. The O 1s spectrum shows a peak at 532.1 which are related to C-OH.[23]

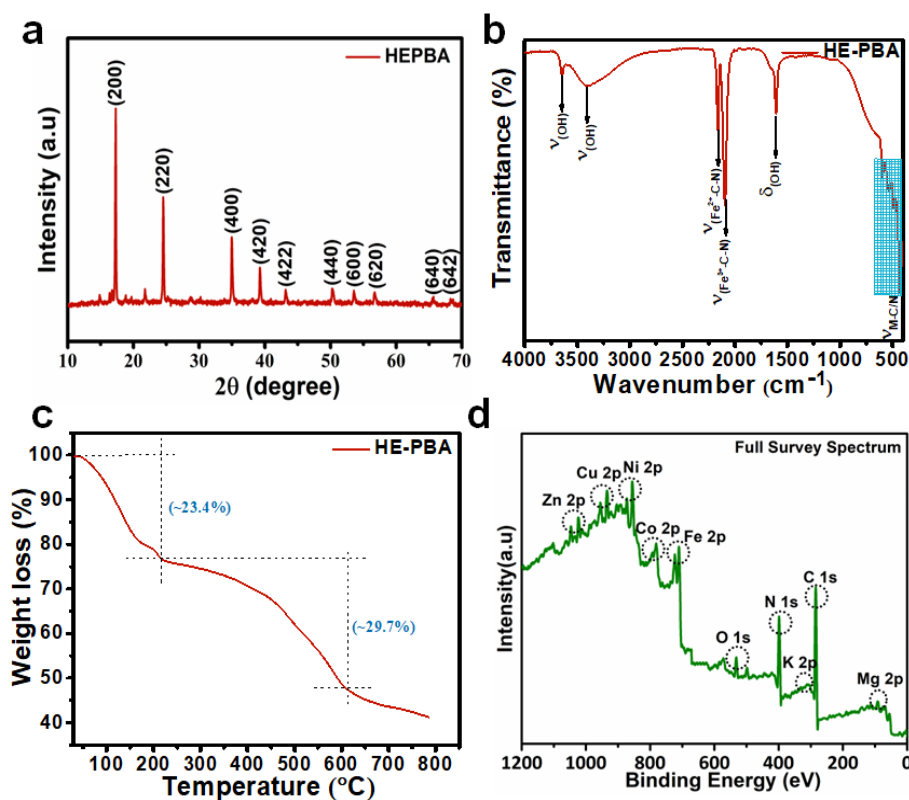


**Figure 5.3** PXR patterns, FTIR, TGA, and XPS patterns of HEPBAs.

The surface morphologies and composition of the samples were investigated by FE-SEM and TEM micrographs depicted in **Figure 5.5-5.6** and **Figure 5.7 a-l**. The ternary PBAs, namely CuNiFe-PBA, CuCoFe-PBA, CuZnFe-PBA, and CuMgFe-PBA, display a consistent cubic morphology with varying particle sizes, matching with typical PBA morphology. Notably, CuZnFe-PBA exhibits a cube with coarse

edges and a uniformly smooth surface, distinguishing it from the other ternary PBAs, which display sharp-edged cubes. For quaternary PBAs (CuNiCoFe-PBA, CuNiZnFe-PBA, and CuNiMgFe-PBA), imperfect cubical structures with an average size of  $\sim 100$  nm were observed.

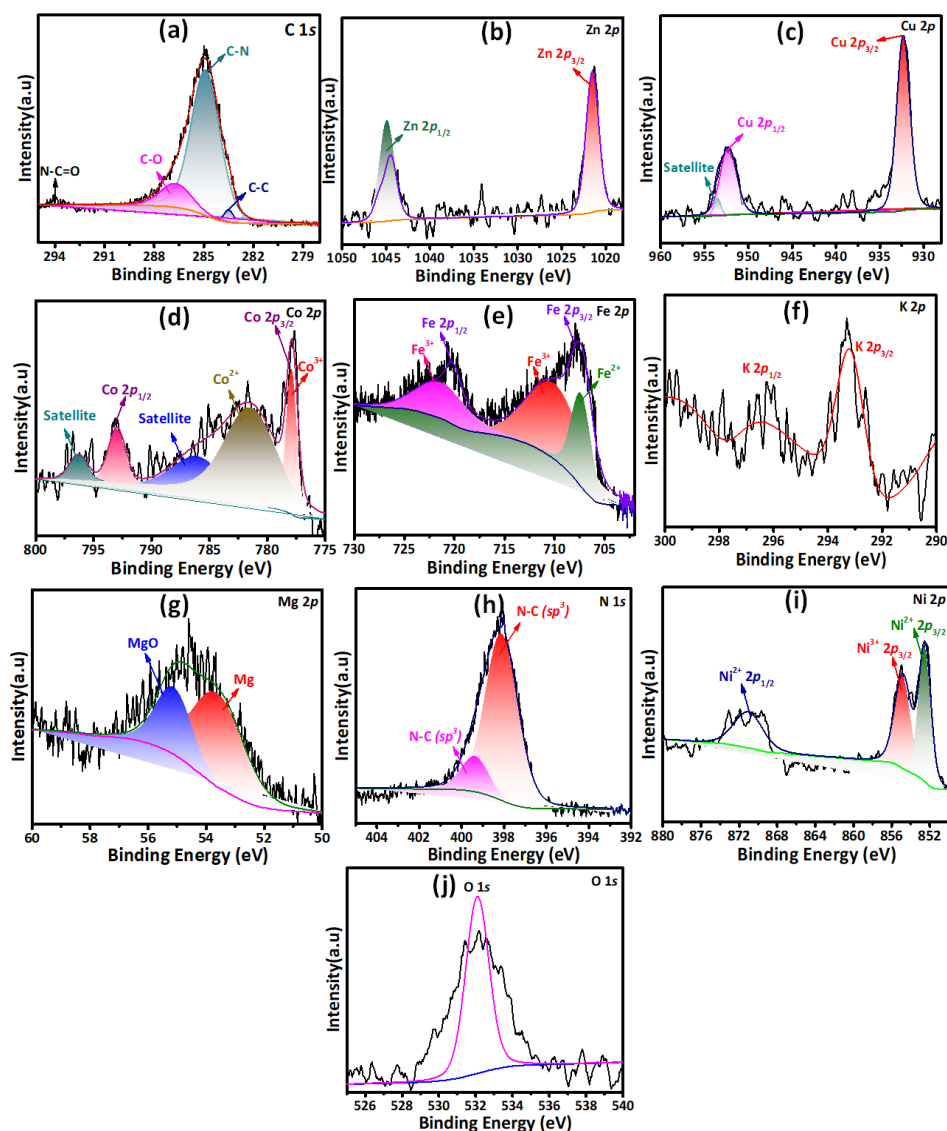


**Figure 5.4 (a-j).** The fitted XPS spectrum of (a) C (b) Zn (c) Cu (d) Co (e) Fe (f) K (g) Mg (h) N (i) Ni (j) O

The morphological investigation of HEPBA reveals a smooth and perfect cubical structure with an average size of  $\sim 150$  nm (**Figure 5.7a,b**). All the PBAs indicate a low defect in the structure due to the uniform growth and nucleation induced by the sodium citrate chelating agent. [R] The EDX spectrum (**Figure 5.7c**) and elemental mapping (**Figure 5.7d**) of HEPBAs show the presence and uniform distribution

of all the elements present in HEPBAs. Further, TEM analysis was also performed to get deeper insight into the morphology, structure, and size of the HEPBA crystals, which is in total agreement with FE-SEM images (**Figure 5.7e-h**).

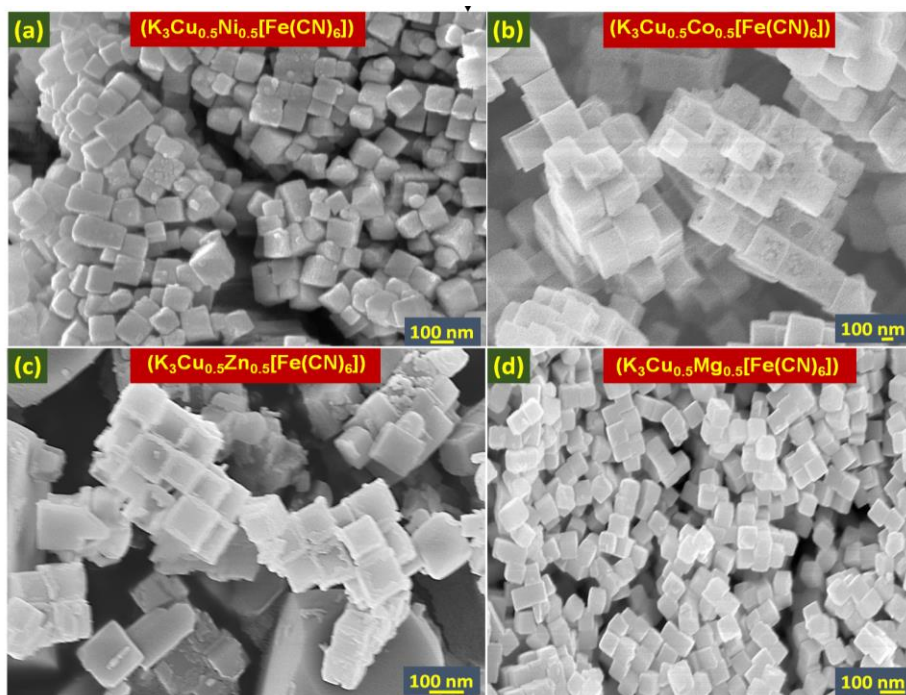


**Figure 5.5** SEM of binary PBAs

The calculated average size from the TEM shows the HEPBA particle size of 132.9 nm (**Figure 5.7f**). **Figure 5.7g-h** depicts a more detailed TEM image of HEPBAs, revealing a perfect cubic structure.

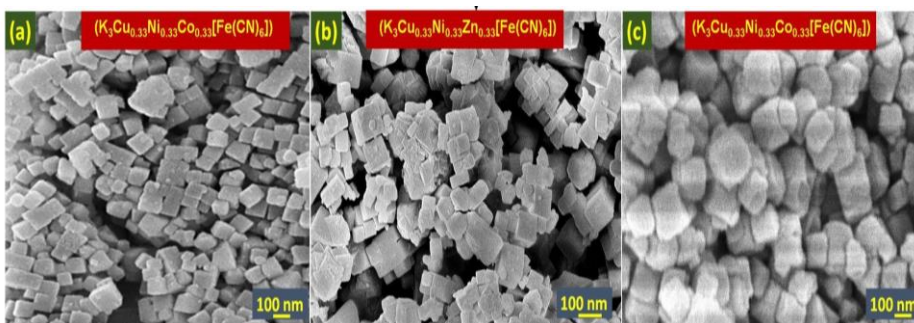


**Figure 5.6** SEM of ternary PBAs

The high-resolution TEM images of HEPBA crystals and their SAED patterns were also examined (**Figure 5.7 i-l**). The HR-TEM reveals an interplanar spacing (d) value of 0.52 nm for the HEPBA crystal

corresponding to its 200 planes. The SAED pattern of HEPBA exhibits multiple concentric diffraction rings, suggesting its crystalline nature.

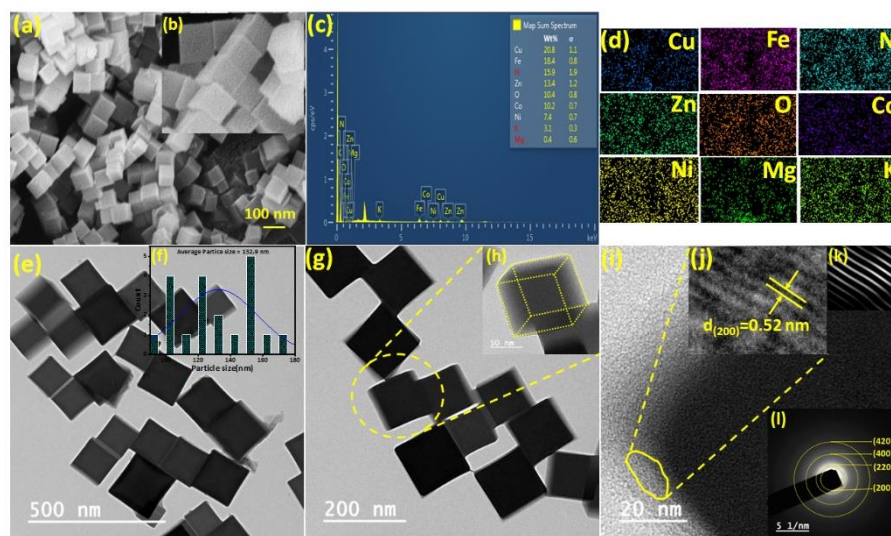


**Figure 5.7** FESEM,EDX, Elemental Mapping, TEM, HRTEM, and SAED pattern of HEPBA.

#### 5.4.2 Electrochemical Measurement

The electrochemical performance of all the synthesized materials was analyzed using various techniques like cyclic voltammetry, galvanostatic charge-discharge, and electrochemical impedance spectroscopy. Initially, the cyclic voltammetry of all multi-metal Prussian blue was performed in the range of 0-1.0 V at a scan rate of 10 mVs<sup>-1</sup> (**Figure. 5.8a-5.9a** and **Figure 5.10a**). The cyclic voltammetry of all the samples show a set of anodic and cathodic peaks which correspond to M<sup>2+/3+</sup> oxidation state couple of redox-active transition metals present in the materials.

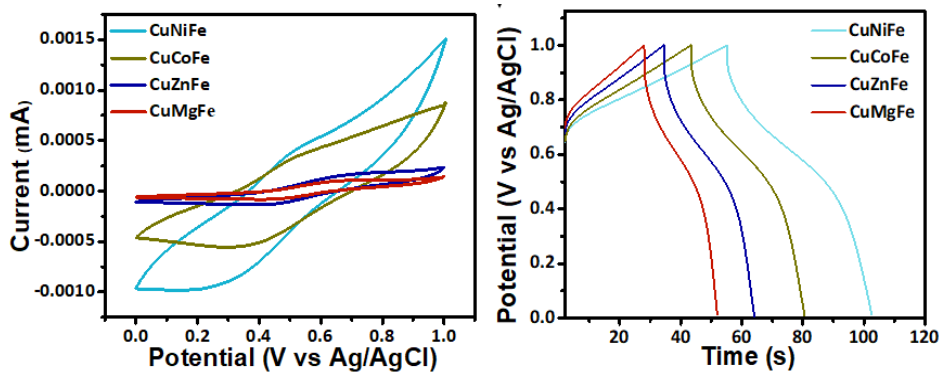


**Figure 5.8** CV and GCD profiles of binary PBAs

Owing to the faradaic process accompanying sodiation and desodiation steps, anodic and cathodic peaks appear significantly shifted on potential axes, and also, the cyclic voltammograms feature a non-rectangular shape, indicative of a battery-type behavior. Upon comparison of peak currents and CV areas of all binary (**Figure 5.8a**), ternary (**Figure 5.9a**), and quinary (HEPBA) PBAs (**Figure 5.10a**), it was observed that HEPBA shows the highest current density and cyclic voltammogram area compared to binary and ternary PBAs. Between binary and ternary PBAs, ternary PBAs were found to exhibit greater values than binary PBAs.

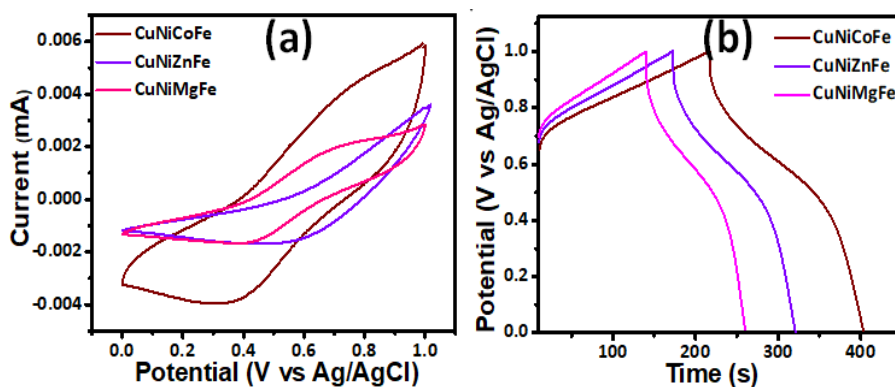


**Figure 5.9** CV and GCD profiles of ternary PBAs

These observations suggest that the highest charge storage capacity is rendered by HEPBA, followed by ternary PBAs and then binary PBAs. It implies that upon increasing the number of principal metals in PBAs, ie. upon increasing the configurational entropy of PBA,

charge storage performance improves due to cocktail effects arising from the synergism of the electronic structure of individual metal centers.

The cyclic voltammetry of HEPBAs was performed at different scan rates ( $10 \text{ mVs}^{-1}$  to  $500 \text{ mVs}^{-1}$ ) (**Figure 5.10a**), and it was also observed that with the increase in scan rate observed current density and area under the curve of the cyclic voltammogram increased. The CV profile of HEPBA shows negligible change upon changing the scan rate signifies the fast insertion mechanism occurring at the electrode. [R] Further, the charge storage mechanism of the HEPBA electrode was assessed using the Power law. The linear fittings of  $\ln i$  vs.  $\ln v$  during cathodic and anodic scans for HEPBA are given in **Figure 5.10 b**, giving the b values of 0.55 and 0.61, respectively, suggesting that charge storage predominantly occurs through a faradaic process with a slight capacitive contribution. Additionally, it is noted that during the anodic scan, the b value increases (0.61) compared to the cathodic scan (0.55), resembling behavior closer to EDLCs, which is attributed to diffusion limitations. To evaluate the specific capacity, galvanostatic charge-discharge (GCD) studies were performed for all multi-metal Prussian blue. The GCD profiles of binary, ternary, and HEPBA at  $1 \text{ Ag}^{-1}$  have been shown in **Figure. 5.8b-5.9b, and 5.10c**, which reveal that the HEPBA exhibits the highest discharging time compared to binary and ternary PBAs. The obtained specific capacities at  $1 \text{ Ag}^{-1}$ , calculated using the discharge curve of the GCD profile, were found to be highest for HEPBA(**Figure. 10d**) with a value of  $435 \text{ Ag}^{-1}$  at  $1 \text{ Ag}^{-1}$ . It is evident from the specific capacity values that the cocktail and high-entropy effects lead to a significant increase in the specific capacity of HEPBA compared to binary and ternary PBAs. The specific capacity of individual binary, ternary, and HEPBA are depicted as a bar chart in **Figure. 10d**.

Further, electrochemical impedance spectroscopy (EIS) in the frequency range of  $0.01 \text{ Hz}$ – $100 \text{ kHz}$  with a  $10 \text{ mV}$  AC amplitude was performed to understand the charge storage behavior and impedance of

the HEPBA electrode, which is shown in **Figure. 10e**. The orientation of the impedance line in the Nyquist plot helps to assess charge storage behavior. From the Nyquist plot, it can be observed that the impedance line corresponding to HEPBA is between the imaginary and real axes. This observation suggests that HEPBA shows EDLC as well as faradaic behavior. The Bode plots for the electrode, showing the variation of impedance phase angle with the frequency, is given in inset **Figure 10e**. The observed impedance phase angle for HEPBA at 0.01 Hz is  $24.3^\circ$ , supporting the conclusion drawn from the Nyquist plots.

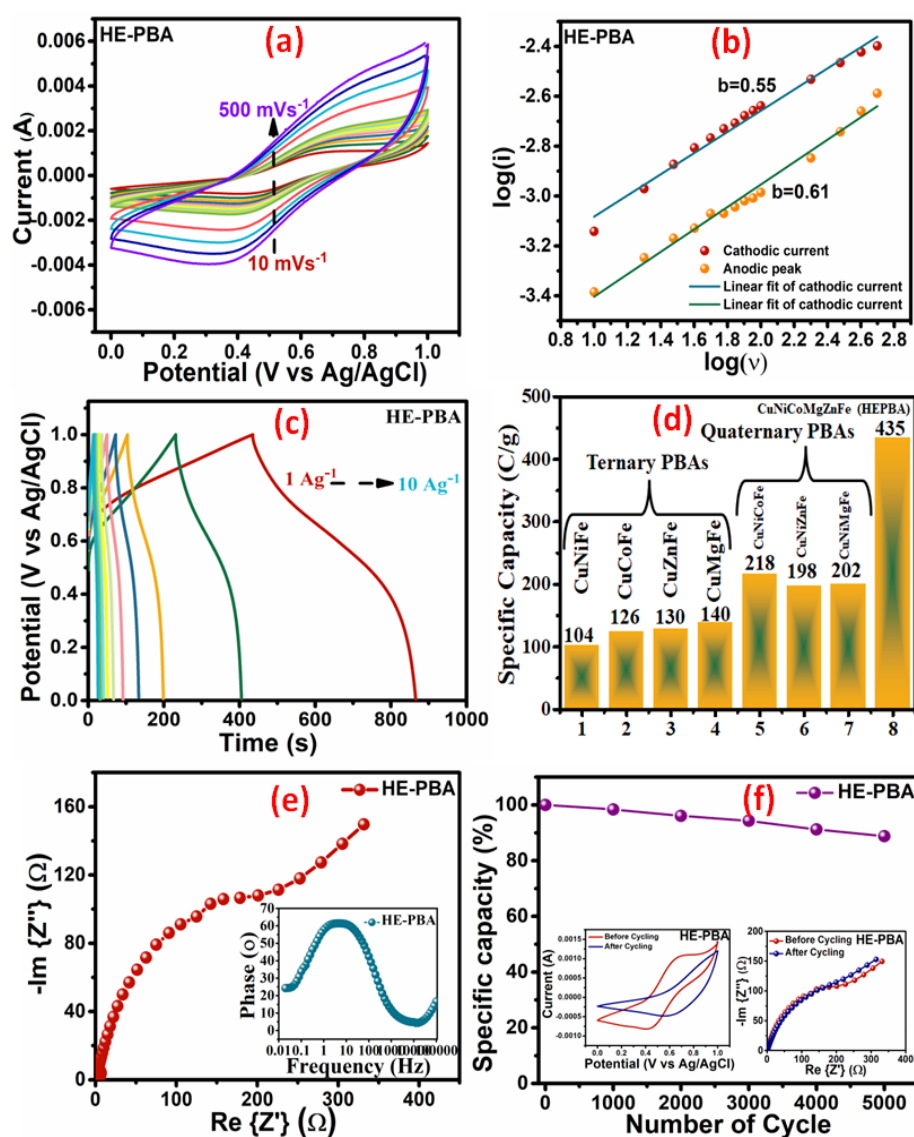


**Figure 5.10.** CV profiles of HEPBAs at different scan rates (10-500  $\text{mVs}^{-1}$ ) (b) Power law for charging and discharging (c) GCD of HEPBA

at different current density (d) Specific capacity of PBAs (e) Nyquist plot (inset) Bode plot (f) stability analysis of 5000 cycles.

Cyclic stability is an important consideration for the practical application of any electrode material. Therefore, the cyclic stability of HEPBA was studied for 5000 GCD cycles at a current density of  $10 \text{ Ag}^{-1}$  (Figure 5.10f). The study reveals that, after 5000 cycles, HEPBA shows 88.1% capacity retention, which is an acceptable value for practical ability. Moreover, the cyclic voltammograms of the initial electrode after 5000 cycles were compared (inset in Figure 5.10f), revealing the absence of oxidation and reduction peaks with only a minor decrease in the CV area after 5000 cycles. The absence of these peaks is attributed to diffusion limitations, resulting in predominantly EDLC charge storage following 5000 cycles. Also, the Nyquist plots of the fresh and after 1000 cycles HEPBA show an almost similar pattern inset (Figure 5.10f). These observations corroborate that the cyclic stability and reversibility of the HEPBA electrode material are maintained for the long run, even in the absence of any conducting additives or expensive commercial binders.

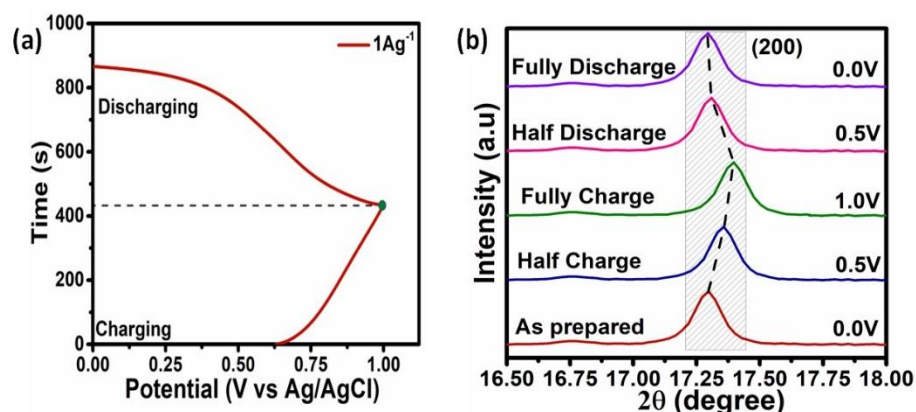


**Figure 5.11 a-c.** GCD of a composite at  $1 \text{ Ag}^{-1}$  and associated P-XRD pattern (c) zoomed portion of the change in peak position at  $17.2$  and  $35.2^\circ$ .

In addition, powder X-ray diffraction (P-XRD) was employed to confirm the intercalation mechanism of charge storage in the HEPBA, in which charging and discharging of HEPBA is accompanied by intercalation and de-intercalation of  $\text{Na}^+$  in its cubic structure. P-XRD

diffraction patterns (positions of (200) peak) of HEPBAs at various charging stages from 0.0 V to 1.0 V versus Ag/AgCl are depicted in **Figure 5.11a-c** to discern structural changes that occur during the charging and discharging process.

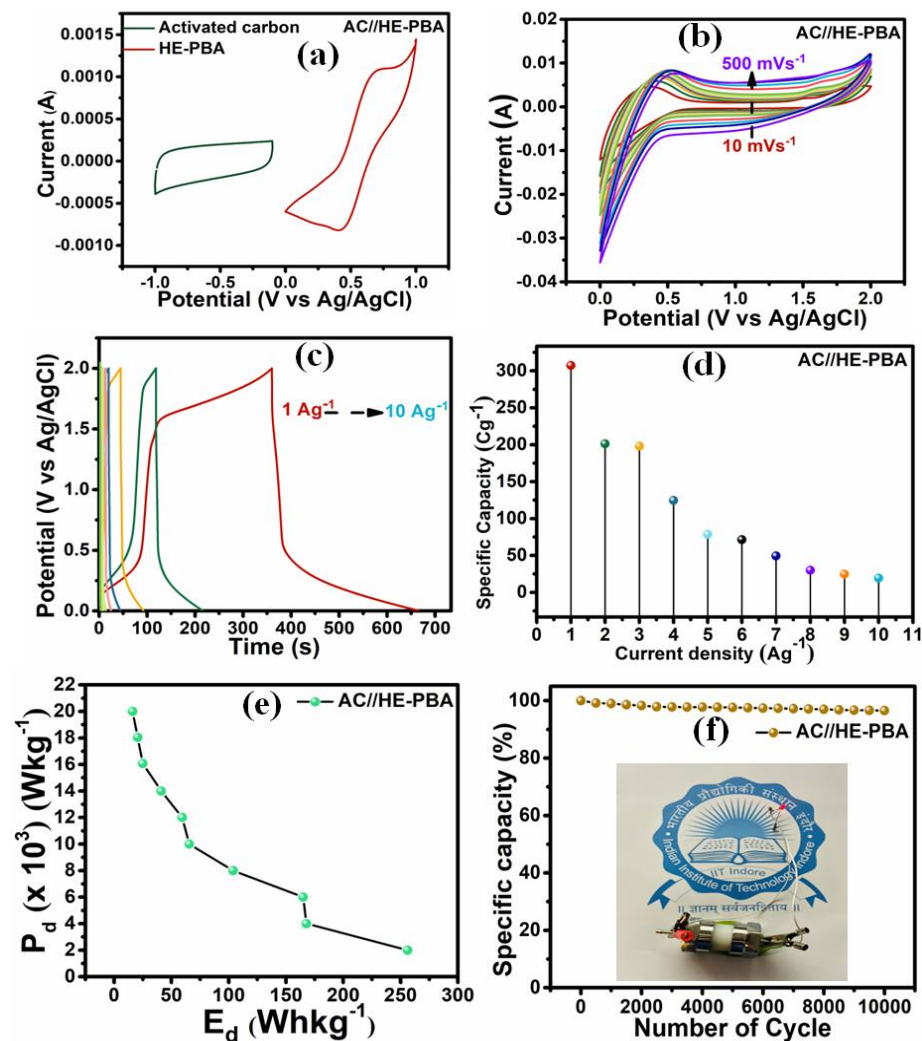


**Figure 5.12** (a) CV profiles of AC and HEPBA in negative and positive range respectively. (b) CV profiles of HEPBA at different scan rates (c) GCD profiles at different current densities (1-10 Ag<sup>-1</sup>) (d) Specific capacitance variations with changing current densities. (e) Specific capacity at different current density (e) Ragone plot (energy density vs. power density) of the fabricated device (f) Cycling performance for 10000 consecutive cycles (insets show Glowing LED using the fabricated device).

As can be observed during charging, the (200) peak gradually shifts towards a higher angle, indicating the reduction in the interlayer spacing of 200 planes due to the de-intercalation of Na<sup>+</sup> ions. However, upon discharging, the (200) peak returns to its original position, suggesting the re-intercalation of Na<sup>+</sup> ions. These observations, along with the calculated *b* value from Power law, clearly corroborate that the charging-discharging in HEPBA is dominated by the faradaic process, accompanying desodiation and sodiation, respectively.

To understand the practical applicability of HEPBA, a solid-state asymmetric device (AC//HEPBA) was assembled using activated carbon as an anode, HEPBA as a cathode, and a cellulose membrane as a separator in a Swagelok cell. Initially, individual cyclic voltammetry of the anode and cathode at 10 mVs<sup>-1</sup> in their respective operating potential was performed to do the mass balancing in fabricating the final device. Apart from the calculation of mass balancing, it is also important for estimating the stable electrochemical windows of individual electrode materials to prevent any parallel electrochemical process. As shown in **Fig. 12a**, the CV curve of activated carbon recorded within a potential window of -1.0 to 0 V displays a nearly rectangular shape, and no redox peaks are observed, indicating a typical characteristic of electrical double-layer capacitor behavior. On the other hand, the HEPBA electrode features anodic and cathodic peaks related to M<sup>2+/3+</sup> redox couple in the potential window 0 to 1.0 V without any sign of HER or OER reactions. Consequently, the cell voltage of the assembled full cell was optimized, achieving an operational voltage of 2 V. Afterwards, the CV of the asymmetrical device was recorded within 2 V cell voltage at various scan rates (10 to 500 mVs<sup>-1</sup>), showing a voltammogram featuring combined effect of EDLC and faradaic process originating from activated carbon and HEPBA, respectively (**Fig. 12b**). Further, the specific capacity of the device was calculated using the GCD studies at various current densities (1–10 Ag<sup>-1</sup>) (**Fig. 12c**). The change in specific capacity at different current densities is given in **Fig. 12c**, showing a decreasing trend with the increasing current density due to diffusion limitation. The device displays a maximum specific capacity of 315 Cg<sup>-1</sup>

<sup>1</sup> at 1 Ag<sup>-1</sup>, which reduces to 41 Cg<sup>-1</sup> at 10 Ag<sup>-1</sup> current density (**Fig. 12d**). Energy density and Power density are essential criteria for the practical applications of any energy storage device. The Ragone plot of the energy density ( $E_d$ ) vs. power density ( $P_d$ ) for the fabricated device is given in **Fig 12e**, which shows an expected pattern of increasing energy density with a decrease in the power density and vice versa. The as-prepared device shows a maximum energy density of 252 Whkg<sup>-1</sup> at a power density of 2 kWkg<sup>-1</sup> and a maximum power density of 20 kWkg<sup>-1</sup> at 25 Whkg<sup>-1</sup> energy density. The cyclic stability of the fabricated prototype device has been investigated for 10000 GCD cycles at 10 Ag<sup>-1</sup> current density in the potential window of 0 – 2.0 V (**Fig. 12f**). After 10000 charging-discharging cycles the device shows a capacity retention of 93.2%, confirming exceptional cyclic stability. Moreover, the demonstration of practical usage of the device has been done by glowing a Red LED (inset **Fig. 12f**). The obtained results are comparable to or higher than the recently reported PBAs for energy storage applications.

## 5.5 Summary

The study presented reports on the synthesis and characterization of a new series of multi-metallic Prussian blue analogs (PBAs) for application in Na-ion hybrid capacitors. The PBAs were synthesized using a co-precipitation method with metal salt precursors (Co, Ni, Cu, Mg, Zn) and  $K_3[Fe(CN)_6]$ . Various binary, ternary, and quinary PBAs were prepared, with a focus on increasing entropy (number of transition metal ions) to enhance charge storage capabilities. The electrochemical performance of these PBAs was evaluated using a three-electrode setup, revealing that PBAs with higher entropy exhibited significantly improved charge storage performance. Notably, the quinary PBA (HEPBA) demonstrated the highest performance with a charge storage capacity of  $435\text{ Cg}^{-1}$ . Furthermore, an asymmetrical Na-ion hybrid capacitor device was assembled using a HEPBA cathode and activated carbon (AC) anode in a Swagelok cell, with  $Na_2SO_4$  gel electrolyte. This device exhibited impressive performance metrics including a maximum energy density ( $252\text{ Whkg}^{-1}$ ) and maximum power density ( $20\text{ kWkg}^{-1}$ ). Importantly, the capacitor demonstrated excellent capacity retention of 93.2% after 10,000 charge-discharge cycles. In summary, the investigation highlights HEPBAs as promising candidates for future advancements in electrochemical energy storage technologies

## References

- [1] J. Ding, W. Hu, E. Paek, D. Mitlin, Review of Hybrid Ion Capacitors: From Aqueous to Lithium to Sodium, *Chem. Rev.* 118 (2018) 6457–6498. <https://doi.org/10.1021/acs.chemrev.8b00116>.
- [2] H. Wang, C. Zhu, D. Chao, Q. Yan, H.J. Fan, Nonaqueous Hybrid Lithium-Ion and Sodium-Ion Capacitors, *Advanced Materials* 29 (2017) 1702093. <https://doi.org/10.1002/adma.201702093>.
- [3] J. Sun, B. Luo, H. Li, A Review on the Conventional Capacitors, Supercapacitors, and Emerging Hybrid Ion Capacitors: Past, Present, and Future, *Adv Energy and Sustain Res* 3 (2022) 2100191. <https://doi.org/10.1002/aesr.202100191>.
- [4] P.R. Bommireddy, J.B. Karnam, C.S. M, S.-H. Park, Ni-Co PBA-decorated CNTs as battery-type cathode materials for potassium-ion hybrid capacitors, *Journal of Energy Storage* 62 (2023) 106870. <https://doi.org/10.1016/j.est.2023.106870>.
- [5] T. Miao, J. Zhang, Y. Wang, K. Fang, Z. Wang, K. Zhan, B. Zhao, Composite cathode with low-defect NiFe Prussian blue analogue on reduced graphene oxide for aqueous sodium-ion hybrid supercapacitors, *Journal of Colloid and Interface Science* 648 (2023) 768–777. <https://doi.org/10.1016/j.jcis.2023.06.035>.
- [6] J. Choi, J. Lim, D. Kim, S. Park, B. Yan, D. Ko, Y. Cho, L.Y.S. Lee, Y. Piao, CoFe Prussian blue analogues on 3D porous N-doped carbon nanosheets boost the intercalation kinetics for a high-performance quasi-solid-state hybrid capacitor, *J. Mater. Chem. A* 10 (2022) 14501–14512. <https://doi.org/10.1039/D2TA03033K>.
- [7] X. Wu, Y. Ru, Y. Bai, G. Zhang, Y. Shi, H. Pang, PBA composites and their derivatives in energy and environmental applications, *Coordination Chemistry Reviews* 451 (2022) 214260. <https://doi.org/10.1016/j.ccr.2021.214260>.
- [8] X. Xiao, G. Zhang, Y. Xu, H. Zhang, X. Guo, Y. Liu, H. Pang, A new strategy for the controllable growth of MOF@PBA architectures, *J. Mater. Chem. A* 7 (2019) 17266–17271. <https://doi.org/10.1039/C9TA05409J>.

- [9] F. Wang, X. Wang, Z. Chang, X. Wu, X. Liu, L. Fu, Y. Zhu, Y. Wu, W. Huang, A Quasi-Solid-State Sodium-Ion Capacitor with High Energy Density, *Advanced Materials* 27 (2015) 6962–6968. <https://doi.org/10.1002/adma.201503097>.
- [10] K. Jiang, S. Yang, W. Chen, K. Wang, M. Gao, L. Ning, R. Lv, H. Yu, M. Fu, Free-Standing  $\text{Co(OH)}_2$  /Prussian Blue Analogue Nanostructured Electrodes for Flexible Na-Ion Supercapacitors with an Ultrawide Potential Window, *ACS Appl. Nano Mater.* 7 (2024) 6650–6658. <https://doi.org/10.1021/acsnm.4c00603>.
- [11] J. Nai, X.W. (David) Lou, Hollow Structures Based on Prussian Blue and Its Analogs for Electrochemical Energy Storage and Conversion, *Advanced Materials* 31 (2019) 1706825. <https://doi.org/10.1002/adma.201706825>.
- [12] J. Chen, L. Wei, A. Mahmood, Z. Pei, Z. Zhou, X. Chen, Y. Chen, Prussian blue, its analogues and their derived materials for electrochemical energy storage and conversion, *Energy Storage Materials* 25 (2020) 585–612. <https://doi.org/10.1016/j.ensm.2019.09.024>.
- [13] X. Zhao, Z. Xing, C. Huang, Investigation of high-entropy Prussian blue analog as cathode material for aqueous sodium-ion batteries, *J. Mater. Chem. A* 11 (2023) 22835–22844. <https://doi.org/10.1039/D3TA04349E>.
- [14] P.A. Ibrahim, İ. Özkul, C.A. Canbay, An overview of high-entropy alloys, *Emergent Mater.* 5 (2022) 1779–1796. <https://doi.org/10.1007/s42247-022-00349-z>.
- [15] Y. Wang, N. Jiang, C. Yang, J. Liu, S. Sun, X. Wang, J. Yang, Y. Liu, High-entropy prussian blue analogs with 3D confinement effect for long-life sodium-ion batteries, *J. Mater. Chem. A* 12 (2024) 5170–5180. <https://doi.org/10.1039/D3TA07671G>.
- [16] M.K. Singh, S. Krishnan, K. Singh, D.K. Rai, Effective assembling of nickel oxide-reduced graphene oxide heterostructures for ultrahigh capacity supercapattery, *Journal of Power Sources* 595 (2024) 234060. <https://doi.org/10.1016/j.jpowsour.2024.234060>.

- [17] A. Singh, A. Chandra, Significant Performance Enhancement in Asymmetric Supercapacitors based on Metal Oxides, Carbon nanotubes and Neutral Aqueous Electrolyte, *Sci Rep* 5 (2015) 15551. <https://doi.org/10.1038/srep15551>.
- [18] M. Nakayama, In situ FTIR studies on Prussian blue (PB)-, polyaniline (PAn)- and inner PBlouter PAn film-modified electrodes, (n.d.).
- [19] O.F. Dippo, K.S. Vecchio, A universal configurational entropy metric for high-entropy materials, *Scripta Materialia* 201 (2021) 113974. <https://doi.org/10.1016/j.scriptamat.2021.113974>.
- [20] S.-C. Wang, M. Gu, L. Pan, J. Xu, L. Han, F.-Y. Yi, The interlocked *in situ* fabrication of graphene@prussian blue nanocomposite as high-performance supercapacitor, *Dalton Trans.* 47 (2018) 13126–13134. <https://doi.org/10.1039/C8DT02331J>.
- [21] Y. Xu, M. Chang, C. Fang, Y. Liu, Y. Qiu, M. Ou, J. Peng, P. Wei, Z. Deng, S. Sun, X. Sun, Q. Li, J. Han, Y. Huang, In Situ FTIR-Assisted Synthesis of Nickel Hexacyanoferrate Cathodes for Long-Life Sodium-Ion Batteries, *ACS Appl. Mater. Interfaces* 11 (2019) 29985–29992. <https://doi.org/10.1021/acsami.9b10312>.
- [22] Z. Li, M. Dadsetan, J. Gao, S. Zhang, L. Cai, A. Naseri, M.E. Jimenez-Castaneda, T. Filley, J.T. Miller, M.J. Thomson, V.G. Pol, Revealing the Thermal Safety of Prussian Blue Cathode for Safer Nonaqueous Batteries, *Advanced Energy Materials* 11 (2021) 2101764. <https://doi.org/10.1002/aenm.202101764>.
- [23] X. Yan, Y. Yang, E. Liu, L. Sun, H. Wang, X.-Z. Liao, Y. He, Z.-F. Ma, Improved cycling performance of prussian blue cathode for sodium ion batteries by controlling operation voltage range, *Electrochimica Acta* 225 (2017) 235–242. <https://doi.org/10.1016/j.electacta.2016.12.121>.

# Chapter 6

## Conclusions and Future Research Directions

### 6.1 Conclusion

The research presented in this thesis focuses on investigating diverse charge storage mechanisms and their application in designing efficient energy storage devices, particularly supercapacitors. To achieve optimal performance in the supercapacitor, the electrode materials should have various properties such as high surface area, high conductivity, redox-active metal centers, good electrochemical stability, fast ion transport, compatibility with different electrolytes, cost-effectiveness, and earth-abundant precursor. Based on these rationales, this study explores various electrode materials like metal-organic frameworks (MOFs), metal oxides and sulfide composites, and high entropy Prussian blue analogs to understand different charge storage mechanisms essential for sustainable energy technologies.

The introductory chapter elaborates on the fundamental aspects of supercapacitors, including types, electrode materials, and their different charge storage mechanisms. This chapter serves to incite interest and establish the context for the research undertaken in this thesis.

The second chapter focuses on the synthesis of Cu(II) metal-organic framework (Cu-MOF) composites with carbonaceous materials such as reduced graphene oxide (rGO) and carbon nanotubes (CNTs). This research explores the synergistic effects of blending 2D (rGO) and 1D (CNTs) carbon materials showing EDLC behavior with Cu-MOF showing pseudocapacitive behaviors. The compositization of Cu-MOF with carbon materials significantly improves the capacitive (Cu-MOF/rGO:  $C = 365 \text{ Fg}^{-1}$ ,  ${}^{\text{max}}E_d = 57.2 \text{ Whkg}^{-1}$ ,  ${}^{\text{max}}P_d = 2.10 \text{ kWkg}^{-1}$ ; Cu-MOF/CNT:  $C = 348.6 \text{ Fg}^{-1}$ ,  ${}^{\text{max}}E_d = 27.7 \text{ Whkg}^{-1}$ ,  ${}^{\text{max}}P_d = 1.14 \text{ kWkg}^{-1}$ )

and cyclic performance, highlighting the importance of composite electrode design for optimizing supercapacitor performance.

The third chapter details a new method to synthesize NiO and further use it in developing a uniform composite with rGO. This uniform composite acts as a binder-free NiO-rGO composite electrode material exhibiting a unique combination of battery-like and EDLC behaviors. This composite demonstrates an ultra-high charge storage capacity ( $C = 850 \text{ Cg}^{-1}$ ) and excellent capacity retention over extended charge/discharge cycles. The assembled symmetric supercapacitor device using this composite shows superior energy density and power density ( ${}^{\max}E_d = 56.6 \text{ Whkg}^{-1}$ ,  ${}^{\max}P_d = 9.65 \text{ kWkg}^{-1}$ ) with stable performance over 10,000 cycles. The integration of first-principal density functional theory (DFT) methods corroborates experimental findings, providing valuable insights into ion-electrode interaction energetics.

The fourth chapter introduces a novel  $\text{Ti}_3\text{C}_2\text{T}_x/\text{CoS}$  composite combining pseudocapacitive and battery-type electrodes fabricated on a carbon cloth (CC) substrate for flexible supercapacitor applications. This hierarchical material boasts excellent pseudocapacitive performance attributed to its high conductivity, rapid charge/discharge rates, improved electrochemical stability, and large surface area. The flexible symmetrical supercapacitor device utilizing this composite electrode exhibits good charge storage ( $C = 120 \text{ Cg}^{-1}$ ,  ${}^{\max}E_d = 13.13 \text{ Wh.kg}^{-1}$ ,  ${}^{\max}P_d = 1.91 \text{ kW.kg}^{-1}$ ) and high stability even after 10,000 cycles, indicating its potential for next-generation flexible energy storage solutions.

The fifth chapter discusses the high-entropy Prussian blue analogs (HEPBAs) as cathode materials for Na-ion hybrid capacitors. This study demonstrates the battery-like behavior of HEPBAs, having enhanced entropy stability leading to improved charge-discharge efficiency, resulting in exceptionally high energy density and power density ( $C = 435 \text{ Cg}^{-1}$ ,  ${}^{\max}E_d = 252 \text{ Wh.kg}^{-1}$ ,  ${}^{\max}P_d = 20 \text{ kW.kg}^{-1}$ ).

Overall, the electrochemical performance of various composite electrodes incorporating carbonaceous materials and MXene composites, and HEPBA alone is summarized in Table 9. Interestingly, the high-entropy Prussian blue analog (HEPBA), which does not contain any composite component, exhibits the best overall performance among the tested electrodes. Notably, the data highlight the exceptional performance of HEPBA, which stands out despite any composite component, underscoring its remarkable efficacy in energy storage applications.

In summary, this thesis contributes significantly to advancing the field of energy storage technologies by investigating diverse electrode materials featuring different combinations of charge storage mechanisms and their application in designing efficient supercapacitor devices. The outcomes of this research are not only important in realizing clean and affordable energy solutions but also pave the way for future innovations in energy storage device design and development.

**Table 9.** Comparison of charge storage performance of different electrode materials investigated in the thesis.

	Electrode	Specific capacitance (F/g) or Capacity (C/g) of electrode	Specific capacitance (F/g) or Capacity (C/g) of device	Energy and power density
Chapter 2 (Part-1)	(Pseudo + EDLC) Cu-MOF/rGO	366 F/g at 1 A/g	156 F/g at 1 A/g	57.2 Wh.kg <sup>-1</sup> 2.10 kW.kg <sup>-1</sup>
Chapter-2 (Part-2)	(Pseudo + EDLC) Cu-MOF/CNT	348.6 F/g at 1 A/g	200 F/g at 1 A/g	27.7 Wh.kg <sup>-1</sup> 1.67 kW.kg <sup>-1</sup>
Chapter 3	(Battery + EDLC) NiO-rGO	850 C/g at 1 A/g	283.3 C/g at 1 A/g	56.6 Wh.kg <sup>-1</sup> 19.6 kW.kg <sup>-1</sup>
Chapter 4	(Pseudo + Battery ) Ti <sub>3</sub> C <sub>2</sub> T <sub>x</sub> /CoS	120 C/g at 1 A/g	118 C/g at 1 A/g	13.13 Wh.kg <sup>-1</sup> 1.91 kW.kg <sup>-1</sup>
Chapter 5	(Battery) HEPBA	435 C/g at 1 A/g	315 C/g at 1 A/g	252 Wh.kg <sup>-1</sup> 20 kW.kg <sup>-1</sup>

## 6.2 Future research directions

Electrochemical energy storage devices, such as supercapacitors, play a crucial role in the present scenario, supporting the speedy transition of green and renewable energy sources as primary energy sources from

conventional fossil fuels. The ongoing research and development in this field aims to create devices with high energy density and power density, essential for advancing energy storage technologies. This thesis explores some of the electrode materials that hold great promise to be integrated into future energy storage in order to develop more efficient systems. However, to further push the performance limit, several critical areas require further exploration and development.

- **Exploration of New Composite Materials:** Our research underscores the importance of composite materials in enhancing charge storage performance. Future investigations can focus on exploring novel combinations of carbonaceous materials, MXenes, and other nanomaterials to develop advanced composite electrodes with improved energy storage capabilities. By systematically studying the synergistic effects of different materials, researchers can identify optimal combinations that maximize specific capacitance and cycling stability.
- **Advanced Characterization Techniques:** Future research efforts should be focused on advanced characterization techniques, including in situ and operando methods, to gain deeper insights into the electrochemical behavior of electrodes. Real-time monitoring of structural and chemical changes during charge-discharge cycles can provide crucial information for optimizing electrode design and performance.
- **Theoretical Modeling and Simulation:** Computational modeling and simulation play a vital role in predicting and understanding the behavior of electrode materials at the atomic and molecular levels. Future studies can employ density functional theory (DFT) and molecular dynamics (MD) simulations to understand fundamental charge storage mechanisms and guide the rational design of high-performance electrode materials.
- **Scale-up and Practical Applications:** Transitioning from laboratory-scale level to scalable manufacturing processes is

essential for the practical implementation of advanced energy storage technologies. Future research should focus on developing scalable synthesis methods and techniques to facilitate the commercialization of composite electrode materials for real-world applications. Moreover, the optimization of mass loading of electrode materials investigated in the thesis on different current collectors is a crucial exercise that should be performed. In short, the focus should be on improving the TRL level of the work.

- **Environmental Sustainability and Cost-effectiveness:** As the demand for sustainable energy solutions grows, future research should also prioritize the development of environmentally friendly and cost-effective electrode materials. Exploring green synthesis routes can minimize the environmental impact of energy storage technologies. For example, in the case of HEPBA electrodes explored in this thesis, cheaper and more environmentally benign alternatives of redox-active transition metal ions may be explored.
- **Multi-functional Energy Storage Devices:** Beyond supercapacitors, future research can explore the integration of composite electrodes in different energy storage devices, such as batteries. By combining the advantages of different energy storage mechanisms, these devices can offer enhanced performance and versatility for diverse applications.

In conclusion, the future of energy storage research lies in the continuous exploration of novel materials, advanced characterization techniques, and innovative electrode architectures to achieve higher energy density, improved cycling stability, and scalable synthesis processes. By addressing these challenges and embracing interdisciplinary approaches, researchers can accelerate the development of affordable, sustainable, and high-performance energy storage solutions for a cleaner and greener future.